論文 / 著書情報
Article / Book Information

題目(和文)	高周波熱プラズマによる金属ホウ化物ナノ粒子の合成
Title(English)	Synthesis of metal boride nanoparticles by RF thermal plasmas
著者(和文)	ChengYing Ying
Author(English)	Yingying Cheng
出典(和文)	学位:博士(工学), 学位授与機関:東京工業大学, 報告番号:甲第9596号, 授与年月日:2014年6月30日, 学位の種別:課程博士, 審査員:渡邉　隆行,馬場　俊秀,山元　公寿,山口　猛央,石谷　暖郎
Citation(English)	Degree:Doctor (Engineering), Conferring organization: Tokyo Institute of Technology, Report number:甲第9596号, Conferred date:2014/6/30, Degree Type:Course doctor, Examiner:,,,,
学位種別(和文)	博士論文
Type(English)	Doctoral Thesis

Table of contents

1. General Introduction

1.1 Plasma technology

Plasma is one of the four fundamental states of matter (the others being solid, liquid, and gas), comprising more than 99% of the visible universe, and permeate the solar system, interstellar and intergalactic environments. Plasma is an ionized gas, consisting of electrons, atomic ions, molecular ions, neutral atoms and molecules in the ground and excited states. The negative and positive charges compensate each other, and thus most of them are electrically neutral. This is known as the property of quasi-neutrality. The presence of the charged particles in the plasma causes it to have a high electrical conductivity. So it is an electrified gas with both positive ions and negative electrons moving freely. This usually happens when a gas is given more energy and the negatively charged electrons, which are held by the pull of the nucleus, breaks free. The word "PLASMA" was first applied to ionized gas by Dr. Irving Langmuir, an American chemist and physicist, in 1929 [1-5].

Plasma temperature and density ranges from relatively cool and tenuous (like aurora) to very hot and dense (like the central core of a star). So plasma can be described in terms of the difference between the electron temperature and the temperature of the heavy particles. Either at low pressure or at lower power levels, or in different kinds of pulsed discharge systems plasma is labeled a cold, or non-equilibrium plasma. The electrons gain a large amount of energy from the electric field and have a high mean free path, but the rate of energy transfer to ions and neutral particles is low. Because of their high energy, the temperature of the electrons is much greater than that of the heavy particles. It can be conventionally presented in the collisional weakly ionized plasma $T_e > T_v > T_r \approx T_i \approx T_o$. Electron temperature T_e is highest in the system, followed by the temperature of vibrational excitation of molecules T_v, the lowest temperature is usually shared in plasma by heavy neutrals T_o, temperature of translational degree of freedom or simply gas temperature, ions T_i, as well as rotational degree of freedom of molecules T_r [5-8].

As the pressure increases the collision rate rises and the electron and heavy particle temperatures approach each other. When temperatures come to within a few percent, the plasma

is termed hot or thermal plasma. The plasma is then in a state of local thermodynamic equilibrium (LTE). This means that at any point in the plasma a unique temperature can be defined, although it may not be the same throughout. Thermal plasmas are usually more powerful, whereas non-thermal plasmas are more selective [5-8].

The temperature difference between electrons and heavy neutral particles due to Joule heating in the collisional weakly ionized plasma is conventionally proportional to the square of the ratio of the electric field (*E*) to the pressure (*P*). Only in the case of small values of E/p, the temperature of electrons and heavy particles approach each other.

Each of these two categories of plasmas has distinctive properties and gives rise to different processing conditions, e.g., because of relatively lower particle densities (less than 10^{20} m^{-3}) and higher electron temperature, the non-thermal plasmas can provide the possibility of usages for low temperature plasma chemistry and for heat sensitive materials treatment including polymers and biological tissues. In contrast, in thermal plasmas, the gas temperature has reached up to 10^4 K or more and the electron density is of the order of 10^{23}-10^{28} m^{-3} [9-12]. These unique properties of the thermal plasmas are widely used in various industries [11, 12].

1.2 Thermal plasma

Thermal plasmas can be characterized as a high enthalpy flame with extremely high temperature fields (1,000~20,000 K) and a wide range of velocity fields from several m/s [11-17] to supersonic values [17, 18], high electron densities (10^{23}-10^{28} m^{-3}). Since the resultant huge enthalpy can be realized for various kinds of plasma forming gases and easily controlled by electricity, thermal plasmas have been expected to facilitate not only fast chemical reactions but also rapid heat transfer in a variety of synthetic routes for nano-sized materials [19-22].

Thermal plasmas and their plasma generators have achieved high technical and scientific importance because of their outstanding properties which are above all.

1.2.1 Properties of thermal plasmas

In this section, brief overview of the most important properties of the thermal plasma will be given, including fundamental processes, species composition, thermodynamic properties, and transport properties.

1) Fundamental Processes

Thermal plasmas are often combined with the presence of steep property gradients and the simultaneous presence of particulate matter. The special characteristics of thermal plasmas offer a combination of unique advantages:

Thermal plasmas are a processing medium with one of the highest energy densities; the results are high processing rates, high fluxes of radical species, the potential for smaller installations, a wide choice of reactants, and high quench rates. Use of electricity as the primary energy source assures independence from the oxygen potential of the medium and, therefore, a controlled environment [11-17]. Furthermore, gas flow rates are reduced, control of energy flow is facilitated, and a short response time is possible.

LTE requires that transitions between energy states of the plasmas particles and chemical reactions are controlled by micro-reversible collisions with radiative processes playing a negligible role. In LTE plasmas, local gradients of plasma properties (temperature, density, thermal conductivity etc) are small enough to allow particles to arrive at the equilibrium: the diffusion time is significantly longer than the time that the particles take to reach equilibrium. Thermal plasmas approach a state of LTE, which are characterized by their high-energy density and the equality between the temperatures of the heavy particles and those of the electrons [7, 23-26]. For optically thin, homogeneous plasmas, the electron number density is an indicator of whether LTE is satisfied [27, 28], according to the Griem criterion. Research into thermal plasmas under the LTE assumption has in recent years been mainly driven by potential industrial applications and by the ever-increasing demand for existing plasma technology [29-32]. Non-LTE plasmas is microwave-sustained plasmas, where the inelastic collisions between electrons and heavy particles are excitative or ionizing and do not increase the heavy-particle temperature to that of electrons [33-36].

The two temperatures are the electron temperature (T_e) and the heavy-particle temperature (T_h). Since the mass difference between the heavy particles is tiny compared to that between electrons and heavy particles, all the heavy particles have the same temperature T_h, which is sometimes called the plasma temperature or gas temperature.

The LTE conditions can be expressed by:

$$\frac{T_{\mathrm{e}}-T_{\mathrm{h}}}{T_{\mathrm{e}}}=\frac{m_{\mathrm{h}}}{8m_{\mathrm{e}}}=\frac{\lambda_{\mathrm{e}}-E}{\frac{3}{2}k_B T_e}\approx\left(\frac{E}{P}\right)^2<<1 \tag{1}$$

where T and m indicate the temperature and mass of electron and heavy species, respectively. E is the electric field strength and P is the pressure. The parameter E/P plays an important role for

determining the kinetics equilibrium conditions.

2) Species Composition

A prerequisite to obtaining thermodynamic properties of LTE and non-LTE nitrogen plasmas is the determination of the species composition; this is also the starting point to obtain the transport coefficients. If the assumption of LTE is applicable, the distribution of atoms and their ionization products (ions and electrons) obeys the Saha equation. If the volume V and temperature T are maintained constant, the thermodynamic equilibrium is achieved when the total free energy is minimum. If the lowering of ionization potentials due to non-ideal effects is taken into account, the Saha equation can be written as [37-41]

$$\frac{n_e n_{r+1}}{n_r} = 2\left[\frac{U_{r+1}}{U_r}\right]\left(\frac{2\pi m_e K_B T_e}{h^2}\right)^{\frac{3}{2}} \exp\left(-\frac{I_i^{eff}}{K_B T_e}\right), \tag{2}$$

$r = 0,1,..., (Z_{max}-1)$,

where n_e is the number density of free electrons, n_r is the number density of all r-fold ionized atoms, U_r is the state dependent partition function of r-fold ionized atoms, m_e is the mass of an electron, h is Planck's constant, Z_{max} is the maximum allowed ionization stage (atomic number), T_{ex} is the excitation temperature of the relevant chemical reaction, and $I_i^{eff} = I_r - \Delta I_r$ is the effective ionization energy for the ionization process $r \rightarrow (r+1)$, ΔI_r is the lowering of ionization potential as described below.

The lowering of the ionization potential due to interactions between plasma particles, whose influence on the chemical equilibrium concentration increases with the non-equilibrium degree, was not considered in the calculation of the partition functions.

The system of Saha equations, supplemented by the condition of electro-neutrality

$$\sum_{i=1}^{Z_{max}} i n_i = n_e \tag{3}$$

and requiring a constant number of heavy particles (conservation of nuclei in the ionization and recombination processes)

$$\sum_{r=0}^{Z_{max}} n_r = n_h \tag{4}$$

is sufficient for the calculation of the composition of a single chemical species plasma. In Eq. n_h is the total number of heavy particles.

In the case of a mixture containing molecules, the set of mass action laws

(Guldberg-Waage equations) have to be taken into account.

The equilibrium composition of argon at atmospheric pressure and temperature below 15000 K is relatively simple, consisting essentially of Ar, Ar^+, and e. If the plasma is generated from a molecular gas, the number of possible species comprising the plasma is large due to the presence of the products of the initial molecular dissociation step. The chemical processes that may occur in the plasma will include the dissociation of molecules into atoms (AB→A+B) and ionization of some atoms ($A^{z+} \rightarrow A^{(z+1)+}$+e). This work considers N_2 as example, which contains the following gaseous species: molecules N_2, molecular ions N_2^+, atoms N, singly-, doubly- and triply-ionized ions N^+, N^{++} and N^{+++} and electrons *e*, and therefore five independent chemical reactions are included in the calculation:

$N_2 \rightarrow N+N$, $N \rightarrow N^+ + e$, $N_2 \rightarrow N_2^+ + e$, $N^+ \rightarrow N^{++} + e$, $N^{++} \rightarrow N^{+++} + e$

Taking dissociation, ionization, and the presence of species into account, the composition of the plasmas can be calculated through the minimization of Gibbs free energy, which in turn depends on the chemical potentials of the different chemical species present in the plasma gas.

3) Thermodynamic Properties

It defines macroscopic variables (such as mass density, specific heat, temperature, internal energy, entropy, and pressure) that characterize materials and radiation, and explains how they are related and by what laws they change with time.

The energy of a molecular can be divided into translational energy and internal energy [42], these energy are associated with the corresponding translational and internal degrees of freedom of a molecular. The partition function of a species, which establishes the link between the coordinates of microscopic systems and macroscopic thermodynamic properties [43], is the product of its translational and internal partition functions. The translation of particles is of a continuous nature while the internal states are of discrete nature.

In general, the translational contribution to the total partition functions of a molecular or atom is the largest one [44-46]. The translational partition function of species *i* can be obtained by integration over all spatial and momentum coordinates to give

$$Q_i^{tr} = \left(\frac{2\pi m_i k T_i}{h^2} \right)^{\frac{3}{2}} V \tag{5}$$

where *V* is the volume of the system and mi the mass of species *i*.

The internal partition functions for monatomic species consist of the summation over all possible energy. According to Born–Oppenheimer (BO) approximation [47], internal degrees consist of the nuclear potential, electronic excitation, rotation, and vibration. In molecular spectroscopy, because the ratios of the periods of the electronic, vibrational and rotational energies are each related to each other on scales in the order of a thousand, the BO name has also been attached to the approximation where the energy components are treated separately. Therefore, the internal energy of a molecular can be expressed as [48, 49]:

$$Q_t = Q_{tr} \cdot Q_{rot} \cdot Q_{vib} \cdot Q_{el} \cdot Q_{nucl} = \left(\frac{2\pi m_i k T_i}{h^2} \right)^{\frac{3}{2}} V \cdot Q_{el} \cdot Q_{nucl} \tag{6}$$

The main contribution of the electronically excited states is that of the ground state [50]

$$Q_{el} = \sum_s g_s \exp\left(-E_s / kT\right) = g_{0i} \exp\left(-E_0 / kT\right) \tag{7}$$

where g_{0i} and E_0 are the statistical weight and the energy of the ground state.

After obtaining the partition functions of each nitrogen species, the calculation of the thermodynamic properties proceeds in a straightforward manner, employing the following standard thermodynamic relationships.

Mass density [51]:

$$\rho = \sum_{i=1} m_i n_i \tag{8}$$

where m_i and n_i are the mass and the number density of species i in the plasma, respectively. The system is closed and therefore m depends on neither T nor p. The composition of a system generally depends on p and T, $n = n(p, T)$. The volume $V = V(p,T)$ of a system is determined using the state equation of ideal gas $V = nRT/p$.

Internal energy [52]:

$$e = \frac{3}{2}\frac{k}{\rho}\sum_i n_i T_i + \frac{1}{\rho}\sum_i n_i E_i + \frac{k}{\rho}\sum_i n_i T_i^2 \frac{\partial \ln Q_i^{\text{int}}}{\partial T_i} \tag{9}$$

where E_i is the formation energy of species i.

Enthalpy [52]:

$$e = \frac{5}{2}\frac{k}{\rho}\sum_i n_i T_i + \frac{1}{\rho}\sum_i n_i E_i + \frac{k}{\rho}\sum_i n_i T_i^2 \frac{\partial \ln Q_i^{\text{int}}}{\partial T_i} \tag{10}$$

Specific heat C_p at constant pressure is one of the important properties since it determines the magnitude of the convection loss and transient response of thermal plasma. The value C_p can be estimated by [52]

$$C_P = \frac{\partial h}{\partial T_e} \tag{11}$$

4) Transport Properties

Actual plasmas are not uniform and therefore reveal the gradients in such characteristics as particle number densities (n), applied electrical potentials (V), temperature (T), and velocity component (v_x). These gradients can be considered as "driving forces" that give rise to fluxes. The temperature gradient in the gas is the driving force and the physical quantity that is transported in this process is energy [53-57].

In most transport processes, there is a linear relationship between fluxes and driving forces [58]: Flux = (coefficient) (driving force). Such a relationship is called a phenomenological law, and in general case the corresponding transport coefficient is related to the flux density of a quantity x:

J_x = flux density of x – net quantity of x transported across per unit area and unit time. (12)

Where x may be a number of particles (n), a transverse momentum (mv_x), energy ($3kT/2$), or a change (e), corresponding to the following coefficients:

Diffusion (D) expressed in m^2/s:

$$\vec{J}_n = - D grad(n) \tag{13}$$

Viscosity (μ) expressed in kg/ms:

$$\frac{\vec{F}_x}{A} = \vec{J}_{P_x} = \mu \frac{d\vec{v}_x}{d_z} \tag{14}$$

Thermal conductivity (κ)

$$\vec{J}_E = -\kappa \cdot grad(T) \tag{15}$$

Electrical conductivity σ_e expressed in (Ωm^{-1}):

$$\vec{J}_e = - \sigma_e grad(V) \tag{16}$$

where –grad (V) = $\vec{E}$ is the electric field.

In addition, since thermal plasma is a highly luminous body, radiative transport must be considered [59, 60]. The spectrum from typical thermal plasma generated from a monatomic gas reveals continuous as well as line radiation. The electronic transitions of excited atoms or ions from higher to lower energy states cause the emission of spectral lines. The total energy transport by line radiation is frequently only a small fraction of the total radiation energy from the plasmas. The energy transport depends on the number and wavelength of the emitted lines,

which in turn depend on the nature of the plasma fluid, in particular, on the number of possible species at a given temperature. The plasma of a given gas may be a “strong” or “weak” line radiator, depending on the plasma density and composition, which are the functions of pressure and temperature. On the other hand, the continuous radiation in the plasma results from recombination of ions with electron (free-bound radiation) and from bremsstrahlung (free-free radiation). In the process of the radiative recombination, a free electron is captured by a possible ion into a certain bound energy state and the excess energy is converted into radiation. The recombination may occur into all energy level of an ion, thus the number of continuous spectra for a particular species coincides with the number of electronic energy states of this ion. The entire free-bound continuum consists, therefore, of a superposition of all continuous spectra emitted by the different species that exist in the plasma.

1.2.2 Generation of thermal plasmas

Plasma is created by applying energy to a gas in order to reorganize the electronic structure of the species (atoms, molecules) and to produce excited species and ions. This energy can be thermal, or carried by either an electric current or electromagnetic radiations [61]. It is rather straightforward to produce such plasmas either by means of high intensity arcs (I > 50 A) at atmospheric or higher pressures, or by means of high frequency (RF) discharges in a similar pressure range, hybrid plasma, and microwave discharge etc [12, 62-75]. All types of plasmas found widespread application for chemical and material processing. In the available time only the basic features of these plasmas can be discussed, including some of the technical developments designated as plasma torches or plasma gas heaters.

High intensity arcs at atmospheric or higher pressures are characterized by strong macroscopic flows induced by the arc itself [76]. Generally, there are two types of high intensity arcs, i.e., AC or DC arcs. In the case of DC arcs, both non-transferred and transferred arcs have been used to promote chemical reactions. The plasma jet can be operated in a transferred/non-transferred arc mode depending on whether the arc is electrically transferred to the work piece or not. Arc plasmatrons have a high efficiency (60-90%) and provide high power of up to 2-5MW [69].

1) DC non-transferred arc plasma torches

The non-transferred arcs can be operated in the low voltage (20-150 V) mode and are

characterized by their ability to sustain at relatively low flows and high exit gas enthalpies. Typically, the flow through the device is mildly turbulent, and the gas flow has minimum swirl content. The low flow condition in the low voltage mode is ideal for materials synthesis. But there is one disadvantage with the low voltage mode for high power operation, because the device will operate at higher currents thus leading to significant electrode erosion. The high voltage mode uses longer anode nozzles and has a significant amount of swirl gas. The more intense the swirl, the longer the arc and the higher the voltage. Typical voltages range between 150 and l000 V. The advantages are operation at lower amperages, minimizing electrode erosion at high power levels. They produce a high-temperature plasma arc that interacts with a flowing gas to produce a hot jet into which the material to be processed can be injected for in-flight melting and vaporization. A schematic diagram of a DC non-transferred arc plasma torch is shown in **Figure 1 (a)**. Here, an arc is established between an axial, pointed/tip-type cathode and a toroidal/annular anode. The anode is concentric and parallel to the jet axis; the gas crosses the boundary layer between the arc column and the anode inner surface, and is pushed downstream by the pressure of the gas flow. The arc attachment point of the anode continuously changes due to the abatement of the anode electrode material, whereas the profile of the cathode generally leads to a fixed plasma arc attachment point. To ensure satisfactory working lives the electrodes are large components, making them tolerant of the gradual abatement and are generally water cooled. However the disadvantages of this type of torch are that they contaminate the product and have very low energy efficiencies, i.e. their power output can be as low at 50% of their power input [62].

2) DC transferred arc plasma torches

The transferred arc operation can be divided into two arc modes: either transfer to the work piece to be heated or to an intermediate electrode. In the first case, the arc is transferred from the cathode directly to a work piece to be heated. In the second case, the transferred arc is terminated on a secondary electrode and the device produces a non-transferred free burning arc. Transferred arcs are characterized by a relatively large physical separation between the cathode and anode that can range from a few centimeters to almost 1 m long in high power industrial furnaces. This allows for the increase of the operating voltage and consequently the plasma power for the same arc current [75]. The latter is a key parameter which has a strong influence on the energy efficiency of the arc and electrode life. Torches can be anodic or cathodic; the

electrode is concentric with the jet axis and the arc is transferred to the external electrode. This is an electrically conductive material, usually the work piece in a single torch arrangement, as shown schematically in **Figure 1 (b)**. Transferred arc torches can produce extremely high thermal fluxes because the plasma arc is formed outside the water-cooled body of the torch. This means they are inherently more efficient than non-transferred arc torches because radiant heat transfer losses to the cold torch body are minimized [75, 77-79].

Another advantage of transferred arc devices is their ability to be used in a coupled twin-torch mode. Inclined anode and cathode torches (or graphite electrodes) each produces plasmas that are initially repulsive close to the devices, but then couple to form a plasma flame in free space. The advantage of this arrangement is that there is no need for the work-piece to form the return electrode so it is ideal for the melting of non-conducting materials and for the in-flight vaporization of powders [75].

3) Multiphase AC arc

Multiphase AC arc is a hot topic as an innovative in-flight technology in recent years because of its high energy efficiency, large plasma volume, low velocity, easy scale up, and low cost [80]. Rutberg et al. [81,82] investigated a multiphase plasma generator. The device can be operated at atmospheric pressure in the power range 100-500 kW and the gas flow rates 10-70 g s^{-1} with thermal efficiency of 70-90% and electrode lifetime of more than a hundred hours. In contrast to the DC arc, the multiphase arc seems to be more expedient for applying in large scale plasma process.

The multiphase AC arc was examined for utilization in the in-flight melting technology for the purpose of saving energy and shortening production cycle for glass industry [83]. For a 6-phase AC arc, the maximum plasma velocity was up to 20 m s^{-1} and the plasma temperature was over 6000 K at 22 kW input power and 36 L min^{-1} sheath gas. The lower plasma velocity may lead to comparatively longer residence time of particles during plasma in-flight treatment.

4) High Frequency Discharge

There are two types of plasmas which can be sustained by high frequency discharges. The first one is RF inductively coupled plasma (ICP) and the second is microwave plasma. These types of plasmas are referred to as electrodeless discharges. ICP and MWP produce ultraclean, high temperature, large diameter and low velocity plasmas which are particularly suitable for

chemical reactions. The reactor is insensitive to the type of gas used. This type of reactor is ideal for producing reactive plasmas for chemically specify reactions. High frequency induction plasmatrons have relatively small power (up to 1 MW) with efficiencies from 50 to 75%.

a) Radio Frequency (RF) Thermal Plasma

RF discharges are characterized by the absence of electrodes, which avoids the contamination of the plasma by metallic vapors [84]. In RF torches, energy coupling to the plasma is accomplished through the electromagnetic field produced by the electrical induction coil and the partially ionized gas in plasmas with low velocity (in the range of 10-20 m/s) and with high temperature. The plasma gas does not come in contact with electrodes, thereby eliminating possible sources of contamination, and allowing for their operation in a wide range of operating conditions including inert, reducing and oxidizing, and other corrosive atmospheres. Therefore, RF plasma have been widely studied and applied in production of high-quality and high-performance materials, such as synthesis of ultrafine powders, deposition of thin films, sintering of ceramics, plasma spraying, and treatment of powders [85-94].

Pure argon or its mixture with other gases is still the usual choice for the plasma gas largely because of its ease of ionization. The local power density is lower than that of DC plasma. The excitation frequency is typically between 200 kHz and 40 MHz. Laboratory units run at power levels of the order of 30-50 kW, while large-scale industrial units have been tested at power levels up to 1 MW [12].

A schematic diagram of an RF inductively coupled discharge facility is shown in **Figure 1(c)**. The RF plasma is confined in a water-cooled quartz or ceramic tube with several gaseous streams introduced into the discharge. These include the sheath gas, which serves to reduce the heat flux to the walls of the plasma confinement tube and thus protect it from damage due to overheating. The intermediate gas mainly serves for plasma stabilization and is often introduced into the discharge with both axial and tangential (swirl) velocity components. The carrier gas is axially injected into the center of the discharge using a water-cooled probe. It serves to introduce the material to be treated in the plasma. Because of the nature of the coupling mechanism that limits energy dissipation to the outer annular region of the discharge, the maximum plasma temperature is off-axis, with the central region of the discharge heated by conduction and convection from its surroundings. This offers a particularly attractive means of in-flight processing of materials through their axial injection of the material into the center of

the discharge without disturbing the current-carrying regions of the plasma.

b) Microwave Plasma

Microwave plasmas (MWP) differ significantly from DC arc plasmas and ICPs by higher electron densities and higher reactivity at lower input power levels. However, the operating pressure range for MWP is very narrow and the plasma volume is rather small at high pressures. Microwaves are guided along the system and transmitted energy to the plasma gas electrons. Elastic collisions between electrons and heavy particles occur. Due to the large mass of heavy particles, the collided electrons rebound whereas the heavy particles remain static. The electrons are thus accelerated (they get kinetic energy) and the heavy particles are slightly heated. After several elastic collisions (which follow probabilistic laws), the electrons get enough energy to produce inelastic exciting or even ionizing collisions. The gas is partially ionized and becomes plasma which supports microwave propagation. Various types of microwave reactors have been developed by many researchers in recent years [95-98].

Microwave thermal plasma has been attracted great attentions as new candidates in numerous areas. High deposition efficient and high deposition rates in production of optical fibers for telecommunication attained when using microwave plasma [95, 99] have studied the microwave plasma ultraviolet lamp (MPUVL) for germicidal applications such as water and wastewater sterilization. In their experiment, the microwave source is standard industrial microwave oven magnetron operating at 2.45 GHz with power ratings up to 1 kW. Real power consumption in the case of using the microwave discharge was relatively lower than that in RF or DC discharge. However, the industrial application of microwave discharge was limited at a low level in contrast to DC or RF discharge because of its lower plasma temperatures.

5) Hybrid Plasma

Hybrid plasma torches have been developed by the superposition of more than one plasma-generating device, such as in the combination of DC and RF plasma torches developed by Yoshida and Akashi [100] and the combination of two RF plasma torches in tandem operating at two different frequencies [101]. Such a hybrid system is more flexible and offers a number of advantages in material processing. While they have undoubtedly proven to be useful in specific applications involving plasma chemical synthesis, it is unlikely because of their complexity that their use will grow to replace alternate simpler plasma systems. In contrast to

DC arc discharges, which exhibit maximum temperatures in the core of the plasma, the RF plasma torch shows an off-axis temperature maximum. In general, the core of the RF plasma torch is rather cold and the maximum temperature is lower than that of DC plasma. The superimposed DC plasma or RF plasma torch acts as an ignition source, and the second RF plasma torch adds auxiliary heat downstream to maintain a high temperature level. It is also possible to superimpose successive RF plasma torch beyond the first one to produce a longer hot reaction zone with uniform temperature [102-104]. **Figure 1 (d)** displays the apparatus of DC-RF hybrid plasma.

1.3 Applications of thermal plasmas processing

1.3.1 Thermal plasmas in the aerospace industry

One of the early applications for thermal plasmas in the aerospace industry had as objective the simulation of the conditions meet during high and low altitude supersonic flight, and reentry of space vehicles [74]. Numerous large scale wind tunnels were developed around the world for this purpose in the sixties and seventies. ICP devices were used exclusively for the high altitude, low pressure testing. They have the main advantage of being able to be operated with air as the plasma gas with no potential metal-vapor contamination generated through electrode erosion which is the case in some of the high power dc plasma devices. DC devices on the other hand provide an excellent tool for high power and high energy density testing conditions which are mostly associated with lower altitude high speed flight conditions.

1.3.2 Thermal plasmas in the materials industry

Thermal plasmas as a powerful tool for the synthesis and processing of a wide range of high added value materials, has been used for over 35 years, since the development of the initial plasma arc gas heaters. It should be recognized that in the thermal plasma processing of materials we have not only the means of achieving relatively high temperatures, but also that the plasma state for molecular gases is composed of a mixture of reactive species with higher specific enthalpies and higher thermal conductivities than most gases have at normal temperature and pressure. This, combined with the high temperature of the plasma, can give rise to considerably high reactivity and material heating and quenching rate (in the order of 10^5- 10^7 k/s) which are characteristics of thermal plasma processing.

In this section a description is given of typical applications in materials processing [61-72]. These can be grouped into two broad categories, depending on the role played by the plasma. The simplest and most widely used technologies such as in spheroidization, melting and deposition, plasma spray-coating, and plasma metallurgy make use of the plasma only as a high-temperature energy source [67]. The transformations involved in the materials in this case are mostly limited to physical changes involving melting and rapid solidification, vaporization, and condensation. Thermal plasmas have also been used in applications involving chemical synthesis, such as in the preparation of pigments and high purity synthetic silica as well as in the synthesis of a large number of high-purity ultrafine ceramic powders such as SiC, Si_3N_4, AIN, TiN, and others. In these cases the plasma is used as a source of chemically active species, with both physical and chemical transformations involved in the process.

1) Plasma Coating

a. Plasma Spraying

The plasma provides high heat and momentum transfer rates to melt and accelerate spray particles or to melt the wire tips and atomize the molten metal [62, 65, 68, 74, 105, 106].

The formation of protective coatings by spraying a stream of molten metal or ceramic particles was first developed using combustion flames into which the spray material was fed as a powder, wire or rod. In the 1960's commercial plasma spraying equipment became available in which a DC plasma jet was used to melt a powder feed and project the droplets at high velocity against the material to be coated. In typical plasma spraying operation, schematically represented in **Figure 2**, the material to be deposited is injected into the plasma flow in the form of powder, which is heated and melted in-flight, before, impacting on the surface of the substrate where it is flattened in the form of splats, accumulates on the top of each other thus forming the coating. The quality of the coating in terms of its apparent density and adhesion to the substrate is a direct function of the temperature and velocity of the individual droplets prior to their impact on the substrate. These depends, in-turn, on the spraying conditions such as the plasma power, plasma composition, chamber pressure, and the trajectory of the individual powder particles in the plasma flow. Almost any material that can be melted without decomposing can be used to form the coating. The major advantage over the flame spraying process is the higher particle velocity obtainable (up to 500 m/s*)*, but the high temperature achieved in the plasma jet (up to 15 000 K) also make it possible to melt even the most

refractory material to produce high quality coatings. Plasma spraying is therefore particularly suitable for the formation of ceramic coatings for wear, thermal and corrosion protection.

Besides the most common atmospheric pressure plasma spray process in ambient air (APS), other plasma spray processes have been developed, including spraying at low pressures (LPPS), at supersonic velocities, under controlled ambient conditions (in argon), and even under water.

Plasma spraying differs considerably from other surface treatments by its specific characteristics via: (1) the energy source is separated from the substrate. For that reason thermal spraying is a cold process and the substrate can be maintained below 373K the particles interfere in some way chemically and physically with the environment during the flight; (2) the sprayed layer is built up particle by particle; (3) the particles are cooled very fast after arriving at the substrate (equivalent to splat cooling); (4) the sprayed layer shows a structure of lamellas thermal spraying makes it possible to produce coatings of essentially different materials with high purity; (5) very dense coatings are possible (more than 98%); (6) melting, quenching and consolidation are made in one operation; (7) with the help of sophisticated robots, spraying very complex shapes can be achieved and even free standing bodies can be made.

b. Chemical vapor deposition

A new technology makes use of thermal plasmas for chemical vapor deposition of an array of materials, and this process gained prominence by demonstrating the highest deposition rates for diamond coatings. This emerging technology will fill the void between the high quality, but extremely slow coating processes (sputtering, physical vapor deposition) and the rapid, but difficult to control thermal spray processes.

In thermal plasma CVD and the following thermal plasma applications, the plasma is predominantly used as source of specific chemical radicals driving the formation of the desired product. Because of its unique features, TPCVD may find numerous applications, and some of them are already considered for industrial fabrication as, for example, diamond and dense ceramic or superconducting films [107-114]. **Figure 3** presents the schematic of diamond TPCVD with a dc plasma torch. There are indications that TPCVD may play an important role in the fabrication of nanostructured films.

In the process of TPCVD, high-energy-density plasma produces high density vapor-phase precursors for the deposition of relatively thick films. Besides DC plasma jets, other types of plasma reactors have also been utilized which make use of high-frequency (RF), hybrid and

microwave plasmas. For increasing the available plasma volume, multiple torch arrangements have been developed.

2) Plasma Welding and Cutting

Cutting, welding and spraying with plasma belong to the most developed and applied plasma techniques [12, 67, 115]. For plasma cutting probably more than 100.000 installations are in operation worldwide**.** For melting and removing the molten metal they operate with a highly localized plasma energy coupled with an exothermic reaction and also a high plasma gas momentum**.** High heat flux is achieved by transferring the arc to the work piece which serves a**s** anode in discharge originating from a torch with stickor button-type metal cathode. Such cathodes mostly consist of thoriated tungsten for Ar-H_2 or N_2 plasma, of Hf for O_2 and Zr for air. To get a high plasma and gas momentum small diameter nozzles are used applying in some devices for improvement purposes a water vortex**.** With such a device using W-electrodes and a high current arc of around 600 A steel plates with a thickness of 40 mm can be cut at a speed of 0.7 m/min**.** With such an application the plasma cutting method is superior to all the other cutting methods using lasers, oxyflames or water jets.

3) Plasma Consolidation of Powders

Plasma consolidation includes the processes of spheroidization, densification, and sintering. The first two of these processes are already commercially developed, whereas plasma sintering is still in the laboratory stage [65].

Powder densification involves in-flight melting of the material in particulate form, followed by gradual cooling and freezing before being collected at the bottom of the densification chamber or in an appropriate collection device, depending on the particle density and its size range. Frequently, spheroidization and densification processes occur simultaneously as porous, irregularly shaped agglomerates are injected into a thermal plasma. As the particles sinter and/or melt in plasma, they assume a nearly spherical shape and densify at the same time. Commercially, fine particles are spheroidized in plasma for a variety of applications, including materials with a controlled porosity, catalysts [116, 117], abrasives, and materials to transfer ink in photo copiers. A wide range of different materials have been spheroidized, including oxides [117-121] and carbides [119, 122]. **Figure 4** shows schematic representation of the basic phenomena involved in the process of spherodization through the in-flight heating and melting

of individual particles.

Plasma densification of pre-sintered agglomerates of metals (e.g. W, Mo) and of carbide-metal mixtures (e.g. WC-Co) has been used to produce spherical, densified powders. Such powders possess excellent flowability which is beneficial to subsequent plasma coating.

Plasma sintering refers to the process of bonding particles and densification of materials by applying heat from plasma. Plasma sintering of refractory materials, mainly ceramics, is a relatively new technology [123-131]. Sintering of high-tech ceramics in thermal plasmas has the potential of drastically reducing the time period required for this process. In addition, plasma sintering offers the opportunity of restrained grain growth and for tailoring heat transfer during the sintering process which may result in desirable structures and properties of the sintered materials. Plasma sintering is a pressureless sintering process which may cover a pressure range from 760 to a few Torr to achieve the increase in density and strength of a cold pressed powder compacted sample upon heating. Rapid sintering of ceramics has been observed by various investigators, using gaseous plasmas produced by microwaves, glow or RF discharges.

The advantage of plasma sintering over conventional sintering is the extremely high heat transfer rate to the sample, which may result in rapid sintering (minutes) with minimal grain growth. The essential characteristics of plasma sintering and of any other sintering process are an increase in density and strength of a powder compact upon heating.

4) Plasma Metallurgy

Extractive metallurgy refers to the extraction of metals in either pure or alloyed form from their respective ores [132, 133]. Thermal plasma reactors for re-melting, melting or refining operations represent highly concentrated heat sources that allow for high processing rates per unit reactor volume. In metal melting and re-melting, the plasma is used primarily as an effective source of process heat, making use of the anode heat transfer characteristics of an arc between a cathode and the metal [65, 105]. The relatively long characteristic process times (from 0.1 s to min) reduce the importance of instability effects. With the increased use of recycled scrap material, the metal melting and re-melting application has seen considerable expansion. New approaches have concentrated mainly on more efficient overall operation of the installation and less on the control of the plasma heat transfer.

Two different types of furnaces have been used for plasma extractive metallurgy: transferred arc reactors for ferroalloy production and reactors where a reducing gas is preheated

and upgraded by using plasma torches. The reduction of the ores to be treated is performed in a furnace filled with coke, which is mainly used as a refractory material for providing a sufficiently long residence time for the injected ore particles to be reduced.

5) Plasma Waste Destruction

In plasma waste treatment, the major advantages of using thermal plasma are the fast heating rates, the high processing temperatures allowing the formation of stable vitrified slags, and the low off-gas flow rates. Off-gas cleaning is a major economic factor in any waste processing installation, and the costs scale with increasing gas flows [12, 65, 68, 134-137].

Thermal plasma reactors offer the following unique advantages for the destruction of hazardous wastes [16, 138-140]:

1. The high-energy density and temperature, and the correspondingly fast reaction times, offer the potential for a large throughput with a small reactor footprint.

2. The steep thermal gradients in the reactor permit species exiting it to be quenched at very rates so allowing the attainment of meta-stable states and non-equilibrium compositions, thereby minimizing the reformation of persistent organic pollutants (POPs).

3. Plasmas can be used for the treatment of wastes including liquids, solids and gases.

4. The high heat flux densities at the reactor boundaries lead to fast attainment of steady state conditions. This allows rapid start-up and shutdown times, compared with other thermal treatments such as incineration, without compromising refractory performance.

5. Oxidants are not required to produce the process heat source, as no fuel is combusted, therefore, the gas stream volume produced is much smaller than with conventional combustion processes and so is easier and less expensive to manage.

6. The combination of the above characteristics allows plasma treatment to be integrated into a process generating hazardous wastes, thus permitting the destruction of wastes at source and giving a truly proximal solution.

In addition, increased process controllability and flexibility, and smaller installation size, allow integration of the waste treatment process into the manufacturing process.

The major disadvantages associated with the plasma process, besides the already mentioned (largely perceived) lack of reliability, lie in the use of electricity, the most expensive form of energy. Consequently, economic considerations provide the strongest barrier for use of plasmas for waste treatment.

The most frequently used plasma gas is air, for economic reasons and providing oxygen for reactions with carbonaceous materials. Use of oxygen as plasma gas reduces the total gas flow in the reactor and the amount of nitrogen. Use of argon as plasma gas provides long electrode life; however, the low specific heat of argon results in relatively low torch power levels and enthalpy fluxes of the gases leaving the torch. Furthermore, reactive species such as oxygen atoms are generated only indirectly through energy transfer from argon to oxygen, and the relatively low thermal conductivity of argon leads to low energy transfer rates.

6) Plasma Synthesis of Nanoparticles

Plasma synthesis of nanoparticles with diameters between 5 and 50 nm has seen much renewed interest with the emergence of nano-phase materials with specific desirable properties. A thermal plasma process provides high reactant flow and particle generation rate. The characteristic process time can be considered the time from reactant injection to nucleation and is in the range between 0.01 to 1 ms [12, 71, 74].

The synthesis of nanoparticles by thermal plasma is mostly carried out through the vaporization of the precursor material under plasma conditions followed by the rapid quenching of the formed vapors under controlled conditions in order to condense the vapors in the form of an ultrafine aerosol with a controlled morphology, crystal structure and particle size distribution.

Recent advances in novel reactor and process designs have enhanced the quality of powders produced in thermal plasma. These novel designs include the RF-DC hybrid reactor, the reactive submerged arc (RSA), multiple plasma jets, and counter flow liquid-injection plasma reactors. They aim at maximizing the heating, the mixing, and the residence time of materials in the plasma. Either the discharge itself or the plasma flame downstream of the discharge may be used for synthesizing the powders. In thermal plasma synthesis, the reactants may be gases, liquids, or solids before injection into the plasma. However the availability of gas-phase precursors for metals is severely limited. Therefore, the most commonly used reactants for plasma synthesis have been solids. Several years ago, a liquid injection method was developed to overcome the problems associated with solid injection and to capitalize on the benefits of gaseous reactants [141-149].

In general, nitrogen or hydrogen is used as a plasma generating gas, since the energy content of nitrogen and hydrogen is higher than that of argon or helium, due to its diatomic

nature. But, in order to have an inert atmosphere in the reaction environment, argon is usually preferred. Reactive gases like hydrogen, oxygen (air), chlorine and nitrogen can be used to impart reducing, oxidizing, chloriding or nitriding effects in the material processing. Ceramic powders such as carbides, nitrides, oxides, and solid solutions have been successfully synthesized in thermal plasma reactors.

1.4 Nanoparticles synthesis by thermal plasmas

The supersaturation of vapor species, which provides the driving force for particle condensation, can be very large in thermal plasma, leading to the production of ultrafine particles by homogeneous nucleation. Since the resultant huge enthalpy can be realized for various kinds of plasma forming gases and easily controlled by electricity, thermal plasmas have been expected to facilitate not only fast chemical reactions but also rapid heat transfer in a variety of synthetic routes for nano-sized materials. For example, reactive gases, such as, nitrogen and oxygen can be chemically activated in the form of various radicals dissociated or ionized in their thermal plasma state. As reported in many other papers, these radicals can be directly used in the formation of nitrides and oxides with very small sizes. Thermal plasmas suitable for the synthesis of fine powders are primarily produced by means of high-intensity arcs and high-frequency discharges [12, 16, 74, 150].

1.4.1 Synthesis by DC thermal plasma

DC arc can be regarded as an innovative tool that automatically creates nanoparticles with a notable production rate at low cost. For example, metal, oxide, alloys, intermetallic, and surface-coated nanoparticles prepared successfully by DC arc have been reported. The synthesis of titanium dioxide pigment through the oxidation of titanium tetrachloride in oxygen plasma is an example of an important commercial success that has been in operation for a number of years by Ti oxide. A DC plasma torch is used in this case to produce a jet of high-temperature oxygen in which titanium tetrachloride is injected in the tail flame. A similar process was developed in the USSR using an induction plasma torch at a power level of 0.5 MW.

Tanaka and Watanabe [151] successfully prepared Sn–Ag alloy nanoparticles at a high production rate using Ar–H_2 plasma. In their experiment, increased H_2 concentration resulted in the increase of not only the particle size but also the ratio of Sn to Ag in the nanoparticles. Conceptual diagram of the DC arc method is shown in **Figure 5**. Meanwhile, Kulkarni et al

[152] reported the dc transferred arc synthesis of nanoparticles of Al_2O_3, AlN and FexOy. They were able to control the crystalline phases of these compounds by altering the operating pressure.

Thermal plasma jets generated by a DC non-transferred arc device have also been applied to nanoparticle synthesis from injection of precursor powders. Tong et al prepared nanoparticles of carbides, such as TiC [153] and SiC [154]. They reported that SiC nanofibres as well as nanoparticles were synthesized using SiO_2 and CH_4 as precursors. Furthermore, they also synthesized TiC–Al (Ti) nanocomposite powders forming core–shell microstructures [155]. Meanwhile, Ryu et al have investigated the synthesis of W [156], WC [157, 158], WC–Co composite [159] and yttria-stabilized zirconia (Y_2O_3– ZrO_2) [160] nanoparticles.

Furthermore, a new DC mini-arc plasma source was developed and utilized for nanoparticle production by Chen et al [161]. Their mini-arc plasma reactor consisted of a 1.6 mm-diameter tungsten rod cathode and a 6.35 mm diameter graphite rod anode. They successfully produced nanoparticles of Ag or mixtures of Sn, SnO and SnO_2 at rates of 1-10 mg h^{-1}. Haidar [162] reported nanoparticle synthesis using a unique arc discharge called the 'anodic arc', which was struck between a refractory rod anode and a hollow cathode, and used to produce nanoparticles of Al and Al_2O_3.

1.4.2 Synthesis by RF thermal plasma

The induction plasma technology allows the processing of a wide variety of materials at a relatively high yield and affordable production cost. This convenient technology is well suitable to face the growing interest that arises not only from academic institutions and research centers, but more recently from industries in their search for a reliable and high capacity manufacturing technology. The two fundamental key features that make ICP technology attractive are the very high temperature processing and high quenching rate. Since the temperature prevailing in the center of the discharge can reach 10,000 $^{\circ}$C, reaction rates under such conditions are much faster than those found in conventional methods. On the other hand, the high quenching rate at the exit of the reactor, which is typically ~10^5 K/s, prevents products dissociation and is responsible for particle condensation as an ultrafine powder with a typical particle size in the nanometer range (10-100 nm) [88-96, 163-167]. Various types of nanomaterial can be synthesized by carefully selecting the plasma gases and the appropriate reactant (gases, liquid solutions or suspensions and solids).

1) Metal Nanoparticle

Ultrafine iron powder was synthesized in an atmospheric-pressure RF plasma reactor by injecting relatively course iron powder into the plasma. The particles are spherical and non-agglomerated, with volume-mean diameter range about 20~70 nm depending on the powder feed rate of iron powder; particle size increased with increasing powder feed rate. A detailed two-dimensional numerical model was developed, which calculated temperature and velocity profiles and modeled particle nucleation, growth and transport. The predicted mean particle sizes were in good agreement with those found experimentally [168, 169].

Copper and alumina particles are considered to be injected in argon inductive coupled plasma under atmospheric pressure. The parameters investigated are particle loading, particle size, and the central carrier gas flow rate. Up to 18% of the total energy dissipated in the torch can be absorbed by the particles. It is found that powders with large number of small particles will absorb more heat than powders which are composed of larger particles. The thermophysical properties of the particles are also an important factor in this problem. The evaporated powder might play an important role in altering the electrical properties of the gas and thus change the energy dissipation pattern and tend to moderately cool the plasma core. Low central flow-rates cause the particles to travel around the recirculating zone whereas high central flow-rates keep the particles very close to the central axis [170].

Fine nickel powders have great potential technological applications such as conducting paints, rechargeable batteries, chemical catalysts, microwave absorbing materials, and magnetic recording media [171-175]. In addition, they are attracting increasing attention as the substitute for noble metals Pd or Pd/Ag used in the internal electrodes of multilayer ceramic capacitor (MLCC) due to their good electrical conductivity, high melting point, and low cost [176]. Nickel powders as the electrode materials need to be prepared as well-dispersed spheres with a narrow size distribution. Spherical nickel nanoparticles are prepared by RF plasma via hydrogen reduction of nickel hydroxide/carbonate [177]. The metallic nickel powders could be obtained. The product consisted of well-dispread spheres with an average diameter of about 60-100 nm, and exhibited high tap density. The use of nickel hydroxide/carbonate guaranteed the product with high purity and environmental safety. The present plasma-assisted hydrogen reduction is an ideal route for large-scale synthesis of well-dispersed metallic nickel nanospheres used as electrode materials.

2) Intermetallic Compounds Nanoparticles

Nanoparticles of intermetallic compounds have been prepared by RF-ITP-aided evaporation method. The co-condensation process of high temperature metallic vapor are examined to investigate the nucleation and growth phenomena of binary metallic vapor as well as the possibility of synthesizing intermetallic compounds nanoparticles from a vapor state.

Ferries have been of great importance in high-frequency soft magnetic applications owing to their large resistivity, low power loss and high permeability. Two classes of materials are important: the Mn-Zn and the Ni-Zn ferrite. ITP synthesis has been previously shown to be a viable route to produce Ni ferrite nanoparticles [178]. The nanoparticles of Mn-Zn ferrite from metallic precursors were synthesized to characterize their structural and magnetic properties [179]. ITP was also used to produce FeCo nanoparticles with a thin protective oxide coating from metal powder precursors [180-182].

Experimental investigations were made in the Nb-Si, Nb-Al, Ni-Zn and V-Si systems [183-185]. The binary composition controlled metallic vapors generated in a high temperature region of the plasma were quenched at the cool rate of 10^5 K· s^{-1}. In the case of V-Si system, composition could be controlled with the size range from 20 to 100 nm. The small vapor pressure ratio (V/Si=10) leads to the successful synthesis of single phase compound which is related to the equilibrium phase. Meanwhile, the particles of the single phase could not be obtained in the case of large difference in the saturation vapor pressure ratio (Nb/Si=10^{-6}). The identified phases could not be corresponded to the expected phases. The nucleation position and period should be restricted by rapid quenching to overcome wide different saturation vapor pressure ratio.

The vapor pressure ratio is the most important factor for preparation of intermetallic compound particles. For preparation of intermetallic compounds nanoparticles with stoichiometric composition, the vaporization and condensation rates of the constituent metals should be controlled in the case of large different saturation vapor pressure.

3) Oxide Nanoparticles

The nanosized silica is quite attractive since it is an excellent functional material and can be applied in many areas. Scientists are paying much attention to study the properties of silica NPs, for example, the plug flow of silica NPs during fluidization [186], the variation of zeta potential [187], the thermo-mechanical properties when blended with polyolefin [188], the

magnetic properties of core-shell silica microspheres [189], the radiation effects and surface deformation of silica NPs [190], etc. Silica NPs can enhance the performance of many materials such as electric sealing materials, polymer composite materials, biological materials, pharmaceuticals, ceramics, and glasses [191-193]. The synthesis of SiO_2 nanoparticles were synthesized in RF plasma reactor by Behnam M.G. et al [194]. It is demonstrated that the quench gas configuration and reactor geometry can now be designed to control the morphology and size of nanoparticles in these reactors. Various nanostructured products have been synthesized: i.e., highly aggregated nanostructure, partially sintered nanospheres and spherical nanoparticles with very low levels of aggregation. These nanostructures have their primary particles sized between 10 and 200 nm.

Tungsten oxides, WOx, are transition metal oxides with wide ranging applications for their unique chromism, photocatalysis, optoelectronic, sensing, field emission, and high temperature superconducting capabilities [195-207]. As an n-type semiconductor, WO_3 has been intensively studied for gas sensing applications as it enhances sensor capabilities; reduces power consumption, and produces excellent reproducibility [201-207]. A large-scale, crystalline monoclinic-structured tungsten trioxide (WO_3) octahedron has been synthesized by RF thermal plasma. The regular octahedral WO_3 shows good sensing properties to benzene gas, which might mainly be due to its highly exposed {111} faces and the regular octahedral shape.

Zinc oxide nanoparticles are used in cosmetic materials, transparent conductor in the display and the photovoltaic, EL lighting, ultra-violet absorption substance and gas sensors. ZnO_2 nanoparticles were synthesis from Zn powder as the flash evaporation method [208].

Alumina Al_2O_3 nanoparticles are becoming increasing important to a wide range of application used as engineering ceramics, catalysts, semiconductor packing materials and eco-materials. Al_2O_3 nanoparticles were synthesized by oxidation of Al in argon-oxygen ITP with the optical emission spectroscopy and laser light extinction to investigate the powder evaporation [209].

TiO_2 has many industrial and research application, including photocatalystic, photonic crystals, photovoltaic cells, and sensors the key properties include phase composition, grain size, morphology and chemical components [210-214]. TiO_2 were prepared by oxidation of metallic Ti powder in Ar-O_2 ITP.

4) Nitride Nanoparticles

Nitride nanoparticles were prepared through direct nitridation of metal powders by Ar-N_2 ITP. The N_2 radical recombines into nitrogen molecule below 5000K, and then direct reaction between nitrogen radical and metal precursors is not the main route for nitride nanoparticles formation. The radicals of NH and NH_2 formed from NH_3 dissociation are more stable at lower temperature that is favored for nitride nanoparticles formation.

The relatively high thermal conductivity, good dielectric properties, high electrical resistivity, and thermal expansion coefficient of aluminum nitride (AlN), which is matcheable with that of silicon, make it a candidate material for the electronic industry in applications such as integrated circuit substrates, heat sinks, fillers, and semiconductor packaging [215, 216]. However, a high temperature is necessary to obtain a fully dense sintered body. Moreover, the thermal conductivity is extremely sensitive to impurity contents. AlN nanoaprticles were prepared through direct nitridation of Al powders by Ar-N_2 ITP with addition of NH_3 [217]. The production rate of AlN nanoparticles was more than 200 $g \cdot h^{-1}$. The prepared AlN nanoparticles having average diameter of 60 nm showed excellent sinterability, compared with conventional AlN powders.

Silicon nitride has been considered as candidate for structural applications including automotive parts, wear resistant parts, gas turbine parts and others. It is known to have good properties such as hardness, flexural strength at room temperature and at high temperature as well, and low density among ceramics. It has better high temperature capabilities than most metals combining retention of high strength and creep resistance with oxidation resistance. Its low thermal expansion coefficient results in good thermal shock resistance compared with most ceramic materials [218, 219]. Different processes have been developed for the preparation of Si_3N, powders. Many papers have been published on the rf plasma synthesis of Si_3N, powders through reaction of SiC1, and NH_3 [220-226]. According to J. Szepvolgyi [227], the RF thermal plasma synthesis of Si_3N_4, from $SiCl_4$, and NH_3 results in nanosized powders with mean particle sizes of 10-50 nm, and a BET surface area of 30-100 $m^2\ g^{-1}$. In addition, nitridation of Si powders as the reactant in Aar-N_2 ITP. The precursors were injected in the form of particles in the size range of 10 μm. In this work, TiN nanoparticles also can be prepared.

Moreover, TiN, SiN_4 [228], C_3N_4 [229] can be synthesized by RF thermal plasma.

5) Carbide Nanoparticles

Carbides have a number of valuable properties like high melting temperatures, hardness,

strength, chemical resistance, and electrical as well as thermal conductivity. Today they are widespread especially in combination with different binder metals, so called cemented carbides, as cutting tools or as wear protection parts. Transition metal carbides have been found to present exceptionally high catalytic activity [230, 231], similar to noble metals catalysts used in hydrogen-involved reactions [232]. Many carbide nanoparticles have been reported to be successfully prepared by ITP with CH_4 addition. The reactive quenching with CH_4 addition into the tail flame was developed to control the nanoparticles composition without inclusion of free carbon. The decomposition and condensation of CH_4 was considered a key factor for the composition control.

Silicon carbide (SiC) is a non-oxide ceramic engineering materials that has a wide range of industrial applications due to its excellent mechanical properties, high thermal and electrical conductivity, and excellent chemical oxidation resistance [233, 234]. These properties make silicon carbide an attractive candidate material for many applications, such as grinding materials, polishing paste, wear-resistant materials, catalyst supports, filters for molten metals or hot gases, high temperature structural materials, and as reinforcement in composites [232-236]. SiC nanoparticles were prepared by ITP from the starting materials of SiH_4 [237], metallic silicon [238], and SiC [239, 241]. Liquid precursor such as $SiCl_4$ is alternative raw materials for preparation of SiC nanoparticles [241, 242]. The liquid precursors were fed by means of a pump to a atomization probe where the liquid is atomized in microsized droplets. The advantage of the $SiCl_4$ used as the raw materials are the high vapor pressure and the inexpensiveness. On the other hand, nano-silicon carbide powders are synthesized from organic precursors by RF inductively coupled thermal plasma. The XRD patterns of all of the synthesized powders showed the b-SiC, a-SiC and the free carbon phases. The synthesized powders had particle sizes in the range of 30–100 nm. The morphology of the synthesized powders was with globular and hexagonal.

Tungsten carbide is a high refractory material with a boiling point around 6000. Due to the much-desired properties of high hardness and good wear resistance, tungsten carbide has many industrial applications. It is applied to tools in the metalworking and drilling and mining industries under high pressure, high temperature, and corrosive environments [243-251]. Nanosized tungsten carbide powder was obtained by a WC and/or W_2C phase, can be synthesized using WCl_6 and CH_4 as the starting materials by the thermal plasma process. The particle size of WC_{1-x} was affected by plasma torch power, the plasma gas flow rate, and the

addition of secondary plasma gas (H_2), but not by the methane concentration within the range tested.

Ishigaki et al [252] demonstrated the RF-ITP synthesis of TaC nanoparticles from an ethoxide precursor, $Ta(OC_2H_5)_5$. Leparoux et al [253] also used an RF-ITP to prepare α-SiC and WC nanoparticles, followed by the preparation of β-SiC nanoparticles [254] and TiCN nanoparticles [255] using the same RF-ITP reactor.

6) Silicide Nanoparticles

Silicide nanoparticles have excellent mechanical strength and unique high-electric conductivity, thus make them potentially useful in extremely small-scale electronic and mechanical applications such as electromagnetic shielding, and solar control windows with interaction with IR and UV light, gate materials for CMOS and contact materials in microelectronics. Specially, $MoSi_2$ provides high-temperature structural applications in oxidizing and aggressive environments, and $TiSi_2$ has been applied to VLSI electrode materials [91, 93, 256].

However, preparation of silicide nanoparticles in thermal plasma system is a complicated phenomenon with many controlled parameters and it includes co-condensation processes with large or small vapor pressure differences of prepared species. Co-condensation processes of metal vapors were investigated for Nb–Al and Nb–Si systems, Nb–Si and V–Si systems [257]. Vaporization processes for Ti–Si, V–Si and Mo–Si systems were also investigated [256]. For nanoparticle preparation with stoichiometric composition, the vaporization and condensation rates of the constituent metals should be controlled in the case of large difference in the vapor pressure. The formation mechanism of molybdenum and titanium silicide nanoparticles in RF thermal plasma experimentally and numerically has been investigated by Watanabe et al. The parameters that control the metal composition of silicide, particle size distribution and morphology of silicide nanoparticles were also be discussed. In Mo-Si system, nuclei of molybdenum are produced and grow in the upstream region and then silicon vapor condensations on the molybdenum particles. The composition shows wide range since condensations of molybdenum and silicon occur at the different positions. On the other hand in Ti-Si system, it shows narrow range since condensations of titanium and silicon occur simultaneously. The difference of the formation mechanism leads to the preparation of disilicides as well as the sub-products.

7) Boride Nanoparticles

Boride nanoparticles have high melting point, excellent wear resistance, catalytic activity, high thermal conductivity and electrical conductivity; therefore these nanoparticles would be applied for the electromagnetic shielding, and solar control windows interacting with IR and UV light, electrode materials and catalyst in fuel cell. Some reports about the preparation of boride nanoparticles were published previously; TiB_2 nanoparticles were synthesized in the vapor-phase reaction of sodium with $TiCl_4$ and BCl_3 [258]. TiB_2 and VB_2 nanopowders were synthesized by the mechanochemical synthesis [259]. Ni rich amorphous boride nanoparticles were produced by the solid-solid reduction method [260]. It was reported to synthesize nickel nanoparticles by using functionalized AOT reverse micelles [261]. FeB nanoparticles also were produced in nonaqueous solvents [262]. Preparation of niobium borides NbB and NbB_2 by self-propagating combustion synthesis was reported [263]. For the synthesis of boride nanoparticels by RF thermal plasma with required charCeB6acteristics for the application, the prepared nanoparticle composition was correlated with thermodynamic parameters [90].

The thermal plasma chemical method was employed to prepare nanocrystalline YB_{66} particles through melting yttrium and boron directly by J.Y. Huang et al [264]. Fine particles are formed mostly through the coagulation from a vapor phase. The average grain size of the YB_{66} particles is less than 100 nm. All the YB_{66} nanoparticles are cubic in shape, suggesting that they have been formed through a direct coagulation from a vapor phase.

Formation mechanism of rare-earth metal boride nanoparticles are investigated by Watanabe et al. LaB_6 and CeB_6 nanoparticles were successfully synthesized by RF thermal plasma [265]. The average particle size is 15 nm. The prepared amount of LaB_6 nanoparticles are larger at smaller powder feed rate. Addition of He or N_2 enhances the heat transfer rate to the injected powders and then increases the prepared amount of boride nanoparticles. It is demonstrated the phase and composition in nanoparticles can be well controlled and Gibbs free energy and nucleation temperature play an important role in the synthesis processing in RF thermal plasma.

9 systems were chosen to investigate the formation mechanism of boride nanoparticles by Prof. Watanabe [266]. M-B-N system, M = Ti, Cr, V, Co, Fe, Mn, Mo, Ta, and Nb. For M-B-N (Ti, Cr, V) system that has low Gibbs free energy of nitridation and boridation, boride and nitride nanoparticles were prepared. For M-B-N (Co, Fe, Mo) system that has high Gibbs free energy of nitridation, boride nanoparticles were mainly prepared. For M-B-N (Ta, Nb) system

that has much higher nucleation temperature of metal than that of B, nitride with small fraction of boride was prepared because these systems have different nucleation mechanism. The main reason of the little preparation of boride results from the higher nucleation temperature of Ta and Nb than that of boron. At the downstream of the plasma, nucleation and solidification of Ta and Nb occur simultaneously. After the nucleation and solidification of Ta and Nb, boron nucleates around the solidified Ta and Nb particles. The Gibbs free energy and nucleation temperature have considerable effect on the composition off the prepared nanoparticle mixture of boride and nitride.

1.5 Objective of this dissertation

Metal boride nanoparticle has attracted considerable interest for applications in materials sciences, chemistry and medicine due to their unique properties, including high melting temperature and hardness, high wear resistance, chemical stable, catalytic activity and high thermal conductivity. Synthesis with high reaction rate and purity in conventional methods is difficult due to the high melting point of precursors. In addition, impurities will be introduced.

Recently, there has been growing interest in the studying thermal plasma technology for materials processing due to unique properties of thermal plasma. RF thermal plasmas generated in the plasma torch without electrode have large high temperature region and long residence time in high temperature region. Therefore, RF-ICP synthesis of titanium boride nanoparticles provides an attractive alternative to conventional methods, and is regarded as the most reliable plasma for mass-producing nanoparticles with high purity.

The practical fabrication of the functional nanoparticles by an RF-ICP is a complicated phenomenon which involves interaction among the thermofluid field, the induced electromagnetic field and the processed particle phases with numerous variables. The nanoparticles of boron-based intermetallic compounds are formed in a complex situation in which multi-component vapors co-condense and convert into nanoparticles in a few milliseconds. Additionally, the growth mechanism of the functional nanoparticles is dependent on the properties of boron and metal because the difference in the properties results in different vapor pressure ratios, which is a critical factor for the functional nanoparticles growth. If the manufacturing process is well-understood and controlled precisely, mass-production of titanium boride nanoparticles will be easily achieved using RF thermal plasma under atmospheric pressure with low costs. However, the detailed mechanism of their collective growth remains

poorly understood. This is true because it is impossible to observe every process using experimental approaches directly; only the characteristics of the final products can be evaluated.

The objective of this work is to investigate the formation mechanism of metal boride nanoparticle and to control the phase composition and diameter of product by experimental and numerical analysis. Metals with different saturation vapor pressure were chosen as models. The operating parameters including powder feed rate, boron content in feeding powders, gas flow rate and so on are studied to control the phase composition and size of product. Also by comparison with different metals, we investigate the effect of nucleation temperature in the synthesis process of metal boride nanoparticle by RF thermal plasma.

1.6 Contents of this dissertation

In this work, RF thermal plasma was used to generate metal boride nanoparticles. The formation mechanism of metal boride nanoparticle was reported by experimentally and numerically. The flow chart of this study is shown in **Figure 6.** The contents of each chapter in this dissertation are as follows:

In chapter 2, the synthesis of titanium boride nanoparticles by RF thermal plasma and comparison of numerical simulation and experiment results are investigated in detail. Because titanium boride is the easiest to produce, and titanium boride is famous and widely used in industry. Titanium is chosen as typical metal. The nucleation temperature of Ti is lower than that of boron, and boron nucleates first. The powder feed rate, boron content in feeding powders, inner gas, carrier gas flow rate and plasma power have been studied to control the phase composition and particle size of product. In addition, the synthesis of single phase boride nanoparticles TiB_2 with high purity is discussed. The formation mechanism of core-shell structure boride nanoparticles will be investigated.

In chapter 3, the synthesis of iron group metals boride nanoparticle by RF thermal plasma. Since the nucleation temperature of iron group metals and titanium are lower than that of boron, the formation mechanism of iron group metal and titanium is the same. The powder feed rate and boron content in feeding powders are investigated to generate iron group metal borides with controlled phase composition and particle size of product.

In chapter 4, the synthesis of refectory metal boride nanoparticle by RF thermal plasma by experimentally and numerically is studied. The synthesis of Mo, Nb, Ta and W based boride are difficult to generate. The nucleation temperature of Nb, Mo, Ta and W are higher than that of

boron and metal nucleates first. So the formation mechanism of Nb, Mo, Ta and W boride nanoparticle are different from that of titanium boride nanoparticle. The powder feed rate, boron content in feeding powders and quenching gas flow rate are investigated. Moreover, the effect of collection positions including reaction chamber wall and collection filter is studied.

In chapter 5, the synthesis of boron rich boride nanoparticle by RF thermal plasma by experimentally is studied. The synthesis of aluminum and yttrium are difficult to generate, because boron-rich boride requires the clustering of boron nuclei before the boridation. The powder feed rate, input power, work gas species and boron content in feeding powders are investigated in the synthesis process of boride in RF thermal plasma.

In chapter 6, boride can be classified loosely as metal-rich and boron-rich boride nanoparticles. The formation mechanism of metal boride nanoparticle is investigated. The formation mechanism of metal rich boride is divided into two kinds according to the nucleation temperature of constituent composition of boride. The formation mechanism in detail is explained based on the homogeneous nucleation and heterogeneous co-condensation processes. Comparison of different metals is displayed by phase composition and particle size of product.

In chapter 7, all of the results in this dissertation are concluded. The suggestion of future research on the synthesis of boride nanoparticles by RF thermal plasma can be given.

References

[1] P.M. Bellan, Fundamentals of Plasma Physics, 1 (2008)

[2] I. Langmuir, Physical Review, 33, 954 (1929)

[3] F. Richard, Plasmas Physics, 2, 5 (2006)

[4] J.S. Steven, J.O. Christopher and B. David, Astrophysical Plasmas, London E1 4NS, U.K. 2004

[5] N. Vijay, K. Ashok and H.K. Dwivedi, International Journal of Engineering, 2, 53 (1989)

[6] P. Kong, SOHN International Symposium on Advanced Processing of Metals and Materials, 2006

[7] K. Okazaki and T. Watanabe, New York, Wallingford, U.K. 10, 30 (1999)

[8] H. Barankova and L. Bardos, Atmospheric Pressure Plasma Sources and Processing, 2009

[9] K.P. Nick, J. Richter and V. Helbig, Journal of Quantitative Spectroscopy and Radiative Transfer, 32, 1 (1984)

[10] T. Watanabe, N. Tonoike, T. Honda and A. Kanazawa, Journal of Chemical Engineering of Japan, 24, 25 (1991)

[11] J. Heberlein, Pure and Applied Chemistry, 74, 327 (2002)

[12] M.I. Boulos, IEEE Transactions on Plasma Sciences, 19, 1078 (1991)

[13] M.I. Boulos, P. Fauchais and E. Pfender, Plenum Press, New York and London, 1994

[14] P. Fauchais and A. Vardelle, IEEE Transactions on Plasma Sciences, 25, 1258 (1997)

[15] Y.P. Raizer, Gas Discharge Physics, Springer-Verlag, Berlin Heidelberg, 1991

[16] E. Pfender, Plasma Chemistry and Plasma Processing, 19, 1 (1999)

[17] B. Pateyron, M.F. Elchinger, G. Delluc and P. Fauchais, Plasma Chemistry and Plasma Processing, 16, 39 (1996)

[18] T. Yoshida, Materials Transactions Japan Institute of Mater, 31, 1 (1990)

[19] P. R. Taylor and S. A. Pirzada, Advanced Performance Materials, 1, 35 (1994)

[20] P. Fauchais, A. Vardelle and A. Denoirjean, Surface and Coatings Technology, 97, 66 (1997)

[21] D. Vollath, Journal of Nanoparticle Research, 10, 39 (2008)

[22] H.R. Griem, Physical. Review, 131, 1170 (1963)

[23] T. Fujimoto and R.W.P. McWhirter, Physical Review A, 42, 6588 (1990)

[24] G. Faussurier, C. Blancard and A. Decoster, Physical Review E, 56, 3474 (1997)

[25] M.R. Zaghloul, Physics of Plasmas, 10, 527 (2003)

[26] W.L.T. Chen, J. Heberlein and E. Pfender, Plasma Chemistry and Plasma Processing, 14, 317 (1994)

[27] W.H. Gauvin, Plasma Chemistry and Plasma Processing, 9, 65 (1989)

[28] J. Haidar, Journal of Physics D: Applied Physics, 32, 263 (1999)

[29] K. Dzierzega, W. Zawadzki, B. Pokrzywka and S. Pellerin, Physical Review E, 74, 026404 (2006)

[30] S.C. Snyder, G.D. Lassahn and J.D. Grandy, Journal of Quantitative Spectroscopy and Radiative Transfer, 107, 217 (2007)

[31] A.B. Murphy, Physical Review E, 69, 016408 (2004)

[32] R.E. Bentley, Journal of Physics D: Applied Physics, 30, 2880-2886 (1997)

[33] M. Shigeta, N. Atsuchi and T. Watanabe, Journal of Chemical Engineering of Japan, 39, 1255-1264 (2006)

[34] S.C. Snyder, G.D. Lassahn and L.D. Reynolds, Physical Review E, 48, 4124 (1993)

[35] T. Watanabe, N. Atsuchi and M. Shigeta, Thin Solid Films, 515, 4209 (2007)

[36] R. Mofreh Zaghloul, Physics of Plasmas, 10, 527 (2003)

[37] M.N. Saha, Philosophical Magazine, 238, 472 (1920)

[38] A.V. Potapov, High Temperature, 4, 48 (1966)

[39] S. Veis, Czechoslovac Conference on Electronics and Vacuum Phys. (Charles University, Prague), A3-1, 105 (1968)

[40] M.R. Zaghloul, M.A. Bourham and J.M. Doster, Journal of Physics D: Applied Physics, 33, 977 (2000)

[41] G.N. Lewis and E.Q. Adams, Physical Review, 4, 331 (1914)

[42] W.G. Hoover, Annual Review Physical Chemistry, 34, 1037 (1983)

[43] J.W. Ochterski, Gaussian Inc, Pittsburgh, PA, 2000

[44] F. Weinhold, Journal of Chemical Physics, 109, 367 (1998)

[45] Y.B. Yu, P.L. Privalov and M. Gabriel, Biophysical Journal, 81, 1632 (2001)

[46] M. Born and J.R. Oppenheimer, Annals of Physics, 84, 457 (1927)

[47] B.M. Smirnov, “Clusters and small particles: in gases and plasmas”, Springer Verlag, 2000

[48] P.P.J.M. Schram, “Kinetic thwory of gases and plasmas”, Springer, 1991

[49] H. Schbahashi, A. Noels and M. Gabriel, Astronomy and Astrophysics, 123, 283 (1983)

[50] M.M. Hossain, Y. Tanaka and T. Sakuta, Journal of Physics D: Applied Physics, 35, 529 (2002)

[51] W.Z. Wang, M.Z. Rong, J.D. Yan, A.B. Murphy, M.T.C. Fang and J.W. Spence, Plasma Chemistry and Plasma Processing, 32, 495 (2012)

[52] P.S. Aronson, Annual Review Physiology, 47, 545 (1985)

[53] H. Biglari, P.H. Diamond and M.N. Rosenbluth, Physics of Fluids B, 1, 109 (1989)

[54] F.L. Hinton and S.K. Wong, Physics of Fluids B, 28, 3082 (1985)

[55] W. Horton, D.I. Choi and W.M. Tang, Physics of Fluids B, 24, 1077 (1981)

[56] C.J. Fielfing, The Journal of Lipid Research, 25, 1624- (1984)

[57] R.F. Cracknell, D. Nicholson and N. Quirke, Physical Review Letters, 74, 2463 (1995)

[58] M.F. Modest, Radiative Heat Transfer, Academic Press, New York, 2003

[59] V. Aubrecht and E.T. Protasevich, Radiative Transport of energy in SF6 Arc Plasma, Tomsk, Russia, 2000

[60] H. Conrads and M. Schmidt, Plasma Sources Science and Technology, 9, 441 (2000)

[61] A.B. Murphy, Annals New York Academy of Science, 891, 106 (1999)

[62] G. Bonizzoni and E. Vassallo, Vacuum, 64, 327 (2002)

[63] P. Fauchais and A. Vardelle, Plasma Physics and Controlled Fusion, 42, B365 (2000)

[64] J. Heberlein, Pure and Applied Chemistry, 52, 1773 (1980)

[65] J. Heberlein, Pure and Applied Chemistry, 60, 591 (1988)

[66] R. M. Young and E. Pfender, Plasma Chemistry and Plasma Processing, 5, 1 (1985)

[67] S. Ramakrishnan, M.Gershenzon, F. Polivka, T.N. Kearney and M.W. Rogozinski, IEEE Transactions on Plasma Sciences, 25, 937 (1997)

[68] R. Henne, Contributions to Plasma Physics, 39, 385 (1999)

[69] N.N. Rykalin, Pure and Applied Chemistry, 48, 179 (1976)

[70] V. Subramanian, R. Baskaran and H. Krishnan, Aerosol and Air Quality Research, 9, 172 (2009)

[71] J.H. Seo and B.G. Hong, Nuclear Engineering and Technology, 44, 9 (2012)

[72] J.V.R. Heberlei, Pure and Applied Chemistry, 64, 629 (1992)

[73] T. Yoshida, Materials Transaction, Japan Institute of Metals, 30, 1 (1990)

[74] M.I. Boulos, Nuclear Engineering and Technology, 44, 1 (2012)

[75] M.I. Boulos, Diagnostics of Thermal Plasmas, In Frontiers of Low Temperature Plasma Diagnostics III Conference, 1999

[76] H.A. Dinulescu and E. Pfender, Journal of Applied Physics, 51, 3149 (1980)

[77] W.H. Gauvin, Plasma Chemistry and Plasma Processing, 9, 65S (1989)

[78] H. Maecker, in An Introduction to Discharge and Plasma Physics, S.C. Haydon, Ed (The University of New England, N.S.W., Australia) Chap. 20, 245 (1964)

[79] W.H. Gauvin, M.G. Drouet and R.J. Munz, Metals, 39, 14 (1987)

[80] Y.C. Yao, Kazuyuki Yatsuda, TakayukiWatanabea, Fuji Funabiki, Tetsuji Yano, Chemical Engineering Journal 144, 317–323 (2008)

[81] Ph.G. Rutberg, A.A. Safronov, S.D. Popov, A.V. Surov and Gh.V. Nakonechny, Plasma Physics and Controlled Fusion 47, 1681 (2005)

[82] Ph.G. Rutberg, A.A. Safronov, S.D. Popov, A.V. Surov and G.V. Nakonechnyi, High Temperature, 44(2), 199 (2006)

[83] Y.C. Yao, K. Yatsuda, T. Watanabe, T. Matsuura, T. Yano, Plasma Chem Plasma Process, 29, 333 (2009)

[84] A.B. Murphy, Plasma destruction of gaseous and liquid wastes, Ann. NY Acad. Sci., (Heat and Mass Transfer Under Plasma Conditions) 106 (1999)

[85] T. Ishigaki and J.G. Li, Pure and Applied Chemistry, 80, 1971 (2008)

[86] M. Shigeta, T. Watanabe and H. Nishiyama, Thin Solid Films, 457, 192 (2004)

[87] M. Shigeta and T. Watanabe, Journal of Material Research, 20, 2801 (2005)

[88] M. Shigeta and H. Nishiyama, Transactions of ASME Journal of Heat Transfer, 127, 1222 (2005)

[89] M. Shigeta and T. Watanabe, JSME International Journal Series B, 48, 425 (2005)

[90] M. Shigeta and T. Watanabe, Thin Solid Films, 515, 4217 (2007)

[91] M. Shigeta and T. Watanabe, Journal of Physicas D: Applied Physics, 40, 2407 (2007)

[92] M. Shigeta and T. Watanabe, Journal of Thermal Spray Technology, 18, 1022 (2009)

[93] M. Shigeta and T. Watanabe, Journal of Applied Physics, 108, 04330601 (2010)

[94] N. Yadira, M. Gonzalez and P. Proulx, Journal of Thermal Spray Technology, 17, 533 (2008)

[95] A.I. Al-Shamma, I. Pandithas and J. Lucas, Journal Physics D: Applied Physics, 34, 2775 (2001)

[96] Y.A. Lebedev, I.L. Epstein, A.V. Tatarinov and V.A. Shakhatov, Journal of Physics: Conference Series, 207, 012002 (2010)

[97] S. Maeda, H. Matsuo, K. Kuwahara, Y. Matsuda, H. Kuwahara and H. Fujiyama , Surface and Coatings Technology, 97, 404 (1997)

[98] R. Perera, A. Ikeda, R. Hattori and Y. Kuroki, Microelectronic Engineering, 65, 357 (2003)

[99] R. Bajorek, R. Parosa, E. Reszke, J. Wojcik and S. Zbyrad, Plasma Chemistry and Plasma Processing, 7, 341 (1987)

[100] T. Yoshida, T. Tawi, H. Nishimura, and K. Akashi, Journal of Applied Physics, 54, 640 (1983)

[101] T. Kameyama and K. Fukuda, Nat. Chem. Lab. for Industry, Tsukuba, Japan, Internal Rep., 21, 1986

[102] K. Kawajiri, T. Sato and H. Nishiyama, Surface and Coatings Technology, 171, 134 (2003)

[103] K. Kawajiri and H. Nishiyama, Thin Solid Films, 506, 660 (2006)

[104] K. Kawajiri, K. Ramachandran and H. Nishiyama, International Journal of Heat and Mass Transfer, 48, 183 (2005)

[105] R.W. Smith, D. Wei and D. Apelian, Plasma Chemistry and Plasma Processing, 9, 135S (1989)

[106] C.P. Kong and Y.C. Lau, Pure and Applied Chemistry, 62, 1809 (1990)

[107] Z.P. Lu, J. Heberlein and E. Pfender, Plasma Chemistry and Plasma Processing, 12, 35 (1992)

[108] Z.P. Lu, L. Stachowicz, P. Kong, J. Heberlein and E. Pfender, Plasma Chemistry and Plasma Processing, 11, 387 (1991)

[109] S. Matsumoto, M. Hino and T. Kobayashi, Applied Physics Letters, 51, 737 (1987)

[110] N. Ohtake and M. Yoshikawa, Journal of The Electrochemical Society, 137, 717 (1990)

[111] K. Kurihara, K. Sasaki, M. Kawarada and N. Koshino, Applied Physics Letters, 52, 437 (1988)

[112] S. Matsumoto, in Diamond and Diamond-Like Materials Synthesis, edited by G.H. Johnson, A.R. Badzian, and M.W. Geis (Materials Research Society, Pittsburgh, PA), 119 (1988)

[113] M.A. Cappelli, T.G. Owano, and C.H. Kruger, Journal of Material Research, 5, 2326 (1990)

[114] E. Bouyer, G. Schiller, M. Muller and R.H. Henne, Plasma Chemistry and Plasma Processing, 21, 523 (2001)

[115] M. Back and A. Gruchovp, Pure and Applied Chemistry, 64, 665 (1992)

[116] V. Cioca and L. Benes, Revue Roumaine de Physique, 14, 303 (1969)

[117] B. Waldie, Transactions Institute of Chemistry Energy, 48, T90 (1970)

[118] I. Amato, P.G. Capelli, and M. Ravizzam, La Metallurgie Italian, 5, 323 (1967)

[119] V.A. Petrunichev and V.I. Mikhalev, Russian Metallic Fuels, 5, 82 (1966)

[120] B. Waldie, Journal of Materials Science, 4, 648 (1969)

[121] V.M. Slepstov, A.M. Proshedromirskaya, and A.M. Taranets, Russian Metallic Fuels, 7, 113 (1967)

[122] D.L. Houck, Modern Developments in Powder Metallurgy, 14, 485 (1981)

[123] C.E.G. Bennett and N.A. McKinnon, in Kinetics of Reactions in Ionic Systems; T.J. Gray and V.D. Frechette Ed., Plenum Press, N.Y., 408 (1969)

[124] L.G. Gordone and W.E. Martinsen, Journal of the American Ceramic Society, 55, 380 (1972)

[125] G. Thomas, J. Freim and W.E. Martinsen, Transactions of the American Nuclear Society, 2, 177 (1973)

[126] G. Thomas and J. Freim, Transactions of the American Nuclear Society, 21, 182 (1975)

[127] D.L. Johnson and R.A. Rizzo, American Ceramic Society Bulletin, 2, 467-473 (1980)

[128] D.L. Johnson and J.S. Kim, in Sintering-Theory and Practice, Material Science Monographs, 14, D. Kolar, S. Pejonvik and M.M. Ristic Ed., Elsevier, Amsterdam, 573 (1982)

[129] J.S. Kim and D.L. Johnson, American Ceramic Society Bulletin, 62, 620 (1983)

[130] D.L. Johnson, V.A. Kramb and D.C. Lynch, Material Science Research, R.F. Davis, H. Palmour and R.L. Porter Ed., Plenum Press, New York, 207, 1982

[131] D.L. Johnson, W.B. Sanderson, J.M. Knowlton and E.L. Kemer, Proceeding of MqO/$A1_20_3$ Conference, M.I.T., Cambridge, MA, 1983

[132] C.W. Chang and J. Szekely, Journal of Metals, 34, 57 (1982)

[133] S.M.L. Hamblyn, Minerals Science and Engineering, 9, 151 (1977)

[134] S. Shimbara and T. Watanabe, Proceedings of Regional Symposium on Chemical Engineering, Ref. C7 Metro Manila, Philippines, 1 (2004)

[135] L. Tang and H. Huang, Fuel Processing Technology, 88, 549 (2007)

[136] L. Tanga and H. Huang, Fuel, 84, 2055 (2005)

[137] J. Heberlein and A.B Murphy, Journal of Physics D: Applied Physics, 41, 053001 (2008)

[138] E. Gomez, D. Amutha Rani, C.R. Cheeseman, D. Deegan, M. Wise and A.R. Boccaccini, Journal of Hazardous Materials, 161, 614 (2009)

[139] J. Heberlein, Thermal plasmas for the destruction of hazardous wastes Proc. Plasma

Technologies for Hazardous Waste Destruction (Bologna, Italy: Editrice Compositori) 59 (1992)

[140] J. Heberlein, Thermal plasmas for the destruction of hazardous wastes Industrial Applications of Plasma Physics (Bologna, Italy: Italian Physical Society), 219 (1993)

[141] M. Desilets, J.F. Bilodeau and P. Proulx, Journal of Physics D: Applied Physics, 30, 1951 (1997)

[142] Y.I. Chang, P. Kong, and E. Pfender, Plasma Chemistry and Plasma Processing, 9, 73 (1989)

[143] M. Shigeta and T. Watanabe, Journal of Applied Physics, 103, 074903 (2008)

[144] N.Y. Mendoza-Gonzalez, B.M. Goortani and P. Proulx, Materials Science and Engineering C, 27, 1265 (2007)

[145] P. Proulx and J.F. Bilodeau, Plasma Chemistry and Plasma Processing, 11, 371 (1991)

[146] S.L. Girshick, C.P. Chiu, and P.H. McMurry, Plasma Chemistry and Plasma Processing, 8, 145 (1988)

[147] X.F. Guo and G.J. Kim, Plasma Chemistry and Plasma Processing, 30, 75 (2010)

[148] O. Satoru and U. Masahiro, Journal of Institute of Metals and Materials, 4, 640 (1984)

[149] T. Watanabe and M. Tanaka, 16th Asean Proceedings of Regional Symposium on Chemical Engineering, Philippines, 1, 2009

[150] M. Shigeta and A.B Murphy, Journal of Physics D: Applied Physics, 44, 174025 (2011)

[151] M. Tanaka and T. Watanabe, Thin Solid Films, 516, 6645 (2008)

[152] N.V. Kulkarni, S. Karmakar, I. Banerjee, S.N. Sahasrabudhe, A.K. Das and S.V. Bhoraskar, Materials Research Bulletin, 44, 581 (2009)

[153] L. Tong and R.G. Reddy, Scripta Materialia, 52, 1253 (2005)

[154] L. Tong and R.G. Reddy, Materials Research Bulleti, 41, 2303 (2006)

[155] L. Tong and R.G. Reddy, Metallurgical and Materials Transactions B, 37, 531 (2006)

[156] T. Ryu, H.Y. Sohn, K.S. Hwang and Z.Z. Fang, International Journal of Refractory Metals & Hard Materials, 27, 149 (2009)

[157] T. Ryu, H.Y. Sohn, K.S. Hwang and Z.Z. Fang, Journal of Material Science, 43, 5185 (2008)

[158] T. Ryu, H.Y. Sohn, K.S. Hwang and Z.Z. Fang, Journal of the American Ceramic Society, 92, 655 (2009)

[159] T. Ryu, H.Y. Sohn, Y.U. Kim and M. Olivas-Martinez, Journal of Nanoparticle Research,

12, 2851 (2010)

[160] T. Ryu, Y.J. Choi, K.S. Hwang, H.Y. Sohn and I. Kim, Journal of the American Ceramic Society, 93, 3130 (2010)

[161] J.H. Chen, G.H. Lu, L.Y. Zhu and R.C. Flagan, Journal of Nanoparticle Research, 9, 203 (2007)

[162] J. Haidar, Plasma Processing, 29, 307 (2009)

[163] T. Yoshida, A. Kawasaki, K. Nakagawa and K. Akashi, Journal of Material Science, 14, 1624 (1979)

[164] T. Yoshida and K. Akashi, Transactions of the Japan Institute of Metals, 22, 371 (1981)

[165] T. Harada, T. Yoshida, T. Koseki and K. Akashi, Journal of The Japan Institute of Metals, 45, 1138 (1981)

[166] Y. Anekawa, T. Yoshida, T. Koseki and K. Akashi, Journal of The Japan Institute of Metals, 49, 451 (1981)

[167] K. Eguchi, I.Y. Ko, T. Sugawara, H.J. Lee and T. Yoshida, Journal of The Japan Institute of Metals, 53, 1236 (1989)

[168] S.H. Lee, S.M. Oh and D.W. Park, Materials Science and Engineering C, 27, 1286 (2007)

[169] S.L. Girshick, C.P. Chiu, R. Muno, C.Y. Wu, L. YAang, S.K. Singh and P.H. Mcmurry, Journal of Aerosol Science, 24, 367 (1993)

[170] P. Proulx, J. Mostaghimi and M.I. Boulos, ht. Journal of Heat Mass Transfers, 28, 1327 (1985)

[171] H. Shoji, Y. Nakano, H. Matsushita, A. Onoe, H. Kanai and Y. Yamashita, Journal of Materials Synthesis and Processing, 6, 415 (1998)

[172] J.Z. Gao, F. Guan, Y.C. Zhao, W. Yang, Y.J. Ma, X.Q. Lu, J.G. Hou and J.W. Kang, Materials Chemistry and Physics, 71, 215 (2001)

[173] H.J. Zhang, H.T. Zhang, X.W.Wu, Z.L.Wang, Q.L. Jia and X.L. Jia, Journal of Alloys and Compounds, 419, 220 (2006)

[174] H. Niu, Q. Chen, M. Ning, Y. Jia and X. Wang, Journal of Physical Chemistry B, 108, 3996 (2004)

[175] F. Davar, Z. Fereshteh, and M. Salavati-Niasari, Journal of Alloys and Compounds, 476, 797 (2009)

[176] K.H. Kim, H.C. Park, S.D. Lee, W.J. Hwa, S.S. Hong, G.D. Lee and S.S. Park, Materials Chemistry and Physics, 92, 234 (2005)

[177] L. Baia, J. Fan, P. Hu, F. Yuan, J. Li and Q. Tang, Journal of Alloys and Compounds, 481, 563 (2009)

[178] Z. Turgut, J.H.J. Scott, M.Q. Huang, S.A. Majetich and M.E. McHenry, Journal of Applied Physics, 83, 6470 (1998)

[179] Z. Turgut, N.T. Nuhfer, H.R. Piehler and M.E. McHenry, Journal of Applied Physics, 85, 4406 (1999)

[180] J.H.J. Scott, S.A. Majetich, Z. Turgut, M.E. McHenry and M. Boulos, Materials Research Society Symposium Proceedings, 457, 219 (1997)

[181] J.H.J. Scott, Z. Turgut, K. Chowdary, M.E. McHenry and S.A. Majetich, Materials Research Society Symposium Proceedings, 501, 121 (1998)

[182] S. Son, M. Taheri, E. Carpenter, V.G. Harris and M.E. McHenry, Journal of Applied Physics, 91, 7589 (2002)

[183] Y. Anekawa, T. Yoshida, T. Koseki and K. Akashi, Journal of Japan Institute of Metals, 49, 451 (1985)

[184] R. Swaminathan, M.A. Willard and M.E. McHenry, Acta Materialia, 54, 807 (2006)

[185] S. Son, R. Swaminathan and M.E. McHenry, Journal of Applied Physics, 91, 7495 (2003)

[186] D.M. Chen, J.F. Klausner and R.W. Mei, Powder Technology, 124, 127 (2002)

[187] G.L. Xu, J.J. Zhang and G.Z. Song, Powder Technology, 134, 218 (2003)

[188] M. Preghenella, A. Pegoretti and C. Migliaresi, Polymer, 46, 12065 (2005)

[189] Y. Zhu, H. Da, X. Yang and Y. Hu, Colloid Surface A, 231, 123 (2003)

[190] H. Nishikawa, T. Souno, M. Hattori, Y. Nishihara, Y. Ohki, E. Watanabe, M. Oikawa, T. Kamiya and K. Arakawa, Nuclear Instruments and Methods in Physics Research Section B, 191, 342 (2002)

[191] A.V. Rao, G.M. Pajonk and D. Haranth, Materials Science and Technology, 17, 343 (2001)

[192] R. Hilliard, X. Lisa, J. Zhao and W.H. Tan, Analytica Chimica Acta, 470, 51 (2002)

[193] S. Cordelia, Nanotoday, 1, 19 (2006)

[194] B.M. Goortani, P. Proulx, S. Xue and N.Y. Mendoza-Gonzalez, Powder Technology, 175, 22 (2007)

[195] H. Zheng, J.Z. Ou, M.S. Strano, R.B. Kaner, A. Mitchell and K. Kalantar-zadeh, Advanced Functional Materials, 21, 2175 (2011)

[196] R. Abe, H. Takami, N. Murakami and B. Ohtani, Journal of America Chemistry Society,

130, 7780 (2008)

[197] A.A. Ashkarran, A.I. Zad, M.M. Ahadian and S.A.M. Ardakani, Nanotechnology, 19, 195709 (2008)

[198] S.H. Baeck, K.S. Choi, T.F. Jaramillo, G.D. Stucky and E.W. McFarland, Advanced Materials, 15, 1269 (2003)

[199] Z.G. Zhao and M. Miyauchi, Angewandte Chemie International Edition, 47, 7051 (2008)

[200] Z.G. Zhao, Z.F. Liu and M. Miyauchi, Chemical Communications, 46, 3321 (2010)

[201] V. Khatko, E. Llobet, X. Vilanova, J. Brezmes, J. Hubalek, K. Malysz and X. Correig, Sensors and Actuators B, 111, 45 (2005)

[202] X.L. Li, T.J. Lou, X.M. Sun and Y.D. Li, Inorganic Chemistry, 43, 5442 (2004)

[203] W. Qu, Sensors and Actuators B, 64, 42 (2000)

[204] F. Sun, M. Hu, P. Sun, J. Zhang and B. Liu, Journal of Nanoscience and Nanotechnology, 10, 7739 (2010)

[205] M. Righettoni, A. Tricoli and S. E. Pratsinis, Chemistry Materials, 22, 3152 (2010)

[206] M.T. Ke, M.T. Lee, C.Y. Lee and L.M. Fu, Sensors, 9, 2895 (2009)

[207] M.D. Arienzo, L. Armelao, C.M. Mari, S. Polizzi, R. Ruffo, R. Scotti and F. Morazzoni, Journal of America Chemistry Society, 133, 5296 (2011)

[208] T. Satoa, T. Tanigakia, H. Suzukia, Y. Saitob, O. Kidoa, Y. Kimuraa and C. Kaitoa, Journal of Crystal Growth, 255, 313 (2003)

[209] J.W. Shin, H. Miyazoe, M. Leparoux, S. Siegmann, J.L. Dorier and C. Hollenstein, Plasma Sources Science and Technology, 15, 441 (2006)

[210] J.G. Li, H. Kamiyama, X.H. Wang, Y. Moriyoshi and T. Ishigaki, Journal of the European Ceramic Society, 26, 423 (2006)

[211] J.G. Li, H. Kamiyama, X.H. Wang, Y. Moriyoshi, T. Ishigaki and T. Sekiguchi, Thin solid films, 506, 292 (2006)

[212] Y.L. Li, and T. Ishigaki, Journal of Physical Chemistry B, 108, 15536 (2006)

[213] S.M. Oh, J.G. Li and T. Ishigaki, Journal of Material Research, 20, 529 (2005)

[214] S.M. Oh and T. Ishigaki, Thin Solid Films, 457, 186 (2004)

[215] K. Baba, N. Shohata, and M. Yonezawa, Applied Physics Letters, 54, 2309 (1989)

[216] M.H. Bocanegra-Bernala and B. Matovic, Materials Science and Engineering A, 500, 130 (2008)

[217] D.S. Park and C.W. Kim, Journal of Material Science, 36, 785 (2001)

[218] T. Yoshida, H. Endo, K. Saito and K. Akashi, Proceeding of ESPC-6, Montreal, 225 (1983)

[219] H.J. Lee, K. Eguchi and T. Yoshida, Journal of American Chemistry Society, 73, 3356 (1990)

[220] J. Szepvolgyi and I. Mohai-Toth, Proceeding of ISPC-10, Bochum, 1471 (1991)

[221] L.M. Sheppard, American Ceramic Society Bulletin, 70, 692 (1991)

[222] J. Szepvolgyi and I. Mohai-Toth, Proceeding of ISPC-1, Loughborough, 4, 1549 (1993)

[223] T. Hussai and V.J. Ibertson, Proceeding of ISPC-7, Eindhoven, 2, 692 (1985)

[224] P. Humbert and D. Morvan, Journal of Amouroux, 864 (1958)

[225] J. Szepvolgyi and I. Mohai-Toth, Journal of Material Chemistry, 5, 1227 (1995)

[226] M. Yamada, T. Inamoto, M. Fukumoto and T. Yasui, Materials Transactions, 45, 3304 (2004)

[227] K. Dong-Wook, K. Tae-Hee, P. Hyun-Woo and P. Dong-Wha, Applied Surface Science, 257, 5375-5379 (2011)

[228] R.B. Levy and M. Boudart, Science, 181, 547 (1973)

[229] C. Liang, F. Tian, Z. Wei, Q. Xin and C. Li, Nanotechnology, 14, 955 (2003)

[230] M. Leparoux, C. Schreuders, S. Jong-Won and S. Siegmann, Advanced Engineering Materials, 7, 349 (2005)

[231] S.M. Oh, M. Cappelli and D.W. Park, Korean Journal of Chemical Engineering, 19, 903 (2002)

[232] M. Pierre, Surface Science Reports, 48, 1 (2002)

[233] Q.G. Fu, H.J. Li, X.H. Shi, K.Z. L and G.D. Sun, Scripta Materialia. 52, 923 (2005)

[234] B.G. Ravi, O.A. Omotoye, T.S. Srivatsan, M. Petrorali and T.S. Sudarshan, Journal of Alloys and Compounds, 299, 292 (2009)

[235] T. Kameyama, K. Sakanaka, A. Motoe, T. Tsunoda, T. Nakanaga, N.I. Wakayama, H. Takeo and K. Fukuda, Journal of Material Science, 25, 105 (1990)

[236] J.Y. Guo, F. Gitzhofer and M.I. Boulos, Journal of Material Science, 30, 5589 (1995)

[237] J.Y. Guo, F. Gitzhofer and M.I. Boulos, Plasma Chemistry and Plasma Processing, 17, 219 (1997)

[238] P. Buchner, D. Lutzenkirchen-Hecht, H.H. Strhblow and J. Uhlenbusch, Journal of Material Science, 34, 925 (1999)

[239] H.J. Lee, K. Eguchi, T. Yoshida, Journal of America Chemistry Society, 73, 3356 (1990)

[240] E. Bouyer, M. Muller, R.H. Henne and G. Schiller, Journal of Nanoparticle Research, 3, 373 (2001)

[241] K. Sakanaka, A. Motoe, T. Tsunoda, T. Kameyama and K. Fukuda, 882

[242] T. Ryu, H.Y. Sohn, K.S. Hwang and Z.Z. Fang, Journal of Material Science, 43, 5185 (2008)

[243] S. Wahlberg, I. Grenthe and M. Muhammed, Nanostructured Materials, 9, 105 (1997)

[244] Y.T. Zhu and A. Manthiram, Composites Part B: Engineering, 27, 407 (1996)

[245] L. Fu, L.H. Cao, Y.S. Fan, Scripta Materialia, 44, 1061-1068 (2001).

[246] H.H. Nersisyan, H.I. Won and C.W. Won, Materials Chemistry and Physics, 94, 153 (2005)

[247] X.Y. Wu, W. Zhang and W. Wang, Journal of Material Research, 19, 2240 (2004)

[249] M.F. Zawrah, Ceramics International, 33, 155 (2007)

[249] X.L. Shi, G.Q. Shao, X.L. Duan, Z. Xiong and H. Yang, Materials Characterization, 57, 358 (2006)

[250] T. Ishigaki, S.M. Oh, J.G. Li and D.W. Park, Science and Technology of Advanced Materials, 6, 111 (2005)

[251] M. Leparoux, S.C. Schreuders, J.W. Shin and S. Siegman, Advanced Engineering Materials, 7, 349 (2005)

[252] Y. Leconte, M. Leparoux, X. Portier and N. Herlin-Boime, Plasma Chemistry and Plasma Processing, 28, 233 (2008)

[253] M. Leparoux, Y. Kihn, S. Paris and C. Schreuders, International Journal of Refractory Metals and Hard Materials, 26, 277 (2008)

[254] T. Watanabe, H. Itoh, Y. Ishii, Thin Solid Films, 390, 44 (2001)

[255] T. Watanabe, H. Okumiya, Science and Technology of Advanced Materials, 5, 639 (2004)

[256] J.H. Qi, Y.W. Luo, Y.X. Yin and X.Y. Dai, Plasma Science and Technology, 4, 1417 (2002)

[257] K. Etemadi, Plasma Chemistry and Plasma Processing, 11, 41 (1991)

[258] R.L. Axelbaum, D.P. DuFaux and C.A. Frey, Journal of Materials Research, 11, 948 (1996)

[259] J.W. Kim, J.H. Shim, J.P. Ahn, Y.W. Cho, J.H. Kim, K.H. Oh, Materials Letters, 62, 2461 (2008)

[260] V. Singh, P. Banerjee, V. Srinivas and N.H. Babu, AIP Conference Proceeding, 1347, 256

(2011)

[261] J. Legrand, A.Taleb, S. Gota, M.J. Guittet and C. Petit, Langmuir, 18, 4131 (2002)

[262] S. Rades, A. Kornowski, H. Weller and B. Albert, ChemPhysChem, 12, 1756 (2011)

[263] C.L. Yeh, W.H. Chen, Journal of Alloys and Compounds, 420, 111 (2006)

[264] J.Y. Huang, T. Ishigaki, T. Tanaka and S. Horiuchi, Journal of Material Science, 33, 4141 (1998)

[265] T. Watanabe, T. Ibe, Y. Abe, Y. Ishii, K.Adachi, "Formation Mechanism of Boride Nanoparticles by Induction Thermal Plasmas"

[266] T. Watanabe, A. Neza, Y. Abe, Y. Ishii and K. Adachi, Thin Solid Films, 435, 27 (2003)

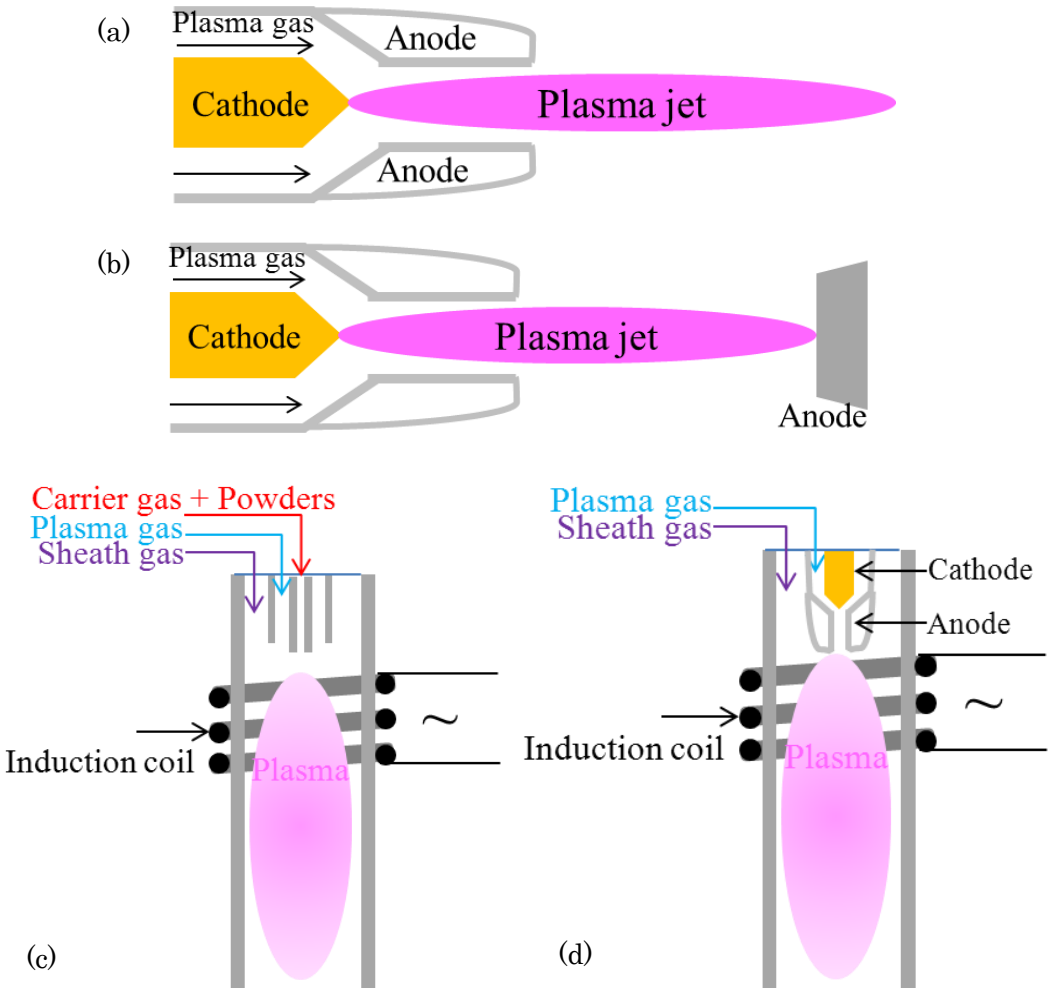

Fig. 1 Basic Setup used for generation of thermal plasma:
(a) DC non-transferred arc; (b) DC transferred arc; (c) RF thermal plasma;
(d) hybrid plasma (DC+RF)

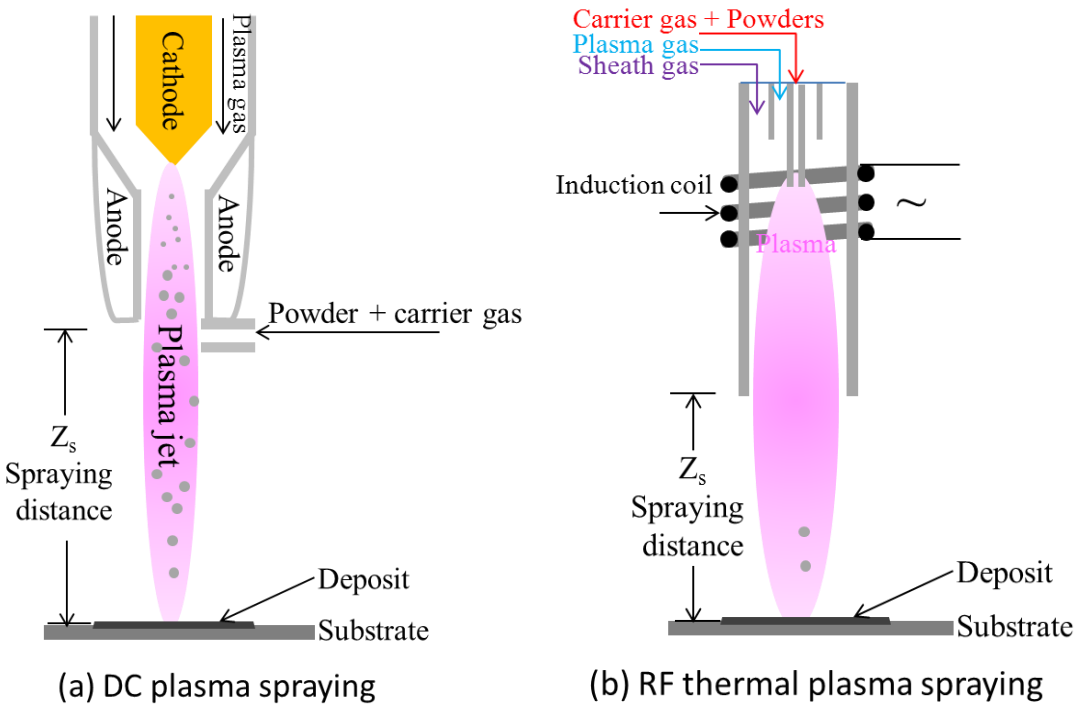

Fig. 2 Basic setup used for DC and RF induction plasma spraying

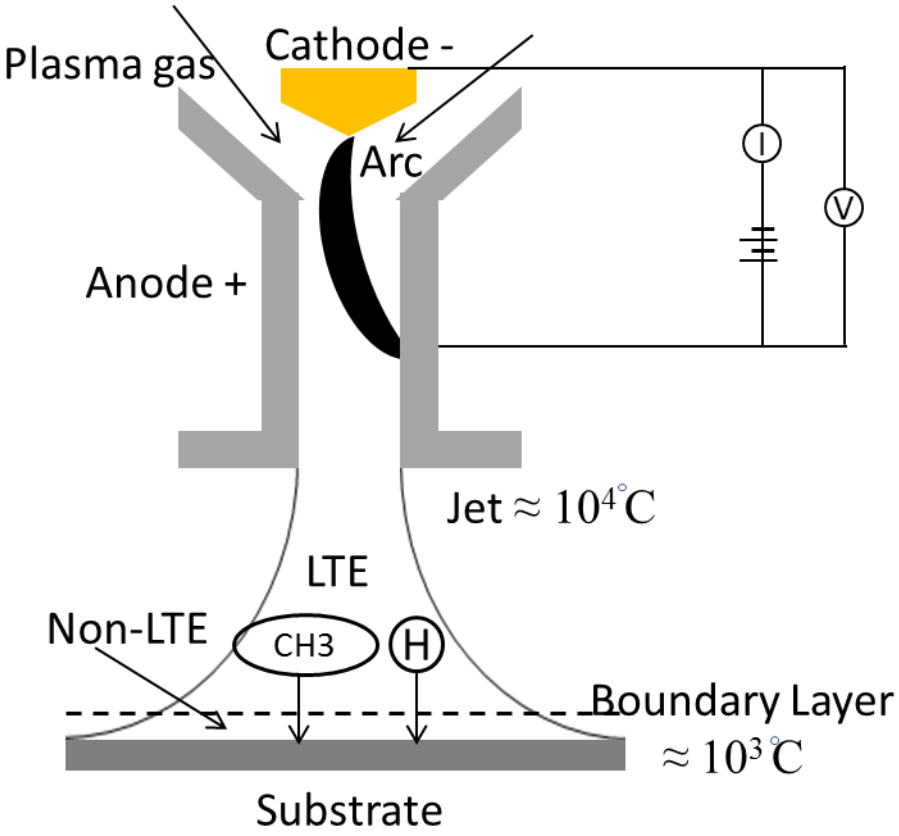

Fig. 3 Schematic of diamond TPCVD with a DC plasma torch

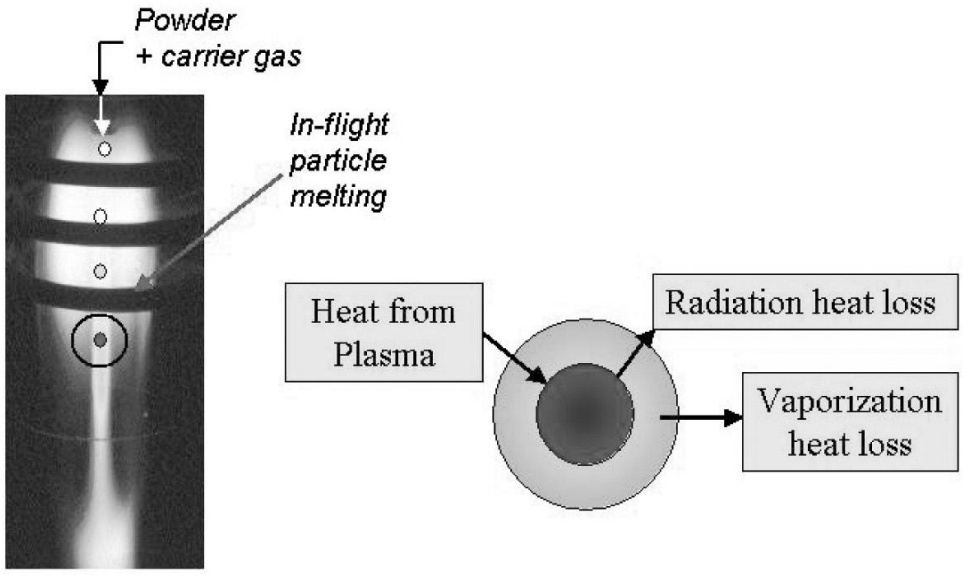

Fig. 4 Schematic representation of the basic phenomena involved in the process of spherodization through the in-flight heating and melting of individual particles

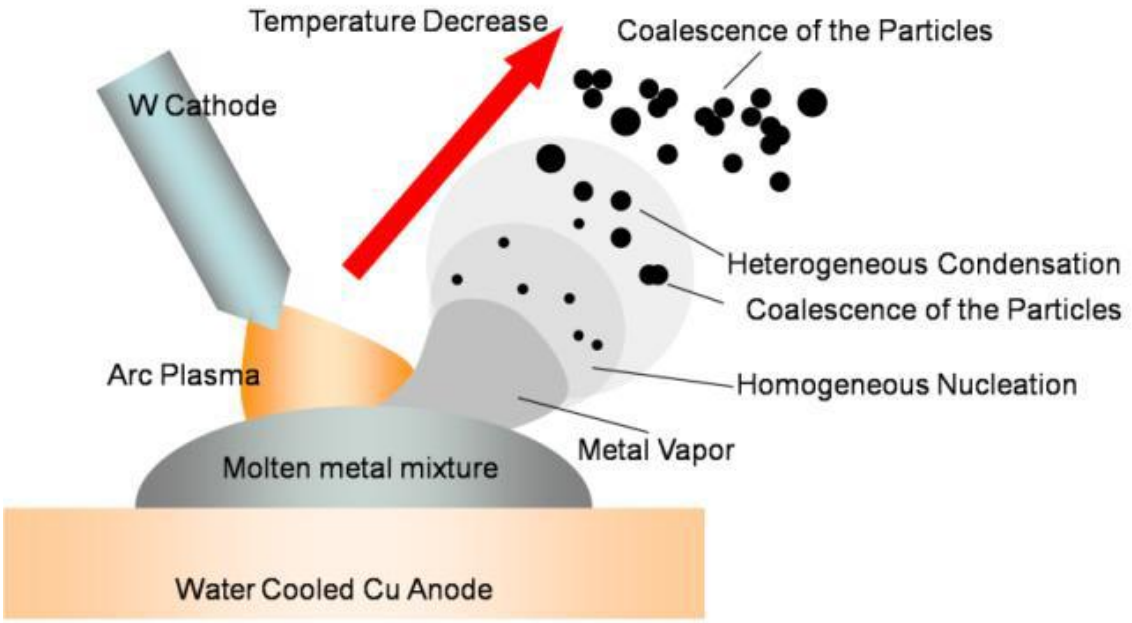

Fig. 5 Conceptual diagram of the DC arc method

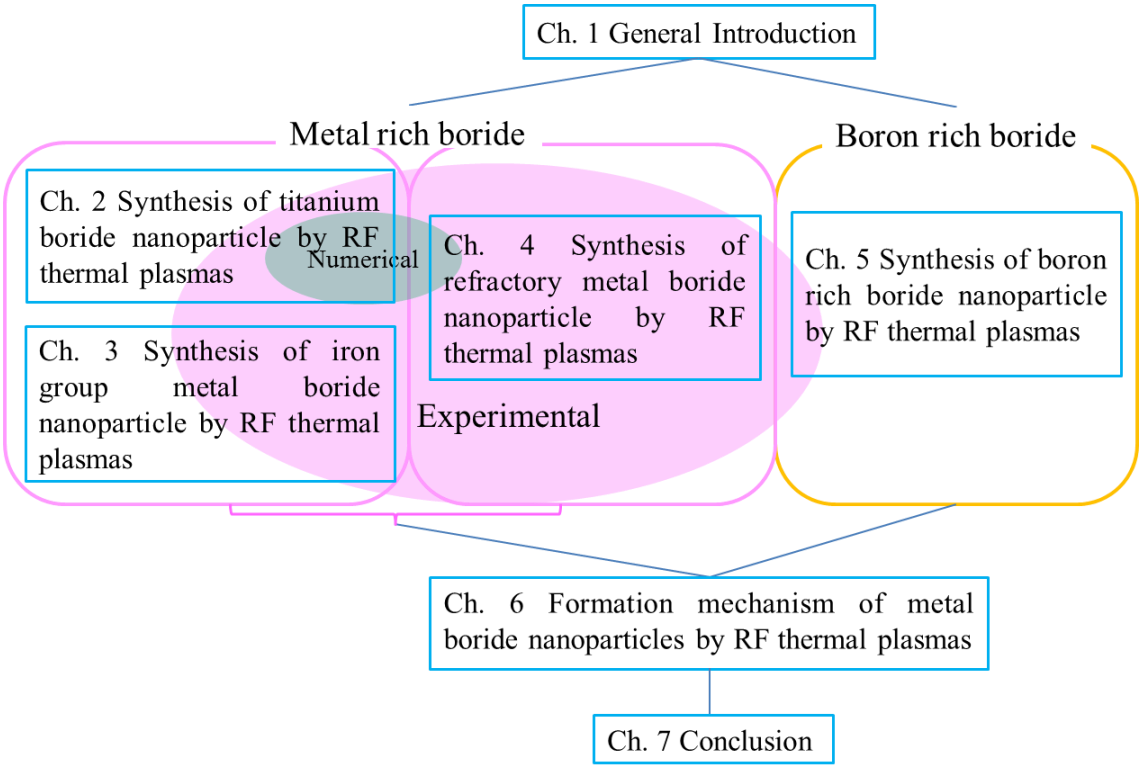

Fig. 6 The flow chart of this study

2. Synthesis of Titanium Boride Nanoparticle by RF Thermal Plasma

2.1 Introduction

Titanium boride nanoparticles have attracted considerable interest, due to high-performance properties, such as high melting temperature, high strength, durability, hardness, wear resistance, high electrical conductivity, low work function and low electrical resistivity. Therefore, titanium boride nanoparticles can be famous and widely applied for the crucibles, electrode materials, protective coatings, armor materials, cutting tools, electromagnetic shielding, wear-resistant coatings, and solar control windows with interaction with IR and UV light [1,2].

However, high-rate and high-purity synthesis of boride nanoparticles is difficult using conventional methods because the raw materials usually have high melting/boiling points. Compared with the other metal boride, the synthesis of titanium boride with low melting point and relatively negative Gibbs free energy is the easiest. In order to investigate the novel method RF thermal plasma better, titanium boride is chosen as model to investigate the formation mechanism by RF thermal plasma.

Several methods have been utilized in the synthesis of TiB_2 such as direction reaction of Ti and B, metal-thermal reduction, chemical vapor deposition, arc-plasma method and gas phase combustion. Normally, TiB_2 powder is produced by reduction of titanium oxide with either boron oxide and carbon or an alkali metal and boron oxide. Among above mentioned processing techniques, the carbothermal reduction process is commercially used by far the cheapest because of inexpensive raw materials and simple process. For each mole of TiB_2 produced, the process generates CO gas which will release energy when burnt with oxygen [3-6].

TiB_2 is also synthesized from non-conventional synthesis methods, such as mechanochcmical synthesis, spark plasma sintering (SPS) [5] or self-propagating high temperature synthesis (SHS) [7].

Thermal plasmas are partially or strongly ionized gases which are usually created by electric arcs or inductively coupled radio frequency (RF) power at atmospheric pressure [8-11].

Radio frequency thermal plasma (RF) has advantages of large volume and high purity. Furthermore, the residence time of treated materials is comparatively long due to the low plasma velocity. Its extremely unique thermofluid field can completely vaporize a large amount of raw materials even with high melting/boiling points [12]. Moreover, since the tail of RF plasma exhibits a high cooling rate (10^4–10^5 Ks^{-1}), effective formation of nanoparticles is simultaneously achieved by nucleation and condensation in a highly supersaturated state. Therefore, RF plasma can be considered an innovative tool that automatically transforms raw materials into functional nanoparticles [12-24]. Additionally, RF thermal plasma is inherently contamination-free because it is produced without any internal electrodes.

Therefore, RF-ICP synthesis of titanium boride nanoparticles provides an attractive alternative to conventional methods, and is regarded as the most reliable plasma for mass-producing nanoparticles with high purity.

The practical fabrication of boride nanoparticles by RF plasma is a complicated phenomenon which involves interaction among the thermofluid field, the induced electromagnetic field and the processed particle phases with numerous variables. The nanoparticles of boride are formed in a complex situation in which multi-component vapors co-condense and convert into nanoparticles in a few milliseconds. Additionally, the growth mechanism of boride nanoparticles is dependent on the properties of boron and metal because the difference in the properties results in different vapor pressure ratios, which is a critical factor for boride nanoparticles growth (e.g. Ti/B: 10^2) [13-24]. Therefore, the growth mechanism of boride nanoparticles in RF plasma has not been elucidated.

Up to now, few studies have been carried out for fabrication of boride nanoparticles by RF plasma with the experimental approach. Therefore, detailed investigation into the growth mechanisms of boride nanoparticles in RF plasma is required for the precise control of the particle size distributions and stoichiometric compositions through the process. If the manufacturing process is well-understood and controlled precisely, mass-production of titanium boride nanoparticles will be easily achieved using RF plasma under atmospheric pressure with low costs. However, the detailed mechanism of their collective growth remains poorly understood. This is true because it is impossible to observe every process using experimental approaches directly; only the characteristics of the final products can be evaluated.

Therefore, theoretical/numerical approach as a powerful tool has to be carried out to clarify the titanium boride nanoparticle growth and to predict the profiles of nanoparticles that will be

synthesized. The temperature and flow profile of thermal plasma are on the basis of the electromagnetic fluid dynamics approach with consideration of chemical non-equilibrium of the plasma species for more accuracy. The precursory powders trajectory and temperature history in the plasma flow is examined by the Lagrangian approach taking into account the rarefied gas effects. The nanoparticle formation is expressed by the aerosol dynamics taking into account not only nucleation, condensation, and coagulation but also convection, diffusion, and thermophoresis. After these computations, numerical analysis is conducted for the fabrication of the titanium boride functional nanoparticles [15-23]. The numerical results will be compared with the experimental results.

In this chapter, the objective is to investigate the formation of Ti-based boride nanoparticles in thermal plasma at atmospheric pressure with experiment and numerical analysis, and find out the effect of parameters, including work gas species, input power, powder feed rate, boron content in the feed powders and carrier gas flow rate on both the diameter and the composition of product.

2.2 Thermodynamic properties

1) Phase diagram of Ti-B system

Ti–B system has been assessed by Murray et al. [26] and Batzner [27], but both of them treated the compound solution phases TiB and TiB_2 as the stoichiometric compounds. Ti–B binary system mainly includes the compound solutions: TiB and TiB_2; stoichiometric compound: Ti_3B_4 [28,29]. The phase diagram of Ti-B systems is shown in **Figure 1**.

The structure of TiB_2 is well established by several experimental studies [30-35] having the AlB_2 structure (P6/mmm) [36-38]. TiB_2 has a very narrow stability region. According to Murray et al. [26], the highest reported congruent temperature, 3498 K, is chosen in the assessed phase diagram. The composition variation for TiB_2 was also found around 65.5-67 at% B from Fenish [36] and 65.5-67.6 at% B from Thebault et al. [37]. The small variation of lattice parameters also confirms the narrow homogeneity range of TiB_2.

Fenish [36] found two different forms of Ti_3B_4, low-temperature form and high-temperature form and the transformation occurs at 2283 K. But this transformation is irreversible.

2) Gibbs free energy

The Gibbs free energy of the system is a state function because it is defined in terms of thermodynamic properties that are state functions. The beauty of the equation defining the free energy of a system is its ability to determine the relative importance of the enthalpy and entropy terms as driving forces behind a particular reaction. The change in the free energy of the system that occurs during a reaction measures the balance between the two driving forces that determine whether a reaction is spontaneous. We can therefore conclude that any reaction for which ΔG is negative should be favorable, or spontaneous.

The Gibbs free energy plays an important role in the synthesis process in the actual experiment. The Gibbs free energy of boridation is very low and negative [39]. Therefore, the chemical stability of boride is the driving force.

The relevant reaction in a composite containing Ti, B and TiB_2 are

$$Ti + 2B \Rightarrow TiB_2 \qquad \Delta G^0_{TiB_2} = -284500 + 20.5T \tag{1}$$

$$Ti + B \Rightarrow TiB \qquad \Delta G^0_{TiB_1} = -53503 + 27.5T \tag{2}$$

Figure 2 shows the curves of the Gibbs free energy vs temperature of the above reactions. It is indicated that all the reactions can take place spontaneously due to their negative ΔG. It is also indicated that the stability of these products is in the following order: $TiB_2 > TiB$.

3) Saturation vapor pressure

Difference of vapor pressure between boron and titanium is the important factor for controlling composition of the prepared nanoparticles. The vapor pressure ratio of titanium to boron is on the order of 10^2 at the melting point of titanium. Preparation of borides with large difference in vapor pressure of the constituent components is quite difficult. Therefore, the control of condensation process is important for preparation of boride nanoparticles.

The saturation vapor pressures of Ti [40] and B [41] were estimated by the following equations (3) and (4), respectively.

$$\log P = 7.782 - \left(\frac{24275}{T}\right) - 0.230 \times 10^{-3} T \tag{3}$$

$$\log P = \left(7.506 - \frac{29630}{T}\right) \cdot 0.1 - 2 \tag{4}$$

where, P is the saturation vapor pressure at the temperature T, and the unit is atm.

Axial evolution of vapor pressure was displayed in **Figure 3**. Boron vapor due to the lower saturation pressure becomes supersaturated earlier than titanium and the nucleation process occurs first at the upstream position. At the downstream position, titanium vapor pressure

reaches its saturation pressure.

2.3 Experimental

2.3.1 Experimental apparatus

A schematic diagram of experimental set-up for the production of boride nanoparticles is shown in **Figure 4**. The set-up mainly consists of an injector for raw materials, a plasma torch, a reaction chamber, and a particle collection filter. The plasma torch works with a water-cooled quartz tube and a water-cooled induction coil (3 turns), coupling its electromagnetic energy to the plasma at a frequency of 4 MHz. In the experiment, the total system was operated at the atmosphere pressure.

2.3.2 Experimental conditions

Feed powders were metal titanium (Wako Pure Chemical Industries. Ltd., particle size 45 μm, purity min 98.0%) and crystalline boron (Kojundo Chemical Laboratory. Co. Ltd., particle size 45 μm, purity 99.0%). Precursors were fed with carrier gas. After the injection of precursors into the plasma from the central nozzle, they are instantaneously evaporated due to the high enthalpy of the thermal plasma. The vapors of the injected titanium and boron are transported with the plasma flow to the reaction chamber and become supersaturated due to the rapid temperature decrease in the tail flame, which leads to homogeneous nucleation. Subsequently, the vapors are co-condensed on the surface of the nucleated particles. Nanoparticles of titanium borides were consequently synthesized from the gas phase.

Table 1 summarizes the operating conditions. Argon was introduced as carrier gas (2 or 3 L/min), plasma supporting gas (5 L/min). Mixture of argon and helium was used as the sheath gas [42], which was injected from the outer slots to protect the inner surface of the quartz tube and stabilize the plasma discharge. The range of powder feed rate was from 0.1 to 1.0 g/min, and boron molar content in feeding powders was controlled from 25.0 to 90.0%.

2.3.3 Analytical methods

The structures of the prepared nanoparticles were determined by X-Ray Diffractometry (XRD, Mac Science MXP3TA). The mean grain-size was calculated from the full widths at the half maximum (FWHM) of the most intensive diffractions according to the Debye-Scherrer’s

equation [43]. The size distribution of the particles was measured from the photographs of Transmission Electron Microscopy (TEM). Debye-Scherrer equation:

$$d = \frac{k\lambda}{\beta \cos\theta} \tag{5}$$

where K is the shape factor, λ is the x-ray wavelength, β is the line broadening at half the maximum intensity (FWHM) in radians, and θ is the Bragg angle; d is the mean size of the ordered (crystalline) domains, which may be smaller or equal to the grain size.

Quantitative phase analysis by XRD was carried out based on the adiabatic method [44]. This method is used for quantitative analysis by powder diffraction in the XRD pattern and based on the ratio of the diffraction data for each phase in the product to the diffraction of standard reference materials selected. The mass fraction of X phase can be calculated by the following equation:

$$W_X = \frac{I_X}{K_A^X \sum_{X=A}^{N} \frac{I_X}{K_A^X}} = \frac{I_X}{K_A^X \cdot (\frac{I_A}{K_A^A} + \frac{I_B}{K_A^B} + \cdots \frac{I_X}{K_A^X} + \cdots \frac{I_N}{K_A^N})} \quad . \tag{6}$$

Here, A can be any phase selected in the product and X (= A, B, … N) denotes each phase in the product. I_X presents the intensity of X phase in the product from the XRD spectrum. K_A^X is the ratio of the reference intensity ratio (RIR) value of X phase to that of the reference phase A, i.e., $K_A^X = RIR_X/RIR_A$. In the experimental measurement, three peaks for Ti, TiB, and TiB_2 were shown in XRD data, and Ti was selected as the reference sample. Based on the powder diffraction file (PDF) cards, RIR values for Ti, TiB, and TiB_2 were determined to be 6.44, 1.72, and 4.11, respectively. Therefore, $K_{Ti}^{TiB} = RIR_{TiB}/RIR_{Ti}$, $K_{Ti}^{TiB_2} = RIR_{TiB2}/RIR_{Ti}$, and $K_{Ti}^{Ti} = 1$ can be calculated. Therefore, the equation for W_X in the present work can be derived from Eq. (1) as follow;

$$W_X = \frac{I_X}{K_{Ti}^X \cdot (\frac{I_{Ti}}{K_{Ti}^{Ti}} + \frac{I_{TiB}}{K_{Ti}^{TiB}} + \frac{I_{TiB_2}}{K_{Ti}^{TiB_2}})} \quad . \tag{7}$$

The size distribution of the particles was measured from the photographs of Transmission Electron Microscopy (TEM) for about 300 particles. TEM observations were performed on JEOL JEM-2010 operated at an accelerating voltage of 200 kV. EELS has historically been a more difficult technique but is in principle capable of measuring atomic composition, chemical bonding, valence and conduction band electronic properties, surface properties, and element-specific pair distance distribution functions. Scanning transmission electron

microscopy (STEM) combined with electron energy-loss spectroscopy (EELS, JEM-2100, JEOL) allows us to make elemental identification possible.

2.4 Experimental results and discussion

2.4.1 Effect of plasma gas

The XRD patterns of as-prepared nanoparticles with different plasma gas are demonstrated in **Figure 5**. Ti and TiB_2 were identified from the XRD spectrum peaks of the as-prepared particles. As seen from fig 5, when injecting He, the intensity of the peak of titanium decreased indicating the enhancement of heat transfer.

The major reason is that He enhances the heat transfer from the plasma to powders due to the high thermal conductivity. The thermal conductivity of Ar is 0.644 $W \cdot m^{-1} \cdot K^{-1}$, while the thermal conductivity of He is 2.453 $W \cdot m^{-1} \cdot K^{-1}$ [45]. In addition, the higher electron temperature in the He plasma is beneficial for mixing more concentration of electronegative gas in the working gas to generate the reactive agents.

2.4.2 Effect of inner gas

Figure 6 shows XRD patterns of as-prepared nanoparticles with different inner gas at powder feed rate 0.2 g/min with initial composition of Ti:B = 1:5. According to the XRD spectrum, Ti and TiB_2 are identified from the XRD spectrum peaks of the as-prepared particles, the dominant product is TiB_2. As seen from fig 6, when injecting He as inner gas, the intensity of the peak of TiB_2 increases indicating the enhancement of heat transfer. Based on the quantitative phase analysis, the mass fraction of TiB_2 in product with He as inner gas is 91.9% compared with 86.2% that with Ar as inner gas.

The use of He improves the heat transfer between the plasma flame and the solid particles due to the high thermal conductivity. Meanwhile, the higher temperature in the He plasma compared to that in the Ar plasma is owed to the different dependence of the total cross section on the electron energy for He and Ar atoms. Thus, higher heating rates and most probably higher reaction temperature are achieved.

2.4.3 Effect of plasma power

Effect of plasma power on the composition of product is shown in **Figure 7.** After

increasing plasma power, the mass fraction of titanium boride in product increases due to higher energy and higher plasma temperature.

2.4.4 Effect of powder feed rate

TEM graph and size distribution of the as-prepared titanium-based boride nanoparticles with powder feed rate 0.2 g/min at the fixed initial composition of Ti:B = 1:5 is shown in **Figure 8**. Particles are almost spherical shape and have core-shell structure. As shown in the fig. 8, the average grain size is about 18 nm.

XRD spectra of the prepared titanium boride nanoparticles are demonstrated in **Figure 9** with different boron content in the feeding powders and powder feed rate. TiB and TiB_2 were identified with unreacted Ti from XRD spectrum peaks, while unreacted boron peak was too little to be identified. However, the relative intensity of unreacted Ti was the highest in the XRD spectrum peaks, indicating there was a large amount of unreacted boron. Because it is relatively difficult for boron to be evaporated even in the thermal plasma owing to higher boron melting point of 2349 K than titanium melting point of 1941 K. In addition, liquids may change to a vapor at temperatures below their boiling points through the process of evaporation. In the boride formation, the vaporization of the raw materials is important for the synthesis process of nanoparticles. The vaporization temperature was estimated by the following equation:

$$\ln(\frac{P_2}{P_1}) = -\frac{\Delta H_{vap}}{R}(\frac{1}{T_2} - \frac{1}{T_1}), \quad (8)$$

where P_1 and P_2 are the vapor pressures at temperatures T_1 and T_2, respectively, ΔH_{vap} is the enthalpy of vaporization, and R is the universal gas constant. In the raw material composition of Ti:B = 1:2, $T_{vap,\,Ti}$ =2701 K, $T_{vap,\,B}$ = 2973 K, which are calculated by Eq. (8). We can choose the temperature as T_1 when saturation vapor pressure P_1 = 1 Pa, and P_2 is the partial pressure in plasma at the fixed phase condition of raw materials. And then evaporation temperature T_2 will be estimated by Eq. (8).

The effect of powder feed rate on the phase composition of as-prepared nanoparticles is displayed in **Figure 10**. The mass fraction of TiB_2 in the final product has the tendency that the mass fraction of metal boride in product decreases along with the increase of powder feed rate. Seen from TEM image in fig. 8, the product consists of nano-size particles, while the diameter of raw materials is 45 μm, which indicates raw materials are fully evaporated in thermal plasma. With the low powder feed rate, both of boron and titanium are quickly evaporated just after the

injection of raw powders, and then the evaporated boron is nucleated in the high temperature area at the upstream region of plasma flow where titanium and boron co-exist and can react with each other. On the other hand, the amount of raw material increases at high powder feed rate, though the heat from the plasma keeps constant at the fixed input power of 30.0 kW. The less heat transferring from the plasma to each particle takes longer time to evaporate raw materials at high powder feed rate rather than the low powder feed rate. In addition, boron is difficult to be evaporated due to the relatively higher melting point, evaporation temperature and latent heat. For this reason, the existence area of evaporated boron is extended along with the thermal plasma flame. The boridization occurs easily in the upstream region of plasma flow due to high temperature and abundant titanium vapor, while it is difficult in the downstream region because of relatively low temperature and diffuse of titanium vapor which is produced in the upstream region. Therefore, the mass fraction of TiB_2 in the final product decreases with increasing powder feed rate. Moreover, the nucleation position shifts more upstream at the higher powder feed rate. The same pattern has also been shown in Ref. [24] for a similar system of metal-silicide nanoparticles. According to the equation for the homogeneous nucleation rate [46], the nucleation rate is lower at larger surface tension or at higher temperature. The boron nuclei become less, and the mass fraction of TiB_2 decreases at higher powder feed rate.

Effect of powder feed rate on the ratio of prepared TiB nanoparticles in TiB and TiB_2 is displayed in **Figure 11**. The mass fraction of TiB in the product of TiB and TiB_2 decreases with the increase of powder feed rate. As mentioned above, TiB_2 is a thermodynamically dominant material, while TiB is a metastable material. In consequence, it is easy to produce TiB_2 at equilibrium state. The temperature in the boron nanoparticles growth region is mainly higher than the melting point of boron. From numerical simulation, the nucleation positions shift upstream at higher feed rate, and the time in which boron nanoparticles grow becomes long. As a result, boron nanoparticles have long time to grow and reach the equilibrium state; the growth tendency of titanium nanoparticles is similar with that of boron nanoparticles. Therefore, in the case of the higher powder feed rate, it is easy to generate TiB_2; on the contrary, metastable materials TiB can be obtained at the lower powder feed rate.

TEM graphs of the prepared nanoparticles at the fixed initial composition of Ti:B = 1:2 with powder feed rate of 0.2 and 0.5 g/min are shown in **Figure 12** (a) and (b), respectively. The particle diameter distribution is demonstrated for as-prepared product at the fixed initial composition of Ti:B = 1:2 with powder feed rate of 0.2 and 0.5 g/min in **Figure 13** (a) and (b),

respectively. The mean diameter of the prepared nanoparticles increases with the powder feed rate. The supersaturated state leads to production of nuclei by homogenous nucleation. Simultaneously, two kinds of vapors boron and metal co-condense on the nucleated boron nuclei. This combined mechanism makes nanoparticles grow. Since the critical diameter of the boron nuclei is the same, the difference of average particle diameter mainly comes from the different growth time and the growth rate of nanoparticles in the nucleation and condensation processes. From numerical simulation [17], the nanoparticles are formed at earlier stage at higher powder feed rate, because the larger amount of vapor reaches the supersaturation state at a more upstream position, the nucleation positions shift upstream and the vapor consumption rate by condensation increases due to the larger vapor concentration with the higher powder feed rate. The temperature upstream is high so that the nucleation rate is low which means a small number of stable nuclei are generated. The smaller number of nuclei shares a larger amount of vapor; consequently the particles can grow larger. Furthermore, since the powder feed rate increases, the monomer density increases which leads to the high growth rate. Finally, the growth progress is not finished until the nucleation temperature of titanium. The different nucleation temperatures of titanium and boron lead to the different temperature gaps between the nucleation temperature of boron and titanium. And then there is a long growth time of boron nuclei from the nucleation process of boron monomers to the co-condensation process of titanium and boron monomers due to the higher nucleation temperature of boron. The nucleation temperature of B is higher at higher powder feed rate. The growth time of boride nanoparticles at higher powder feed rate is longer than that at lower powder feed rate. As a result, the average particle diameter of titanium boride nanoparticle at higher powder feed rate have large diameter.

Effect of powder feed rate on the crystalline diameter of as-prepared nanoparticles is shown in **Figure 14**.

2.4.5 Effect of boron content in feeding powders

XRD patterns of as-prepared nanoparticles and mass fraction of boride in product at different boron content in feeding powders are shown in **Figure 15 (a)** and **(b)**. In the B-rich condition (Ti:B = 1:2 and 1:5), TiB_2 are clearly identified in XRD spectra with unreacted raw materials Ti and the dominant product is TiB_2. However, in the B-poor condition, Ti, TiB_2 and TiB can be synthesized and there is a large amount of Ti in the product. Therefore, we can

estimate that the mass fraction of titanium boride nanoparticles in product increases with boron content in feeding powders due to excessive boron vapor.

The high boron content in feeding powders improves the generation of titanium boride nanoparticles. High content of boron in feeding powders leads to the generation of boron nuclei and more boron vapor and titanium vapor can co-exist in the same area, which is beneficial for the synthesis of titanium boride nanoparticles.

Effect of boron content in feeding powders on the mass fraction of TiB in product of TiB and TiB_2 is shown in **Figure 16**. When a larger amount of titanium is included in the feed powders, the mass fraction of TiB in product of TiB and TiB_2 becomes larger. As seen from the Ti-B phase diagram fig. 3, when the molar fraction of boron is larger than 66.7%, the main materials generated are TiB_2 and boron, and the tendency of generating TiB_2 becomes large; on the other hand, the molar fraction of boron is less than 50%, the main materials generated are TiB and titanium, and the tendency of generating TiB becomes large while the tendency of generating TiB_2 becomes smaller.

TEM graphs of the prepared product at the fixed powder feed rate of 0.2 g/min with initial composition of Ti:B = 1:1 and 1:2 are shown in **Figure 17** (a) and (b), respectively. The particles with different morphology and size exist. Most particles seemed spherical and the average grain size is less than 30 nm. In nanoparticle synthesis using thermal plasmas, the prepared nanoparticles consist mainly of the single crystal. Therefore, the crystalline diameter is almost the same as the grain size of the nanoparticles. The particle diameter distribution is demonstrated for as-prepared product at the fixed powder feed rate of 0.2 g/min with initial composition of Ti:B = 1:1 and 1:2 in **Figure 18** (a) and (b), respectively. The diameter of particles at Ti:B = 1:1 is about 18 nm, while the diameter of particles at Ti:B = 1:2 is about 15 nm. The TEM results are consistent with that of XRD.

The crystalline diameter of the prepared titanium-based boride nanoparticles at different boron content in feeding powders is shown in **Figure 19**. The crystalline diameter of the prepared nanoparticles decreases with increasing the boron content in feeding powders. Because nucleation is promoted in the circumstances where larger amount of vapors can simultaneously nucleation, the promoted nucleation generates more nuclei so that each nuclei shares a less amount of vapors. In addition, nucleation takes place at more upstream position with high supersaturation ratio, so the critical size of the nucleus is smaller. As the result, the nanoparticles with the smaller diameter are generated.

According to figs. 12 and 17, core-shell structured nanoparticles are observed in TEM images of as-prepared product. The thickness of the shell is estimated to be about 2 nm. EELS measurements in the STEM is conducted to analyze chemical components of core and shell separately. **Figure 20** shows SETM-EELS images of particles at fixed initial composition of Ti:B = 1:2 at powder feed rate of 0.2 g/min. Fig. 20 (a) is the STEM image of a particle prepared for long time. Figs. 20 (b)-(d) display corresponding O, Ti, and B projected distributions, respectively. On the basis of XPS result, the constituents of the shell are Ti and O, which is in accord with EELS result. In the comprehensive consideration of EELS and XPS results, the original shell of prepared particle in the experiment is expected to be Ti, which is oxidized in air.

Figure 21 shows SETM-EELS images of particles at fixed initial composition of Ti:B = 1:5 at powder feed rate of 0.2 g/min. Fig. 21 (a) is the STEM image of a particle prepared for a short time. Figs. 21 (b)-(c) display corresponding Ti, and B projected distributions, respectively. O element cannot be identified. Based on EELS results, we can know the shell includes B element. Therefore, the oxidation of the shell in fig. 20 is generated after the plasma treatment, not during the plasma treatment.

The synthesis mechanism of core-shell structured titanium boride nanoparticle is examined based on the calculation of nucleation temperature. Due to the lower saturation vapor pressure, boron nucleates first compared with titanium. The nucleation process of boron occurs only around the boron nucleation temperature. Simultaneously, boron and titanium vapors condense on the surface of boron nuclei in the temperature gap between the nucleation temperature and melting point of boron forming metal boride nanoparticles. In the boron poor condition, the large temperature gap between melting points of titanium and boron leads to excessive titanium on the molten condition promoting the formation of metal shell. During this period, titanium boride nanoparticles act as nucleation sites for titanium monomers creating metal covered boride nanoparticles. In boron rich condition, excessive boron is separated from the generated Ti-B metal compounds.

2.4.6 Effect of carrier gas flow rate

The crystalline diameter of the prepared titanium-based boride nanoparticles for different carrier gas flow rate is shown in **Figure 22**. The carrier gas flow rate is an important factor in determining the trajectories of the particles. When the carrier gas flow rate is high enough, particles will easily go through the discharge. The recirculation which is characteristic of an

inductively coupled plasma is then restricted to a small doughnut shaped region of the central axis. However, for lower carrier gas flow rate, the recirculation zone is expanded and it repels the particles injected in the center. Increasing carrier gas flow rate the crystalline diameter of TiB_2 decreases. The velocity of powders increases with increasing of carrier gas flow rate, while the plasma temperature decreases with the increase of powder feed rate. The higher velocity leads to high quenching rate and short residence time in plasma. The decrease of plasma temperature leads to the reduced amount of titanium boride nanoparticles in product. Therefore, the boride nanoparticle has smaller diameter at higher carrier gas flow rate.

2.5 Numerical simulation

2.5.1 Growth model of binary alloy nanoparticles

The particles trajectories and thermal histories are described by the following equations:

$$\frac{du_P}{dt} = -\frac{3}{4} C_D (u_P - u) U_r \frac{\rho}{\rho_P d_P} + g \tag{9}$$

$$\frac{dv_P}{dt} = -\frac{3}{4} C_D (v_P - v) U_r \frac{\rho}{\rho_P d_P} \tag{10}$$

where, C_D is drag coefficient which is related to the Reynolds number *Re*. *Re* is based on the particle diameter and *Ur*. *Ur* is the relative velocity between the particle and the plasma. Subscript *P* means particles. *v* is plasma velocity (radial). *d* is diameter. *u* is plasma velocity (axial). ρ is density.μ is viscosity. c_p is specific heat.

The particle temperature is determined through an energy balance:

$$Q_T = \pi d_P^2 h_c (T - T_P) - \pi d_P^2 \sigma_s \varepsilon (T_P^4 - T_a^4) \tag{11}$$

$$Q_r = \begin{cases} (\frac{\pi}{6} \rho_P d_P^3 c_P) \frac{dT_P}{dt} & T < T_m \text{ and } T_m < T < T_b \\ (\frac{\pi}{6} \rho_P d_P^3 H_m) \frac{dx}{dt} & T = T_m \\ -(\frac{\pi}{2} \rho_P d_P^2 H_v) \frac{dd_P}{dt} & T = T_b \end{cases} \tag{12}$$

where, h_c is the heat transfer coefficient, ε is the particle emissivity, *x* is the liquid mass fraction of the particle, and T_P, T_m, T_b are the particle temperature, melting point temperature, and the boiling temperature respectively.

The growth processes of titanium boride nanoparticles were also investigated numerically using a recently-proposed model which can calculate two-component nanoparticles' growth in a binary metallic vapor system [24]. The growth process includes binary homogenous nucleation, binary heterogeneous condensation and coagulation of nanoparticles. This model can effectively simulate the whole growth process of binary alloy nanoparticles for thermal plasma synthesis. Additionally, the freezing point depression of nanoparticles due to their small sizes is taken into account to determine the final state of nanoparticles.

The present model is developed based on the following concepts: (A) it is easy to use from an engineering viewpoint; (B) it can express any profile of a nanopowder in a PSCD, which is described by nodal discretization for the two individual directions of the particle size and composition, where nanoparticles composing a nanopowder reside only at the nodes; (C) its numerical solution algorithm is arithmetic and straightforward.

Nanoparticle growth involves three fundamental processes requiring different time resolutions: 10^{-15} s for homogeneous nucleation, 10^{-5} s for heterogeneous condensation, and 10^{-4} s for coagulation among nanoparticles. Numerical calculation is conducted with the time resolution for heterogeneous condensation. Although the transient process in nucleation is not considered, the theory gives the accurate values of size, composition, and birth rate of stable nuclei; and those values are all that the present model requires for its nucleation regime. This manner makes it feasible to simulate the whole growth process.

The model adopts the following assumptions: (i) nanoparticles are spherical; (ii) nanoparticle's inertia is negligible; (iii) the temperature of nanoparticles is identical to that of the bulk gas surrounding them; (iv) heat generated by condensation and the electric charge of nanoparticles are neglected; and (vi) the material vapors are regarded as an ideal gas. To treat the particle size and composition during the growth, the particle size-composition distribution (PSCD) on the basis of two-directional nodal discretization [23] is used instead of the often-used particle size distribution (PSD).

The nodes are spaced linearly on a logarithmic scale along the size axis to cover the wide range of particle sizes:

$$v_{k+1} = f_v v_k \quad (k = 1, 2, \ldots, k_{max}\text{-}1) \tag{13}$$

Therein, v is the particle volume and subscript k represents the node number along the size axis. The geometric spacing factor for size f_v and number of nodes k_{max} are chosen, respectively, as 1.6 and 54. These values provide sufficient accuracy for the size range of a nanopowder

synthesized in thermal plasma processing. The particle volume at the first node is arbitrarily set to a 10-mer of material *M*:

$$v_1 = 10v_{mono(M)} \tag{14}$$

In that equation, $v_{mono(M)}$ is the volume of the monomer of material *M*.

The nodes are linearly spaced along the composition axis:

$$x_{n+1} = x_n + \Delta x \quad (n = 1,2, \ldots, n_{max}\text{-}1) \tag{15}$$

In that equation, x is the mole fraction of material *B* in a particle and subscript n denotes the node number along the composition axis. The increment Δx is chosen as 0.025; the number of nodes n_{max} is 41. The particles at the first node contain only material *A*, whereas the composition of the particles at the n_{max} the node is 100% material *B*:

$$x_1 = 0 \tag{16}$$

and

$$x_{n_{max}} = 1 \tag{17}$$

The net production rate of nanoparticles with the volume v_k and the boron content x_n is written by the increment of the number density ΔN during the infinitesimal time Δt as: [24]

$$\begin{aligned}\frac{\Delta N_{k,n}}{\Delta t} &= J'\xi_k^{(nucl)}\psi_n^{(nucl)} \\ &+ \sum_i \sum_l \frac{(\xi_{i,l,k}^{(cond)}\psi_{i,l,n}^{(cond)} - \delta_{i,k}\delta_{l,n})N_{i,l}}{\Delta t} \\ &+ \frac{1}{2}\sum_i \sum_j \sum_l \sum_m \xi_{i,j,k}^{(coag)}\psi_{i,j,l,m,n}^{(coag)}\beta_{i,j,l,m}N_{i,l}N_{j,m} - N_{k,n}\sum_i \sum_l \beta_{i,k,l,n}N_{i,l}\end{aligned} \tag{18}$$

The first of the right hand side represent the contributions of homogeneous nucleation. The second term means the production rate caused by vapor condensation on the particles with v_i and x_l. In this model [47] which expresses these particles as the particles residing at node (i, l), node (i, l) becomes empty after the condensation. The consequent new particles are distributed to the adjacent nodes (one of them is node (k, n)) under the mass-conserving condition. To express these processes, the second term includes the splitting operators for the size ξ, composition ψ and the Kronecker delta $\delta_{i,k}$. The third and fourth terms express the gain and loss by coagulation among nanoparticles. β is the collision frequency function for nanoparticles which will covers the wider range of particle sizes [48]. That is, the third term means the total contribution of coagulation growth between the particles with v_i and x_l and the particles with v_j and x_m. The fourth term expresses the coagulation between the incident particles with v_k and x_n and all other particles. Subscripts i and j denote the node numbers along the size axis, whereas

subscripts *l* and *m* signify those along the composition axis. To estimate the homogeneous nucleation rate *J'* for a binary system, we used the theoretical formula derived by Wyslouzil and Wilemski [49]. Although the formula of the nucleation rate for a binary system *J'* used in the computation was different from that for a unary system *J* [45], *J'* expresses the unary nucleation as well as the binary nucleation. The present computation includes the unary nucleation of boron even using *J'*, because of the large difference of the saturation vapor pressures between boron and titanium.

A nucleus is in the critical state; its size v^* is determined by the balance between growth and evaporation. Therefore, a nucleus smaller than size v^* easily evaporates and cannot exist as a particle. Consequently, only the next larger nodes can gain the nuclei. Considering the conservation of the particle volume, the splitting operators along the size axis ξ and along the composition axis ψ in the nucleation process are calculation based on the v^* and x^*, respectively. The v^* and x^* are determined by both the material properties and the states of the vapors (e.g., the temperature and the supersaturation ratio). The splitting operators in second and third terms are estimated by the v_k, x_n and $\Delta v_{(M)i,l}$.

Once nuclei are generated by homogeneous nucleation, binary metal vapors condense on the nuclei heterogeneously, resulting in significant growth of the particles. The binary condensation is a key process to determine a nanopowder's profile. When the growth rate of nanoparticles by heterogeneous condensation of the vapor of material *M*, the following equation with the rarefied gas effect correction was used to estimate the volume increment $\Delta v_{(M)i,l}$ during the infinitesimal time increment Δt:

$$\frac{\Delta v_{(M)i,l}}{\Delta t} = 2\pi d_i D_{vap(M)} v_{vap(M)} (N_{vap(M)} - \overline{N}_{S(M)i,l}) \left[\frac{0.75\alpha_{(M)}(1+\mathrm{Kn}_i)}{0.75\alpha_{(M)} + 0.283\alpha_{(M)}\mathrm{Kn}_i + \mathrm{Kn}_i + \mathrm{Kn}_i^2} \right] \tag{19}$$

here, *d* is the diameter, *D* is the diffusion coefficient of the monomers estimated using the formula of Hirschfelder, and Kn is the Knudsen number which is defined as the ratio of the gas mean free path to the particle radius. This expression shown in Eq (15) covers the entire range of Knudsen numbers. The subscript *vap* denotes vapor. α represents the accommodation coefficient which is known to be 0.013-0.38 for representative chemical materials on aqueous surfaces around room temperature. However, the accommodation coefficients of Ti and Nb on their own borides remain unknown at present. For that reason, they were all set to 0.1 for this study. $\overline{N}_S$ means the saturated vapor concentration considering the effects of material mixture

and surface curvature [50].

Coagulation of nanoparticles plays a considerably important role in nanopowder growth. Although the collision frequency function $\beta_{i,j,l,m}$ in Eq (16) is often described in the form for a free molecular regime, it is preferred that it can cover the wider range of particle sizes. Therefore, in this study, the Fuchs form of the collision frequency function is adopted and modified. The collision frequency function between the particles at node (*i*,*l*) and the particles at node (*j*,*m*) is written as

$$\beta_{i,j,l,m} = 2\pi\left(D_i + D_j\right)\left(d_i + d_j\right)\left[\ \frac{d_i + d_j}{d_i + d_j + 2\sqrt{g_{i,l}^2 + g_{j,m}^2}} + \frac{8\left(D_i + D_j\right)}{\left(d_i + d_j\right)\sqrt{c_{i,l}^2 + c_{j,m}^2}}\ \right]^{-1} \tag{20}$$

$$c_i = \sqrt{\frac{8k_B T}{\pi m_i}} \tag{21}$$

$$g_i = \frac{1}{3d_{Pi}l_i}\left[\left(d_{Pi} + l_i\right)^3 - \left(d_{Pi}^2 + l_i^2\right)^{3/2}\right] - d_{Pi} \tag{22}$$

$$l_i = \frac{8D_{Pi}}{\pi c_i} \tag{23}$$

where, m_i is the averaged mass of the particle at the node *i* estimated from its size and material composition.

The population balance equations of the material vapors are also computed simultaneously because the number density of material vapor affects the features of nanoparticles' growth.

$$\frac{\Delta N_{vap(M)}}{\Delta t} = -\sum_k J\xi_k^{(nucl)} n_{(M)}^* - \sum_i \sum_l \frac{N_{i,l}\Delta v_{(M)i,l}}{v_{vap(M)}\Delta t} \tag{24}$$

where, $n^*_{(M)}$ represents the number of monomers of material *M* composing a stable nucleus. The more detailed description of this binary growth model is found in Ref. [24].

In addition to the aforementioned model, the free energy gradients for particle formation in a binary system were taken into account in this study: i.e., the nanoparticles are allowed to grow by condensation if the gradient is negative or zero:

$$\frac{\partial W}{\partial n_{(M)}} \le 0\,. \tag{25}$$

Here, $n_{(M)}$ is the monomer number of material *M* in a nanoparticle. The gradients of the free energy of particle formation, *W*, composed of the chemical potentials and the surface energy are evaluated for nanoparticles with each size and each composition. Also, the melting point

depressions due to nano-scale size and the mixture effect are considered [51]. It is assumed that the nanoparticles with the temperature lower than their melting point cannot grow by coagulation.

2.5.2 Computational conditions

The computation was performed using a one-dimensional profile of a typical bulk gas condition at the plasma's tail where nanoparticles are formed. The numerical data were obtained by a preliminary calculation using electromagnetic fluid dynamics approach [24]. In the reaction chamber, the temperature monotonically decreases. Moreover, the temperature-decrease rate decreases from 1.5×10^{5} K/s to 1.0×10^{4} K/s because of the following reasons: as the flow goes more downstream, the temperature gradient becomes smaller and also the flow slows down with the decrease of temperature to conserve its mass. In response to that decrease of the rate, the time increment Δt for the computation was increased from 5.0×10^{-6} s to 2.0×10^{-5} s, which provided sufficient resolution for the present target process. For the identical conditions to the experiment, the total feed rates of raw materials were set to 0.2, 0.5 and 1.0 g/min with several different material ratios. The material properties of titanium and boron were obtained from Ref. [52].

2.5.3 Numerical results and discussion

Figure 23 shows the evolution of the particle size-composition distribution (PSCD), which expresses the growth behavior of titanium boride nanoparticles. **Figure 24** displays histories of the growth process in Ti-B system, (a), (b) and (c) shows the nucleation rate, the number density of vapors and the conversion ratio which indicates the amount of materials converted from vapors to nanoparticles, respectively. The total powder feed rate of the raw materials was set to be 0.5 g/min at the fixed initial composition of Ti:B = 1:2. When the temperature decreases around 3000 K, boron vapor reaches the supersaturated state earlier than titanium vapor and starts to nucleate; and consequently boron-rich nanoparticles are generated (Fig. 23(a)). Immediately, the vapors of boron and titanium condense on the existing nanoparticles, where the boron vapor has a higher rate of condensation than the titanium vapor (Fig. 23(b)) because the saturation pressure of boron is much lower than that of titanium [53, 54]. Following the consumption of boron vapor, titanium vapor is consumed with a high rate of condensation (Fig. 23(c)). In addition to such nucleation and condensation processes, coagulation among the

nanoparticles takes place. As shown in fig. 24 (c), almost all the vapors are converted into nanoparticles around 2200 K. In this way, titanium boride nanoparticles grow up and finally reach the final state (Fig. 23(d)). As the present computation shown, Ti-B system consequently has a wide range of the boron content in the product owing to the time lag of condensations between boron and titanium.

Figure 25 displays the computational results of the PSCD in the final state with the different powder feed rates at the fixed initial composition of Ti:B = 1:2. The higher feed rate results in the narrower distribution of boron content especially for the well-grown nanoparticles. From the previous report [18], binary-material nanoparticles tend to have more uniform composition consequently, when their growth process has a smaller time lag between the start of nanoparticle formation of the first material and the end of the condensational growth of the second material. Indeed in the present computation, the time periods from when the nucleation rate of boron exceeds 1.0 particle/m^3s until when 99.9% of titanium vapor completes its condensation were estimated to be 17.1 ms for the powder feed rate of 0.2 g/min, 15.7 ms for 0.5 g/min, and 14.8 ms for 1.0 g/min, respectively.

2.6 Comparison of experimental and numerical results

The comparison between the experimental and numerical results is demonstrated in **Figure 26** that displays the effect of powder feed rate on the phase compositions of as-prepared nanoparticles. The tendencies are opposite to each other in the boron-poor initial composition of Ti:B = 1:1. Also, the computation does not predict that TiB nanoparticles are synthesized at the fixed initial composition of Ti:B = 1:2. Such discrepancy might come from the simplification of the present model. Firstly, there is the assumption of complete evaporation of the raw materials in the computation, whereas there was large quantity of unreacted boron in the product in the actual experiment. Since thermal plasmas in the experiment are often accompanied with unsteady thermofluid fields. It should be noted that the content of the reactive boron nuclei determines the product composition as discussed in the experimental results. Secondly, the model for computation does not consider the phase transitions based on Gibbs free energy as shown in fig. 2, but in the experiment it will be considered. Gibbs free energy may explain the difference between the numerical and experimental results. Although Gibbs free energy plays an important role in the synthesis process in the actual experiment, the numerical model did not consider the Gibbs free energy. In computation, the amount of final product is not the actual

final product. The components of the final product display the amount of not only pure stable TiB_2 and TiB, but were estimated by comparing the numerical results with the phase diagrams of Ti-B system [55], which predicted the production of the mixture of TiB_2, TiB, Ti and B in continuous change of boron content as shown in fig. 26, because the principle of lever in the phase diagram was used to estimate the amount of TiB and TiB_2, and then decide the molar ratio of the TiB and TiB_2 in the final product. But it is possible to generate more TiB or TiB_2 through the reactions between TiB_2 and Ti or TiB and B continually according to the fig. 2 in the actual experiment. Because Gibbs free energy of these reactions is negative, indicating these reactions can take place spontaneously. Then the amount of final product TiB and TiB_2 will change instantaneously, and the molar ratio of TiB and TiB_2 will change accordingly. Therefore, the effect of Gibbs free energy on boride formation should be considered in the numerical analysis.

Thirdly, the growth processes were simulated under a simplified cooling condition. But the actual reactor has a three-dimensional field with different cooling rates, where nanoparticles could experience a variety of growth paths. Meanwhile, the different powder feed rate will lead to the different gas temperature profile in the axial direction and gas quenching rate, which will affect the concentration and average size of the final particles. In addition, the present model incorporates neither condensational heat generation nor the electric charge of nanoparticles. The heat generation can possibly increase the temperatures of the particles, which will affect the growth process of the nanoparticles.

Figure 27 present the effects of the powder feed rate and the boron content in feeding powders on the mean crystalline diameter of TiB_2. In both initial composition of Ti:B = 1:1 and 1:2, the experiment and numerical analysis show the same tendency that the higher feed rate of the precursor materials results in the larger mean diameter of TiB_2.

The crystalline mean diameter of as-prepared nanoparticles increases with powder feed rate. When the powder feed rate is higher, nanoparticles are formed at an earlier stage with a higher temperature. Because the larger amount of vapor reaches the supersaturated state at a more upstream position [39]. This supersaturated state leads to production of nuclei by nucleation. As a result, the nucleation positions shift more upstream. Although it was well predicted by this model, this paper does not include this result, because it was already described in Ref. 39 in detail. The higher temperature in the more upstream region causes the lower nucleation rate, and smaller number of stable nuclei shares larger amount of vapor. Consequently, the particles can grow larger with the higher power feed rate. It is noted that the particle diameter is almost the

same as the crystalline diameter for nanoparticles. RF thermal plasma has an important advantage that the quenching rate in the reaction chamber is high, therefore the residence time is very short compared to the other methods synthesizing nanoparticle. The growth time is short, and the crystalline diameter of the product is very small, even several nanometers. At the final state, the size of the particle is also at the nano-scale with single crystal. Accordingly the crystalline diameter of the product indicates the particle diameter.

In addition, the boron content in feeding powders affects the crystalline diameter of TiB_2, because boron has a higher nucleation rate according to the nucleation rate due to a lower surface tension compared with titanium (B: 1.09 N/m; Ti: 1.39 N/m). Therefore, the increase of boron nuclei is more accelerated in the boron-rich condition rather than in the boron-poor condition. The growth rates of TiB and TiB_2 particles are decreased in a lower concentration of titanium vapor, because a smaller amount of the titanium vapors is consumed for each nanoparticle in the boron-rich condition. Therefore, the crystalline diameter of TiB_2 increases with the decrease of boron content in feeding powders as shown in fig. 27. In this experiment we changed the operating parameter phase composition of precursors to investigate this.

Although the tendencies for the crystalline mean diameter changes are in good agreement between the experimental and numerical results, the absolute values for both conditions are different quantitatively in fig. 27. Experimentally measured data based on the analysis of XRD spectrum are larger than numerically analyzed data. It is because that the particle size estimated by XRD is a semi-quantitative result due to the different full widths at the half maximum (FWHM) [56]. In addition, the crystalline diameter of TiB_2 from XRD spectrum is larger than the measured particle size from TEM image in fig. 12 where Ti, B, TiB and TiB_2 are mixed together, because TiB_2 nanoparticles are larger than the other nanoparticles in the final product [39]. On the other hand, in the numerical analysis, the growth processes were simulated under a simplified cooling condition. The actual reactor has a three-dimensional field with different cooling rates, where nanoparticles could experience a variety of growth paths. Nanoparticles which have grown up in a lower-cooling-rate region tend to have larger size, and they would diffuse and interact with other nanoparticles. The different powder feed rate will lead to the change of gas temperature profile in the axial direction and change the gas quenching rate, which affects the concentration and average size of the final particles. As a result, the mean diameter could be different and larger than the numerically predicted values. However, at least, these qualitative agreements sufficiently support the present results and discussion.

2.7 Nucleation temperature

The difference of nucleation temperature between metal and boron is an important factor for the controlled preparation of boride nanoparticles in RF thermal plasmas. Nucleation temperature is based on saturation vapor pressure. The nucleation rate is strongly dependent on the surface tension and the saturation ratio. The critical saturation ratio of boron was estimated to be 2, while titanium has the critical saturation ratio of 98. The nucleation temperature at the critical saturation ratio is presented in **Figure 28** for constituent components of titanium borides; fig. 28 (a) was calculated at the boron molar content of 66.7% with different powder feed rate, and fig. 28 (b) was drawn at the fixed powder feed rate of 0.2 g/min with different initial composition of Ti:B. As shown in fig. 28 (a), the nucleation temperature of boron increases with increasing powder feed rate. The estimation method of nucleation temperature is explained in detail in Ch. 6.

The homogeneous nucleation rate estimated of boron and titanium with different feed rate is shown in **Figure 29**. The temperature in the boron nanoparticles growth region is mainly higher than the melting point of boron. If the powder feed rate becomes large, the larger amount of vapor reaches the supersaturation state at a more upstream position where the temperature is higher, thus the nucleation positions shift upstream and the nucleation rate becomes lower. The homogeneous nucleation rate is lower at larger surface tension. Therefore, titanium with large surface tension (1.39 N/m) has the low nucleation rate; on the other hand, boron (1.09 N/m) has the high nucleation rate.

As depicted in fig. 28, the nucleation temperatures of titanium close to its melting point, while boron has wide liquid range between the nucleation and melting temperature. Then there are more boron nuclei on the molten condition, which is beneficial for the co-condensation of metal and boron on the surface of boron nuclei and well-mixed between metal and boron. Therefore, the wide liquid range of the combination of boron with metal leads to better preparation of boride nanoparticles.

2.8 Conclusions

Parametric studies with experiments and numerical analysis were performed to investigate the synthesis of titanium boride nanoparticle by RF thermal plasma. It is concluded that thermal plasma is notably effective even for the difficult condensation control with the large saturation

pressure difference.

In this research, it is easy to synthesize TiB_2 nanoparticles with a low powder feed rate of precursors in the boron-rich condition. The difference of saturation vapor pressures between titanium and boron plays an important role in generating titanium boride nanoparticles. The powder feed rate and boron content in feeding powders influence the control of crystalline diameter and phase composition of the final product due to the different nucleation temperature. The crystalline diameter of as-prepared particles increases with the powder feed rate; the mass fraction of TiB decreases in the product of TiB and TiB_2 with the increase of the powder feed rate and the mass fraction of titanium boride decreases with the increasing of powder feed rate. When a larger amount of boron is included in feeding powders, nanoparticles provide a smaller diameter and the mass fraction of TiB decreases in the product of TiB and TiB_2. In addition, when helium was used as plasma gas or inner gas, the synthesis of titanium boride nanoparticle in product was improved due to the high thermal conductivity and electron temperature of helium plasma. When the carrier gas flow rate is increased, the velocity increases and plasma temperature decreases, which result in the decrease of particle diameter and the mass fraction of titanium boride nanoparticle in product. The experimental and numerical results show good agreement that the crystalline diameter of the product increases with the powder feed rate and titanium content in the feeding powders. In the boron-rich condition, the mass fraction of TiB_2 decreases with the increase of the powder feed rate. In the boron-poor condition, the mass fraction of TiB_2 increases with the powder feed rate. Although the numerical analysis predicted some different tendency from the experimental results, the boron-rich condition will be the ideal condition to synthesize titanium boride nanoparticle by RF thermal plasma. Based on TEM graphs, the particles in Ti-B system are all almost spherical and have core-shell structure. The composition of the shell depends on the boron content in feeding powders.

In conclusion, the precise control of crystalline diameter and phase compositions of the product is possible through adjusting the operating parameters by RF thermal plasma.

References

[1] T. Lundstrom, Pure and Applied Chemistry, 57, 1383 (1985)

[2] T. Watanabe, A. Nezu, Y. Abe, Y. Ishii and K. Adachi, Thin Solid Films, 435, 27 (2003)

[3] G. Ronald and J. Munro, Journal of Research of the National Institute of Standards and

Technology 105, 709 (2000)

[4] J. Elders and J.D.W. Voors, Applied Surface Science, 54, 135 (1992)

[5] S.H. Kang and D.J. Kim, Journal of European Ceramic Society, 27, 715 (2007)

[6] J. Schmidt, M. Boehling, U. Burkhardt and Y. Grin, Science Technology and Advanced Materials, 8, 376 (2007)

[7] C. Subramanian, T S.R.Ch. Murthy and A.K. Suri, International Journal of Refractory Metals and Hard Materials, 25, 345 (2007)

[8] H.C. Yi and J.J. Moore, Journal of Materials Science, 25, 1159 (1990)

[9] M.I. Boulos, P. Fauchais and E. Pfender, Springer, New York, 1 (1994)

[10] A. Gleizes, J.J. Gonzalez and P. Freton, Journal of Physics D: Applied Physics, 38, 153 (2005)

[11] M.I. Boulos, Materials Research Bulletin, 41, 2303 (2006)

[12] L. Tong and R.G. Reddy, Nanostructured Materials, 58, 62 (2006)

[13] J. Szepvolgyi and Z. Markovic, Plasma Chemistry and Plasma Processing, 26, 597 (2006)

[14] J. F.Bilodeau and P. Proulx, Aerosol Science and Technology, 24, 175 (1996)

[15] M. Desilets, J.F. Bilodeau and P. Proulx, Journal of Physics D: Applied Physics, 30, 1951 (1997)

[16] T. Ishigaki and J.G. Li, Pure and Applied Chemistry, 80, 1971 (2008)

[17] M. Shigeta, T. Watanabe and H. Nishiyama, Thin Solid Films, 457, 192 (2004)

[18] M. Shigeta and T. Watanabe, Journal of Materials Research, 20, 2801 (2005)

[19] M. Shigeta and H. Nishiyama, Transactions of the ASME Journal of Heat Transfer, 127, 1222 (2005)

[20] M. Shigeta and T. Watanabe, JSME International Journal Series B, 48, 425 (2005)

[21] M. Shigeta and T. Watanabe, Thin Solid Films, 515, 4217 (2007)

[22] M. Shigeta and T. Watanabe, Journal of Physics D: Applied Physics, 40, 2407 (2007)

[23] M. Shigeta and T. Watanabe, Journal of Thermal Spraying Technology, 18, 1022 (2009)

[24] M. Shigeta and T. Watanabe, Journal of Applied Physics, 108, 04330601 (2010)

[25] N. Yadira, M. Gonzalez and P. Proulx, Journal of Thermal Spraying Technology, 17, 533 (2008)

[26] J.L. Murray, P.K. Liao and K.E. Spear, (ASM, Metals Park, Ohio) 33 (1987)

[27] C. Batzner, European Commission, Luxembourg, 1998

[28] Y. Nakama1, H. Ohtani and M. Hasebe, Materials Transactions, 50, 984 (2009)

[29] B.F. Decker and J.S. Kasper, Acta Crystallographica, 7, 77 (1954)

[30] R. Maciel Pec¸ F. Ferreira, G.C. Coelho, C.A.Nunes and B. Sundman, Intermetallics, 15, 999 (2007)

[31] P. Ehrlich and Z. Anorg. Chemistry, 259, 1 (1949)

[32] J.T. Norton, H. Blumenthal and S.J. Sindeband, Metallurgical Transactions, 185, 749 (1949)

[33] A.E. Palty, H. Margolin and J.P. Nielsen, Transactions of the American Society of Metals 46, 312 (1954)

[34] R.G. Fenish, NRM, 138, 1 (1964)

[35] E. Rudy and S. Windisch, Technical Report, No. AFML-TR-65-2, Part I, VII, (1966)

[36] R.G. Fenish, NRM-138, 1–37 (1964)

[37] J. Thebault, R. Pailler, G. Bontemps-Moley, M. Bourdeau and R. Naslain, Journal of Less Common Metals, 47, 221 (1976)

[38] X.Y. Ma, C.R. Li, Z.M. Du and W.J. Zhang, Journal of Alloys and Compounds, 370, 149 (2004)

[39] Y.Y. Cheng, M. Shigeta, S. Choi and T. Watanabe, Chemical Engineering Journal, 183, 493 (2012)

[40] M. Beutl, G. Pottlacher and H. Jager, Inter. J. Thermophys. 15, 1323 (1994)

[41] J.L. Murray, P.K. Liao, K.E. Spear, Alloy Phase Diagrams 7, 587 (1986)

[42] T. Watanabe, K. Yanase, T. Honda and A. Kanzawa, Journal of Chemical Engineering of Japan, 23, 389 (1990)

[43] K. Velmurugan, V.S.K. Venkatachalapathy and S. Sendhilnathan, Materials Research, 12,

529 (2009)

[44] A. Xie, X.M. Yuan, F.X. Wang, Science China Technological Sciences, 54, 70 (2011)

[45] S.L. Girshick, C.P. Chiu and P.H. McMurry, Aerosol Science and Technology, 13, 465

[46] H. Nishiyama, S. Takehiko, S. Ito, S. Takeshi and S. Kamiyama, Heat and Mass Transfer, 36, 433 (2000)

[47] R.G. Munro, Journal of Research of the National Institute of Standards and Technology, 105, 709 (2000)

[48] J. H. Seinfeld and S.N. Pandis, Wiley, New York (1998)

[49] B.E. Wyslouzil and G. Wilemski, Journal of Chemistry Physics, 103, 1137 (1995)

[50] T. Vesala, M. Kulmala, R. Rudolf, A. Vrtala and P.E. Wagner, Journal of Aerosol Science, 28, 565 (1997)

[51] M. Wautelet, J.P. Dauchot and M. Hecq, Nanotechnology, 11, 6 (2000)

[52] Japan Institute of Metals, Metal Data Book, (Maruzen, Tokyo, 1993)

[53] G. Angelino, L. Angelino and W. A. Sirignano, New York, USA, 59 (1991)

[54] Y.V. Turov, B.M. Khusid, L.G. Voroshnin, B.B. Khina and I.L. Kozlovskii, Powder Metallurgy and Metal Ceramics, 28, 618 (1990)

[55] T. B. Massalski, 2nd Ed. 3, (American Society for Metals, Materials Park, Ohio, 1990)

[56] Z. Zhang, F. Zhou and E.J. Lavernia, Metallurgical and Materials Transactions A, 34, 1349 (2003)

Table 1 Experimental operating conditions

Process parameter	Value
Sheath gas and flow rate	Ar-He (60:5) 65 L/min
Inner gas and flow rate	Ar 5 L/min
Carrier gas and flow rate	Ar 2, 3 L/min
Powder feed rate	0.1 ~ 1.0 g/min
Plasma power plate	30, 33
Reactor pressure	101.3 kPa
Frequency	4 MHz
Boron molar content in feed powders	25 at% ~ 90 at%

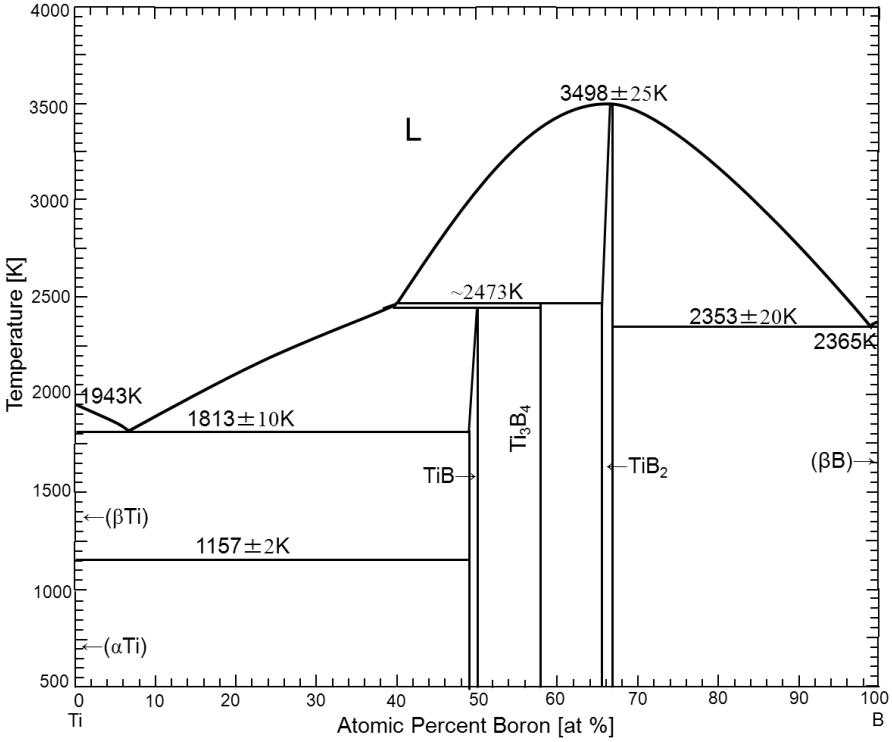

Fig. 1 Binary Ti–B phase diagram.

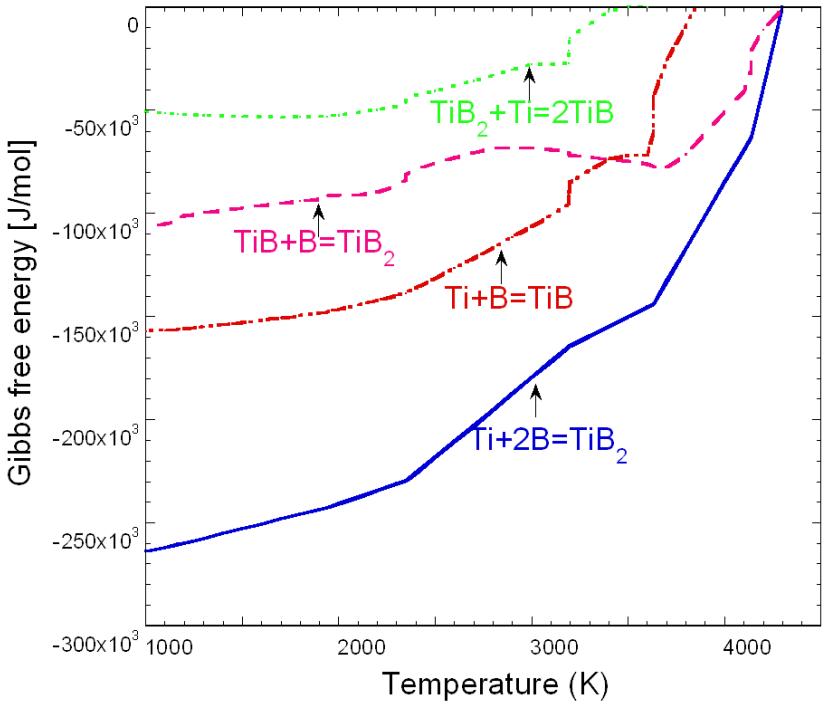

Fig.2 Gibbs free energy of the reactions generating TiB and TiB_2.

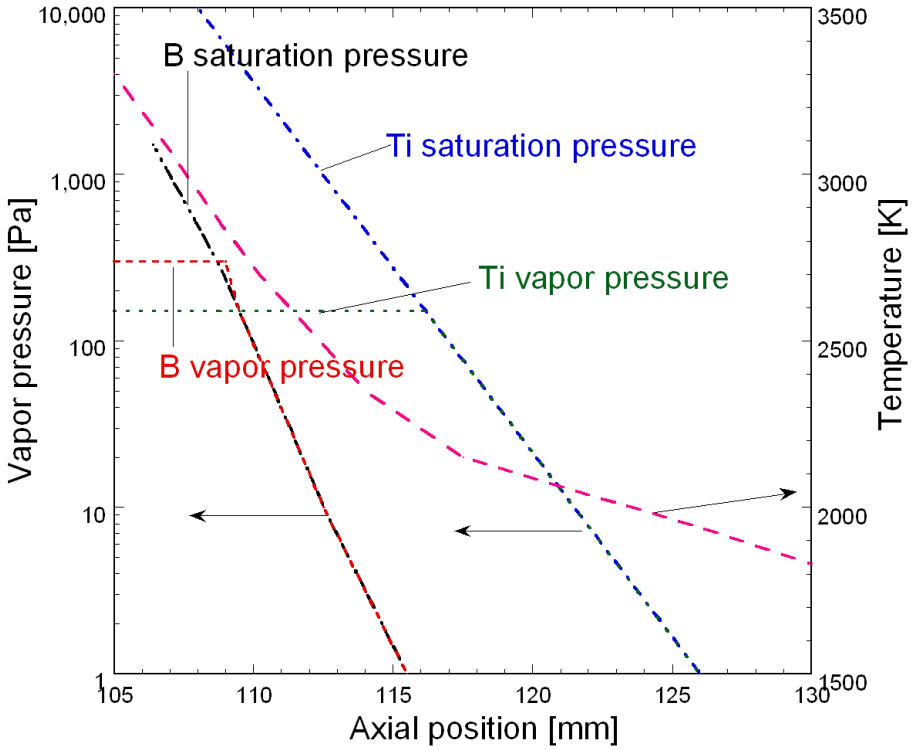

Fig. 3 Axial evolution of saturation vapor pressure.

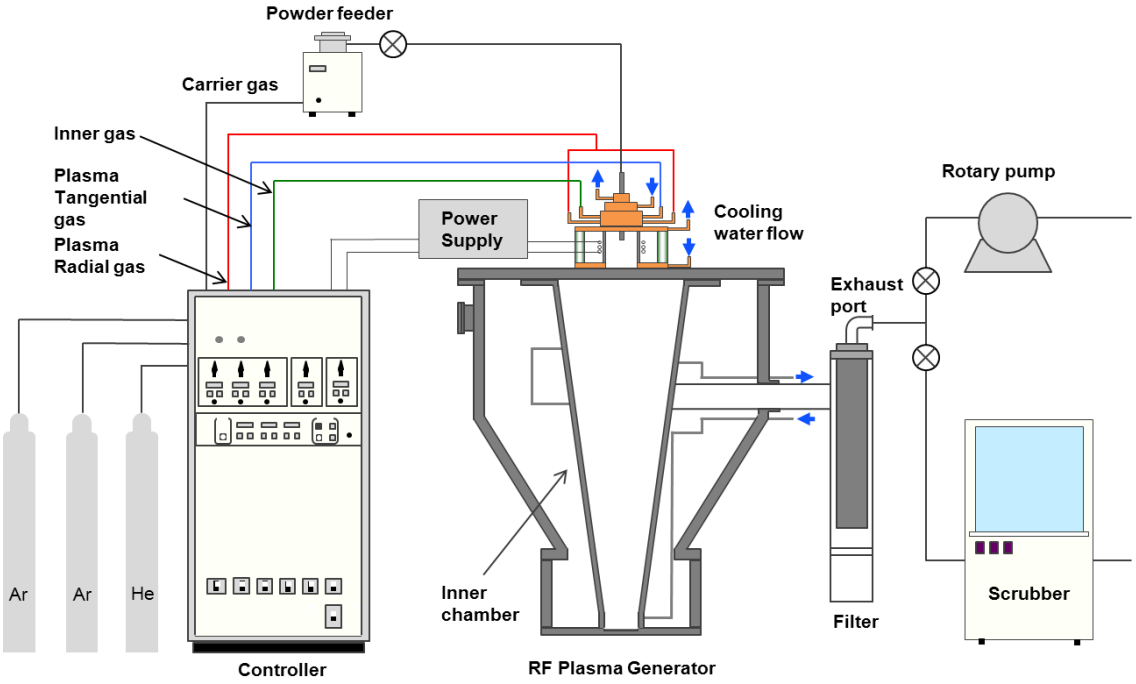

Fig. 4 Schematic diagram of experimental set-up.

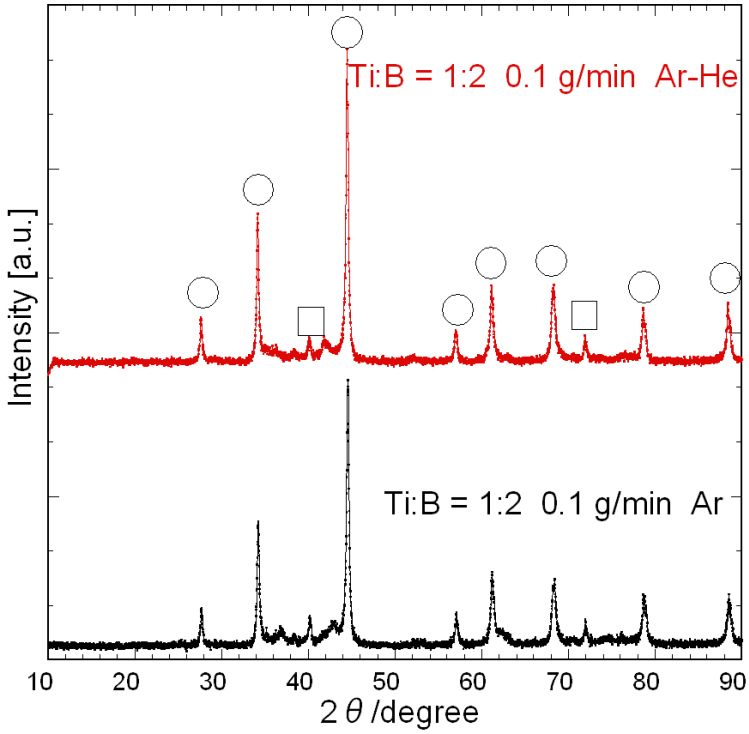

Fig. 5 XRD patterns of prepared nanoparticles with different plasma gas;
Ti: B = 1:2, Feed rate: 0.1 g/min.
(○: TiB_2 △: TiB □: Ti)

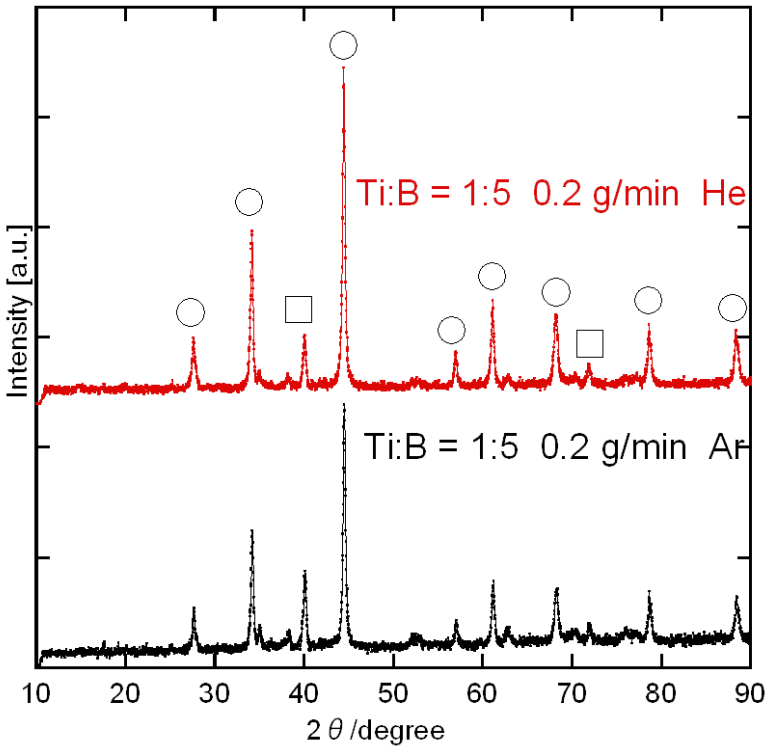

Fig. 6 XRD patterns of prepared nanoparticles with different inner gas at the fixed initial composition of Ti: B = 1:5.
(○: TiB_2 △: TiB □: Ti)

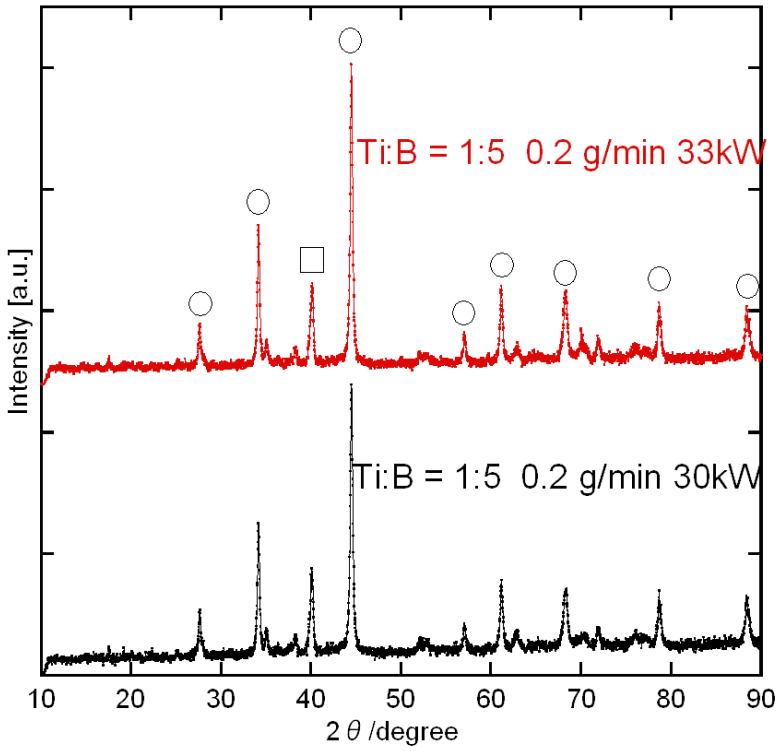

Fig.7 Effect of plasma power on the phase composition of product at initial composition of Ti:B = 1:5 at powder feed rate of 0.2 g/min.

(○: TiB_2 △: TiB □: Ti)

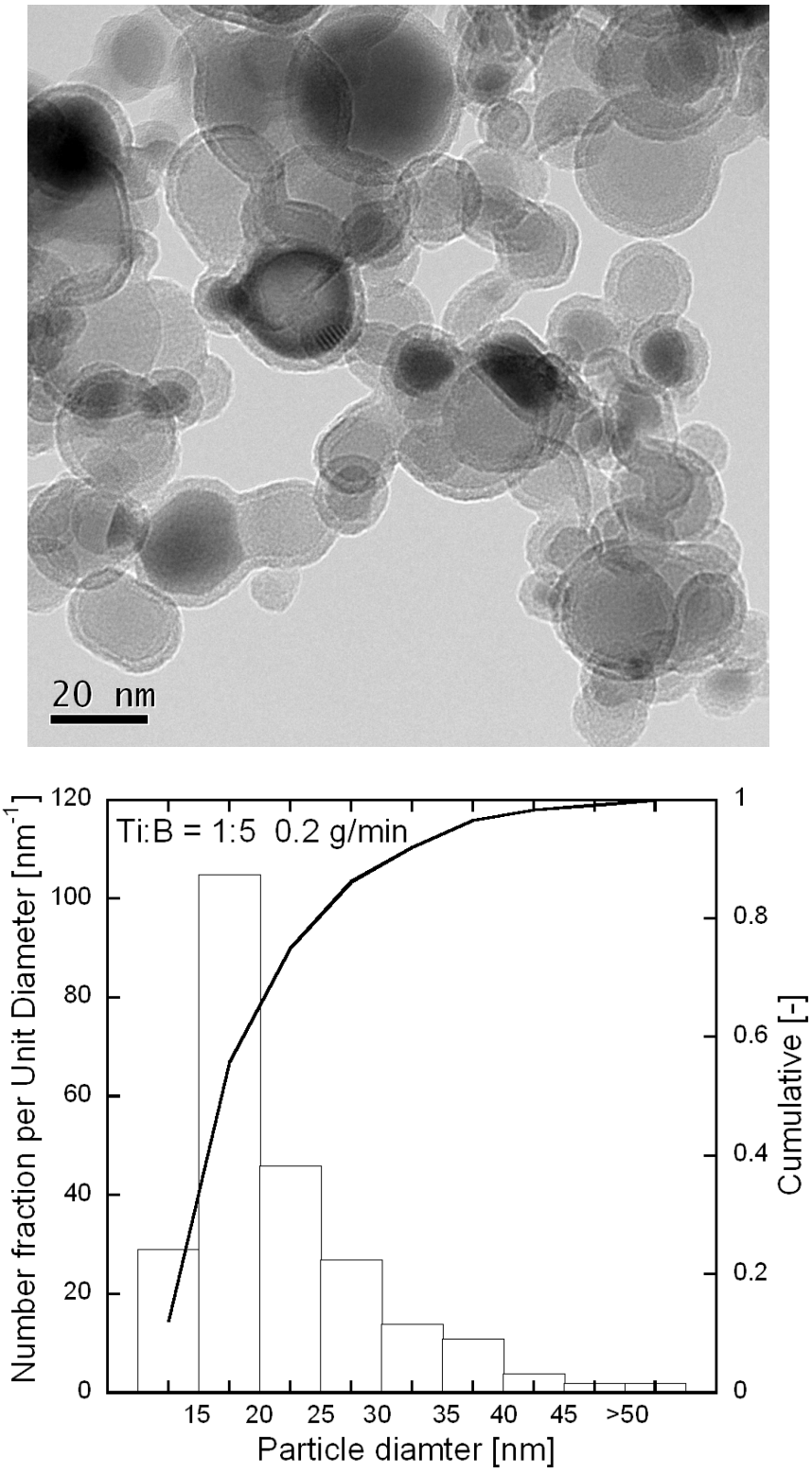

Fig. 8 TEM image and size distribution of titanium boride nanoparticle with the powder feed rate of 0.2 g/min at the fixed initial composition of Ti:B = 1:5.

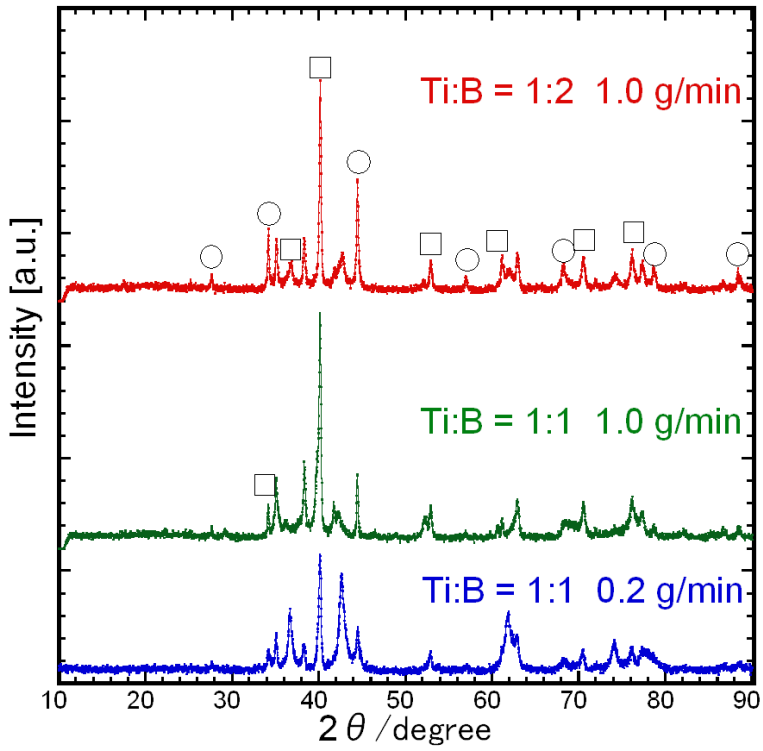

Fig. 9 XRD patterns of product with different powder feed rate and boron content in the feeding powders.

(○: TiB_2 △: TiB □: Ti)

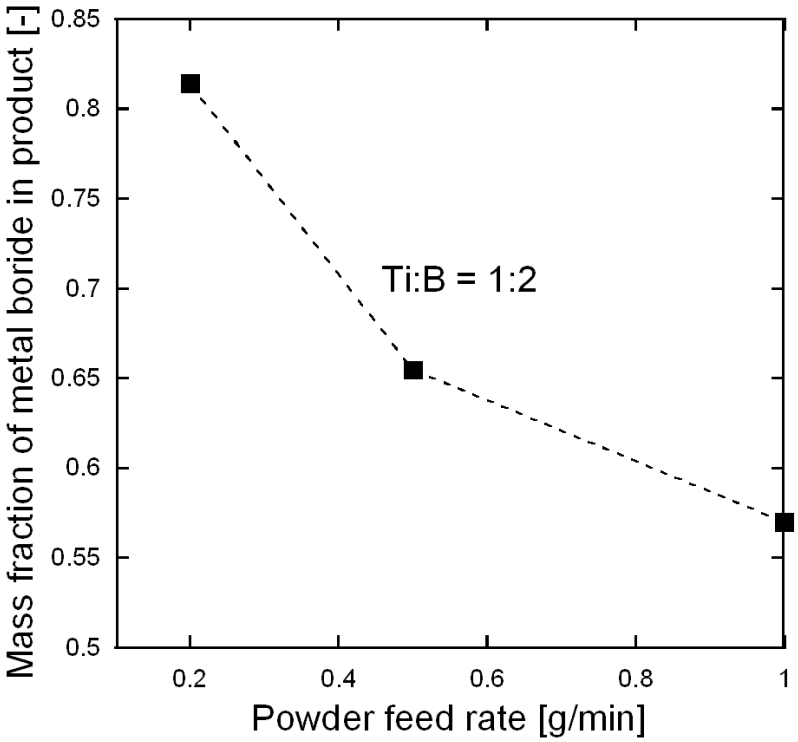

Fig. 10 The effect of powder feed rate on the phase composition of as-prepared nanoparticles in the experiment.

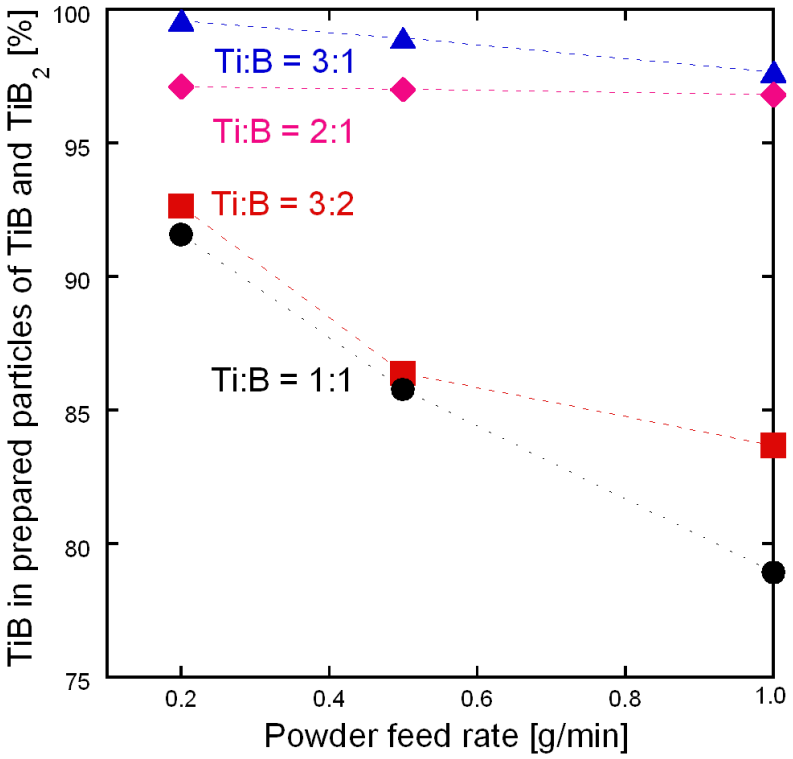

Fig. 11 Effect of powder feed rate on the phase composition of as-prepared nanoparticles.

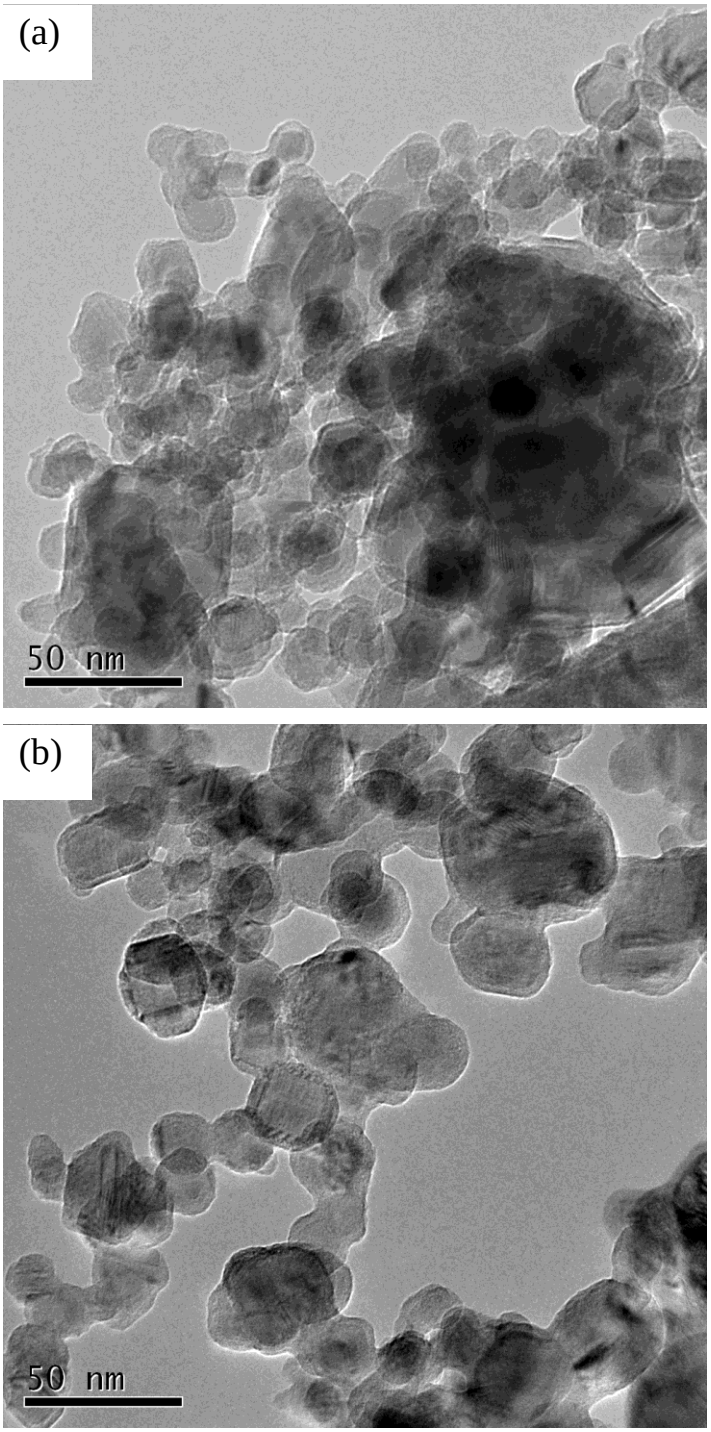

Fig. 12 TEM graphs of as-prepared product at the fixed initial composition of Ti:B = 1:2 with different powder feed rate: (a) 0.2 g/min; (b) 0.5 g/min.

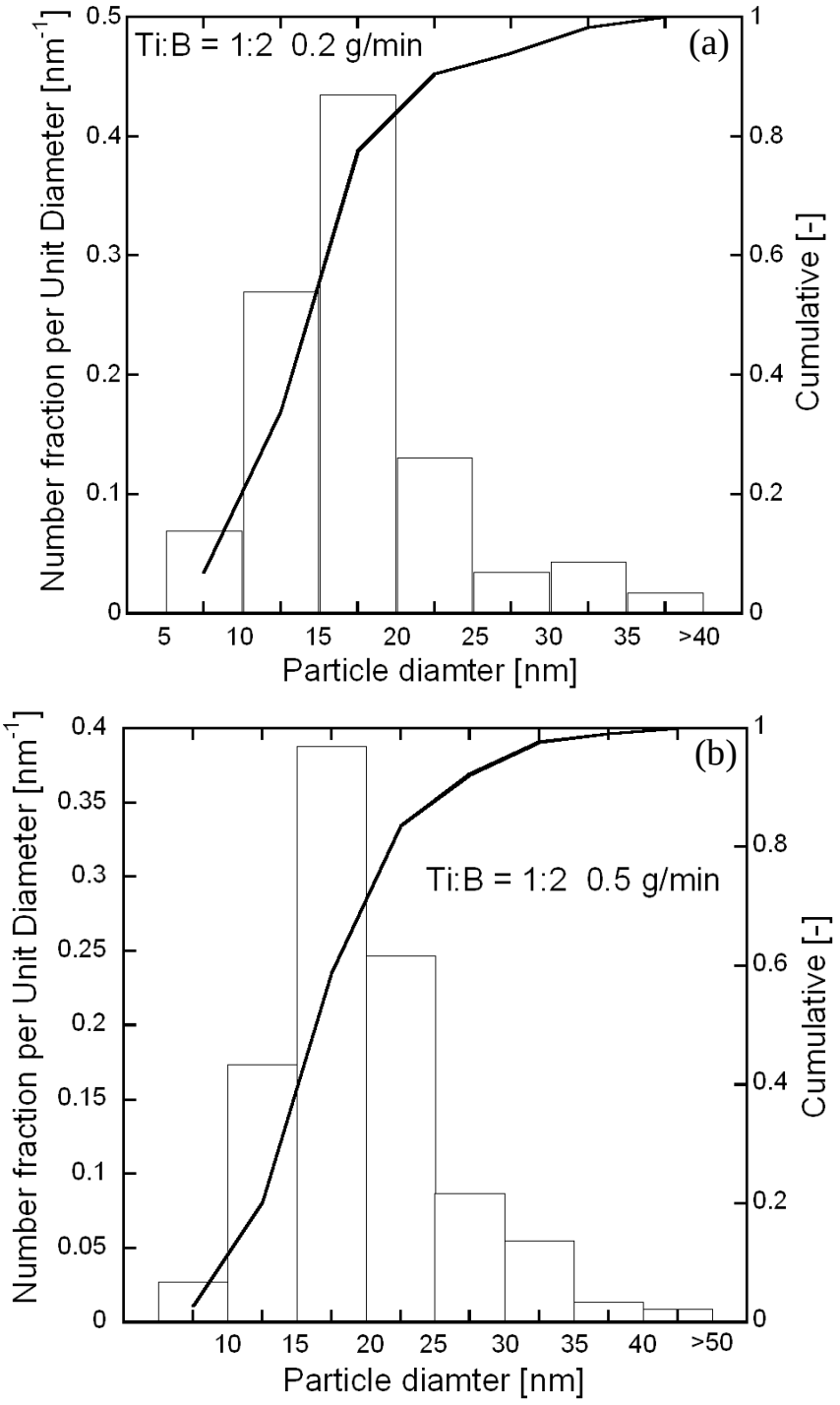

Fig. 13 Particle diameter distribution of as-prepared product at the fixed initial composition of Ti:B = 1:2 with different powder feed rate: (a) 0.2 g/min; (b) 0.5 g/min.

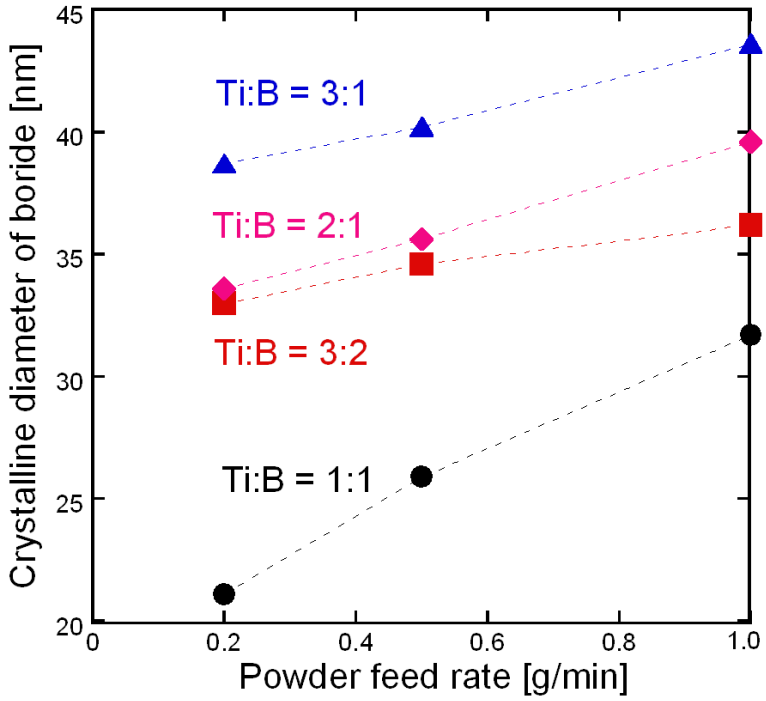

Fig. 14 Effect of powder feed rate on the crystalline diameter of prepared TiB_2 nanoparticles.

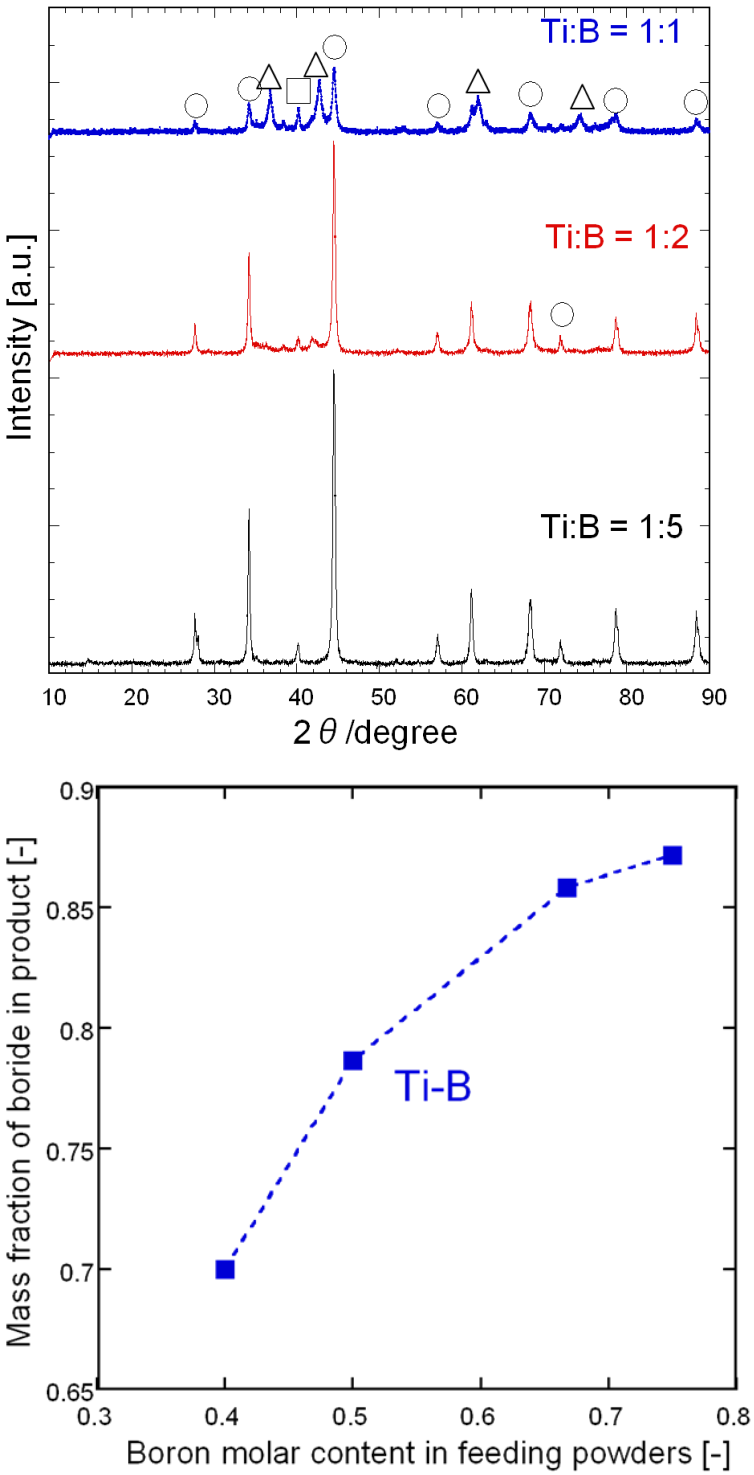

Fig. 15 XRD patterns and mass fraction of prepared nanoparticles at different boron content in feed powders; Feed rate: 120 mg/min, Carrier gas: 1 L/min.
(○: TiB_2 △: TiB □: Ti)

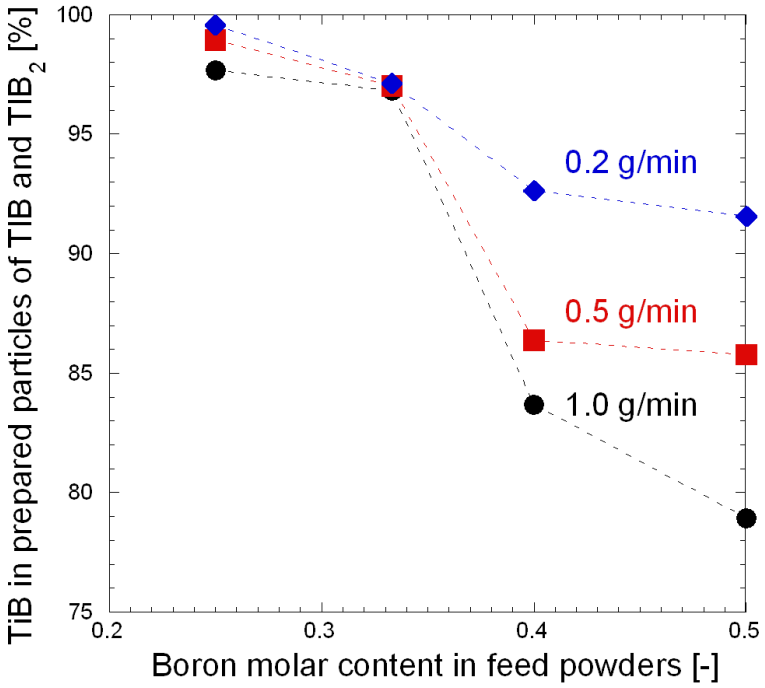

Fig. 16 Effect of boron content in the feed powders on the mass fraction of TiB in product of TiB and TiB_2; Carrier gas: 3 L/min..

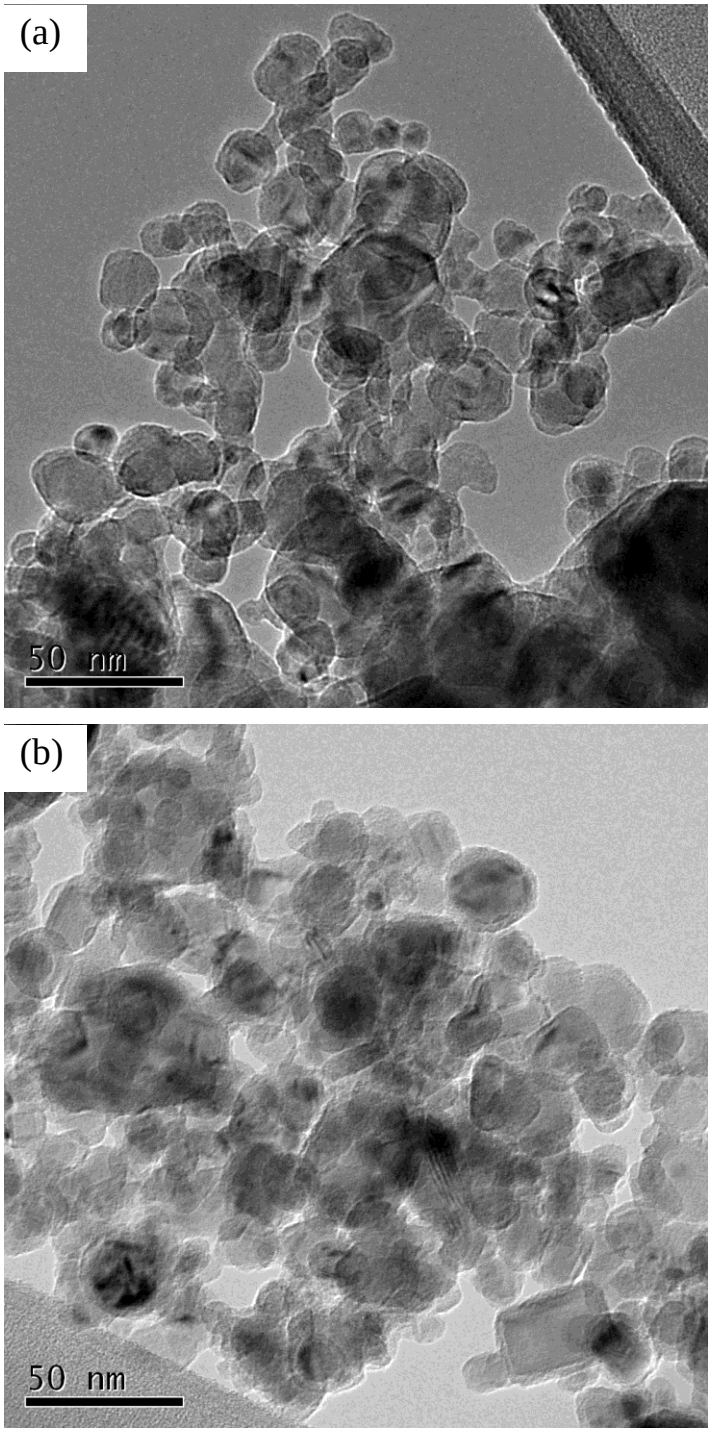

Fig. 17 TEM graphs of as-prepared product at the fixed powder feed rate of 0.2 g/min with different boron content in precursors: (a) Ti:B = 1:1; (b) Ti:B = 1:2.

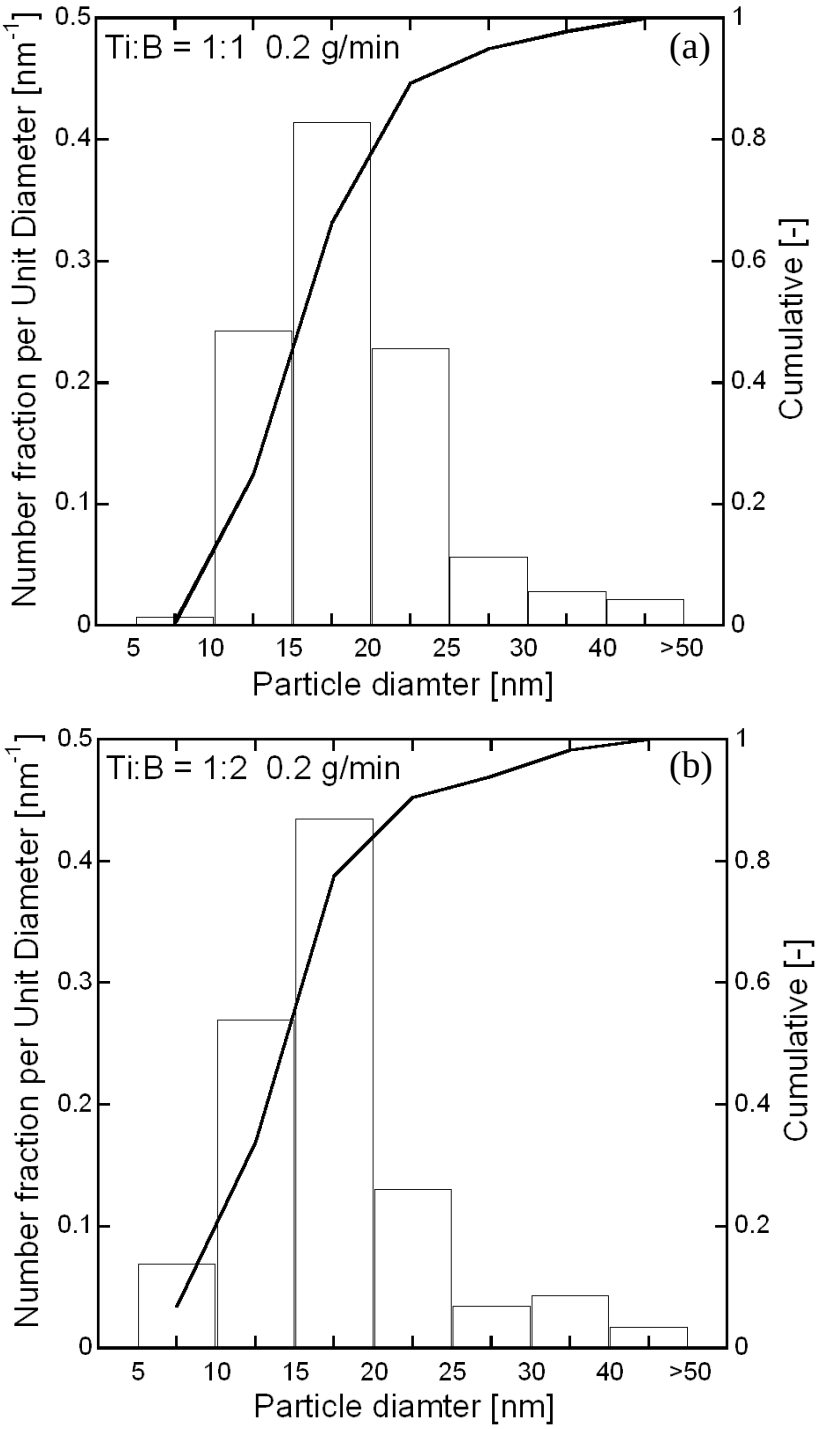

Fig. 18 Particle diameter distribution of as-prepared product at the fixed powder feed rate of 0.2 g/min with different boron content in precursors: (a) Ti:B = 1:1; (b) Ti:B = 1:2.

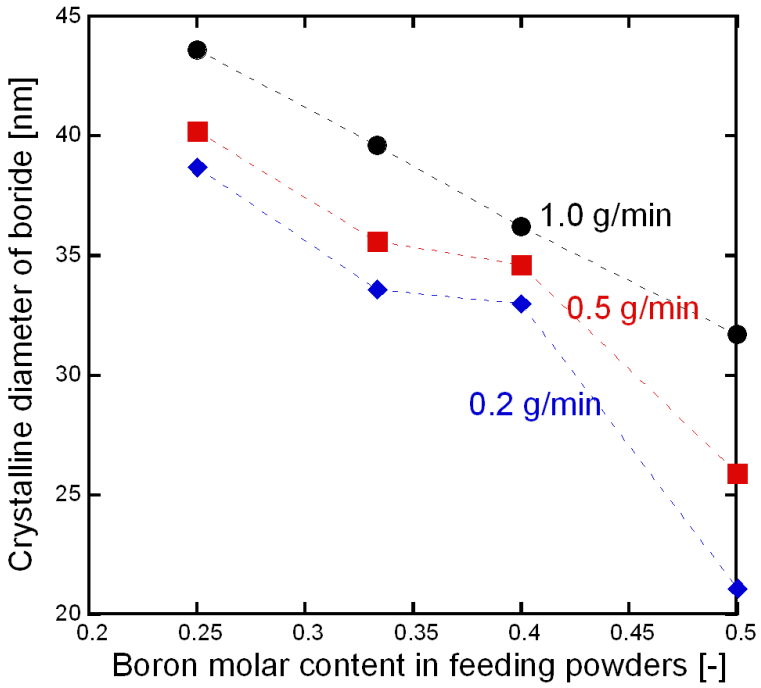

Fig. 19 Effect of boron content in the feed powders on the crystalline diameter of the prepared TiB_2; Carrier gas: 3 L/min.

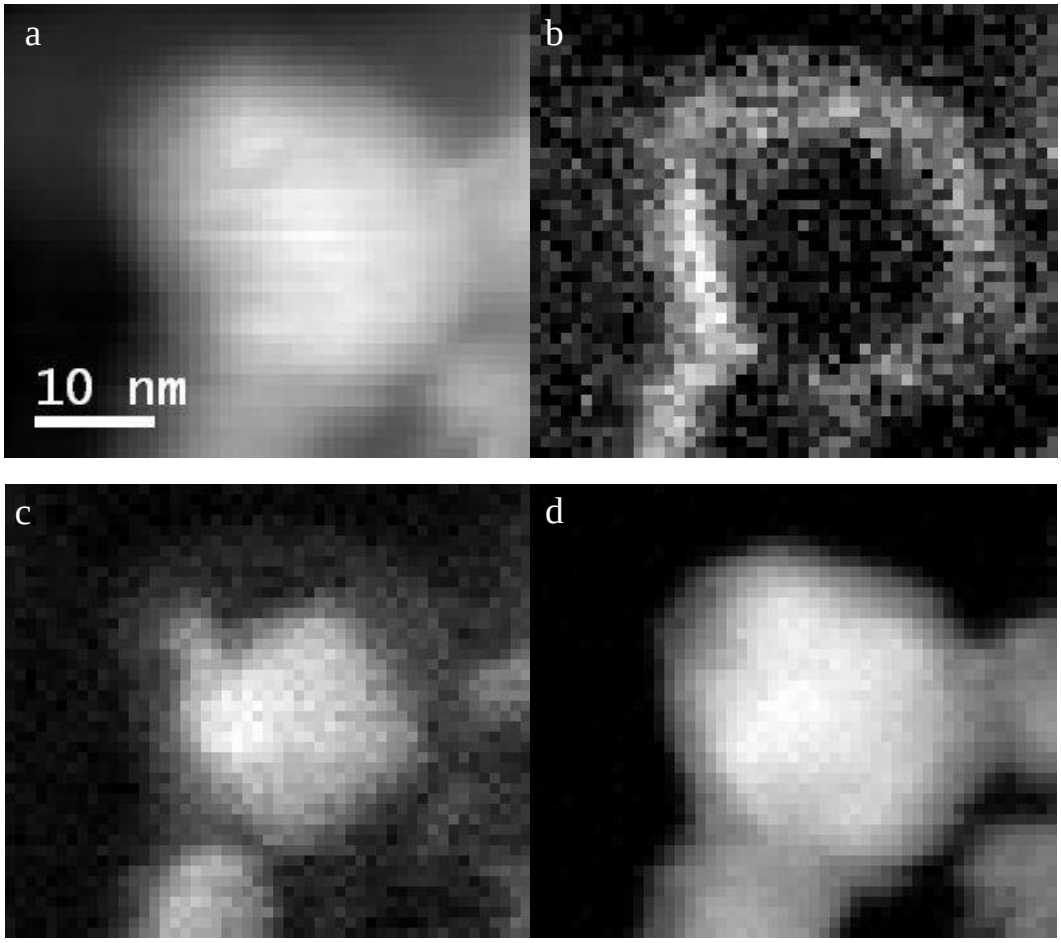

Fig. 20 shows SETM-EELS images of particles at fixed initial composition of Ti:B = 1:2 at powder feed rate of 0.2 g/min: (a): STEM image of a particle prepared for long time; (b)-(d): EELS maps of element of O, B, and Ti, respectively.

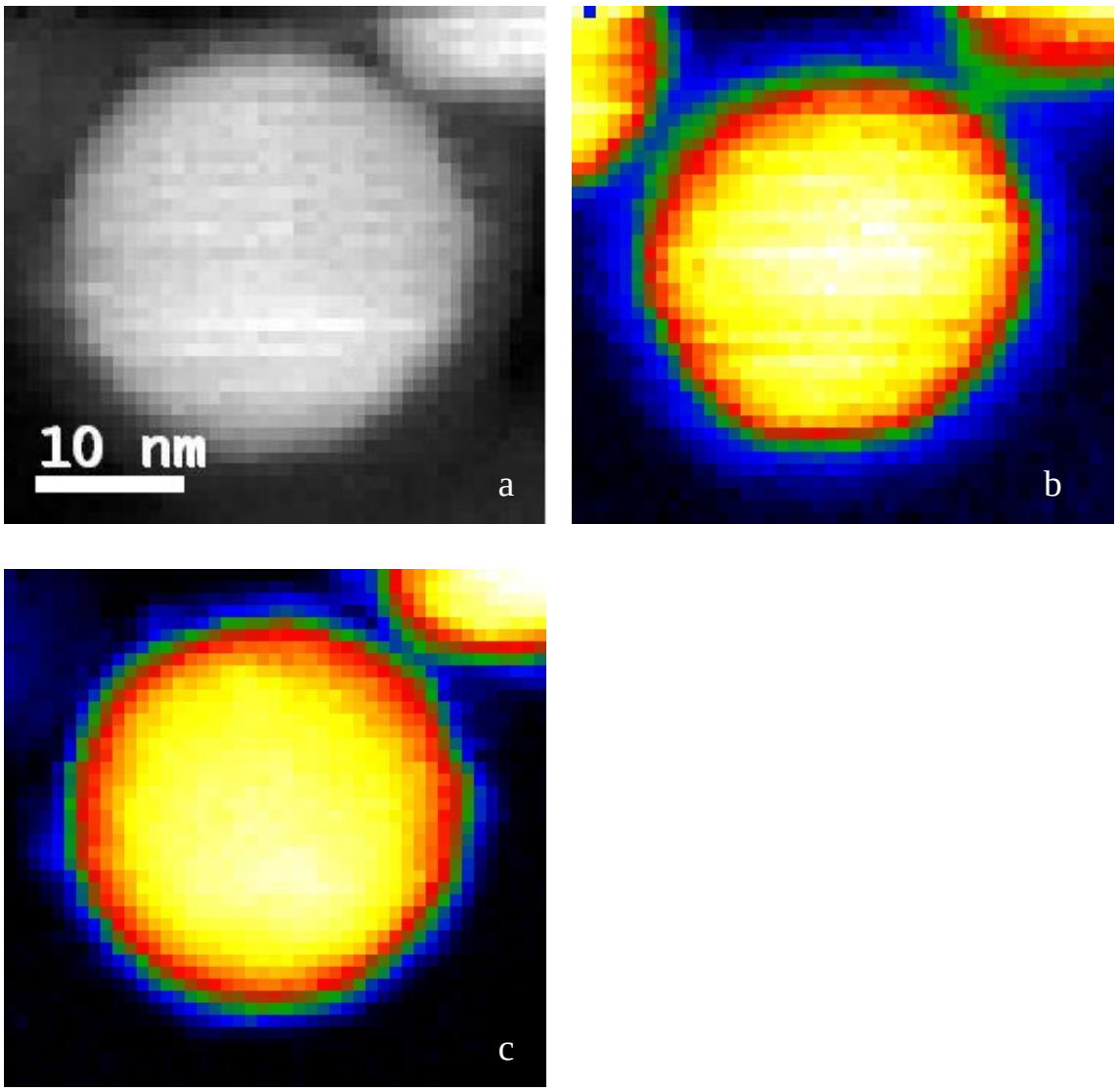

Fig. 21 SETM-EELS images of particles at fixed initial composition of Ti:B = 1:5 at powder feed rate of 0.2 g/min: (a): STEM image of a particle prepared for long time; (b)-(c): EELS maps of element of B and Ti, respectively.

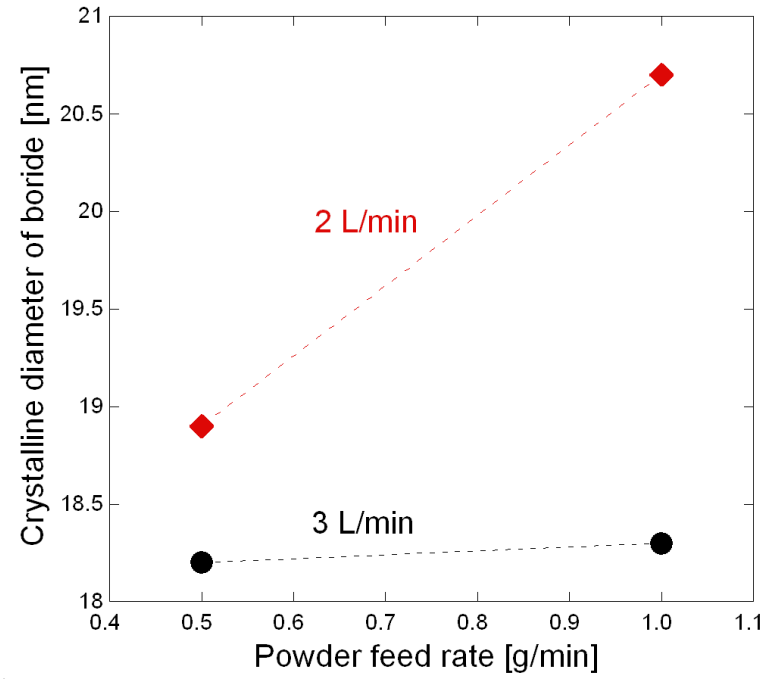

Fig. 22 Effect of carrier gas flow rate on the crystalline diameter of the prepared TiB at the fixed initial composition of Ti:B = 2:1.

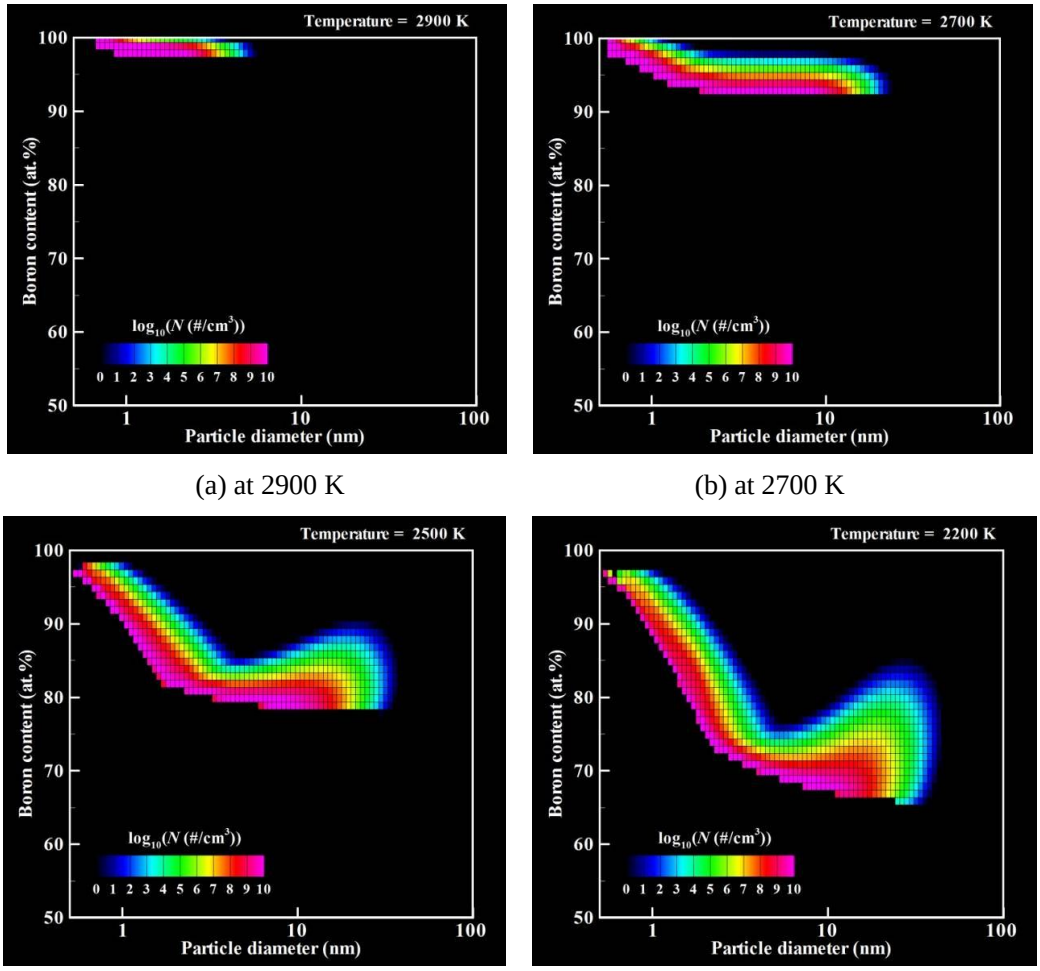

(a) at 2900 K (b) at 2700 K

(c) at 2500 K (d) at 2200 K

Fig. 23 Computational result of the evolution of the particle size-composition distribution according to plasma flow and its temperature in the raw material condition of 0.5 g/min for powder feed rate and Ti:B = 1:2 for powder composition.

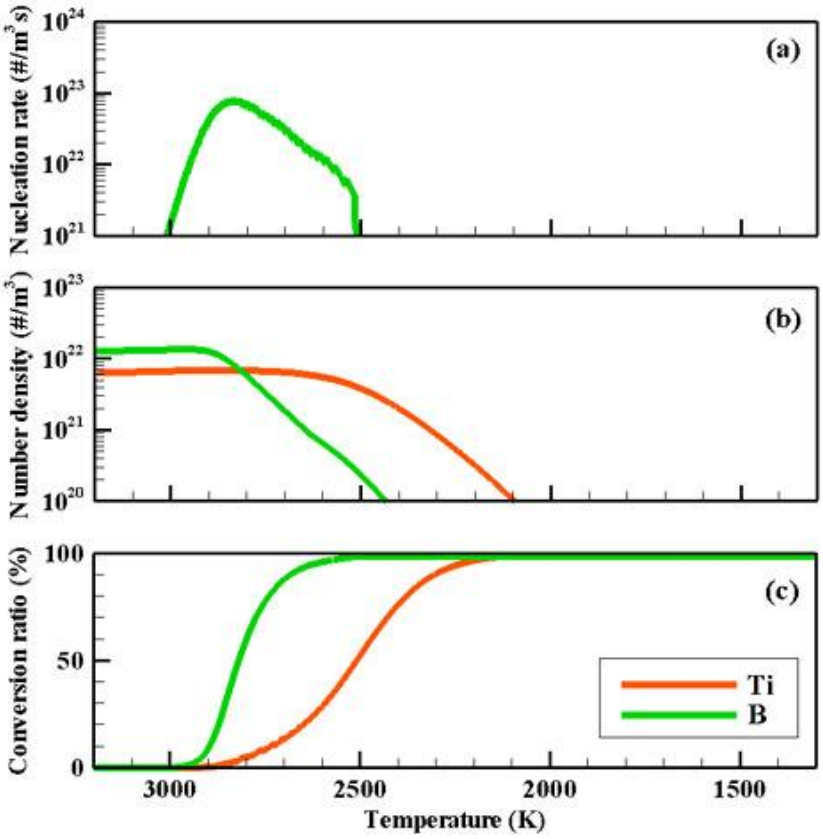

Fig. 24 Histories of the growth process in Ti-B system.

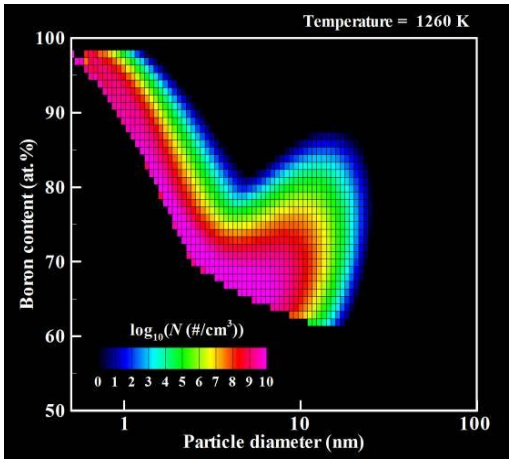

(a) 0.2 g/min

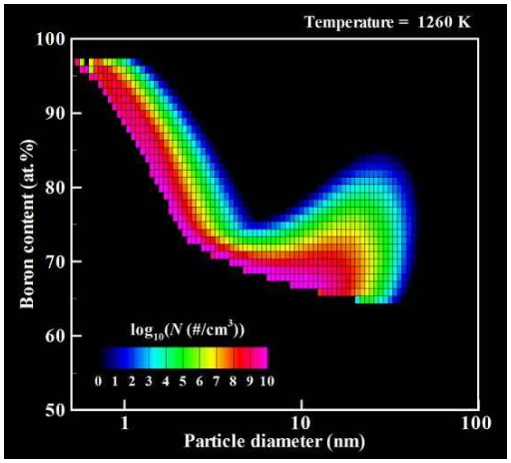

(b) 0.5 g/min

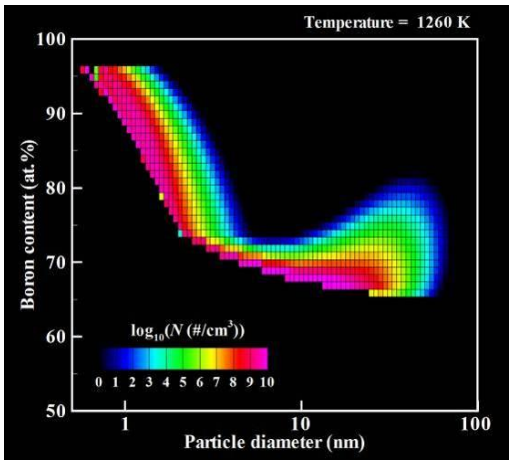

(c) 1.0 g/min

Fig. 25 Numerical results of the particle size and composition distribution at different powder feed rate from 0.2 to 1.0 g/min at the fixed initial composition of Ti:B =1:2.

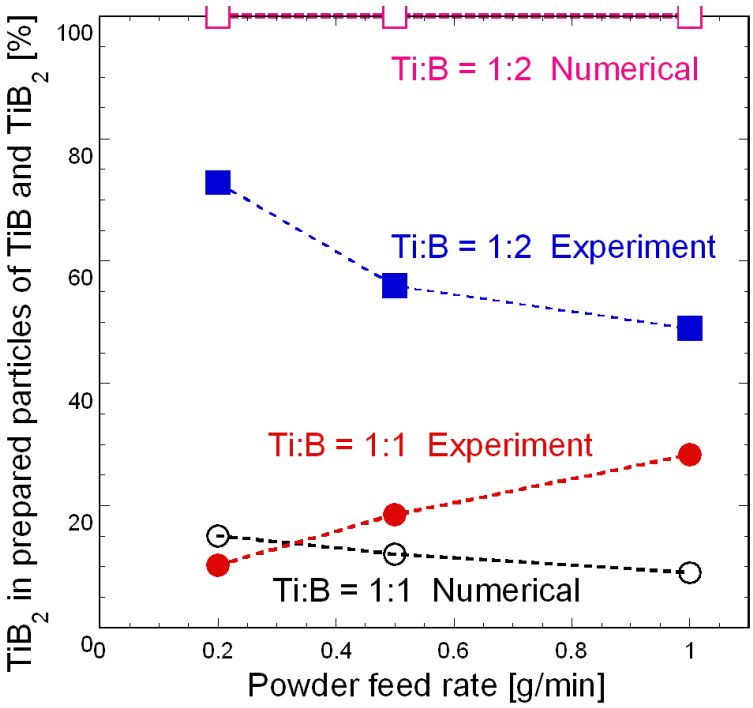

Fig. 26 Comparison of the effect of powder feed rate on the phase compositions of as-prepared nanoparticles between the experimental and numerical results.

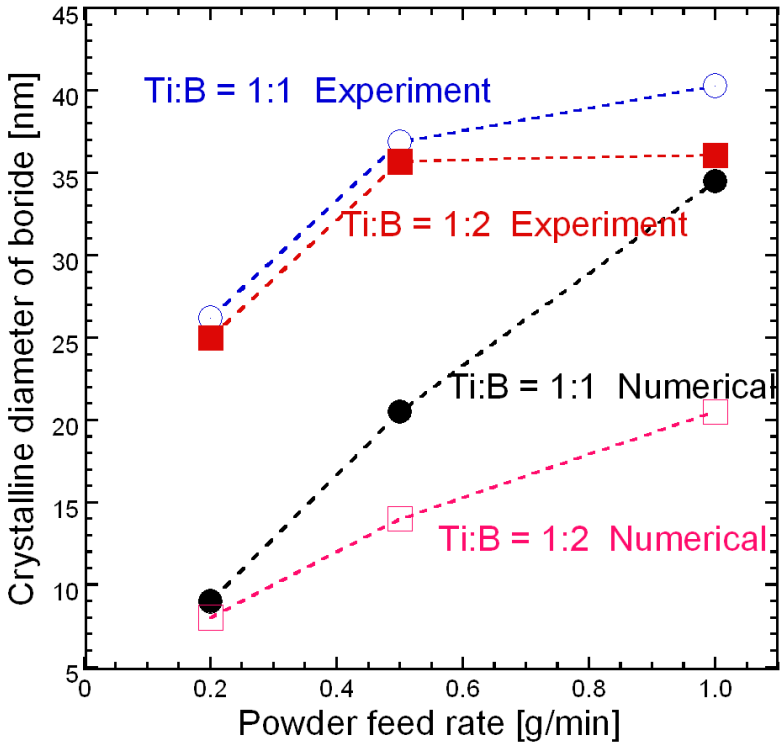

Fig. 27 Effects of the powder feed rate and boron content in the precursors on the crystalline mean diameter of TiB_2.

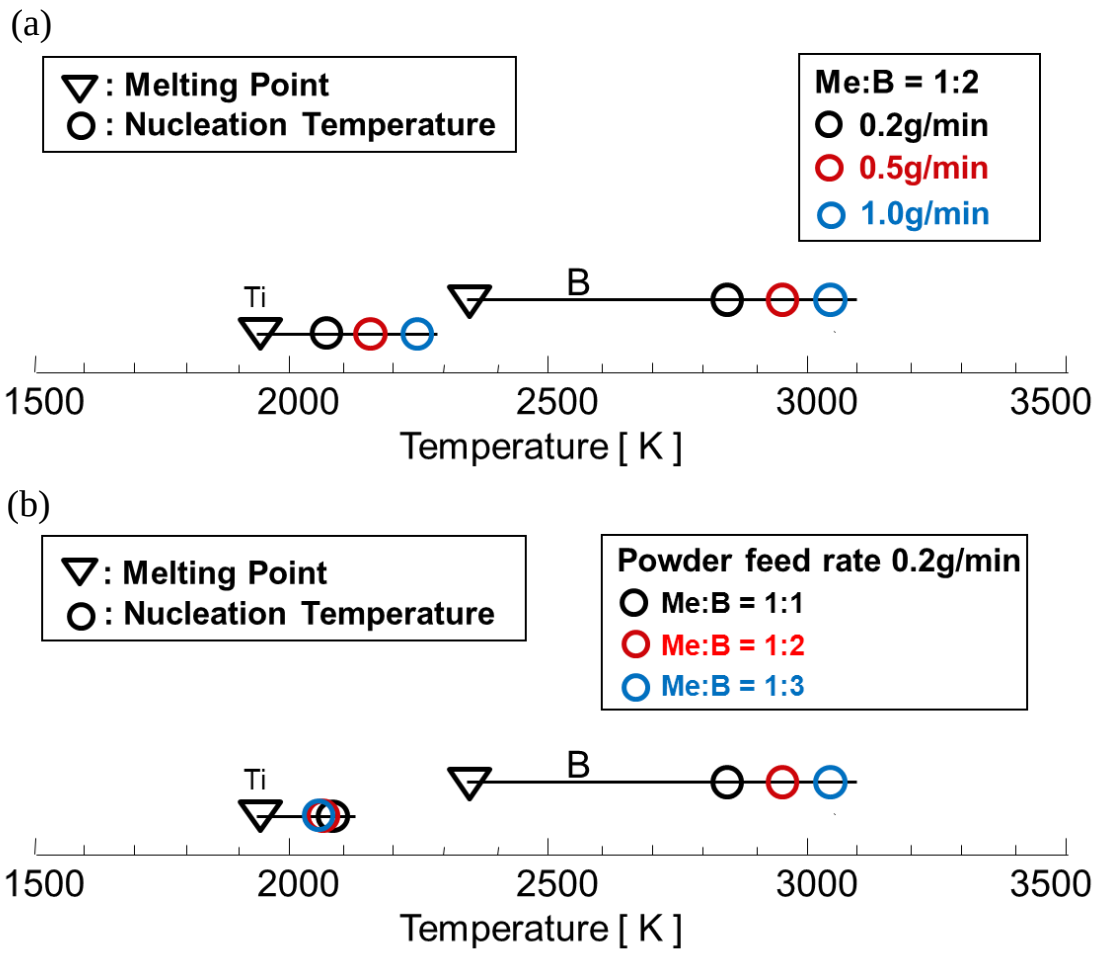

Fig. 28 The nucleation temperature at the critical saturation ratio for constituent components of titanium borides: (a) was calculated at the boron molar content of 66.7% with different powder feed rate (b) was drawn at the fixed powder feed rate of 0.2 g/min with different initial composition of Ti:B;.

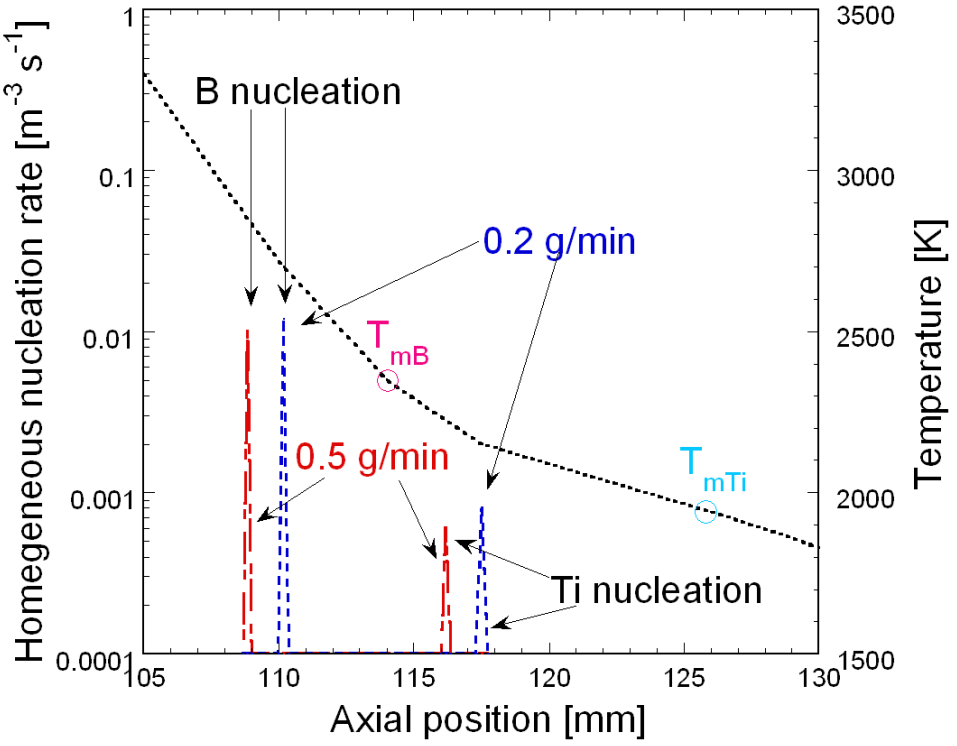

Fig. 29 Homogeneous nucleation rates of boron and titanium with different feed rate; T_{mB}: melting temperature of boron; T_{mTi}: melting temperature of titanium.

3. Synthesis of Iron Group Metals Boride Nanoparticle by RF Thermal Plasma

3.1 Introduction

Iron group refers to elements that are in some way related to iron. The iron group in the periodic table referred to the elements iron, cobalt and nickel. The borides of iron group metals attract our attention by their special properties. The iron group metals borides have high melting points, are very hard, and possess high thermal electric conductivity and catalytic activities. The iron group metals borides exhibit great thermal stability and they are not attacked by dilute acids and bases or concentrated mineral acids. They display considerable resistance to oxidation in air [1.2]. These properties make iron group metals borides most useful in modern technology. The synthesis of iron group metals boride is a little difficult compared with that of titanium boride.

Ultrafine particles of iron borides may exhibit novel and improved magnetic and catalytic properties [3]. Several iron borides are ferromagnets and electrical conductors. Cobalt boride nanoparticles have been actively researched as potential catalysts for hydrogen storage, information storage, magnetic fluids and for fuel cell [4-7]. The oxidation resistance of cobalt boride makes it also an interesting candidate for corrosion and wear-resistant surface coatings [8, 9]. Moreover, other applications seek to make use of these materials for their marked magnetic and magneto restrictive properties [10, 11]. Nickel boride is regarded as a potential industrial catalyst for hydrogenation reactions [12-15]. Ni−B nanoparticles are deposited on various supports to prepare supported catalysts, which exhibit better thermal stability and catalytic activities [16]. The remarkable catalytic activity of nickel boride has been attributed to the ability of boron to donate an electron to nickel [17]

FeB was obtained through solid state reaction routes from the elements [18-21] or via intermediate phases [22-25], and melt-spinning techniques [26, 27]. Further methods have been found to lead to ultrafine particles, for example, co-sputtering [28] and precipitation reactions. They have been extensively studied by a number of authors [29-33] for different solvent systems including water and organic solvents. The conventional wet chemistry method which includes the colloidal synthesis of cobalt boride nanoparticles has been reported in the literature.

The typical synthesis involves the chemical reduction of cobalt salts in liquid solutions and the thermal decomposition of the cobalt carbonyl [4-11]. In these syntheses methods, cobalt and cobalt boride nanoparticles with narrow size distributions and controlled shapes were successfully prepared. However, the preparation of nanoparticles using colloidal chemistry is often connected to liquid effluents and cleaning of liquid effluents is difficult and costly. In addition, the colloidal synthesis of nanoparticles often requires multi-step processes and the amounts of solvents needed in the process are expensive and large [34]. The Ni–B catalyst is usually synthesized by an impregnation-reduction method [14,15]. However, such method is difficult to carry out in industrial preparation. In the preparation of nickel boride catalysts, sodium borohydride is generally used to reduce a nickel salt [35]. Chen et al. synthesized a Ni–B catalyst by an electroless plating method, and found it showed superior catalytic property to the corresponding Ni-B catalyst prepared by a chemical reduction method. Microwave irradiation as a heating method has been used to change the change the properties of Ni–B particle, such as its morphology and particle size.

Nanoparticle syntheses by RF thermal plasma have attracted research attention. In general, RF thermal plasma involves a distinct advantage over conventional techniques in nanoparticles synthesis because it involves a one-step process and capping agents are not required [36-39]. Thus, RF thermal plasma is lowering the cost, shortening the synthesis time in the scale of few minutes, and providing possibility for mass production of nanoparticles due to its high production rate. Specifically, RF thermal plasma holds several advantages such as high enthalpy which enhances reaction kinetics, large plasma volume, long residence time by virtue of its low velocity, and selective oxidation or reduction atmosphere according to required chemical reactions [35]. Moreover, RF thermal plasma is generated in the torch without electrode.

Learning how to synthesize iron group metals boride nanoparticles with size and shape control is an important task in the development of advanced materials and applications. An in depth review of available literature has yielded no studies done on the synthesis of iron group metals boride nanoparticles using RF thermal plasma. Therefore, the growth mechanism of iron group metals boride nanoparticles synthesized using thermal plasma has not been elucidated.

In Ch. 2, the synthesis of titanium boride nanoparticles was investigated and it is concluded that the nucleation temperature of constituent composition of boride is an important factor in the synthesis of boride nanoparticle by RF thermal plasma. Because the nucleation temperature of iron group metals and Ti are all lower than that of B, the formation mechanism of titanium

boride and iron group metal boride is the same. But the thermophysical properties of the particles are an important factor to influence the plasma temperature. Different metal has its unique characteristic and the synthesis processes in plasma are a little different. In this chapter, we describe the synthesis processes of iron group metals boride nanoparticles in the plasma and examine the operating parameters such as initial composition and powder feed rate on phase composition and crystalline diameter to investigate the effect of nucleation temperature further.

In this chapter, the nano-size iron group metals boride particles were synthesized from the vapor phase of iron group metals and boron evaporated from the solid precursors in the RF plasma. The prepared iron group metals boride nanoparticles were characterized using Transmission electron microscopy (TEM) for surface and particle morphology and X-ray diffraction (XRD) techniques, with an emphasis to examine phase composition and particle sizes. The understanding of nanoparticles formation mechanism during thermal plasma synthesis and the control of composition and size are indispensable for industrial applications related to the use of high quality nanoparticles.

3.2 Thermodynamic properties

1) Phase diagram of Fe-B, Co-B and Ni-B system

Figure 1 shows the Fe-B phase diagram including two thermodynamically stable phases Fe_2B and FeB. The iron boride (Fe_2B) contains 8.83 at% B and has the common tetragonal structure of the CuA_{12} type with 12 atoms in the unit cell. The second iron boride (FeB, monoboride) contains 16.23 wt% B and has an orthorhombic lattice with 8 atoms in the unit cell. Out of these, the metastable Fe_3B compound has been reported as a crystallization product of amorphous alloys. It decomposes to stable bcc-Fe and Fe_2B after heating at high temperatures.

The equilibrium phase diagram of the Co-B system, shown in **Figure 2**, was fairly well established by the mid 1960's. The system consists of three intermetallic compounds (Co_3B, Co_2B, and CoB). The system is similar to the Fe-B system, except that the structure and melting mechanism are well established for Co_3B, but are uncertain for Fe_3B. At 1380 K, Co and Co_3B can be generated among 18.5~21 at%. When the range of B is 21~32 at%, Co_3B and Co_2B can be synthesized, while Co_2B and CoB will be synthesized between 32~50 at%.

Figure 3 displays the phase diagram of Ni-B system. A most common phase is amorphous Ni_2B with tetragonal structure, the less common borides NiB, Ni_3B, Ni_4B_3 with orthorhombic structure. The boron content of fewer than 25 at% has the stable phases of Ni and Ni_3B

according to the Ni-B phase diagram. However, the phase diagram also indicates that Ni_2B and other crystalline phases are stable when the boron content of Ni-B alloys exceeds 25 at%. A comparison of the microstructure and characteristics of Ni-B alloy having boron contents above and below 25 at% is interesting from both an academic and a practical viewpoint. Based on fig. 3, boron content is higher than 40 at%, the stable phase NiB and B can exist.

2) Gibbs free energy

Figure 4 reveals the Gibbs free energy of Fe-B, Co-B and Ni-B systems. Below 2800K, the ΔG of FeB and Fe_2B is negative, which means the synthesis of FeB and Fe_2B is spontaneous. The ΔG of FeB is the lowest, so it is the easier to generate FeB.

The ΔG of CoB and Co_2B is negative, which means it is easy to synthesize of CoB and Co_2B. The synthesis of Co_3B is difficult due to the high Gibbs free energy.

According to fig. 4, below 3500K, all of the Gibbs free energy of Ni_3B, Ni_2B and Ni_4B_3 are negative. The synthesis of Ni_3B, Ni_2B and Ni_4B_3 are spontaneous.

3) Saturation vapor pressure

Vapor pressure difference of boron and iron group metals is the important factor for the controlled composition and diameter of the prepared iron group metals boride nanoparticles. The vapor pressure ratio of Fe/B is on the order of 10^4 at the melting point of Fe, that of Ni/B is on the order of $4 \cdot 10^3$ at the melting point of Ni, and that of Co/B is also on the order of $4 \cdot 10^3$ at the melting point of Co. The saturation vapor pressure of constituent components of borides is demonstrated in **Figure 5**. Preparation of borides with large difference in vapor pressure of the constituent components is quite difficult. Therefore, the control of condensation process is important for preparation of iron group metals boride nanoparticles in RF thermal plasma.

3.3 Experimental

3.3.1 Experimental apparatus

Figure 6 shows the illustration of the experimental setup for RF thermal plasma which is used for the production of iron group metals boride nanoparticles. The setup consists of a plasma torch, a reaction chamber, a particle filter, and a power supply of 4 MHz at a plate power of 30 kW. The plasma torch is composed of a water-cooled quarts tube (45 mm inner diameter,

120 mm length) to confine thermal plasma and a water-cooled working induction coil (3 turns) to couple its electromagnetic energy to thermal plasma. The reaction chamber was set below the torch. The prepared nanoparticles were collected at the inner surface of the reaction chamber.

3.3.2 Experimental conditions

Iron group metals boride nanoparticles with raw powder compositions (Me:B) of 2:1, 1:1, 1:2, and 1:3 by molar ratio, have been synthesized using RF thermal plasma method. The starting materials in the feeding powders were iron (particle size: 45 μm, purity: 99%, The Niraco Co., Japan), cobalt (particle size: 45 μm, purity: 98%, Wako Pure Chemical Industries, Ltd., Japan), nickel (particle size: 3~5 μm, purity: 98%, Wako Pure Chemical Industries, Ltd., Japan) and crystalline boron (particle size: 45 μm, purity: 99%, Kojundo Chemical Laboratory Co. Ltd., Japan). Metal and boron particles were premixed at the fixed molar composition. And then the mixture was put into the powder feeder, which is connected with the plasma torch by an injection tube.

The RF thermal plasma system was evacuated and Ar was introduced up to a pressure of 101.3 kPa. The RF plasma was ignited at a low pressure of about 10 kPa, and then chamber pressure was increased up to atmospheric pressure with increasing plasma power up to 30 kW. The iron group metals and boron powders were prepared in the desired molar ratio and were mixed with an agate mortar. The premixed powders were introduced into the top of the plasma torch at a feed rate of 0.2, 0.5, 1.0 g/min through a metallic probe (2 mm inner diameter) penetrating 19 mm into the torch. Before the experiment, we checked powder feed rate several times until it was stabilized. After the experiment, we checked powder feed rate again to confirm consistent powder feed rate and feeding uniformity with the previous measurements.

The experimental parameters are shown in **Table 1**. Argon was introduced as carrier gas (3 L/min), plasma supporting gas (5 L/min). Mixture of argon and helium was used as the sheath gas (65 L/min, Ar:He = 60:5), which was injected from the outer slots to protect the inner surface of the quartz tube and stabilize the plasma discharge.

In the thermal plasma, the feeding powders were evaporated in the high temperature region of the plasma. After the evaporation and reaction, the vapor was rapidly cooled in the tail of plasma flame. Through the nucleation and condensation processes in the cooling region, boride nanoparticles were prepared.

3.3.3 Analytical methods

The analytical methods are the same as those which are introduced in detail in Ch. 2.

3.4 Experiment results and discussion

3.4.1 Effect of powder feed rate

1) Fe-B system

Figure 7 shows XRD spectra of product prepared with different powder feed rate at fixed initial composition of Fe:B = 1:2. In XRD results, the characteristic peaks of Fe and FeB can be clearly identified, while the dominant product is Fe indicating there is still a large amount of unreacted boron in product. However, boron peaks are not identified [39]. According to XRD spectra, the intensity of the peak of FeB decreases with the increase of powder feed rate.

The effect of powder feed rate on the phase composition of product in Fe-B and Ti-B systems are displayed in **Figure 8**. The mass fraction of iron boride in product decreases with increasing powder feed rate. With low powder feed rate, both of boron and iron are quickly evaporated just after the injection of raw powders, and then the evaporated boron is nucleated in the high temperature area at the upstream region of plasma flow where iron and boron co-exist and can react with each other. On the other hand, the amount of raw material increases at high powder feed rate, though the heat from the plasma keeps constant at the fixed input power of 30 kW. The less heat transferring from the plasma to each particle takes longer time to evaporate raw materials at high powder feed rate rather than the low powder feed rate. In addition, boron is difficult to be evaporated due to the relatively higher melting point, evaporation temperature and latent heat. For this reason, the existence area of evaporated boron is extended along with the thermal plasma flame. The boridization occurs easily in the upstream region of thermal plasma flow due to high temperature and abundant iron vapor, while it is difficult in the downstream region because of relatively low temperature and diffuse of iron vapor which is produced in the upstream region. Therefore, less boron nuclei can react with sufficient iron, and the mass fraction of iron boride nanoparticles in product decreases at higher powder feed rate.

In addition, it is observed that the synthesis of titanium boride is easier than that of iron boride. The temperature gap between boron nucleation temperature and boron melting point is almost the same, while the temperature gap between the melting point of boron and iron is wider than the case of titanium. It indicates more boron nuclei on molten state become solid and cannot well mix with iron. Gibbs free energy of iron boride and titanium boride are displayed in

Figure 9. Gibbs free energies are all negative and iron boride and titanium boride can generate spontaneously. Gibbs free energy of titanium boride is relatively low. Based on the factors of nucleation temperature and Gibbs free energy, the generating of titanium boride is easier than that of iron boride.

TEM graphs of as-prepared product at initial composition of Fe:B = 1:2 with powder feed rate of 0.2 and 0.5 g/min as shown in **Figure 10**, the product consists of nano-size particles, are all spherical and have different particle size. The particle size distribution is demonstrated for product at the fixed initial composition of Fe:B = 1:2 with powder feed rate of 0.2 and 0.5 g/min in **Figure 11** (a) and (b), respectively. According to fig. 10 and 11, the diameter of particles at higher powder feed rate is a little lager than that at low powder feed rate. The diameter of particle at 0.2 and 0.5 g/min is 27 nm and 30 nm, respectively. The growth region is from the nucleation temperature of boron to the melting point of iron. From numerical simulation [48, 49], the nanoparticles are formed at earlier stage at higher powder feed rate, and the vapor consumption rate by condensation increases due to the larger vapor concentration with the higher powder feed rate. The temperature upstream is high so that the nucleation rate is low which means a small number of stable nuclei are generated. The smaller number of nuclei shares a larger amount of vapor; consequently the particles can grow larger. Furthermore, since the powder feed rate increases, the monomer density increases which leads to the high growth rate. The growth progress is not finished until the nucleation temperature of iron. The different nucleation temperatures of iron and boron lead to the different temperature gap between the nucleation temperature of boron and iron. And then there is a long growth time of boron nuclei from the nucleation process of boron monomers to the co-condensation process of iron and boron monomers due to the higher nucleation temperature of boron at high powder feed rate. The growth time of boride nanoparticles at higher powder feed rate is longer than that at lower powder feed rate. As a result, the average particle diameter of iron boride nanoparticle at higher powder feed rate have large diameter.

As shown in fig. 10, core-shell structured nanoparticles are observed in TEM graph of as-prepared product. The thickness of the shell was estimated to be about 2 nm. EELS measurements in the STEM were conducted to analyze chemical components of core and shell separately. **Figure 12** shows SETM-EELS images of particles at fixed initial composition of Fe:B = 1:2 at powder feed rate of 0.2 g/min. Fig. 12 (a) is the STEM image of a particle prepared for long time. Figs. 12 (b)-(d) display corresponding O, Fe, and B projected

distributions, respectively. On the basis of EELS result, the constituents of the shell are B and O. In the comprehensive consideration of EELS and XRD results, the original shell of prepared particle in the experiment is expected to be B, which is oxidized in air after plasma treatment.

The synthesis mechanism of core-shell structured iron boride nanoparticle was examined based on the calculation of nucleation temperature. The nucleation process of boron occurs only around the boron nucleation temperature.

2) Ni-B system

XRD spectra of product with different powder feed rate at initial composition of Ni:B = 1:3 is revealed in **Figure 13**. The peaks of NiB, Ni_4B_3, Ni_2B and Ni_3B can be clearly identified, and the dominant product is NiB. The raw material Ni cannot be detected. Because of the negative Gibbs free energy of nickel borides, they can be generated spontaneously.

Figure 14 reveals the effect of powder feed rate on the phase composition of product at initial composition of Me:B= 1:2 in Fe-B and Ni-B systems. Based on fig. 14, the mass fraction of nickel boride in product is much higher than that of iron boride. The chemical stability of boride is the driving force and the generation of metal boride can take place spontaneously. **Figure 15** presents the relationship between Gibbs free energy of nickel boride and iron boride and temperature. Gibbs free energy of nickel boride is lower than that of iron boride, indicating that the synthesis of nickel boride is easier than that of iron boride. In addition, the melting point of nickel is lower compared with iron.

Effect of powder feed rate on the mass fraction of Ni_3B is demonstrated in **Figure 16**, which shows the tendency that the mass fraction of Ni_3B decreases with the increase of powder feed rate. The tendency of the effect of powder feed rate on the phase composition of product is the same as that in Fe-B system and the reason was explained in the Fe-B system.

TEM graphs of as-prepared product at the fixed initial composition of Ni:B = 1:3 with powder feed rate 0.2 and 1.0 g/min are displayed in **Figure 17**. **Figure 18** shows TEM graph with high magnification of as-prepared product at the fixed initial composition of Ni:B = 1:3 with powder feed rate 0.2 g/min. Seen from fig. 18, core-shell structured nanoparticles are observed, while the thickness of the shell is very thin.

The particle size distribution is demonstrated for as-prepared product at the fixed initial composition of Ni:B = 1:3 with powder feed rate of 0.2 and 1.0 g/min in **Figure 19** (a) and (b), respectively. The mean diameter of the prepared particles increases with the increase of powder

feed rate. The diameter of particle at 0.2 and 1.0 g/min is 27.5 nm and 32.5 nm, respectively. The average particle diameter of nickel boride nanoparticle at higher powder feed rate have longer time to grow larger. The reason is the same as that explained in Fe-B system.

Figure 20 reveals SETM-EELS images of a particle at fixed initial composition of Ni:B = 1:3 at powder feed rate of 0.2 g/min. Fig. 20 (a) is the STEM image of a particle prepared. Figs. 20 (b)-(c) display corresponding B and Ni projected distributions, respectively. On the basis of EELS result, the constituent of the shell is boron.

3) Co-B system

The as-prepared cobalt boride nanoparticles were characterized by XRD for crystal phase determination and estimation of crystallite size. The XRD patterns are indexed and matched using dedicated XRD software and all experimental peaks are matched with theoretically generated peaks and indexed. The XRD patterns for cobalt boride nanoparticles prepared from Co:B ratio of 1:2 and 1:3 at different powder feed rate are shown in **Figure 21**. These XRD patterns reveal that at higher feed rate, XRD peaks become clearer and sharper. The CoB and Co_2B crystalline phases are identified from the XRD spectra. The peaks detected at $2\theta = 34.10°$, 37.25°, 41.22°, and 49.18° are the characteristic peaks for CoB crystal phase while the $2\theta = 45.78°$ is the characteristic peak for Co_2B crystal phase, respectively. The cobalt boride results from the negative Gibbs free energy. The XRD patterns also show that the peak of the unreacted Co at $2\theta = 44.26°$ is included for Co:B = 1:2 and 1:3, while the intensity of unreacted Co is relatively low in the case of high feed rate. From fig 21, it is found that the relative intensity of XRD peaks of cobalt boride is increased with the boron content in feeding powders. The raw materials Co co-exist in the product due to the large difference of saturation vapor pressure between the cobalt and boron as shown in fig. 5. All the major peaks are indexed to the standard pattern for cobalt boride (JCPDS No. 9-617 and 089-1994). This observation indicates that there is a large amount of boron vapor that has reacted with cobalt. Some tiny peaks are observed and may correspond to small amounts of unreacted precursor powders.

These XRD data suggests that cobalt boride nanoparticles are easily synthesized in thermal plasma with higher boron content in feeding powders. To our knowledge this study represents the first successful plasma synthesis of cobalt boride nanoparticles. However, it is suggested that more research must be done for optimum control of phase composition in the final product.

The effect of powder feed rate on the phase composition of as-prepared particles is shown

in **Figure 22**. The nucleation position shifts to more upstream position at the higher powder feed rate owing to enhanced boron vapors. The shift of nucleation position to upstream enhances boride nanoparticles due to mixing more boron and cobalt well. Furthermore, it provides relatively long time for the condensation of boron and cobalt monomers on boron nuclei. In the present study, the mass fraction of cobalt boride nanoparticles increases with increasing powder feed rate in boron rich conditions (*i.e.* Co:B = 1:2 and 1:3). One possible explanation to account for it is the increased condensation time due to the production of boron nuclei in the upstream region. Since cobalt boride nanoparticles are produced through the co-condensation of B and Co to the B nuclei, long condensation times are responsible for the large ratio of boride nanoparticles. For these reasons, the mass fraction of CoB and Co_2B in the final product increases with increasing powder feed rate.

TEM images of cobalt boride nanoparticles are shown in **Figure 23**. The operating conditions are Co:B = 1:2 at the initial powder composition and 0.2 and 0.5 g/min for the powder feed rate. These TEM images clearly reveal the as-prepared cobalt boride powder consist of spherical grains which exhibited some tendency of agglomeration. The Particle diameter distribution is demonstrated for as-prepared product at the fixed initial composition of Co:B = 1:2 with powder feed rate of 0.2 and 0.5 g/min in **Figure 24** (a) and (b), respectively. The average diameter of particles at 0.2 g/min is about 10 nm, and the average diameter of particles at 0.5 g/min is about 17.5 nm.

Figure 25 presents the effect of powder feed rate on the mean crystalline diameter at fixed composition of Co:B = 1:2. The crystalline diameter of cobalt boride nanoparticles increases with increasing powder feed rate. The Debye-Scherrer analysis indicates that the average grain size of all the samples are reduced from the 45 μm of precursor powder size to 18 - 22 nm after plasma synthesis. The measured particle size is greater than the diameters of nanoparticles synthesized using colloidal routes. This observation suggests that unlike surfactant stabilized cobalt boride nanoparticles prepared from aqueous solution, cobalt boride nanoparticles prepared from RF thermal plasma tend to coalesce forming bigger aggregates [44-45]. These cobalt boride clusters tends to sinter together into a spherical shape in order to minimize surface energy. The growth time from the nucleation temperature of boron to the melting point of cobalt is longer due to the high nucleation temperature of boron at higher powder feed rate. The higher temperature in the upstream region causes slower nucleation rate and small number of stable nuclei shares large amount of vapor. Consequently, the particles can grow larger with higher

powder feed rate. In the synthesis of cobalt boride, the increase in the crystalline diameter at higher powder feed rate is due to the large amount of vapors which co-condense to B nuclei forming cobalt boride nanoparticles. In addition, the increase of monomer density leads to the increase of growth rate of nanoparticle. The average crystalline diameter of nanoparticles has the good agreement with the result from TEM in fig. 24. However, the average grain size estimated by TEM is less than that measured by the Debye-Scherrer analysis as shown in fig. 24. In the Debye-Scherrer analysis, bigger aggregates are measured, in TEM measurement, only single particles are chosen.

3.4.2 Effect of boron content in feeding powders

1) Fe-B system

XRD spectra of product prepared with different initial composition of Fe:B at constant powder feed rate 0.2 g/min is shown in **Figure 26**. In boron poor condition, only the characteristic peaks of raw materials Fe are identified. And iron boride is not produced. In boron rich condition, the peaks of FeB can be identified, while the dominant product is still Fe. Such result is attributed to the large saturation vapor pressure ratio at melting point of Fe, Fe/B = 10^4.

The relative intensities of peaks of unreacted Fe are high in the XRD spectrums, indicating there is also a large amount of unreacted boron in the product. Coexistence of unreacted iron and boron nanoparticles in the as-prepared product means that the separate nucleation of each constituent vapor at different times and regions owing to the different nucleation temperature. The nucleation temperature gap between iron and boron is large at the constant initial composition and powder feed rate. In other words, there is a relatively small temperature gap between the melting point and nucleation temperature of boron in the boridation process which takes place in the temperature range from the nucleation temperature of boron to iron in Fe-B system, indicating much boron nuclei on molten state become solid. It is difficult for the reaction between the solid nuclei and vapor. Less iron boride nanoparticles are synthesized. Therefore, iron boride nanoparticles are difficult to generate.

2) Ni-B system

Figure 27 displays XRD spectra of product prepared with different initial composition of Ni:B at powder feed rate 0.2 g/min. In boron poor condition (Ni:B = 2:1 and 1:1), the

characteristic peak of Ni and Ni_3B are identified, and the dominant product is Ni_3B. However, in boron rich condition (Ni:B = 1:2 and 1:3), the peaks of NiB, Ni_4B_3, Ni_2B and Ni_3B are all identified, while the dominant product is NiB. Since Gibbs free energy of NiB, Ni_4B_3, Ni_2B and Ni_3B are relatively negative; the synthesis of NiB, Ni_4B_3, Ni_2B and Ni_3B can take place spontaneously. The peaks of Ni are not observed in boron rich condition. According to phase diagram of Ni-B in fig. 3, when the molar content of boron is less than 33.3% (Ni:B = 2:1), the product is possible Ni_3B and Ni. When the molar content of boron is larger than 40%, the product of NiB and Ni_4B_3 is possibly to generate. The mass fraction of NiB in product increases with increasing boron content in feeding powders due to the excessive boron vapor in plasma.

Effect of boron content in feeding powders on the mass fraction of Ni_3B at powder feed rate 0.2 g/min is revealed in **Figure 28**. The mass fraction of Ni_3B in product decreases with the increase of boron content in feeding powders. According to phase diagram of Ni-B system, it is easier to generate NiB compared with the synthesis of Ni_3B in boron rich condition.

Figure 29 displays XRD patterns of product with different boron molar content in feeding powders at quenching gas flow rate of 20 L/min. In boron poor condition, the dominant product is Ni_3B. The peak of unreacted Ni has the highest intensity in boron rich condition, while Ni_3B are not observed. The highest intensity of Ni_2B in product is generated with the phase composition of Ni:B = 2:3. Compared with fig. 27, quenching gas plays an important role in the synthesis of metal boride nanoparticles. Without quenching gas, the dominant product is metal boride nanoparticles and unreacted Ni cannot be observed. With quenching gas, the main product is unreacted Ni and Ni_2B can be identified. The addition of quenching gas reduces the plasma temperature.

The effect of boron molar content in feeding powders on the mass fraction of each phase in product with quenching gas flow rate of 20 L/min is shown in **Figure 30**. The highest mass fraction Ni_2B in product is observed with the initial composition of Ni:B = 2:3. In the boron poor condition, Ni_2B cannot be generated, while the mass fraction of Ni_2B decreases with increasing boron content in feeding powders in boron rich condition. We can get the high mass fraction of Ni_4B_3 with the initial composition of Ni:B = 1:3. The quenching gas can stop the reaction at certain temperature and phase composition. The synthesis of Ni_2B and Ni_4B_3 need special temperature and composition. Adequate temperature and boron content improve the synthesis of Ni_2B and Ni_4B_3. The synthesis of Ni_2B is the most difficult compared with that of Ni_4B_3 and Ni_3B due to the narrow composition region in phase diagram. The Ni_3B were

generated only in the boron poor condition. In addition, the mass fraction of unreacted boron increases with the increase of boron content in feeding powders because of larger amount boron in feeding powders.

TEM graphs of the prepared nickel boride nanoparticles at powder feed rate of 0.2 g/min with initial composition of Ni:B = 1:1 and 1:3 are shown in **Figure 31** (a) and (b), respectively. The particles with different morphology and size exist. Most particles seem spherical and the average grain size is less than 45 nm. In thermal plasma, the prepared nanoparticles consist mainly of the single crystal. Therefore, the crystalline diameter is almost the same as the grain size of the nanoparticles. The particle diameter distribution is demonstrated for as-prepared product at the fixed powder feed rate of 0.2 g/min with initial composition of Ni:B = 1:1 and 1:3 in **Figure 32** (a) and (b), respectively. The diameter of particles at Ni:B = 1:1 is about 20 nm, while the diameter of particles at Ni:B = 1:3 is about 28 nm. Since the critical diameter of the boron nuclei is the same, the difference of average particle diameter mainly comes from the different growth time and the growth rate of nanoparticles in the nucleation and condensation processes. The growth progress is not finished until the melting point of nickel. There is a long growth time of boron nuclei from the nucleation process of boron monomers to the co-condensation process of nickel and boron monomers with high boron content in feeding powders. Therefore, nickel boride nanoparticles with high boron content in feeding powders have longer time to grow larger.

3) Co-B system

Shown in **Figure 33** are XRD patterns for as-synthesized samples with various cobalt and boron compositions. XRD patterns in fig. 33 (c) and (d) are for the cobalt boride system prepared from a premixed powder of cobalt and boron (Co:B) in molar ratio of 2:1 and 1:1, respectively. The XRD patterns only reveal peaks at 2θ = 44.26°, 51.52°, and 75.92° that are characteristic peaks of the fcc and hcp phases of cobalt [17]. The most intense peak in the diffractogram in fig. 33 (c) and (d) is at 2θ = 44.26°. This peak which is characteristic of crystalline cobalt might indicate that there is a large amount of unreacted boron. One reason for this observation is the relative difficultly for boron to be evaporated in thermal plasma due to its higher boiling point of 4200 K than cobalt (3200 K). Moreover, boron content in feeding powders is not sufficient to synthesize cobalt boride nanoparticles in boron poor condition. XRD patterns for Co:B = 2:1 and 1:1 suggests that cobalt boride nanoparticles are not

synthesized in boron poor condition.

CoB and Co_2B crystalline phases are identified from XRD spectra peaks from Co:B ratio of 1:2 and 1:3 as shown in fig. 33 (a) and (b). The difference in the saturation vapor pressure which is directly related with the nucleation temperature is an important factor for the controlled preparation of boride nanoparticles in RF thermal plasma. Since the nucleation temperature of cobalt is notably lower than the melting point of boron, the solidification of boron nuclei occur before the nucleation of cobalt. It is impossible of boron nuclei in solid state to generate cobalt boride, because the cobalt vapor cannot condensate on the surface of boron nuclei and not well-mixed. Then the cobalt vapor starts to nucleate and generate cobalt nanoparticles in dependent to cobalt boride and boron nanoparticles.

The calculation of Gibbs free energy for the preparation of cobalt boride nanoparticles is important in order to account the formation of CoB and Co_2B in the final product. Fig. 4 shows Gibbs free energy of CoB and Co_2B. Gibbs free energies for CoB and Co_2B are both negative, indicating that cobalt boride nanoparticles are thermodynamically stable phase and can be easily synthesized. In boron poor conditions (*i.e.* Co:B = 2:1 and 1:1), however, the number of boron vapor is not enough to synthesize cobalt boride nanoparticles due to its high boiling point. In addition, the large difference of saturation vapor pressure between cobalt and boron hinders the formation of cobalt boride nanoparticles. Therefore, XRD data in suggests that cobalt boride nanoparticles can be synthesized at higher boron contents in feeding powders.

Comparison between the crystalline diameters of product in Ti-B, Fe-B, Ni-B and Co-B systems is demonstrated in **Figure 34**. The particle in Co-B system has the smallest size, while nickel boride has the largest size among four systems. The growth process including nucleation and co-condensation does not stop until the melting point of metal. The temperature range from the boron nucleation temperature to nickel melting point in Ni-B system is widest, indicating nickel boride has the longest time to grow in plasma. As a result, the particles in Ni-B system provide the largest diameter. In addition, surface tension is an important factor for the control of particle size. It is demonstrated that large surface tension leads to large particle diameter. Nickel surface tension of 2.1 N/m is higher than iron surface tension of 1.92 N/m and titanium surface tension of 1.39 N/m, while the surface tension of cobalt is 1.29 N/m. As shown in fig. 4, iron boride has wider temperature range than these of titanium boride and cobalt boride, and the surface tension of iron is higher compared with titanium and cobalt. So particles in Fe-B system have larger diameter. For particles in Ti-B and Co-B systems, the particles in Ti-B system is a

little larger than particles in Co-B system. The growth time of particle in Co-B system is longer than that of particles in Ti-B system; while the surface tension of titanium is higher than that of cobalt. Therefore, it is concluded that the influence of surface tension in the control of particle diameter is more important than the growth in the temperature range between the melting point of metal and metal. In other words, the growth process of condensation in the in the temperature range between the melting point of metal and metal is not very important.

Figure 35 shows the effect of powder feed rate on the composition of product in Ti-B, Co-B, Fe-B and Ni-B systems. Due to the same formation mechanism of boride nanoparticle, the results have the same tendency that the mass fraction of boride in product decreases with increasing powder feed rate except in Co-B system. One possible reason is the full evaporation of raw materials in Co-B system due to the low melting point and small loading effect. At high powder feed rate, the evaporation time and region of boron and metal do not extend and exist in the same region. As a result, more boron and metal can react with each at high powder feed rate.

3.5 Nucleation temperature

The nucleation temperature at the critical saturation ratio is presented in **Figure 36**; fig. 36 (a) was drawn at the boron molar content of 66.7% with different powder feed rate, and fig. 36 (b) was calculated at the fixed powder feed rate of 0.2 g/min with different initial composition of Me:B. The nucleation temperatures of iron group metals are lower than that of boron, indicating boron vapor firstly nucleates. And then the co-condensation of metal and boron vapors takes places on the surface of boron nuclei. The temperature region between the nucleation temperature and melting point of boron is wide, means many boron nuclei are on molten state. In addition, the temperature region between the nucleation temperature of metal and the melting point of boron in Fe-B system is the widest in Fe-B, Co-B and Ni-B system. The iron boride nanoparticles is the most difficult to generate by RF thermal plasma. The estimation method of nucleation temperature is explained in detail in Ch. 6.

3.6 Conclusions

Experiments were performed to investigate the nucleation and condensation of mixture of iron group metals (Fe, Ni and Co) with boron in RF thermal plasma for the preparation of iron group metals boride nanoparticles. The study concluded that RF thermal plasmas were notably effective even for the difficult co-condensation processes with the large vapor pressure

differences.

In this research, iron group metals (Fe, Ni and Co) boride nanoparticles can be synthesized by RF thermal plasma. The experimental parameters of the powder feed rate and boron content in the feeding powders played an important role in generating the iron group metals (Fe, Ni and Co) based boride nanoparticles. The crystalline diameter of as-prepared particles increases with the powder feed rate in Fe-B, Ni-B and Co-B systems. The cobalt boride nanoparticles have the smallest diameter due to lowest surface tension, and nickel boride nanoparticles have the largest size because of highest surface tension. The mass fraction of FeB in the product decreases with the increase of powder feed rate in Fe-B system, and the effect of powder feed rate on the mass fraction of Ni_3B has the same tendency. While the mass fraction of cobalt based boride nanoparticles increases with increasing powder feed rate. When a larger amount of boron is included in the feed powders, nanoparticles provide a smaller diameter and the mass fraction of nickel based boride increases in the product. Based on TEM graphs, the particles in Fe-B, Ni-B and Co-B systems are all almost spherical and have core-shell structure. The composition of the shell depends on the boron content in feeding powders. Quenching gas can improve the synthesis of Ni_2B nanoparticles with catalytic activity.

Therefore, induction thermal plasmas provide a powerful tool for the preparation of functional nanoparticles. The precise control of the particle size and stoichiometric compositions is possible through adjusting the experimental parameters.

References

[1] R.M. Minyaev and R. Hoffmann, Chemistry of Materials, 3, 547 (1991)

[2] T. Venkateswaran, B. Basu, G.B. Raju and D.Y. Kim, Journal of the European Ceramic Society, 26, 2431 (2006)

[3] S. Rades, A. Kornowski, H. Weller and B. Albert, Chemical Physics and Physical Chemistry, 12, 1756 (2011)

[4] J.C. Ingersoll, N. Mani, J.C. Thenmozhiyal and A. Muthaiah, Journal of Power Sources, 173, 450 (2007)

[5] P. Krishnan, S.G. Advani and A.K. Prasad, International Journal of Hydrogen Energy, 33, 7095 (2008)

[6] C. Wu, F. Wu, Y. Bai, B. Yi and H. Zhang, Materials Letters, 59, 1748 (2005)

[7] S. Li, X. Yang , H. Zhu , Y. Chen and Y. Liu, Journal of Power Sources, 196, 5858 (2011)

[8] D. Mu, C. Yang, B.L. Shen and H. Jiang, Journal of Alloys and Compounds, 479, 629 (2009)

[9] A. Trueman, D. Schweinsberg and G. Hope, Corrosion Science, 41, 1377 (1999)

[10] C. Petit, A. Taleb and M.P. Pileni, Journal of Physics Chemistry B, 103, 1805 (1999)

[11] T. Kanomata, Y. Ise, N. Kumagai, A. Haga, K. Kamishima, T. Goto, H.M. Kimura, H. Yoshida, T. Kaneko and A. Inoue, Journal of Alloys and Compounds, 259, L1 (1997)

[12] P. Schwarzkopf, R. Kieffer, W. Leszynski and F. Benesovsky, Refractory Hard Metals: Borides, Carbides, Nitrides, and Silicides, The Macmillan Company, New York, 1953

[13] B. Ganem and J.O. Osby, Chemical Reviews, 86, 763 (1986)

[14] H.C. Brown and C.A. Brown, Journal of American Chemical Society, 85, 1005 (1963)

[15] Z.J. Wu, W. Li, M.H. Zhang and K.Y. Tao, Frontiers of Chemical Engineering in China, 1, 87 (2007)

[16] E.Z. Min and C.Y. Li (Eds.), Base of Science and Engineering of Green Petrochemical Technology, Chinese Petrochem Press, Beijing, 2002

[17] Y. Okamoto, Y. Nitto and T. Imanaka, Journal of Chemical Society, Faraday, 75, 2027 (1979)

[18] R. Fruchart, Annadi di Chimica, 4, 1247 (1959)

[19] D.B. DeYoung and R. G. Barnes, Journal of Chemical Physics, 62, 1726 (1975)

[20] T. Kanaizuka, Physica Status Solidi A, 69, 739 (1982)

[21] V.A. Tsurin, Y.E. Turkhan, V.A. Kazantsev, V.V. Fedorenko, S.I. Novikov, V.A. Barinov, V.T. Surikov and G.A. Dorofeev, The Physics Metals and Metallography, 96, 36 (2003)

[22] C. Fetzer, L. Grnsy, T. Kemny, E. Ktai, M. Tegze, I. Vincze, W. Hoving and F. Woude, Physical Review B, 42, 548 (1990)

[23] V.A. Barinov, G.A. Dorofeev, L.V. Ovechkin, E.P. Elsukov and A.E. Ermakov, Physica Status Solidi A, 123, 527 (1991)

[24] G.A. Dorofeev, L.V. Ovechkin, E.P. Elsukov, V.A. Barinov, The Physics Metals and

Metallography, 76, 107 (1993)

[25] E.P. Yelsukov, G.A. Dorofeev and V. A. Barinov, Czechoslovak Journal of Physics, 47, 499 (1997)

[26] K. Fukamichi, M. Kikuchi, S. Arakawa, T. Masumoto, Solid State Communications, 23, 955 (1977)

[27] R. Ray, R. Hasegawa, C.P. Chou and L.A. Davis, Scr Metall Mater, 11, 973 (1977)

[28] S. Ohnuma, Y. Nakanouchi, C.D. Graham and T. Masumoto, IEEE Transactions on Magnetics, 21, 2038 (1985)

[29] H. Schlesinger, H.C. Brown, A.E. Finholt, J.R. Gilbreath, H.R. Hoekstra and E.K. Hyde, Journal of American Chemical Society, 75, 215 (1953)

[30] S. Linderoth and S. Morup, Journal of Applied Physics, 69, 5256 (1991)

[31] E. Lugowska and I.D. Brindle, Analyst, 122, 1559 (1997)

[32] C. Kapfenberger, K. Hofmann and B. Albert, Solid State Science, 5, 925 (2003)

[33] G.N. Glavee, K.J. Klabunde, C.M. Sorensen and G.C. Hadjipanayis, Inorganic Chemistry, 34, 2 (1995)

[34] D. Vollath, Kona, 25, 39 (2007) www.nanoconsulting.de.

[35] H.I. Schlesinger and H.C. Brown, Journal of American Chemical Society, 75, 215 (1953)

[36] Watanabe, T. Ibe, Y. Abe, Y. Ishii, K.Adachi, Transactions of the Materials research Society of Japan, 29, 3407 (2004)

[37] M. Shigeta and T. Watanabe, Thin Solid Films, 515, 4217 (2007)

[38] Y.Y. Cheng and T. Watanabe, Journal of Chemical Engineering of Japan, 44, 583 (2011)

[39] Y.Y. Cheng, M. Shigeta, S. Choi and T. Watanabe, Chemical Engineering Journal, 183, 483 (2012)

[40] S.L. Girshick, C.P. Chiu and P.H. Mc McMurry, Aerosol Science Technology, 13, 465 (1990)

[41] R.J.M. Blocherj and I.E. Campbell, Battelle Memorial Institute, 71, 4040 (1949)

[42] K. Velmurugana, V.S.K. Venkatachalapathyb and S. Sendhilnathanc, Materials research, 12,

529 (2009)

[43] V.V. Matveev, D.A. Baranov, G.Y. Yurkov, N.G. Akatiev, I.P. Dotsenko and S.P. Gubin, Chemical Physics Letters, 422, 402 (2006)

[44] Y. Bao, M. Beerman and K.M. Krishnan, Journal of Magnetism Magnetic Materials, 266, L245 (2003)

[45] V. Salgueirino-Maceira, M.A. Correa-Duarte, M. Farle, M. A. Lopez-Quintela, K. Sieradzki and R. Diaz, Langmuir 22, 1455 (2006)

[46] B.D. Cullity, Elements of X-ray Diffraction, 2nd ed., (Addison-Wesley, New York, 1978) 101

[47] X. Xie, M. Yuan and F.X Wang, Science China Technological Sciences, 54, 75 (2011)

[48] M. Shigeta, T. Watanabe and H. Nishiyama, Thin Solid Films, 457, 192 (2004)

[49] M. Shigeta and T. Watanabe, Journal of Materials Research, 20, 2801 (2005)

Table 1 Experimental operating condition for the preparation of metal boride nanoparticles

Process parameter	Value
Sheath gas and flow rate	Ar-He(60:5) 65 L/min
Inner gas and flow rate	Ar 5 L/min
Carrier gas and flow rate	Ar 3 L/min
Plasma power plate	30.0 kW
Reactor pressure	101.3 kPa
Frequency	4 MHz
Quenching gas flow rate	10, 20 L/min
Quenching distance	18 cm
Feed rate	0.1 ~ 1.0 g/min
Boron molar content in feeding powder	25 ~ 90 %

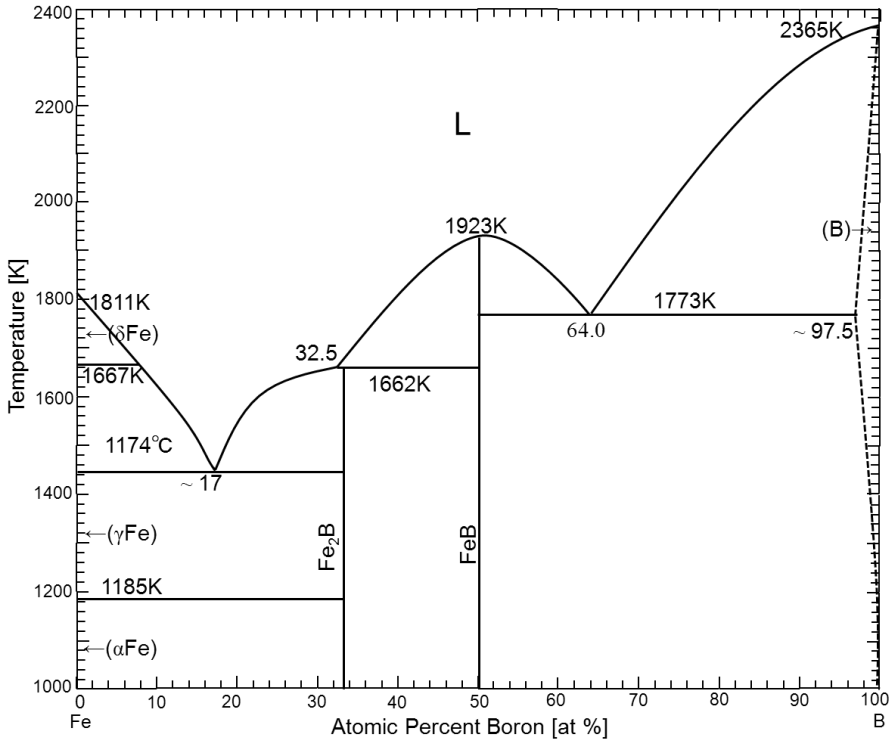

Fig. 1 Binary Fe–B phase diagram.

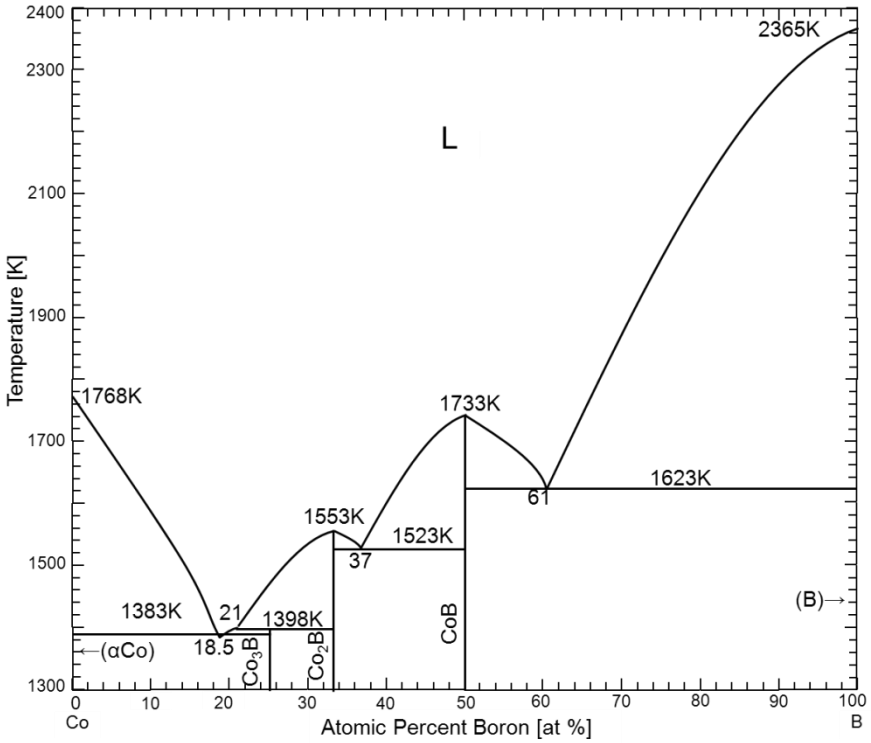

Fig. 2 Binary Co–B phase diagram.

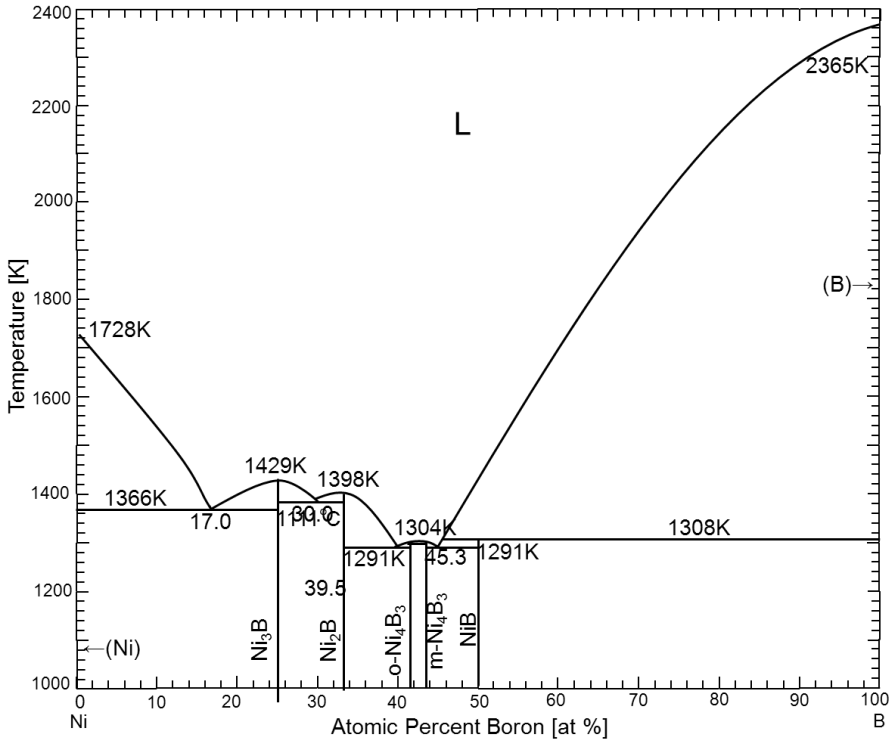

Fig. 3 Binary Ni–B phase diagram.

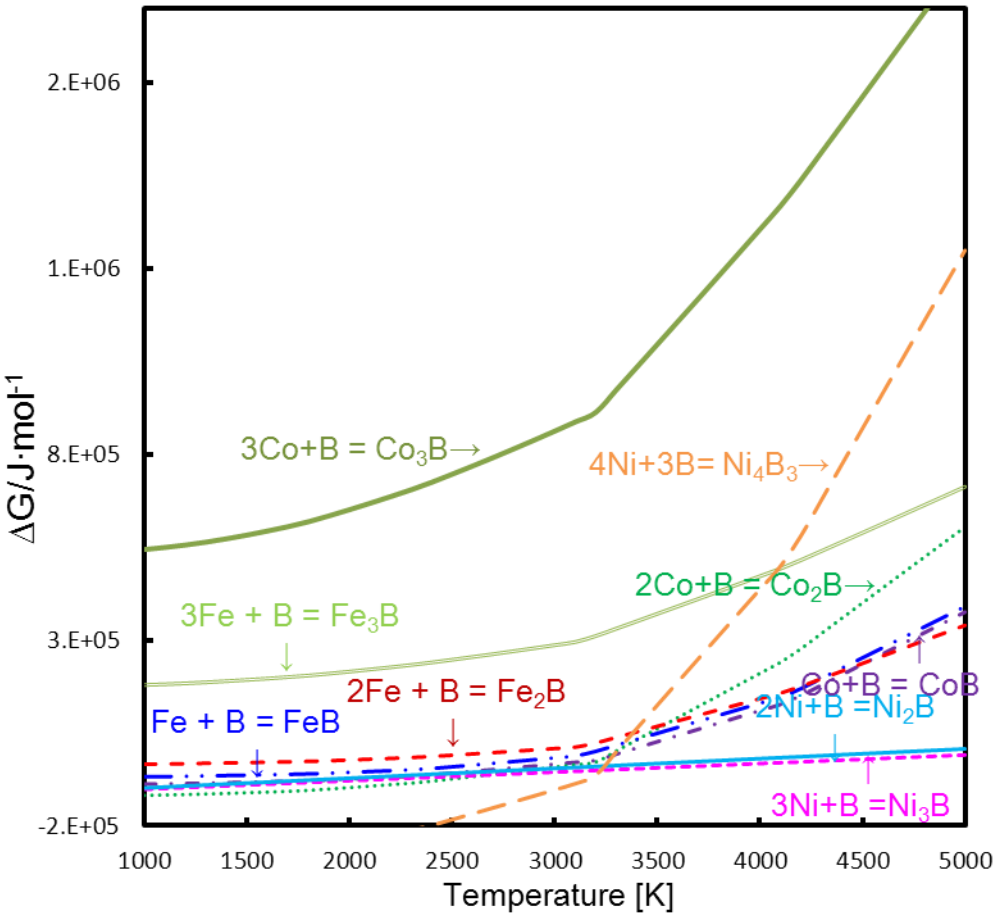

Fig.4 Gibbs free energy of Fe-B, Co-B and Ni-B systems.

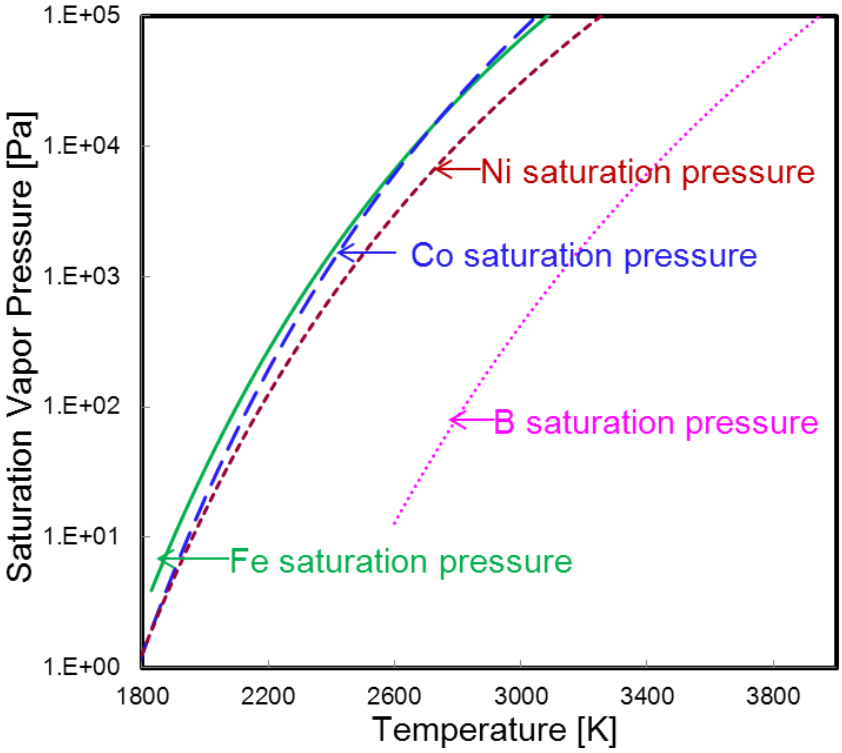

Fig. 5 Saturation vapor pressure of Fe, Co, Ni and B.

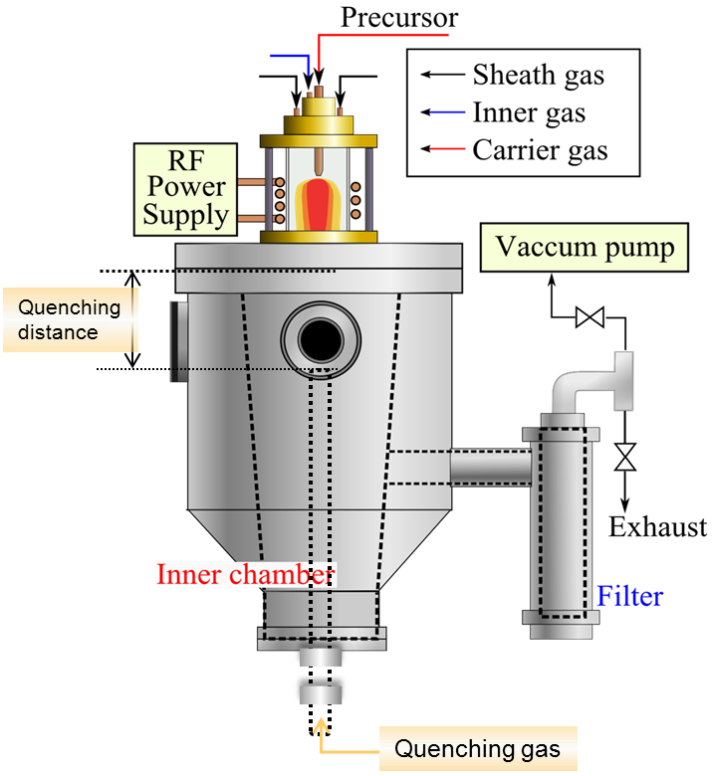

Fig. 6 RF thermal plasma reactor for the preparation of boride nanoparticles with quenching system.

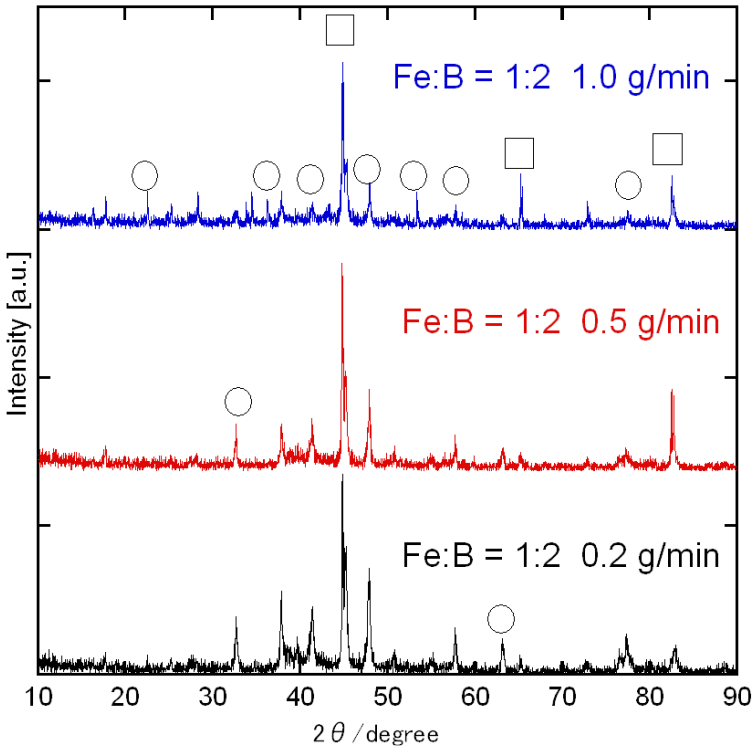

Fig. 7 XRD patterns of product with different powder feed rate at fixed initial composition of Fe:B = 1:2.
(○: FeB □: Fe)

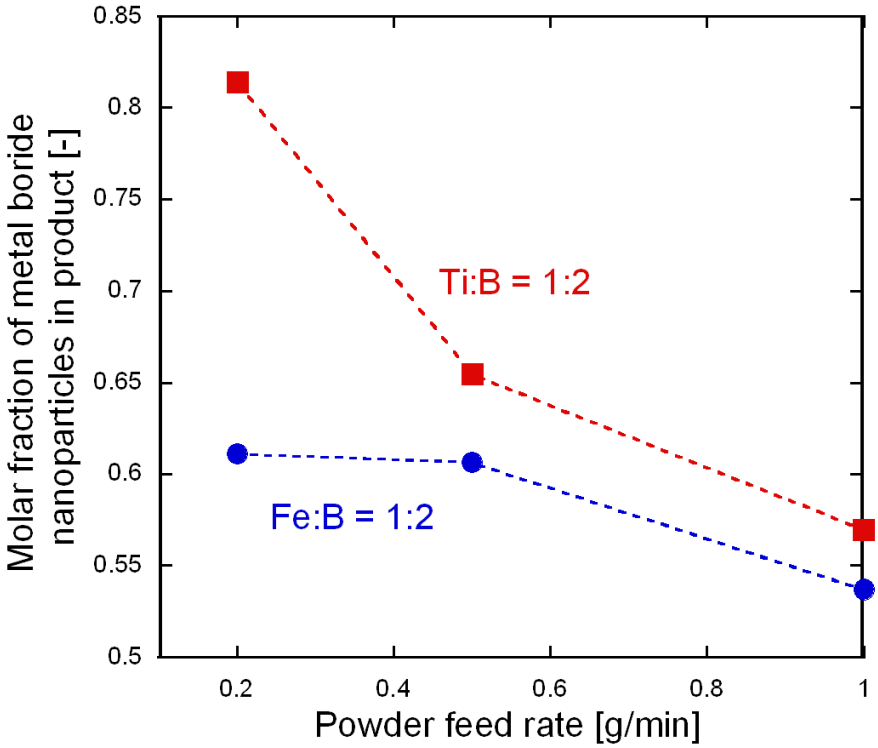

Fig. 8 Effect of powder feed rate on the phase composition of product at the fixed initial composition of Me:B = 1:2.

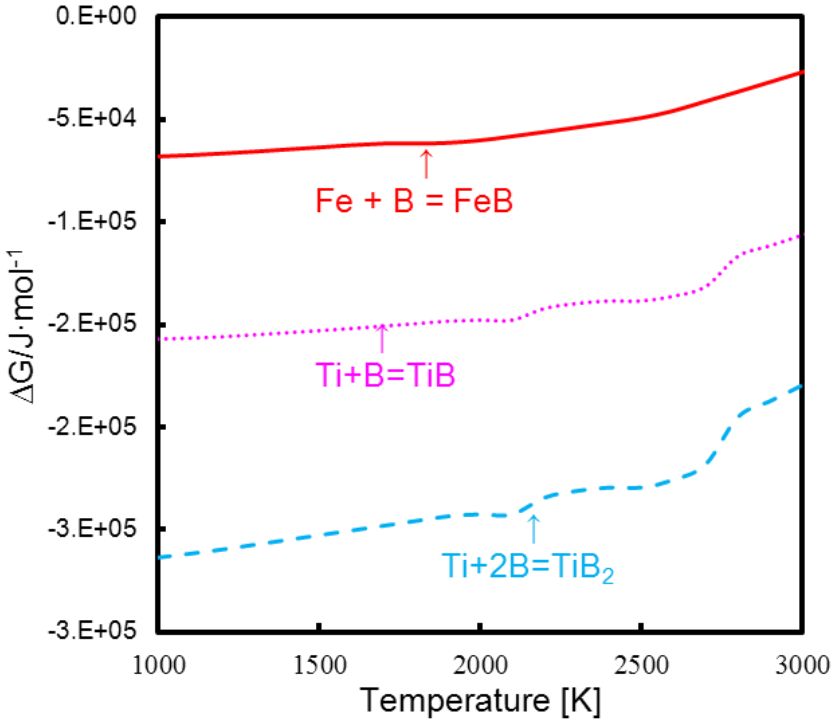

Fig.9 Gibbs free energy of generating FeB, TiB and TiB_2.

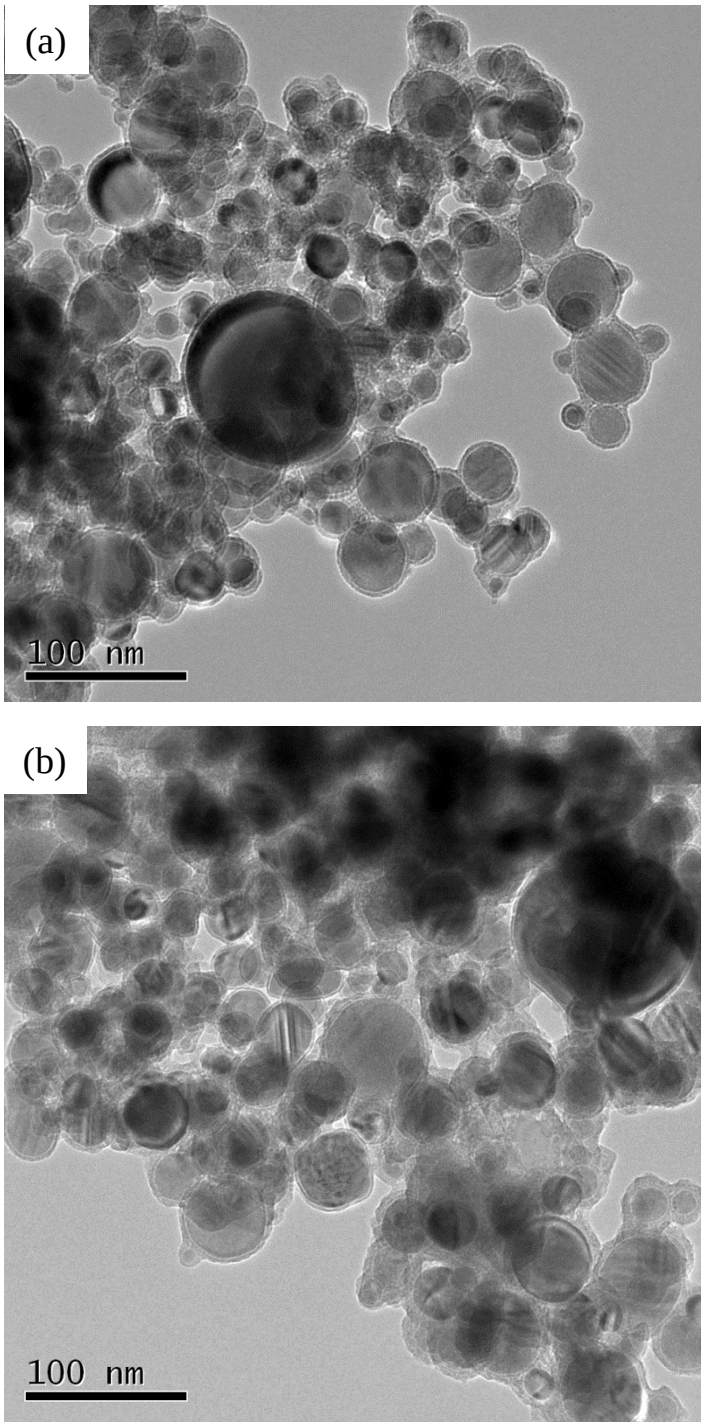

Fig. 10 TEM graphs of as-prepared product at the fixed initial composition of Fe:B = 1:2 with different powder feed rate: (a) 0.2 g/min; (b) 0.5 g/min.

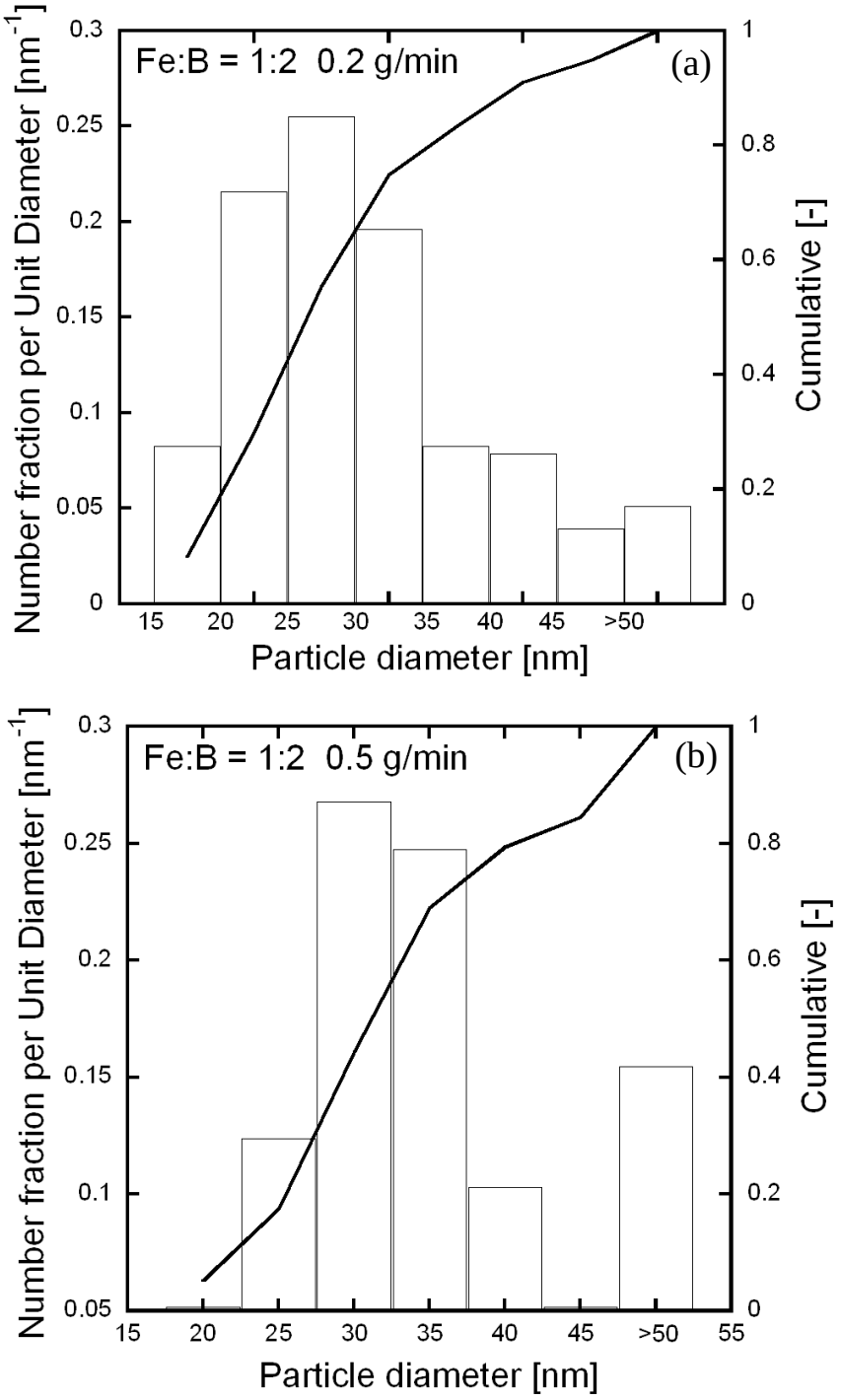

Fig. 11 Particle size distribution of as-prepared product at the fixed initial composition of Fe:B = 1:2 with different powder feed rate: (a) 0.2 g/min; (b) 0.5 g/min.

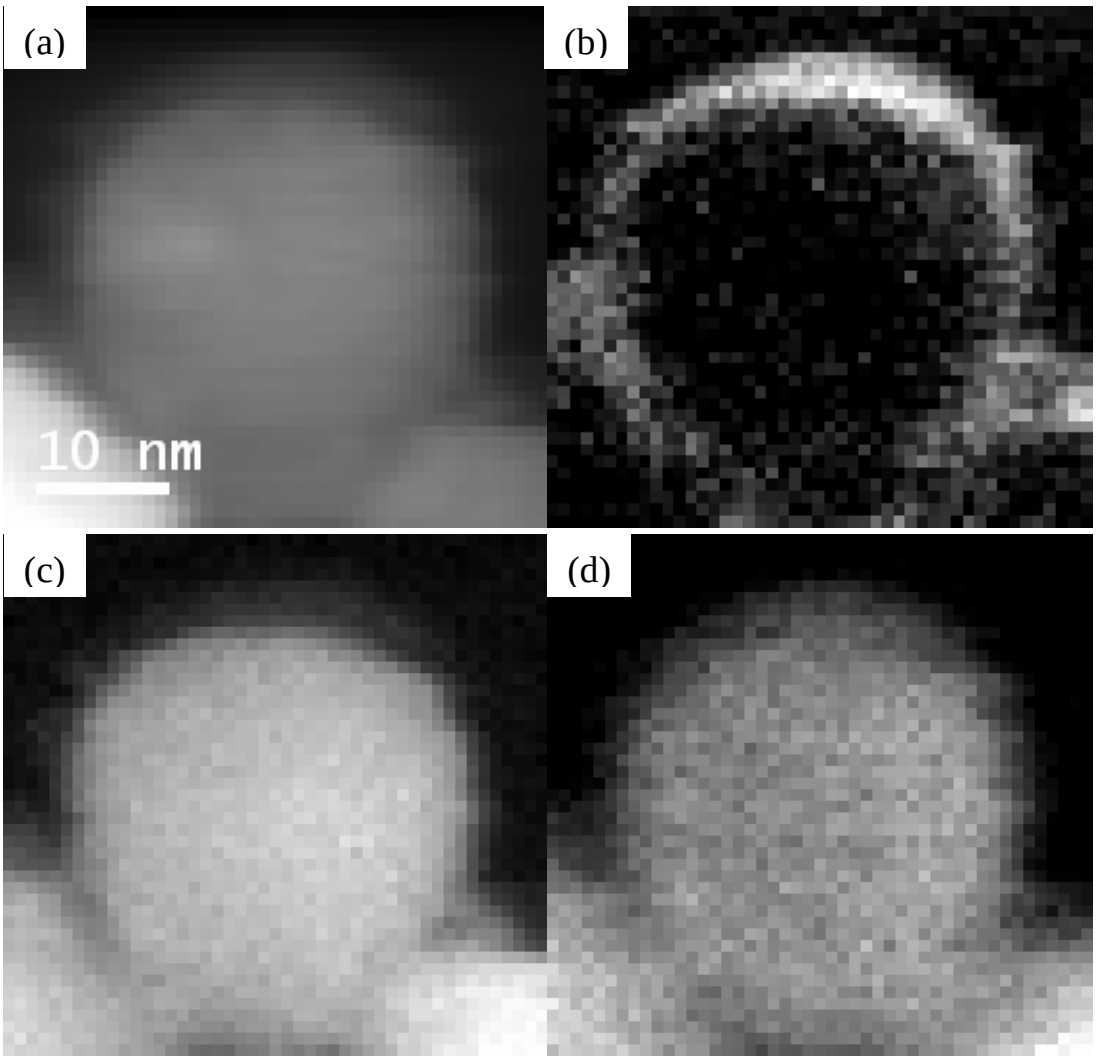

Fig. 12 SETM-EELS images of particles at fixed initial composition of Fe:B = 1:2 at powder feed rate of 0.2 g/min: (a): TEM image of a particle prepared for long time; (b)-(d): EELS maps of element of O, Fe, and B, respectively.

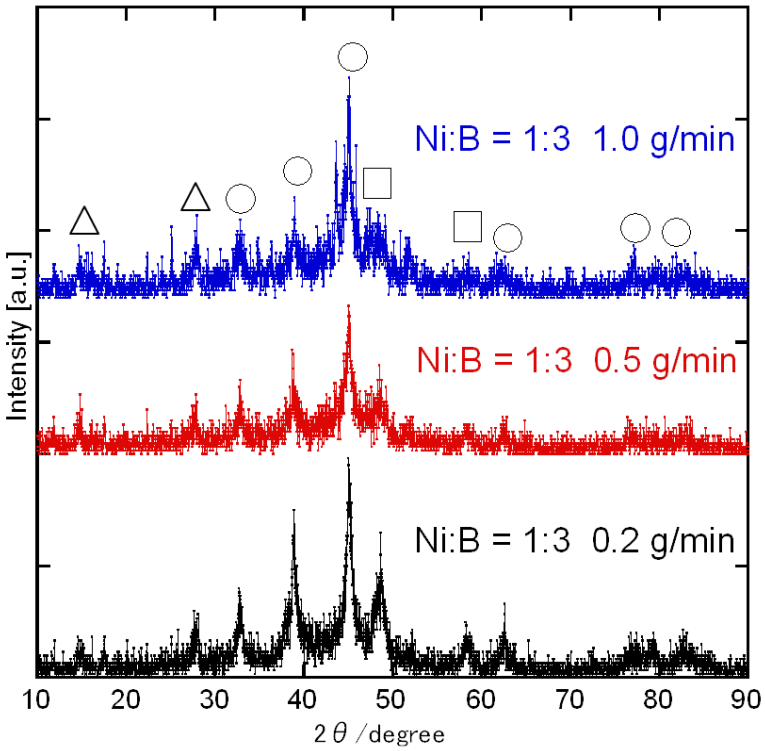

Fig. 13 XRD patterns of product with different powder feed rate at constant initial composition of Ni:B = 1:3.
(○: NiB □: Ni_3B △: Ni_4B_3)

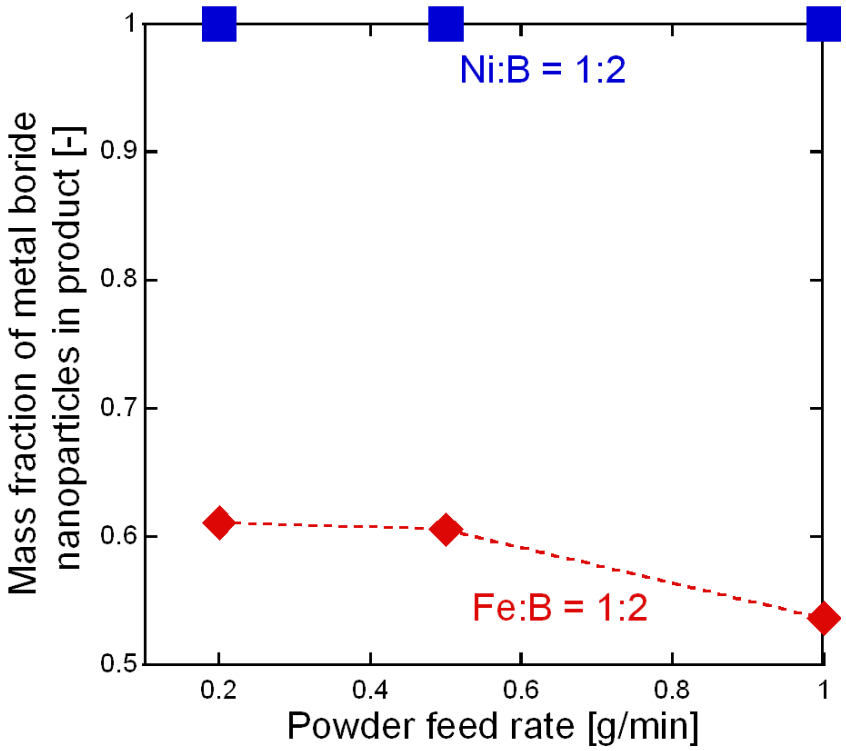

Fig. 14 Effect of powder feed rate on the phase composition of product at the fixed initial composition of Me:B = 1:2 in Ni-B and Fe-B systems.

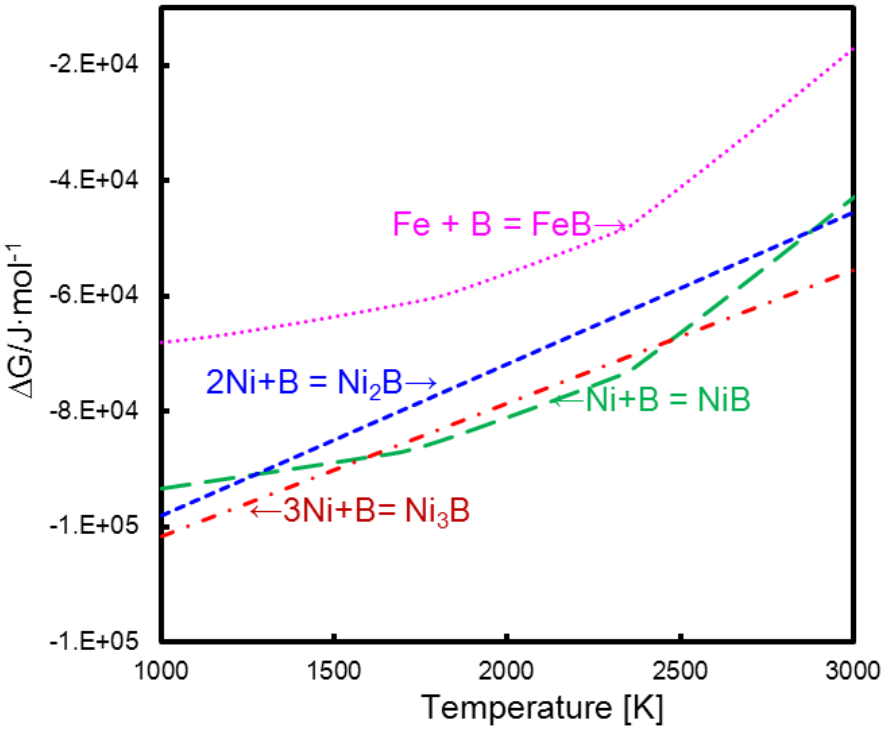

Fig. 15 Gibbs free energy of generating FeB, NiB, Ni_2B and Ni_3B.

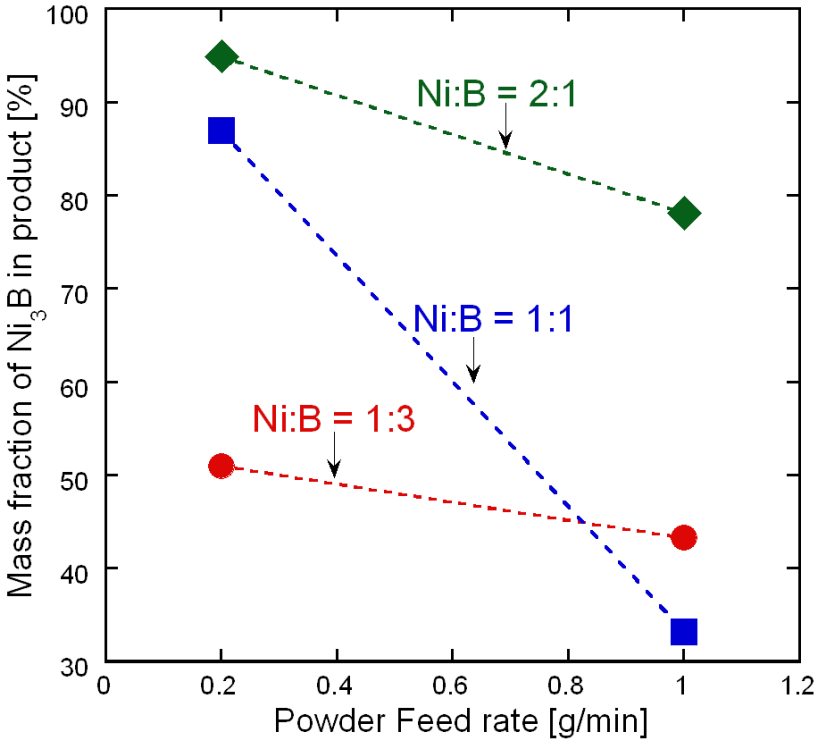

Fig. 16 Effect of powder feed rate on phase composition of product at different initial composition of Ni:B.

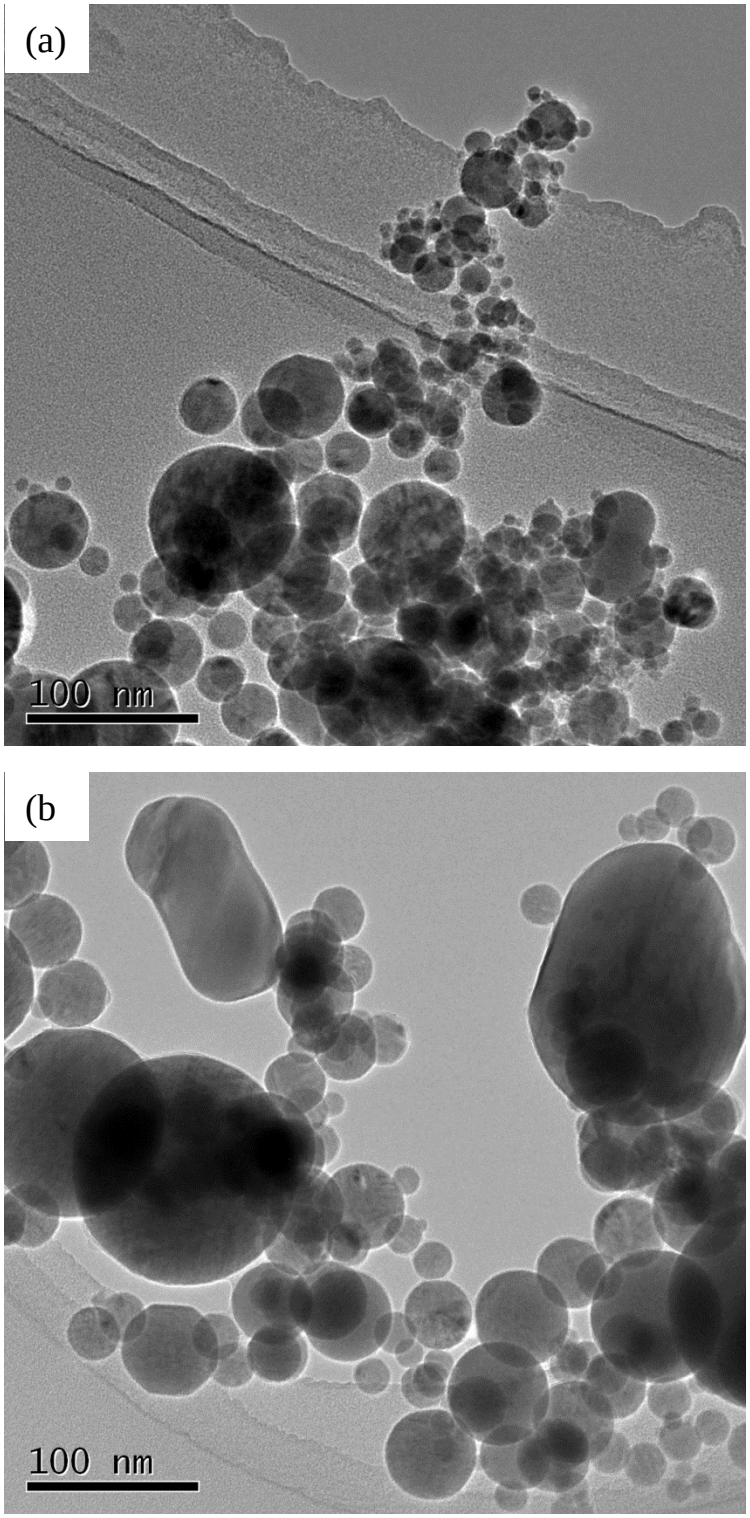

Fig. 17 TEM graphs of as-prepared product at the fixed initial composition of Ni:B = 1:3 with different powder feed rate: (a) 0.2 g/min; (b) 1.0 g/min.

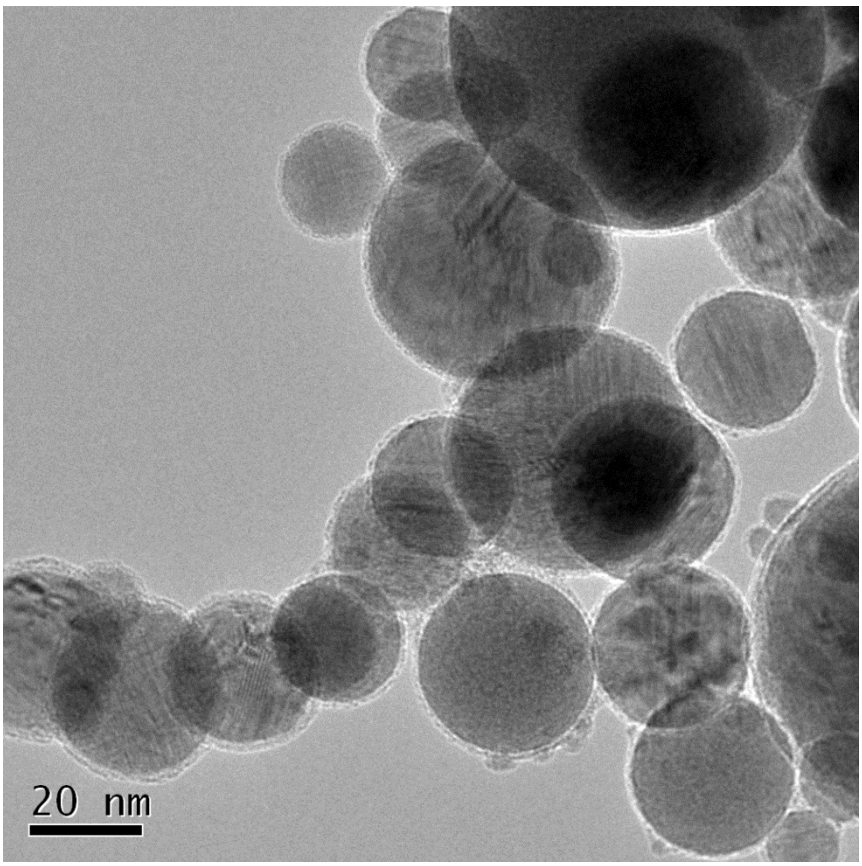

Fig. 18 TEM graph with high magnification of as-prepared product at the fixed initial composition of Ni:B = 1:3 with powder feed rate 0.2 g/min.

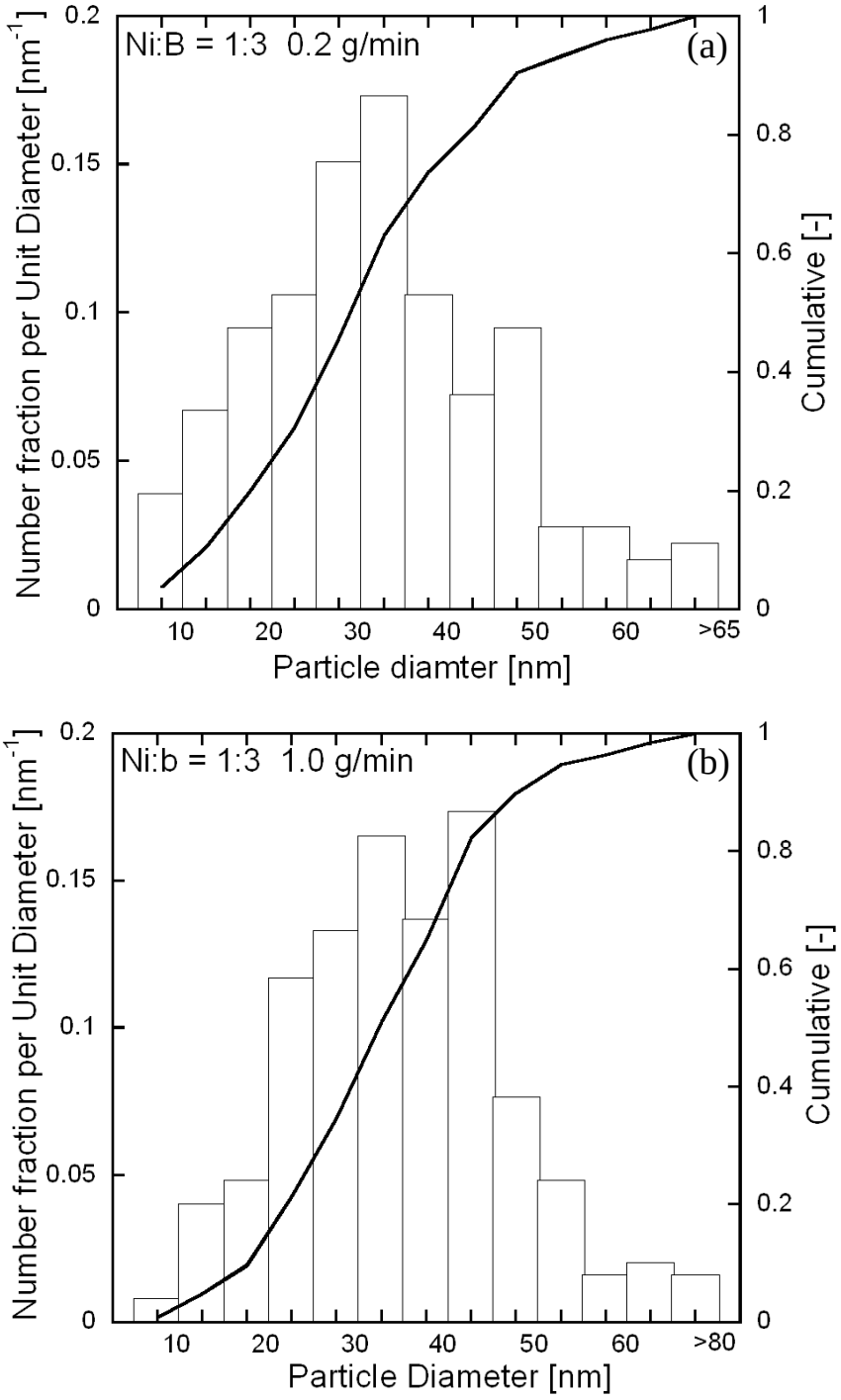

Fig. 19 Particle size distribution of as-prepared product at the fixed initial composition of Ni:B = 1:3 with different powder feed rate: (a) 0.2 g/min; (b) 1.0 g/min.

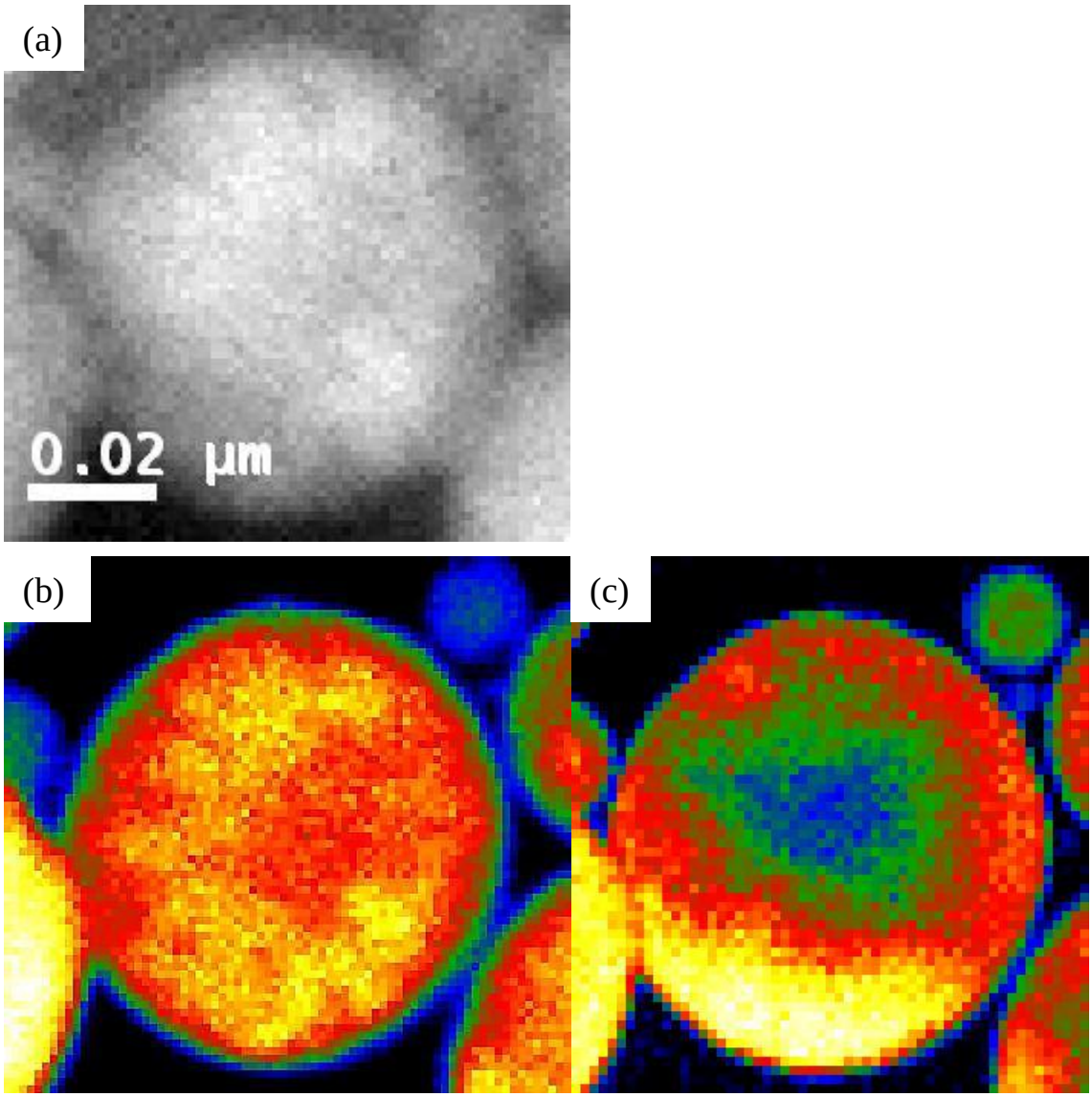

Fig. 20 SETM-EELS images of particles at fixed initial composition of Ni:B = 1:3 at powder feed rate of 0.2 g/min: (a): STEM image of a particle prepared for long time;
(b)-(c): EELS maps of element of B and Ni, respectively.

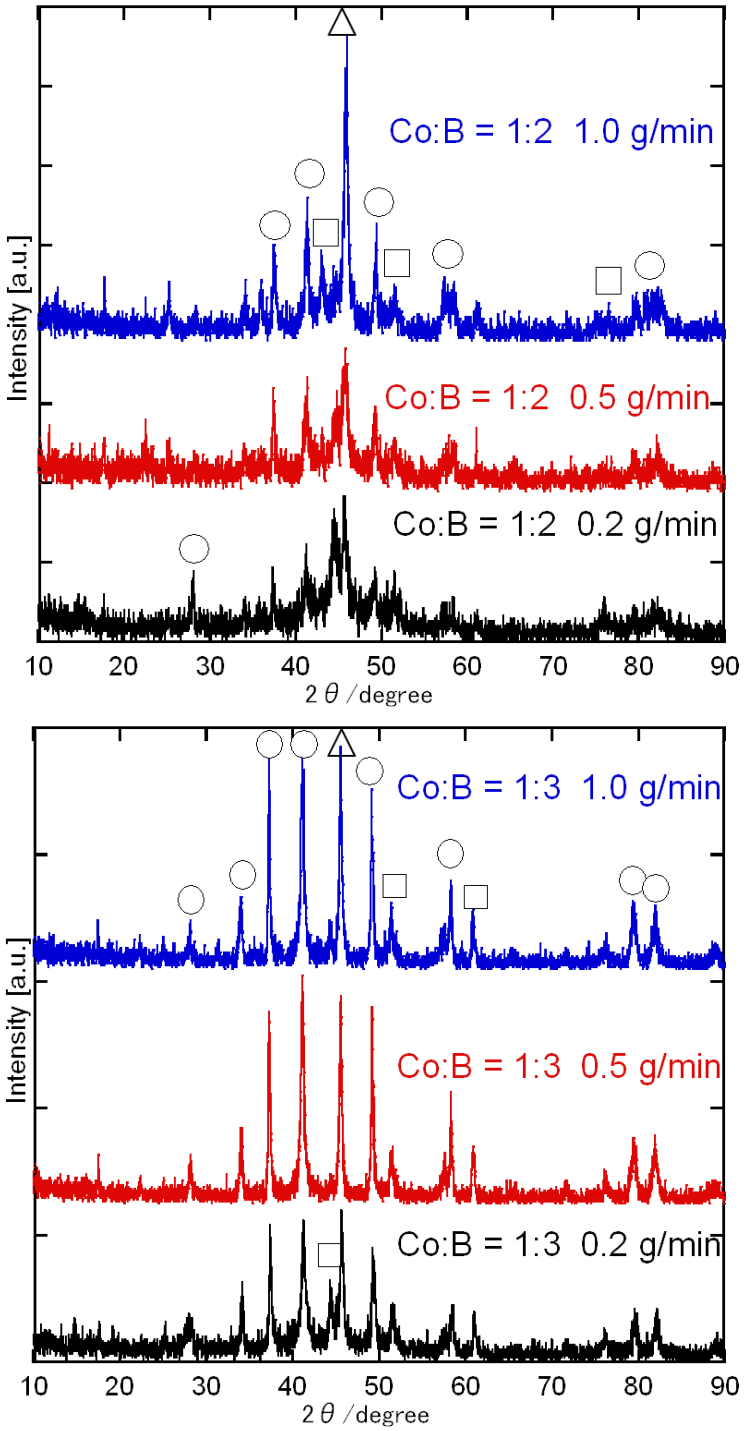

Fig. 21 XRD patterns of cobalt boride nanoparticles prepared with different boron content in feeding powders and powder feed rate.
(○: CoB □: Co △: Co_2B)

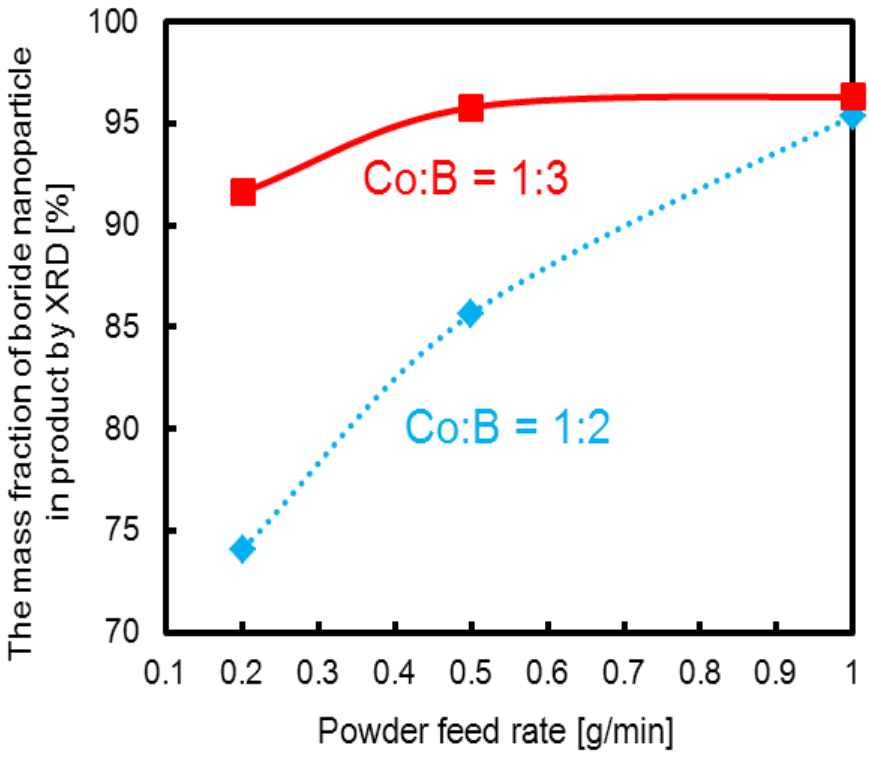

Fig. 22 Effect of powder feed rate on the phase composition of as-prepared nanoparticles.

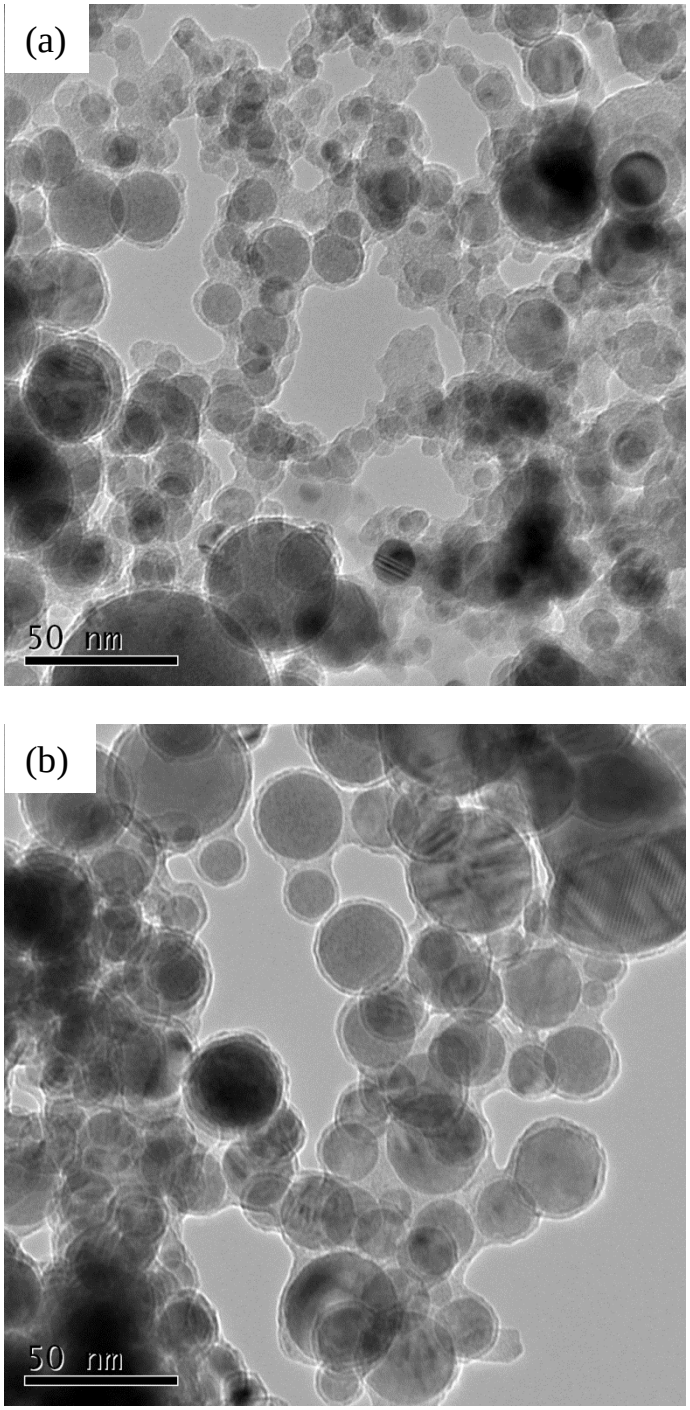

Fig. 23 TEM graphs of as-prepared product at the fixed initial composition of Co:B = 1:2 with different powder feed rate: (a) 0.2 g/min; (b) 0.5 g/min.

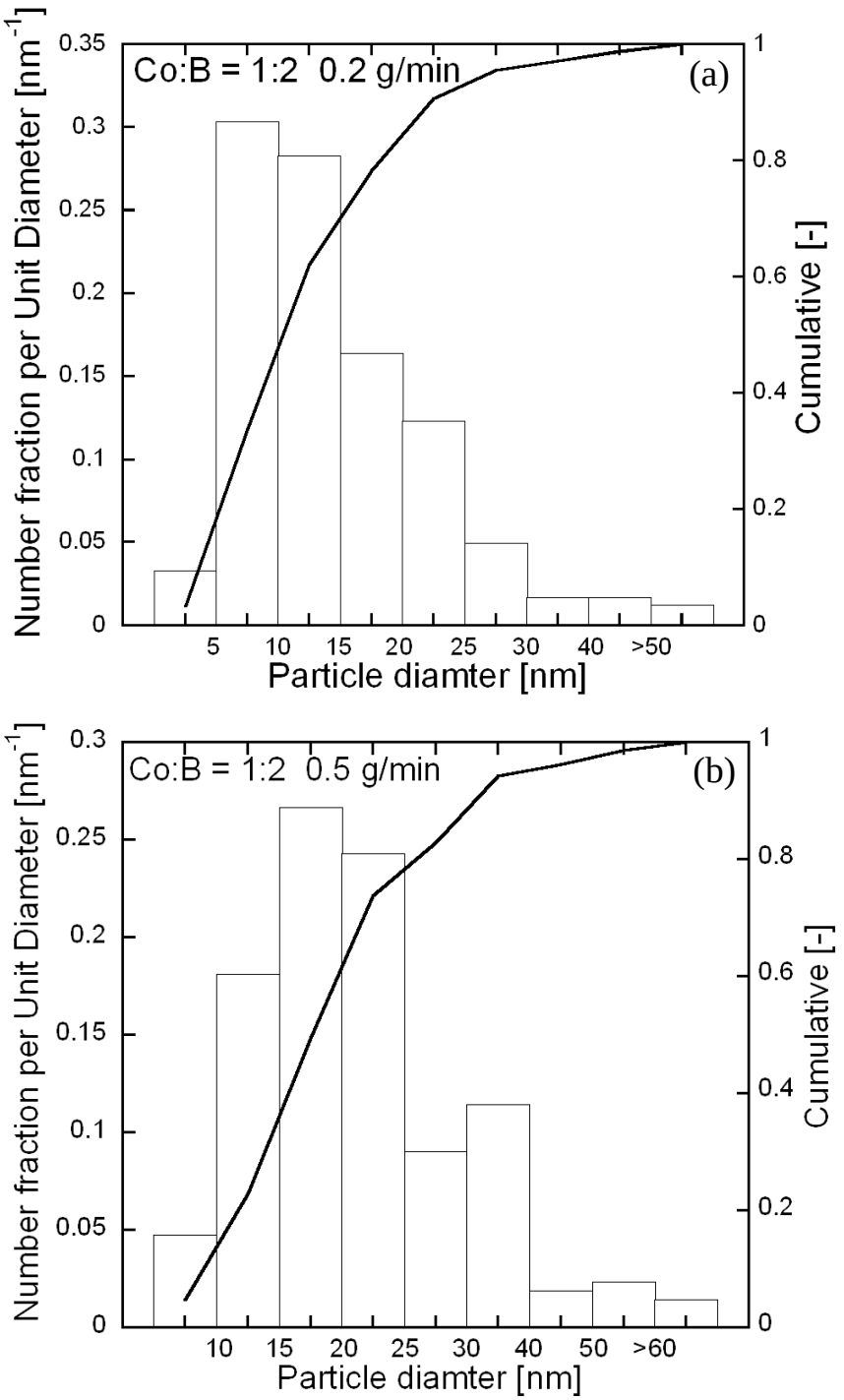

Fig. 24 Particle size distribution of as-prepared product at the fixed initial composition of Co:B = 1:2 with different powder feed rate: (a) 0.2 g/min; (b) 0.5 g/min.

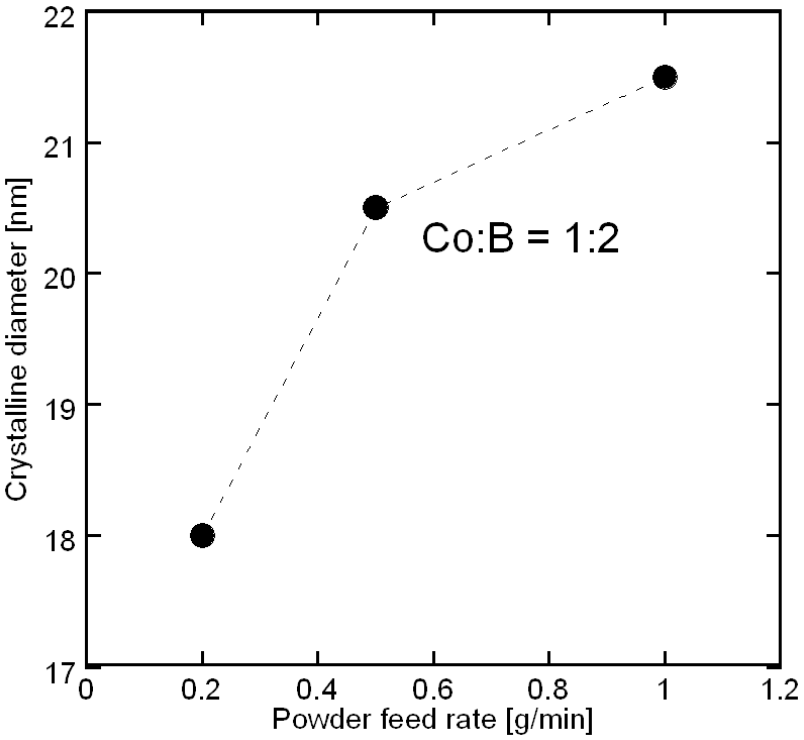

Fig. 25 Effect of powder feed rate on the crystalline diameter of as-prepared nanoparticles in the experiment.

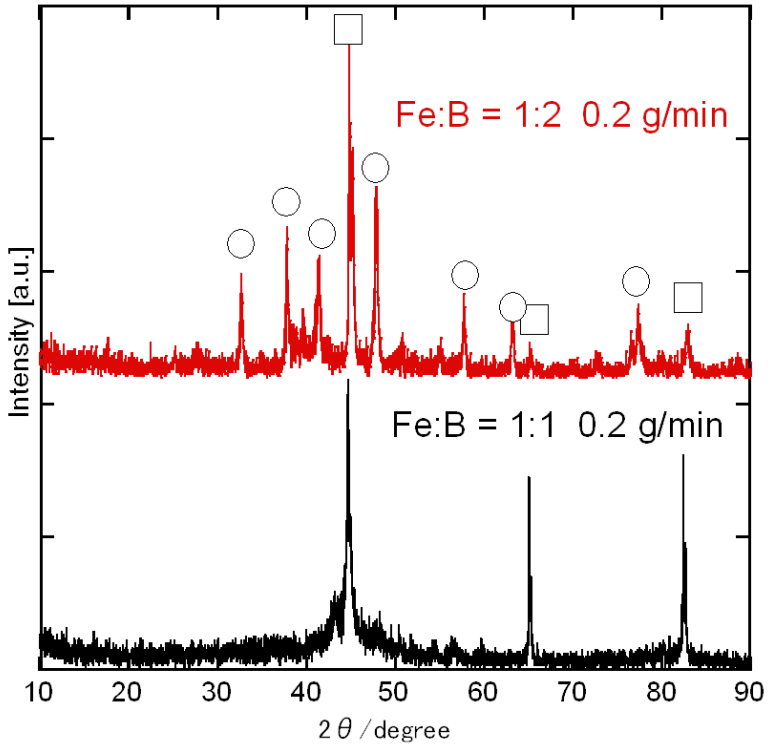

Fig. 26 XRD patterns of product with different initial composition of Fe:B at constant powder feed rate 0.2 g/min.
(○: FeB □: Fe)

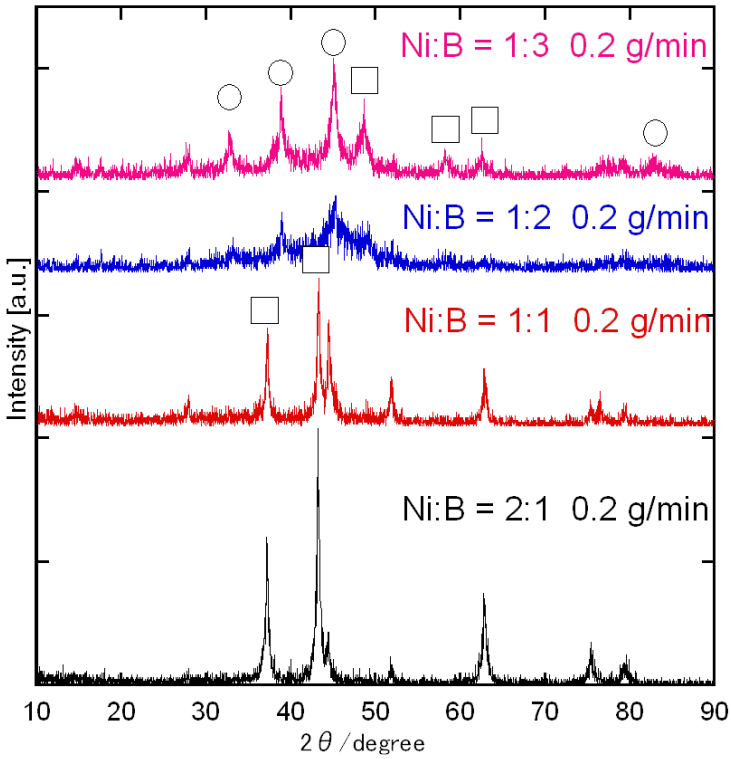

Fig. 27 XRD spectra of product prepared with different initial composition of Ni;B at constant powder feed rate 0.2 g/min.
(○: NiB □: Ni_3B △: Ni_4B_3 ◇: Ni)

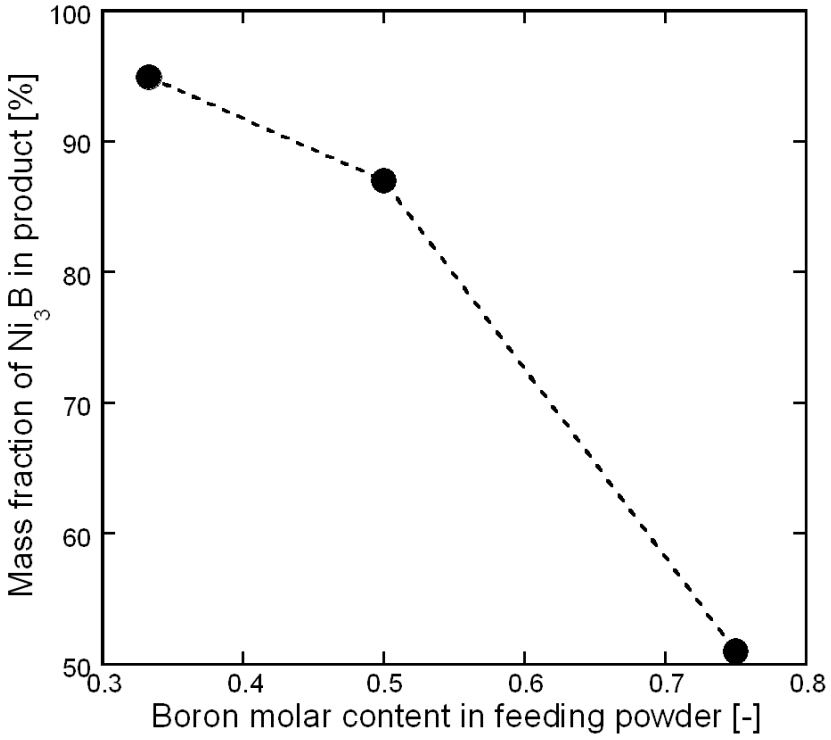

Fig. 28 Effect of boron molar content in feeding powders on the phase composition of product at constant powder feed rate 0.2 g/min.

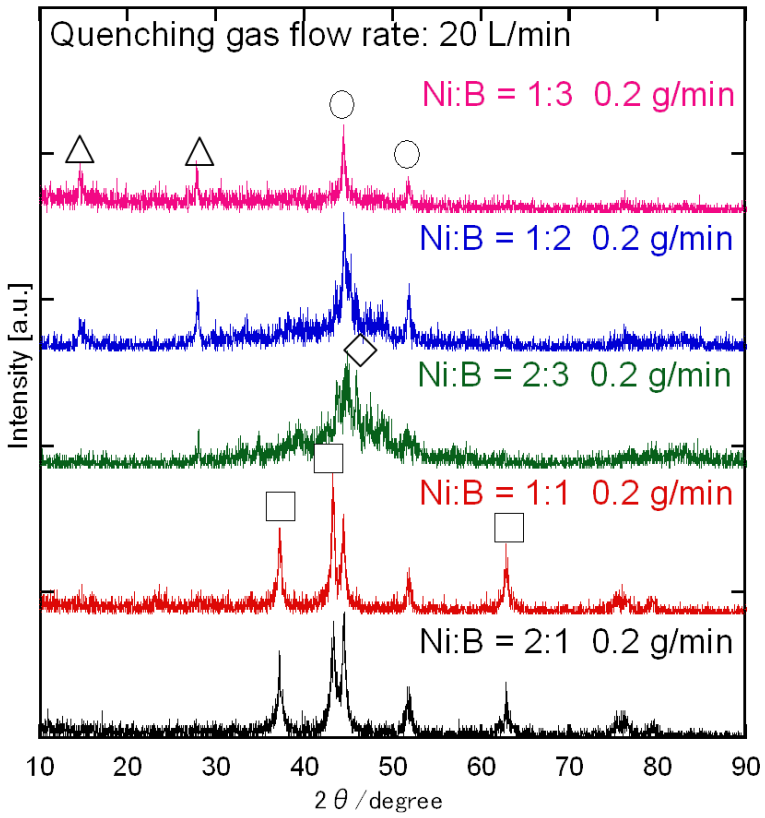

Fig. 29 XRD spectra of product prepared with different initial composition of Ni;B at constant powder feed rate 0.2 g/min with quenching gas flow rate of 20 L/min. (○: Ni □: Ni_3B △: Ni_4B_3 ◇: Ni_2B)

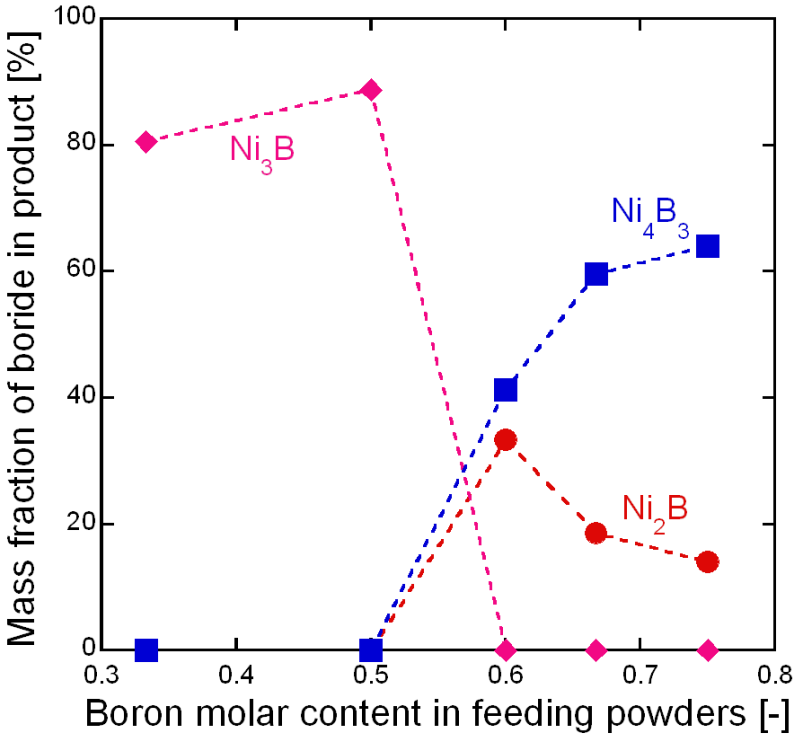

Fig. 30 Mass fraction of each phase in product with different boron molar content in feeding powders with quenching gas flow rate of 20 L/min.

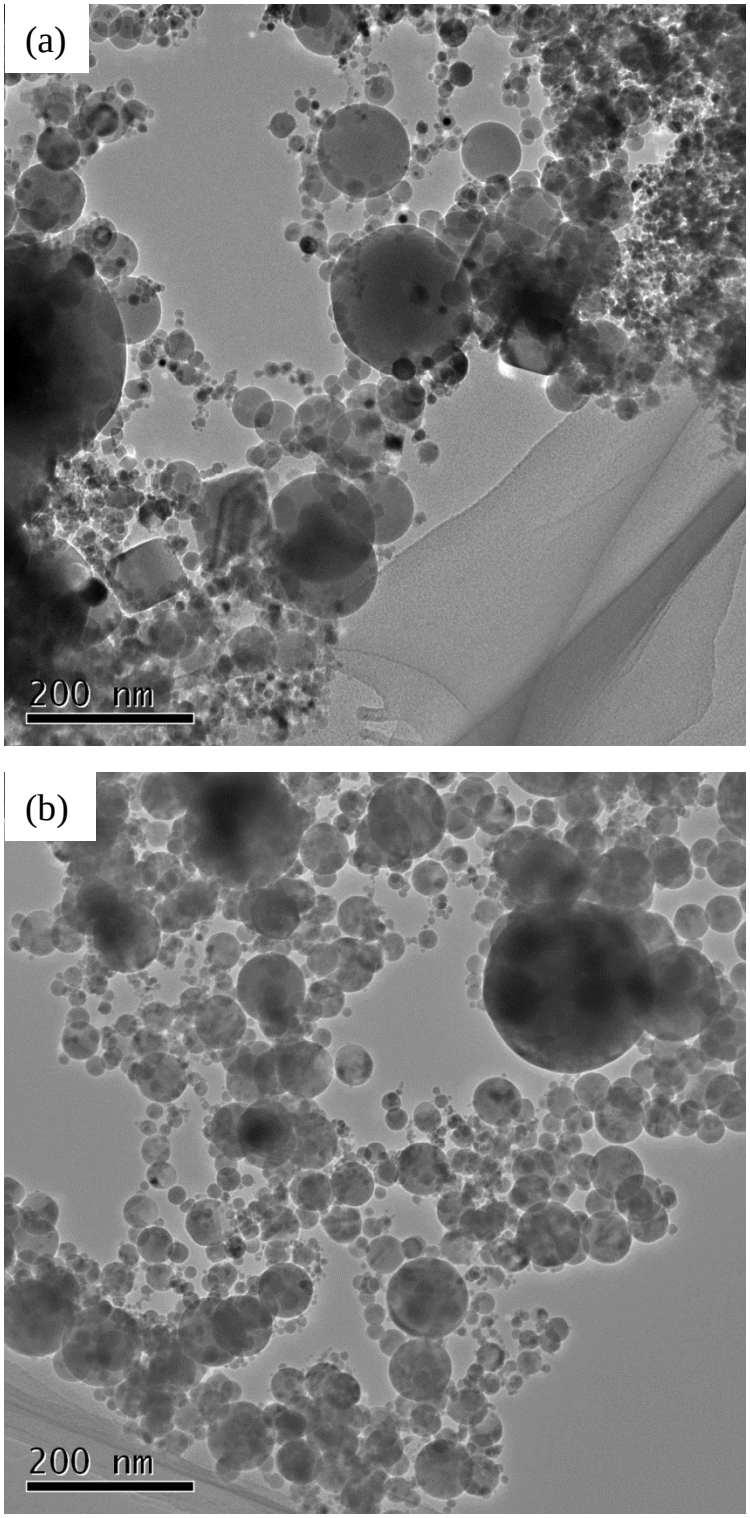

Fig. 31 TEM graphs of as-prepared product at the fixed powder feed rate of 0.2 g/min with different boron content in precursors: (a) Ni:B = 1:1; (b) Ni:B = 1:3.

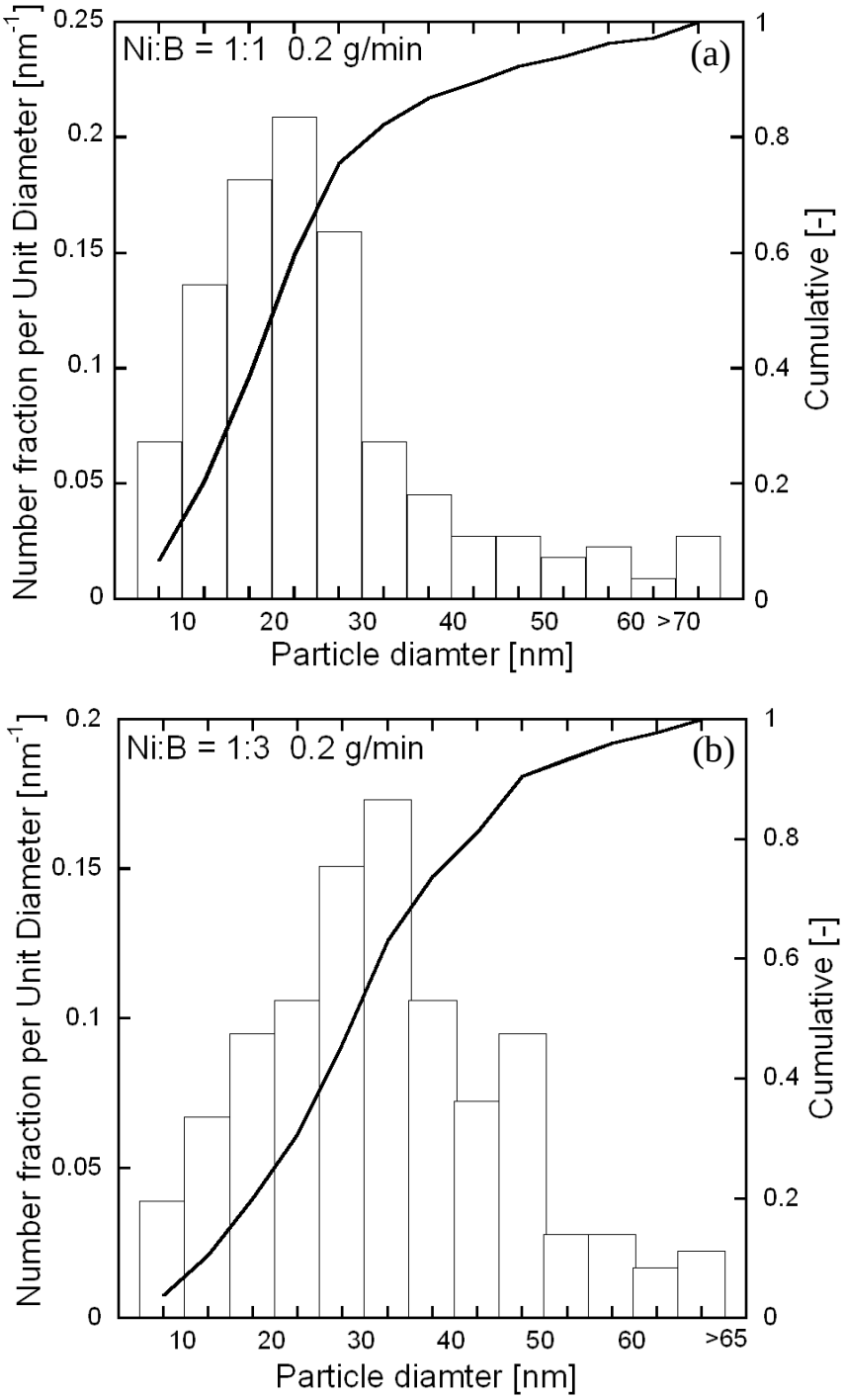

Fig. 32 Particle diameter distribution of as-prepared product at the fixed powder feed rate of 0.2 g/min with different boron content in precursors: (a) Ni:B = 1:1; (b) Ni:B = 1:3.

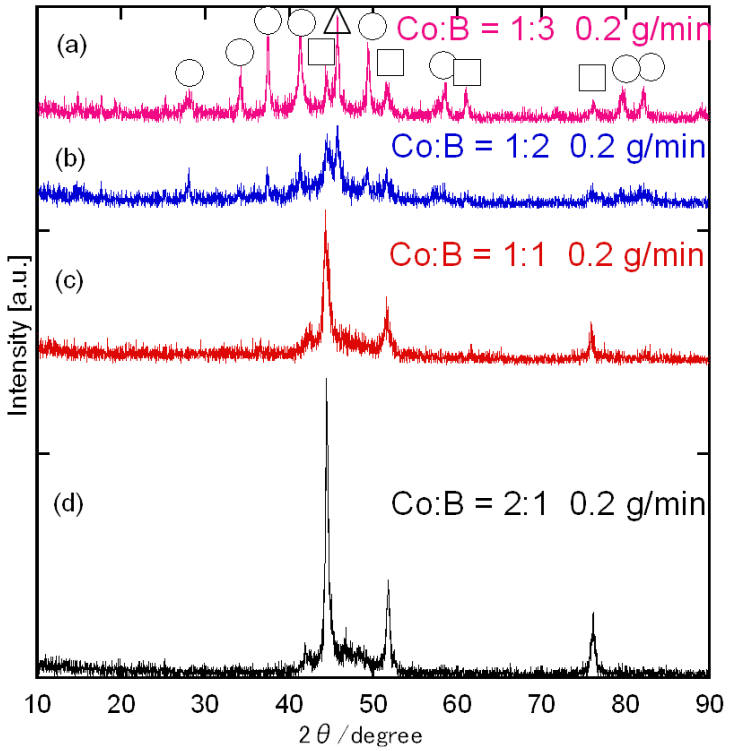

Fig. 33 XRD patterns of cobalt boride nanoparticles prepared with different cobalt to boron (Co:B) feed powder ratio of (a) 1:3, (b) 1:2, (c) 1:1, and (d) 2:1. The powder feeding rate used in this experiment was 0.2 g/min.

(○: CoB □: Co △: Co_2B)

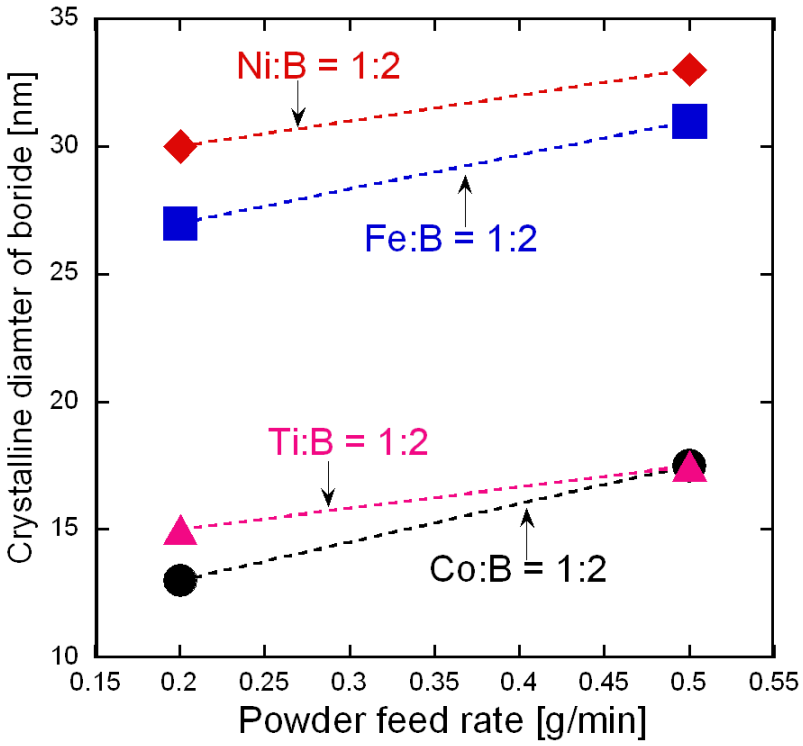

Fig. 34 Comparison of the particle diameter of product in Ti-B, Fe-B, Ni-B and Co-B systems.

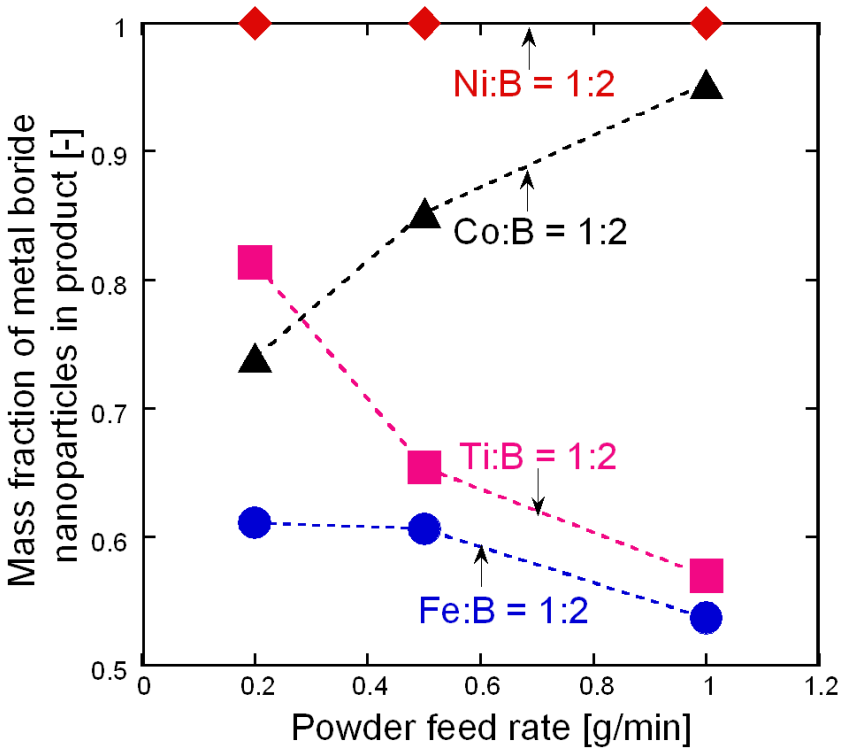

Fig. 35 Effect of powder feed rate on the phase composition of product in Ti-B, Co-B, Fe-B and Ni-B systems.

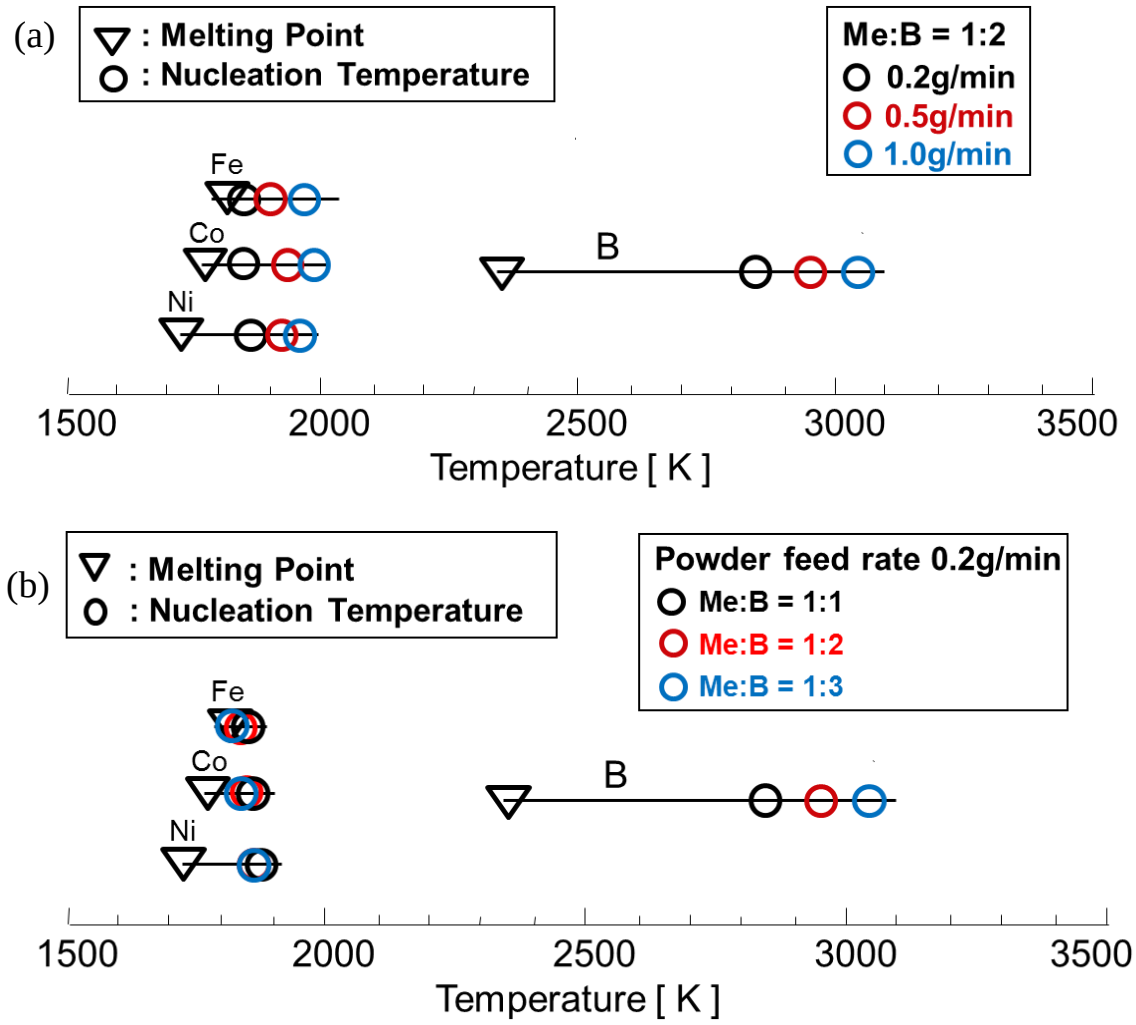

Fig. 36 Nucleation temperature at the critical saturation ratio for constituent components of boride: (a) Effect of different powder feed rate at the fixed initial composition of Me:B = 1:2; and (b) Effect of different initial composition of Me:B at the fixed powder feed rate of 0.2 g/min.

4. Synthesis of Refractory Metals Boride Nanoparticle by RF Thermal Plasma

4.1 Introduction

RF thermal plasmas has many unique advantages including high enthalpy, high chemical reactivity, large plasma volume, long residence time, and selective oxidation or reduction atmosphere according to the required chemical reactions. The high temperature enables the evaporation of a large amount of raw materials even with high melting and boiling temperatures [1-3]. The formation of nanoparticles in supersaturated state by homogeneous nucleation and heterogeneous condensation can be accomplished due to the rapid quenching rate in the tail flame [4-7]. Furthermore, it is available to synthesize nanoparticles with high purity by RF thermal plasma, because thermal plasma is generated in the torch without an internal electrode.

Fabrication of functional nanoparticles with high purity is strongly required for enormous industrial applications. In particular, nanoparticles of refractory metals boride, boron-based intermetallic compounds, provide various unique properties such as high melting temperature, electrical conductivity and heat/oxidation resistance, which in many cases are of great importance from technological viewpoints. Niobium borides are recognized as potential candidates for the application of high-temperature structural materials due to their excellent properties. Attractive properties of niobium borides are high thermal and electrical conductivity, and excellent chemical stability [8,9]. Molybdenum borides have attracted considerable interest for technological application (e.g., as hard coatings, high performance gear parts, golf shoe spikes and snow tires) because of their chemical stability, extremely high hardness and strength, and excellent resistance against mechanic and corrosive wear [10-14]. The TaB_2 (hexagonal of AlB_2-type) is interesting as a material for refractory, wear-resistant, metallic conductor and oxidation resistant [15] applications. W-B compounds have many excellent physicochemical properties, such as chemical inertness and good electrical conductivity [16]. As a result of these properties, tungsten boride are widely applied in the field of aviation, mechanism, chemical industry and metallurgy as structural materials, abrasives, cutting tools, electrode and anticorrosion materials. In addition, tungsten can slow down fast neutron and boron can absorb

thermal neutron, so tungsten boride can be used in nucleus industry as neutron radiation shield materials [17,18]. Because of the high melting point of raw materials, the synthesis of refractory boride is much more difficult than that of titanium and iron group metals boride.

In general, several methods have been developed for synthesis of refractory metal boride: solid-state reaction [14,19], mechanochemical synthesis [20,21], electrochemical synthesis [22,23], thermo-synthesis [24] and multiphase diffusive reaction [25]. RF thermal plasma which can provide very high temperature without oxygen is a promising alternative to conventional methods in the synthesis of refractory metals boride nanoparticles with high purity.

Nb-B, Mo-B, Ta-B and W-B systems were selected as models for the investigation in the Ch. 4. The ratio of saturation vapour pressures between refractory metal and boron is a critical factor which affects the synthesis process of boride nanoparticles [26]. In Nb-B, Mo-B, Ta-B and W-B systems, metals with low saturation vapor pressures have high nucleation temperatures compared with that of boron. As a result, the formation mechanism of refractory metal borides is different from that in Ti-B system. In Ti-B system, boron nucleates first, followed by the condensation of titanium and boron monomers on boron nuclei [27].

The synthesis of refractory metal boride nanoparticles is a difficult manufacturing process, and the production efficiency is still low compared with the cost. If the manufacturing process is well-understood and controlled precisely, mass-production of refractory metal boride nanoparticles will be easily achieved using RF thermal plasma under atmospheric pressure with low costs. The process of the synthesis includes a co-condensation process with large or small vapor pressure differences of prepared species. Only a few studies and researches have been conducted concerning the synthesis of refractory boride nanoparticles using RF thermal plasma up to now [1, 2, 27-32], the growth mechanism of refractory boride nanoparticles by RF thermal plasma is still poorly understood. Therefore, detailed investigation into the growth mechanism of refractory metals boride nanoparticles by RF plasma is required for the precise control of the particle size distribution and stoichiometric composition through the process.

The objective of this study was to experimentally and numerically investigate the synthesis of refractory metal borides by RF thermal plasma. The experiments were carried out with controlling powder feed rate, boron content in feeding powders and quenching gas flow rate. The nanoparticle products collected from the inner wall of the reaction chamber and the collection filter were compared in terms of phase composition and crystalline size based on X-ray diffractometry (XRD). Particles morphology and size distribution were investigated by

transmission electron microscope (TEM).

4.2 Thermodynamic properties

1) Phase diagram of Nb-B, Mo-B, Ta-B and W-B systems

The currently accepted Nb-B phase diagram in **Figure 1** is mainly based on the studies of Nowotny et al. [33] and includes the stability of the Nb_5B_6 boride proposed by Bolmgren and Lundstrom [34]. The equilibrium phase diagram of the Nb–B binary system contains the liquid (L) phase, the terminal solutions of Nb (α) and B (βB), and six intermetallic compounds: Nb_3B_2, NbB, Nb_5B_6, Nb_3B_4, Nb_2B_3, and NbB_2. As Shown in Fig. 1, the solution phase NbB_2 shows an extensive homogeneity range (65~70 at% B) [35-39]. The crystal structures of the stoichiometric borides include Nb_3B_2, NbB, Nb_5B_6, Nb_3B_4, and Nb_2B_3.

The equilibrium solid phases of the Mo-B system as shown in **Figure 2** are the 5 intermediate compounds including Mo_2B, MoB, MoB_2, Mo_2B_5, MoB_4 [40]. The α-MoB is a low temperature form occupying a composition range from 48.6 to 50 at% B. The high temperature form β-MoB exists between 49 and 51 at% B [8]. The diboride MoB_2 exists under a substoichiometric boron content from a lower boundary of 62 at% B at 1800°C to an upper limit of 66.7 at% B at 2140°C. The Mo_2B_5 phase is also a substoichiometric compound with a homogeneity range between 67 and 70 at% B. Compared with the above boride phases; both Mo_2B and MoB_4 have narrower homogeneity ranges. They are more difficult to synthesize [8].

Figure 3 shows the phase diagram of Ta-B system. In the system of Ta-B, five borides are known; Ta_2B, Ta_3B_2, TaB, Ta_3B_4, and TaB_2.

Currently, various kinds of tungsten borides such as W_2B, WB, WB_2, W_2B_5, WB_4, and WB_{12} are known to exist in the W–B system [41-43]. The binary phase diagram of W-B system is displayed in **Figure 4**.

2) Gibbs free energy

Figure 5 (a) shows the relationship between the temperature and Gibbs free energy of Nb-B system. Based on this graph, only the Gibbs free energy of NbB_2 is negative, and NbB_2 can be generated easily. The Gibbs free energy of NbB, Nb_3B_4, Nb_3B_2 and Nb_5B_6 are positive, which indicates these borides are difficult to generate.

Gibbs free energy of Mo-B system is calculated in **Figure 5 (b)**. This figure displays the relationship between the temperature and Gibbs free energy of Mo-B system. When the temperature is below 4000 K, all of the Gibbs free energies are negative and these reactions can take place spontaneously. According to the graph, Mo_2B_5 has the lowest Gibbs free energy, which means the Mo_2B_5 is the easiest to generate. MoB has relatively high Gibbs free energy

3) Saturation vapor pressure

The saturation pressures of the vapours decrease drastically along with the temperature decrease and fall below their actual vapour pressures. This supersaturated state consequently leads to production of nuclei by nucleation. Difference of saturation vapour pressure of boron and metals plays an important role in the synthesis of refractory metal boride nanoparticles with the controlled composition and diameter. The vapour pressure ratios of B/Mo, B/Nb, B/Ta and B/W are on the order of 10^2, 10^3, 10^4 and 10^5 at the melting points of Mo, Nb, Ta and W, respectively. The saturation vapour pressure of constituent components of borides is displayed in **Figure 6**. Preparation of borides with large difference in vapour pressure of the constituent components is quite difficult. Small difference in vapour pressure of the constituent components leads to better preparation of boride nanoparticles. Therefore, the control of condensation process is important for preparation of boride nanoparticles by RF thermal plasma.

4.3 Experimental

4.3.1 Experimental apparatus

The schematic apparatus of RF thermal plasma system for the production of boride nanoparticles is shown in **Figure 7**. The system consists of a plasma torch, a reaction chamber, a particle collection filter, and a power supply. The plasma torch is composed of a water-cooled quartz tube and a water-cooled induction coil. The coil consists of three turns and applies the actual power 30.0 kW and the induction frequency 4.0 MHz to the plasma. Total system was evacuated and then Ar was introduced up to a pressure of 101 kPa.

4.3.2 Experimental conditions

The feeding powders used in this study were niobium (particle size: 20 μm, purity: 98.0%, Kojundo Chemical Laboratory Co. Ltd., Japan), molybdenum (particle size: 5 μm, purity:

99.0%, Kojundo Chemical Laboratory Co. Ltd., Japan), tantalum (particle size: 45 μm, purity: 99.9%, Kojundo Chemical Laboratory Co. Ltd., Japan), tungsten (particle size: 3.06 μm, purity: 99.0%, Kojundo Chemical Laboratory Co. Ltd., Japan) and crystalline boron (particle size: 45 μm, purity: 99.0 %, Kojundo Chemical Laboratory Co. Ltd., Japan). Metal and boron particles were premixed at the fixed initial molar composition before they were injected into the RF thermal plasma from the plasma torch at different powder feed rate through the powder feeder.

After the precursors were introduced into the plasma region with argon carrier gas, they were instantaneously evaporated due to the very high enthalpy of the RF thermal plasma. Therefore, the metal boride nanoparticles are synthesized from the gas phase.

The operating conditions are summarized in **Table 1**. Argon was introduced as the carrier gas of 3 L/min, the inner gas of 5 L/min, and the sheath gas of 60 L/min. Helium of 5 L/min was also used as the sheath gas. The sheath gases were injected from the outer slots of the plasma torch located between the injection tube and the quartz tube to protect the inner surface of the quartz tube and to stabilize the plasma. The powder feed rate was 0.2, 0.5 and 1.0 g/min and the molar content of boron in the feeding powder was controlled from 33.3 to 80.0 at%. The RF plasma was operated at the fixed input power of 30.0 kW under atmospheric pressure. Quenching distance from the top of the probe of quenching gas to the top of the chamber is 15 or 18 cm. The quenching gas flow rate was 5, 10, 20 L/min.

4.3.3 Analytical method

The analytical methods are the same as those which are introduced in detail in Ch. 2.

4.4 Experimental results and discussion

4.4.1 Effect of powder feed rate

1) Nb-B system

Figure 8 shows XRD spectra of product collected from reaction chamber wall at the fixed initial composition Nb:B = 1:2 with different powder feed rate. From XRD spectra, the characteristic peaks of NbB_2 are identified with unreacted Nb. The dominant product is unreacted Nb, and the intensity of NbB_2 peaks is very low. Gibbs free energy of NbB_2 is negative, indicating NbB_2 can be produced easily. The other phase of niobium boride has

positive Gibbs free energy. XRD result indicates that the synthesis of niobium boride nanoparticle is difficult compared with titanium borides [28].

In Nb-B system, niobium vapor with low saturation vapor pressure reaches its supersaturated state first. Simultaneously, the nucleation of niobium takes place and niobium-rich nuclei are generated on molten state. Immediately, the condensation of niobium and boron vapor occurs dominantly on the surface of niobium nuclei. The nucleation of niobium takes place only around the niobium nucleation temperature in a short time. During the high temperature region between the nucleation temperature and melting point of niobium, niobium and boron vapors can be mixed well on the liquid state. But this temperature range is relatively narrow, meaning less boron and niobium vapors can be mixed well. On the other hand, niobium and boron vapors are not mixed well in the relatively low temperature gap with diffusion of boron vapor between the melting point of niobium and boron. The solidification of niobium nuclei takes place. It is difficult for the reaction between vapor and solid phase. In addition, raw material Nb with high melting point, specific heat and latent heat is difficult to evaporate in plasma. In a word, the synthesis of niobium boride is difficult.

Effect of powder feed rate on phase composition of product in Nb-B, Ti-B and Fe-B systems is displayed in **Figure 9**. They have the same tendency that the mass fraction of metal boride in product decreases with increasing powder feed rate. Take Nb-B as example, the amount of raw materials increases at high powder feed rate, though the heat from the plasma keeps constant at the fixed input power of 30.0 kW. The evaporation of raw materials requires relatively long time with less heat transferring from the plasma to each particle. In addition, Nb is more difficult to evaporate than that of boron due to the relatively high melting point (2890 K), boiling point (5120 K) and latent heat ($7.5 \cdot 10^6$ J/Kg). So the existence area of evaporated Nb is extended along with plasma flame. The vapors of niobium and boron co-exist in the upstream region of plasma flow. The boridization occurs easily in the co-exist area due to high temperature and abundant boron vapor, while it is difficult in the downstream region because of relatively low temperature for the boridization and diffuse of boron vapor which is produced in the upstream region. In the downstream region, the solidification process of niobium nuclei occurs. The nuclei on the liquid state are important in the formation of metal boride nanoparticles, because chemical reactions between nuclei and the other monomers are impossible after the solidification of nuclei. In addition, high powder feed rate leads to high the nucleation temperature of niobium. According to the equation of nucleation rate, high

nucleation temperature results in low nucleation rate. Less niobium nuclei were generated. Therefore, the mass fraction of metal boride is reduced with high powder feed rate.

In Ti-B and Fe-B systems, boron nucleates first. The temperature region between the nucleation temperature and melting point of boron is wide. More boron nuclei on molten state can be generated compared with the generation of niobium nuclei on molten state with the same condition. Additionally, larger surface tension results in lower nucleation rate. The surface tension of boron is 1.09 N/m, while the surface tension of niobium is 1.90 N/m. Niobium with large surface tension provides lower nucleation rate, and less niobium nuclei can be generated. As a result, the mass fraction of titanium and iron boride is higher than that of niobium boride nanoparticles.

Figure 10 display TEM graphs of as-prepared product collected from the reaction chamber wall at the fixed initial composition of Nb:B = 1:2 with powder feed rate 0.2 and 0.5 g/min. The particles are almost spherical and have core-shell structure. The range of size distribution is not very large. Based on TEM graphs, the particles prepared at higher powder feed rate have relatively large diameter. Particle size distribution of as-prepared product collected from the reaction chamber wall at the fixed initial composition of Nb:B = 1:2 with powder feed rate 0.2 and 0.5 g/min is demonstrated in **Figure 11** (a) and (b), respectively. The average size of particles with powder feed rate 0.2 and 0.5 g/min is about 16.2 and 21.3 nm, respectively.

Effect of powder feed rate on the crystalline diameter of as-prepared product is shown in **Figure 12**. The crystalline diameter of the prepared nanoparticles increases along with the increase of powder feed rate. At high powder feed rate, the enhanced monomer density in the plasma leads to the high growth rate of niobium boride. The nanoparticles are formed at earlier stage at the higher feed rate with relatively large amount of vapour compared with the case of low feed rate. For this reason the nucleation positions shift to the upstream region of plasma. The nucleation temperature is high at high powder feed rate, the nucleation rate of niobium is reduced accordingly. As a result, a small number of stable niobium nuclei which share a large amount of vapour are generated. The condensation rate is increased which improves the growth of nanoparticles. In addition, the growth process including the nucleation and co-condensation processes occurs from the nucleation temperature of niobium to the melting point of boron. The growth time increases with powder feed rate due to the high nucleation temperature. Consequently, niobium boride nanoparticles have longer growth time and higher growth rate to from large particle size in the high feeding rate condition.

2) Mo-B system

Figure 13 presents XRD spectra and crystalline diameter of product collected on the reactor wall at fixed initial composition of Mo:B = 2:1 with different powder feed rate. According to XRD spectra, the peaks of MoB, MoB_2, and Mo_2B_5 can be observed with the existing of unreacted Mo. According to fig. 5 (b), Gibbs free energy of all of molybdenum borides is negative. Molybdenum boride is possible to produce spontaneously. Mo_2B_5 has the most negative Gibbs free energy, so it is the easiest to generate among all of molybdenum. The dominant product is unreacted Mo. The relative intensity of the peaks of molybdenum boride in product decreases with increasing powder feed rate due to the less heat transferring from the plasma to each particle. The reasons are explained in detail above. Moreover, the diameter of the MoB and Mo increases with increasing powder feed rate is shown in **Figure 14**.

3) Ta-B system

XRD spectra of product at fixed initial composition of Ta:B = 1:4 with different powder feed rate is displayed in **Figure 15**. The peaks of TaB, Ta_5B_6, Ta_3B_4, and TaB_2 can be observed at high powder feed rate. With lower powder feed rate, the dominant product is TaB_2 with detected Ta_3B_4. In my opinion, Gibbs free energy of tantalum borides are all negative, and TaB_2 has the lowest Gibbs free energy among all of borides. The effect of powder feed rate on the mass fraction of TaB_2 and unreacted Ta and diameter of TaB_2 is presented in **Figure 16**. The mass fraction of TaB_2 decreases with increasing powder feed rate. And the mass fraction of unreacted Ta increases with the increase of powder feed rate. The reasons in detail are explained in Nb-B system. The diameter of TaB_2 also increases with the increase of powder feed rate as displayed in **Figure 17**.

4.4.2 Effect of boron content in feeding powders

1) Nb-B system

Figure 18 shows XRD spectra of product collected from the reactor wall with different boron content in feeding powders at powder feed rate 0.2 g/min. In boron poor condition (Nb:B = 1:1), only the peaks of Nb can be identified. Niobium boride nanoparticles are not generated in boron poor condition. In boron rich condition (Nb:B = 1:2 or 1:3), the peaks of NbB_2 and unreacted Nb can be observed, while the dominant product is unreacted Nb. The intensity of the

peaks of NbB_2 is relatively low. The synthesis of NbB_2 is attributed to the negative Gibbs free energy of NbB_2 as shown in fig. 5 (a). Meanwhile, the intensity of niobium boride increases with boron content in feeding powders. In Nb-B case, niobium nuclei are generated in the high temperature region of the upstream of plasma. The niobium with high melting/boiling points is more difficult to evaporate in plasma compared with boron, so the existence area of niobium is extended along with the plasma flame to the relatively downstream region with low temperature. Boron can evaporate in the upstream region in plasma and co-exist with niobium vapour in the high temperature region. So the partial of niobium vapour can react with boron in the high temperature region. In the downstream region of plasma, there is little boron vapour due to the diffusion of boron vapour can react with evaporated niobium vapour. Diffusion of boron will make the synthesis of metal boride difficult in the relatively downstream region of plasma. High boron content in feeding powders will overcome this problem. More boron vapour still stays with niobium vapour in the same region with high boron content in feeding powders. The diameter of Nb increases with increasing boron content in feeding powders as presented in **Figure 19**. In summary, high boron content in feeding powder results in the better synthesis of metal boride nanoparticles with larger diameter.

2) Mo-B system

XRD spectra of as-prepared product collected from reaction chamber wall with different boron content in feeding powders at constant powder feed rate 0.2 g/min is revealed in **Figure 20**. According to XRD results, the characteristic peaks of MoB, MoB_2 and Mo_2B_5 are observed in boron poor and boron rich condition. However, the main product is unreacted Mo.

Effect of boron content in feeding powders on the relative ratio of the intensity of molybdenum boride to unreacted Mo in product is shown in **Figure 21**. The relative ratio of the intensity of molybdenum boride to unreacted Mo in product is increased by increasing boron content in feeding powders due to improved evaporation of boron vapor in plasma. The intensity of molybdenum boride is increased with high boron content in feeding powders. The reasons are the same with these in Nb-B system. The diameter of MoB and Mo both increase along with the increase of boron content in feeding powders as displayed in **Figure 22**. Mo with high nucleation temperature nucleates first, and then the condensation of Mo and B vapor takes place. Because nucleation is suppressed in the circumstances where larger amount of vapors can simultaneously co-condense, the suppressed nucleation generates fewer nuclei so that each

nucleus shares a larger amount of vapors. As the result, the nanoparticles with the larger diameters are fabricated.

3) Ta-B system

XRD measurements of product with powder feed rate of 0.2 g/min at initial composition of Ta:B = 1:3 and 1:4 is shown in **Figure 23**. The peaks of TaB, Ta_5B_6, Ta_3B_4, and TaB_2 can be detected at Ta:B = 1:3 and 1:4. While the main product is TaB_2 at Ta:B = 1:4 compared with that in 1:3. The synthesis of TaB_2 is improved by the increase of boron content in feeding powders. According to the nucleation temperature of tantalum, tantalum nucleates first and the temperature region between the nucleation temperature and melting point of tantalum is narrow. The generation of tantalum boride will be difficult. Actually, the main product is TaB_2; indicating TaB_2 is easy to produce in RF plasma. I think the main reason is the negative Gibbs free energy of tantalum boride. The size of TaB_2 decreases with the increase of boron content in feeding powders as shown in **Figure 24**.

4) W-B system

XRD spectra of product with powder feed rate of 0.2 g/min at initial composition of W:B = 1:2, 1:3 and 1:4 is shown in **Figure 25**. In the case of W:B = 1:2, W_2B and unreacted B are detected. The main product is unreacted W. Because the temperature region from the nucleation temperature of tungsten to the melting point of tungsten is relatively narrow. In addition, the raw material tungsten with high melting/boiling point is impossible to evaporate in plasma entirely in short time. Tungsten boride is in the narrow composition region in phase diagram of W-B system. Therefore, it is difficult to produce tungsten boride. In the case of W:B = 1:3 and 1:4, the peaks of WB_4, W_2B_5, WB with unreacted W are all identified. The main product is WB_4. Based on the discussion above, boron content in feeding powders is better for the generation of tungsten boride. Also Gibbs free energy of WB_4 is negative possibly. WB_4 would be the dominant product in boron rich condition. The tendency of the effect of boron content in feeding powders on the diameter indicated in **Figure 26** is complicated and it is difficult to explain.

4.4.3 Effect of collection position

Figure 27 demonstrates XRD spectra of product from the filter and the inner wall of the reaction chamber at initial composition of Nb:B = 1:3 with powder feed rate of 0.2 g/min. Seen

from XRD results, the characteristic peaks of NbB_2 and unreacted Nb are observed in product collected from the reaction chamber wall and filter. The dominant product from the filter is NbB_2, while the main product from the inner wall is unreacted Nb. **Table 2** displays the mass fraction of niobium boride in the product from the filter and the inner wall. The filter case has much higher mass fraction of niobium boride in the product than the inner wall case. In the reaction chamber, the high temperature region for the existence of niobium nuclei is limited in the centre region of the plasma flame due to the high melting temperature (2890 K) and boiling point (5120 K) of niobium. For this reason, the formation of niobium borides is difficult near the inner wall of the chamber because of the lower temperature. On the other hand, synthesized niobium borides in the centre region are transported to the filter along with plasma flow. Moreover, relatively low niobium boride density of 6.97 g/cm^3 compared with niobium density of 8.57 g/cm^3 promotes enhanced niobium boride fraction in the filter. The comparison between the diameter of product from wall and filter is displayed in **Figure 28**.

Figure 29 demonstrates TEM graph and size distribution of as-prepared product collected from the filter at the fixed initial composition of Nb:B = 1:2 with powder feed rate 0.2 g/min. Seen from TEM graph, the particles are spherical and have core-shell structure. The average diameter is about 16.2 nm, which is the same with that of particles from inner wall.

Figure 30 displays the XRD spectra of products from the filter and the inner wall of the reaction chamber at initial composition of Mo:B = 2:5 with powder feed rate of 0.2 g/min. Seen from XRD results, the peaks of Mo_2B, MoB, Mo_2B_5 and unreacted Mo are observed in the product collected from the reaction chamber wall and filter. The dominant product from the filter is MoB, while the main product from the inner wall is unreacted Mo. Molybdenum borides in the canter region are transported to the filter along with plasma flow. Moreover, relatively low molybdenum boride density of 6.45 g/cm^3 compared with molybdenum density of 10.22 g/cm^3 promotes enhanced molybdenum boride fraction in the filter. The comparison between the diameter of product from wall and filter is presented in **Figure 31**.

4.4.4 Effect of quenching gas flow rate

1) Ta-B system

Figure 32 displays XRD spectra of product at initial composition Ta:B = 1:4 with different quenching gas flow rate. In all of the conditions, TaB_2 can be identified. My target product is TaB_2 with catalytic activity. Unreacted Ta, TaB, Ta_3B_4 and Ta_5B_6 can be detected without

quenching gas. The dominant product is TaB_2. The high relative intensity of TaB_2 can be achieved with quenching gas flow rate of 10 L/min. Generating TaB_2 needs some special temperature and phase composition according to the phase diagram. Quenching gas can stop the reaction at certain temperature. Moreover, if the quenching rate is increased for a given monomer concentration, the result is that the supersaturation reaches a higher value before the nucleation occurs due to the increased temperature gradient. A higher supersaturation causes a decrease in the critical nucleus size before the onset of nucleation occurs based on the equation of critical size. Recalling that the cluster size distribution for early times is monotonically decreasing, the result is that a larger number of mostly smaller stable nuclei are made available for condensation. Therefore, we would expect a higher cooling rate to produce more and smaller particles. Therefore, high mass fraction of TaB_2 in product was prepared with adequate quenching gas and phase composition. **Figure 33** presents the relationship between the quenching gas flow rate and the mass fraction and diameter of TaB_2 and Ta_3B_4 in product at the initial composition of Ta:B = 1:4. The high mass fraction of TaB_2 is reached with the quenching gas flow rate of 10 L/min. The diameter of TaB_2 decreaases with the quenching gas flow rate as shown in **Figure 34**, since quenching gas can stop the growth.

2) W-B system

Figure 35 displays XRD spectra of product at the fixed initial composition W:B = 1:4 with different quenching gas flow rate. In all of the conditions, unreacted W is observed. My target product is W_2B_5. In the low quenching gas flow rate, the peaks of WB, W_2B,WB_2 and WB_4 are identified. The dominant product is W. In the high quenching gas flow rate, W_2B_5 can be identified. Generating W_2B_5 needs some special temperature and phase composition according to phase diagram. Quenching gas can stop the reaction at certain temperature. Therefore, W_2B_5 can be prepared with adequate quenching gas and phase composition. **Figure 36** displays the effect of quenching gas flow rate on the mass fraction and diameter of each phase in product at the initial composition of W:B = 1:4. The mass fractions of W_2B and WB_4 decrease with increasing quenching gas flow rate, while the mass fractions of W_2B_5, WB and unreacted W increases with the increase of quenching gas flow rate. The diameter of W also decreaases with quenching gas flow rate as indicated in **Figure 37**.

4.5 Numerical simulation

4.5.1 Concept and assumptions

The simulation is explained in detailed in Ch. 2.

4.5.2 Computational conditions

The target process of this study is thermal plasma synthesis of nanoparticles composed of binary alloy nanoparticles. Hence, the computation was conducted using a typical cooling condition at the plasma's tail where nanoparticles are created. The precursory coarse powders of a metal Nb and B were supplied as the raw materials at the total feed rate of 0.2 g/min with the B content of 66.7 at% and 80.0 at%. Our previous numerical study confirmed that the raw materials were completely vaporized in the plasma. Because the vapors were transported with the gas flow to the plasma's tail, the material vapor concentrations corresponding to those operating conditions were given as the initial condition. The temperature-decrease rate also decreases from $1.5\cdot 10^5$ to $1.0\cdot 10^4$ K s^{-1} as time passes.

4.5.3 Numerical results and discussion

Figure 38 shows the evolution of the particle size-composition distribution (PSCD), which expresses the growth behaviour of niobium boride nanoparticles. The powder feed rate was set to be 0.2 g/min at initial composition of Nb:B = 1:2. Fig. 38 (a) shows that Nb-rich nuclei are generated at the early stage of the growth, and B vapor is decreased simultaneously by conversion, which is attributed to the close nucleation temperatures of Nb and B. Following nucleation around τ = 2.3 ms, Nb and B vapors are consumed dominantly by co-condensation. Following nucleation, the nanoparticles are formed through co-condensation of the material vapors on the nuclei and coagulation among themselves. In fig. 38 (b), the nanoparticles are still Nb-rich at this stage, where Nb vapor has a higher rate of condensation than B vapor because the saturation pressure of Nb is much lower than that of B. Afterwards, because B vapor condenses on those nanoparticles; their B contents as well as their diameters are increased. Following the consumption of Nb vapor, boron vapor is consumed with a high rate of condensation as shown in fig. 38 (c). During nanoparticles'growth, the binary nucleation is progressing simultaneously. It is noted that the nuclei are generated changing their size and composition because the material vapor pressures are also being changed by the vapor consumptions. Because of the absence of the material vapors, the nanoparticles grow only

through coagulation slowly. Finally, the nanoparticles form its mature state of the Nb-B binary nanoparticle at τ =19.9 ms in fig. 38 (d). The mature nanoparticle is composed mainly of the nanoparticles around d =15 nm and $X_{(B)}$ = 66.7 at%. The boron content of 66.7 at% was given as the initial condition, which intended the effective synthesis of NbB_2 nanoparticle because the boron content of 66.7 at % is the stoichiometric composition of NbB_2. Therefore, the mature nanoparticle mainly consists of nanoparticles with the boron content identical to the initially given boron content. However, nanoparticle has the widely ranging compositions. The particle size also ranges widely even though the calculation was conducted under the simple condition.

Figure 39 shows the evolution of the particle size-composition distribution (PSCD), which expresses the growth behaviour of niobium boride nanoparticles prepared with powder feed rate 0.2 g/min at initial composition of Nb:B = 1:4. Fig. 39 (a)-(c) shows the nucleation of Nb at the early stage. Following nucleation around, Nb vapors are consumed dominantly by co-condensation. Following nucleation, the nanoparticles are formed through co-condensation of Nb and B vapors on the nuclei and coagulation among themselves. Finally, nanoparticles form its mature state of the Nb–B binary nanoparticle in fig. 39 (d). The mature nanoparticle is composed mainly of nanoparticles around d = 25 nm and $X_{(B)}$ = 80.0 at%. The boron content of 80.0 at% was given as the initial condition, which intended the effective synthesis of NbB_4 nanoparticle because the boron content of 80.0 at % is the stoichiometric composition of NbB_4.

Figure 40 shows XRD spectrum of product with powder feed rate of 0.2 g/min at initial composition of Nb:B = 1:4. The dominant product in experiment is NbB_2, not NbB_4. Such discrepancy might come from the simplification of the present model. Firstly, there is the assumption of complete evaporation of raw materials in the computation, whereas there was large quantity of unreacted Nb in product in the experiment. Since thermal plasmas in the experiment are often accompanied with unsteady thermofluid fields. It should be noted that the content of the reactive Nb nuclei determines the composition as discussed in the experimental results. Secondly, the model for computation does not consider Gibbs free energy, but in the experiment it will be considered. Gibbs free energy may explain the difference between the numerical and experimental results. Although Gibbs free energy plays an important role in the synthesis process in the experiment, the numerical model did not consider Gibbs free energy.

4.6 Nucleation temperature

They derived the expression as an extension of kinetic nucleation theory. The proposed expression can be used over a wide range of physical conditions. The equation of estimation of nucleation temperature is explained in Ch. 6. The nucleation temperature at the critical saturation ratio is presented in **Figure 41**; fig. 41 (a) was drawn at the boron molar content of 66.7% with different powder feed rate, and fig. 41 (b) was calculated at powder feed rate of 0.2 g/min with different initial composition of Me:B. According to fig. 41, the nucleation temperature of refractory metal is higher than that of boron. Refractory metal nucleates firstly, and then the condensation of refractory metal and boron vapors occurs on the surface of metal nuclei. Because the temperature region between the nucleation temperature and melting point of metal is narrow, indicating less metal nuclei are on the molten state. The metal nuclei and boron cannot be mixed well. Therefore, the narrow temperature region leads to the little preparation of refractory metal boride nanoparticles.

4.7 Conclusions

This study presents an experimental investigation and numerical simulation on the preparation of refractory metal borides nanoparticles using RF thermal plasma from elemental powders. Experimental observations indicate that the nucleation temperature of constituent compositions of metal boride nanoparticles and quenching rate are important factors in the controlled synthesis of boride nanoparticles by RF thermal plasma.

In this chapter, the effect of powder feed rate, boron content in feeding powders and quenching gas flow rate on the phase composition and crystalline size of product were investigated. The little production of metal boride nanoparticles collected from the reaction chamber wall results from the relatively narrow temperature gap between the nucleation and melting temperatures of metal. The mass fraction of refractory metal boride nanoparticles in product is decreased with increasing powder feed rate due to the extended evaporation region of raw materials, and increases with the increase of boron content in feeding powders. The crystalline size of nanoparticles increases with the increase of powder feed rate. High mass fraction of niobium and molybdenum boride nanoparticle in product is found from the collecting filter due to high melting/boiling temperatures of metal and lower density of boride. High mass fraction of tantalum and tungsten borides is reached with adequate quenching gas flow rate. Based on the numerical simulation, Nb-rich nuclei are generated at the early stage in plasma, and boron vapor spontaneously condenses on the surface of Nb-rich nuclei.

References

[1] T. Watanabe, Nezu A, Abe Y, Ishii Y and K. Adachi, Thin Solid Films, 435, 27 (2003)

[2] T. Watanabe and H. Okumiya, Science Technology and Advanced Materials, 5, 639 (2004)

[3] J. Szepvolgyi, Z. Markovic and S. Scheier PandFeil, Plasma Chemistry and Plasma Processing, 26, 597 (2006)

[4] M. Shigeta and T. Watanabe, Journal of Materials Research, 20, 2801 (2005)

[5] M. Desilets, J.F. Bilodeau and P. Proulx, Journal of Physics D: Applied Physics, 30, 1951 (1997)

[6] N.Y.M. Gonzalez, M.E. Morsli and P. Proulx, Journal of Thermal Spraying Technology, 17, 533 (2008)

[7] M. Shigeta and T. Watanabe, Journal of Applied Physics, 108, 043306 (2010)

[8] C.L. Yeh and W.H. Chen, Journal of Alloys and Compounds, 422, 78 (2006)

[9] O. Shigeru, H. Kenya, L. Torsten and H. Iwami, AIP Conf. Proc. 231, 456 (1991)

[10] S.T. Oyama, A.T. Santhanam and S.T. Oyama, The Chemistry of Transition Metal Carbides and Nitrides, Blackie Academic Professional, Scotland, 1996

[11] A.W. Weimer, Chapman & Hall, London, 1997

[12] P. Dearnley and T. Bell, Surf. Eng. 1, 203 (1985)

[13] S. Robert, B. Ira and M. David, J. Metal, September 983 (1952)

[14] R. Steinitz, Powder Metall. Bull. 6, 54 (1951)

[15] V.A. Lavrenko and L.A. Glebov, Zh. Fiz. Khim 48, 2449 (1974); Chem. Abstr. 82, 77 (1975)

[16] S. Bartels, W. Gruber, B. Cappi, R. Telle and H. Schmidt: Mater. Lett. Vol. 62 (2008), p. 3836

[17] S.L. Lindbek, W.H. Stergelmann and E.F. Wklliams: Nucl. Eng. Des. Vol. 9 (1969), p. 311

[18] X.Z. Cao, X.X. Xue, T Jiang and Z.F. Li: J. Rare Earth. Vol. 28 (2010), p. 482

[19] R. Steinitz, I. Binder and D. Moskowitz, J. Metall. 4, 983 (1952)

[20] K. Kudaka, K. Iizumi, T. Sasaki and S. Okada, J. Alloys Compds. 315, 104 (2001)

[21] T. Sasaki, K. Iizumi, K. Kudaka and S. Okada, Nippon Kagaku Kaishi 11, 821 (2000)

[22] S. Prasad, F.A. Marinho and F.S.M. Santana, J. Chem. Eng. 17, 423 (2000)

[23] S. Prasad, F.A. Marinho, L.B. Silva, J. Ind. Chem. Soc. 77, 311 (2000)

[24] V.V. Malyshev, Chem. Papers-Chemicke Zvesti 52, 86 (1998)

[25] L. Yuanzhi, F. Yining and C. Yi, Journal of Solid State Chemistry, 170, 135 (2003)

[26] J. Brandstotter and W. Lengauer, Journal of Alloys and Compounds, 262-263, 390 (1997)

[27] M. Shigeta and T. Watanabe, Journal of Thermal Spray Technology, 18, 1022 (2009)

[28] Y.Y. Cheng, M. Shigeta, S. Choi and T. Watanabe, Chemical Engineering Journal, 183, 493 (2012)

[29] Y.Y. Cheng and Watanabe T, Journal of Chemical Engineering of Japan, 44, 583 (2011)

[30] M. Shigeta and T. Watanabe, Journal of Physics D: Applied Physics, 40, 2407 (2007)

[31] M. Shigeta and T. Watanabe, Journal of Applied Physics, 108, 043306 (2010)

[32] J.Y. Huang, T. Ishigaki, T. Tanaka and S. Horouchi, Journal of Materials Science, 33, 4141 (1998)

[33] H. Nowotny, F. Benesovsky and R Kieffer, Zeitschrift fu r Metallkunde, 50, 417 (1959)

[34] H. Bolmgren and T Lundstroem, Journal of the Less-Common Metals, 159, L25 (1990)

[35] E. Rudy, Windisch St. Ternary phase equilibrium in transition metal boron-carbon-silicon systems, AFML-TR-65-2, part I, vol. X. OH: Wright-Patterson Air Force Base; 1966.

[36] H. Nowotny, F. Benesovsky, E. Rudy and A. Wittmann, Monatshefte fur Chemie, 91, 975 (1960)

[37] E. Rudy, F. Benesovsky and L. Toth, Zeitschrift fur Metallkunde, 54, 345 (1963)

[38] C.A. Nunes, D. Kaczorowski, P. Rogl, M.R Baldissera., P.A Suzuki., G.C. Coelho, et al. Acta Materialia, 53, 3679 (2005).

[39] M. P. Rockfeller, F. Flavio, C.C.Gilberto, A.N. Carlos and S. Bo, Intermetallics, 15, 999 (2007)

[40] K.E. Spear and P.K. Liao, BuUetin of Alloy Phase Diagrams, 9, 457 (1988)

[41] E. Lassner and W.D. Schubert, Tungsten: Properties, Chemistry, Technology of the Element, Alloys and Chemical Compounds, Kluwer Academic, New York, NY, 1999

[42] Y. Itoh and Y. Ishiwata, The journal Society of Mechanical Engineers Int. J. A-Mech. M, 39 429 (1996)

[43] P. Peshev, G. Bliznakov and L. Leyarovska, Journal of Less-Common Metalls, 13, 241 (1967)

[44] S.L. Girshick, C.P. Chiu and P.H. McMurry, Aerosol Science and Technology, 13, 465 (1990)

[45] R.J.M. Blocherj and I.E. Campbell, Battelle Memorial Institute, 71, 4040 (1949)

[46] S.K. Friedlander, John Wiley & Sons: New York, 1977

[47] R.G. Fenish, NRM, 138, 1 (1964)

[48] R.G. Munro, Journal of Research of the National Institute of Standards and Technology, 105, 709 (2000)

[49] J. H. Seinfeld and S.N. Pandis, Wiley, New York (1998)

[50] B.E. Wyslouzil and G. Wilemski, Journal of Chemistry Physics, 103, 1137 (1995)

[51] T. Vesala, M. Kulmala, R. Rudolf, A. Vrtala and P.E. Wagner, Journal of Aerosol Science, 28, 565 (1997)

[52] M. Wautelet, J.P. Dauchot and M. Hecq, Nanotechnology, 11, 6 (2000)

Table 1 Operating condition for the synthesis of niobium boride nanoparticles

Process parameters	Value
Sheath gas and flow rate	Ar-He(60:5) 65 L/min
Inner gas and flow rate	Ar 5 L/min
Carrier gas and flow rate	Ar 3 L/min
Plasma power	30.0 kW
Reactor pressure	101.3 kPa
Frequency	4 MHz
Powder Feed rate	0.1-1.0 g/min
Boron molar content in feeding powder	25-80 at %
Quenching gas flow rate	5, 10, 20 L/min
Quenching distance	15/18 cm

Table 2 Mass fraction of niobium boride in the product from the filter and the inner wall of the reactor at the powder feed rate of 0.2 g/min.

Initial Composition	Filter (%)	Wall (%)
Nb:B = 1:2	96.6	16.9
Nb:B = 1:3	96.8	19.3
Nb:B = 1:4	96.7	33.8

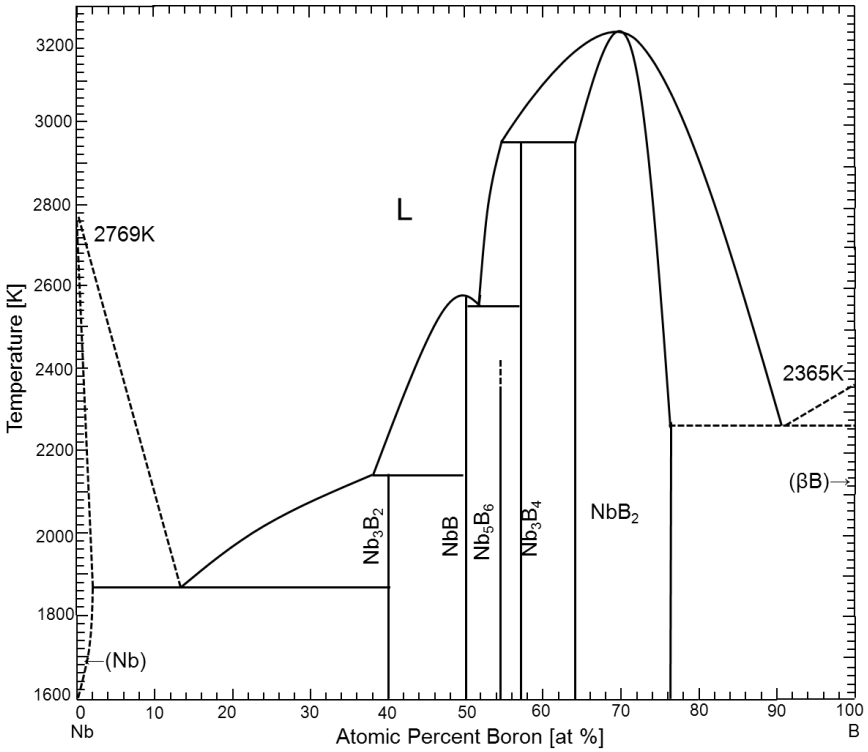

Fig. 1 Binary Nb–B phase diagram.

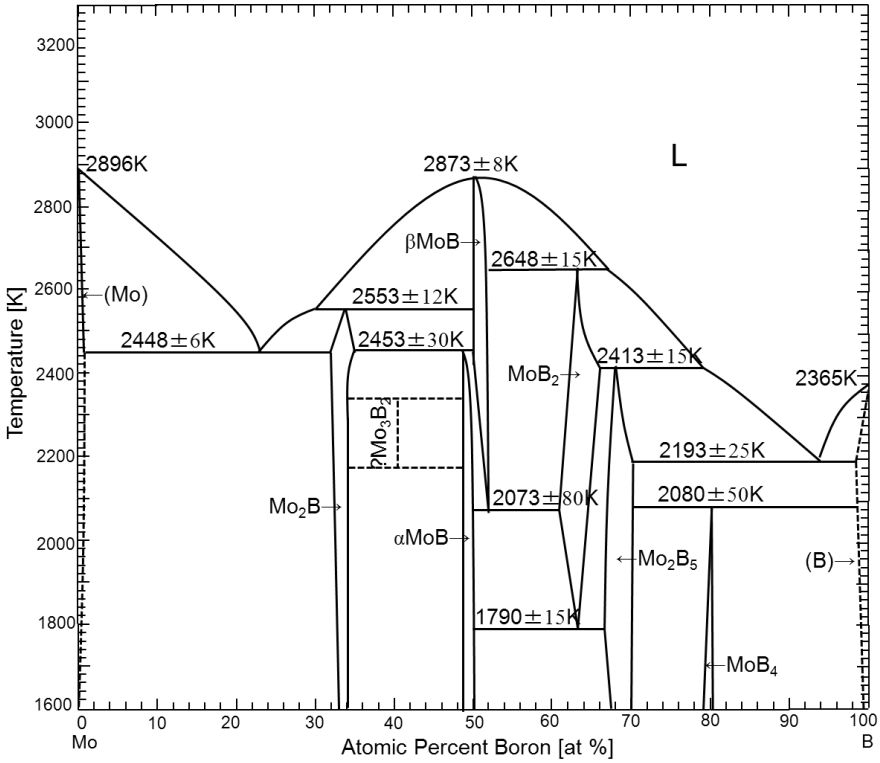

Fig. 2 Binary Mo–B phase diagram.

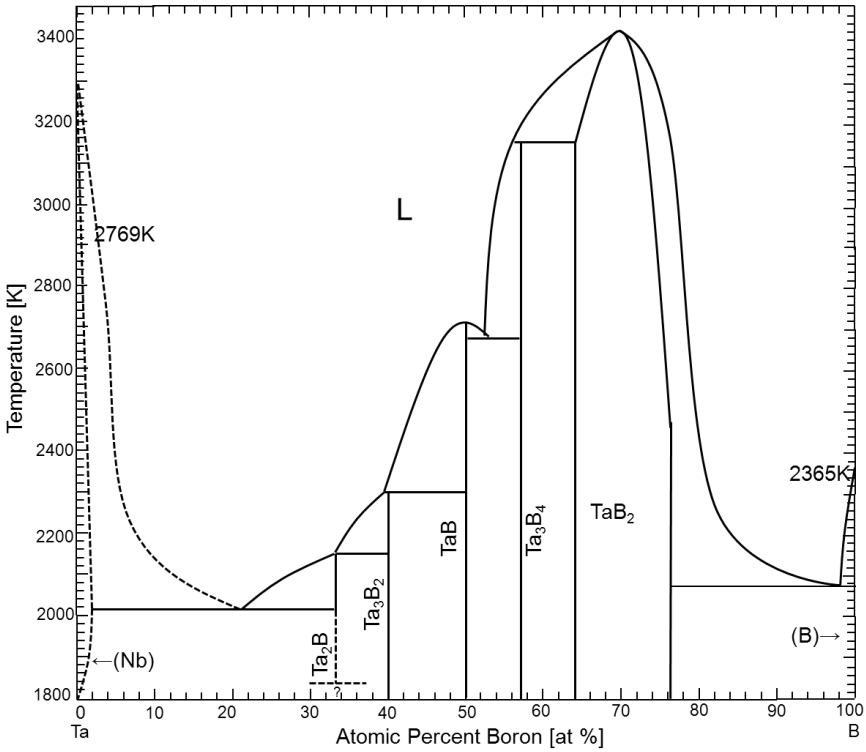

Fig. 3 Binary Ta–B phase diagram.

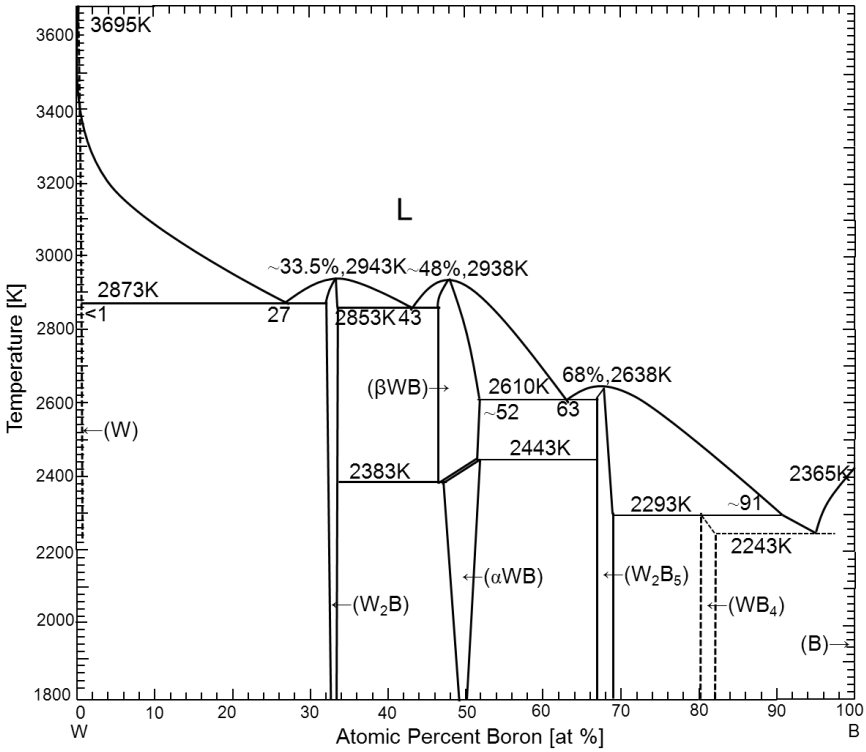

Fig. 4 Binary W–B phase diagram.

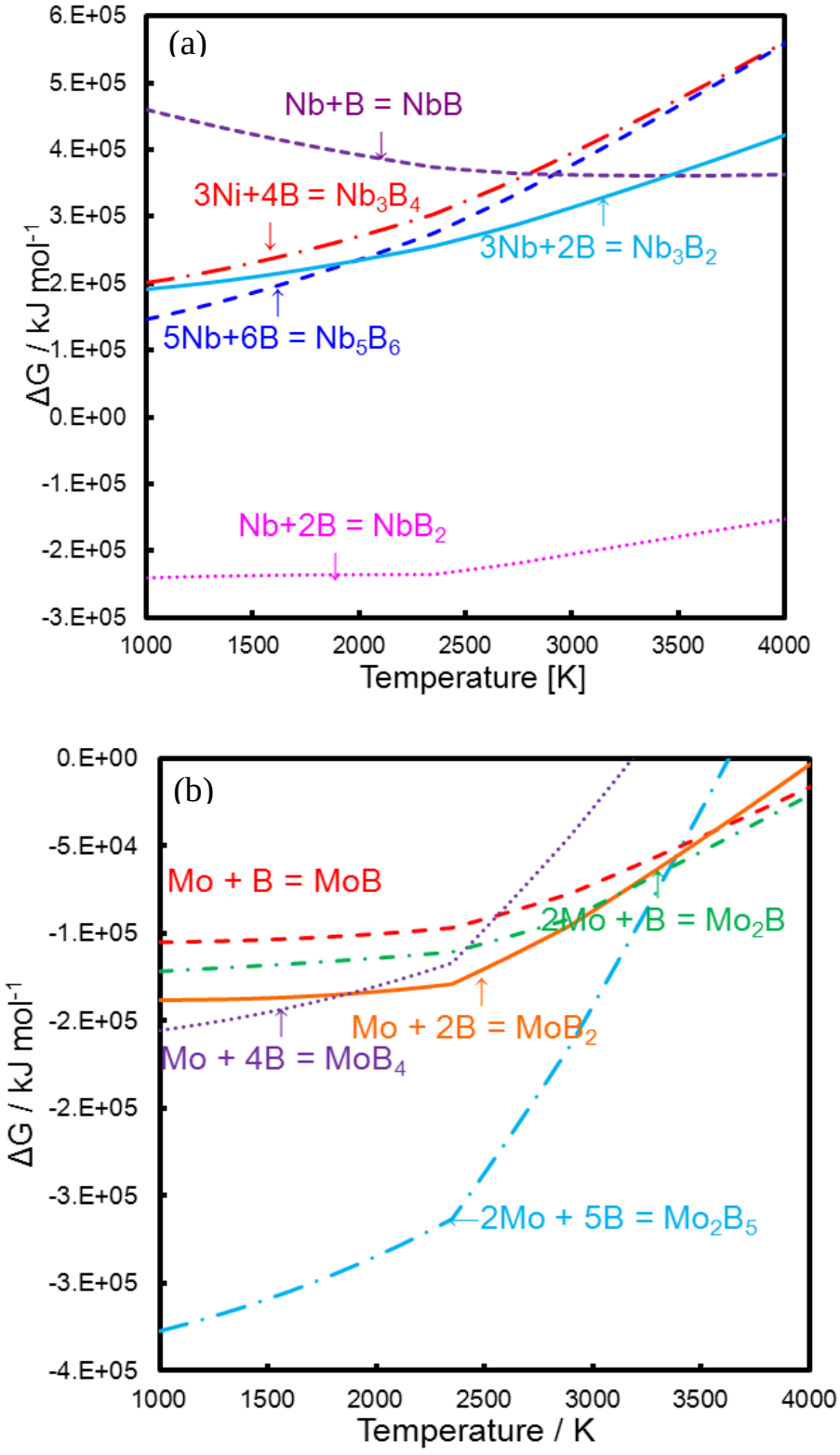

Fig.5 Gibbs free energy of: (a) Nb-B (b) Mo-B.

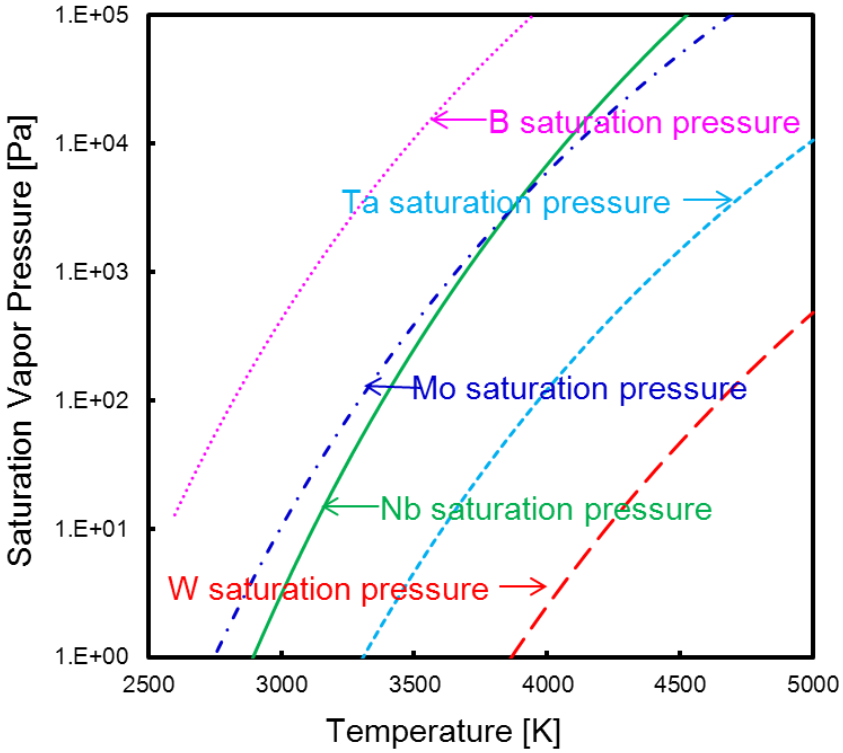

Fig. 6 The relationship between the temperature and saturation vapor pressures of Mo, Nb, Ta, W and B.

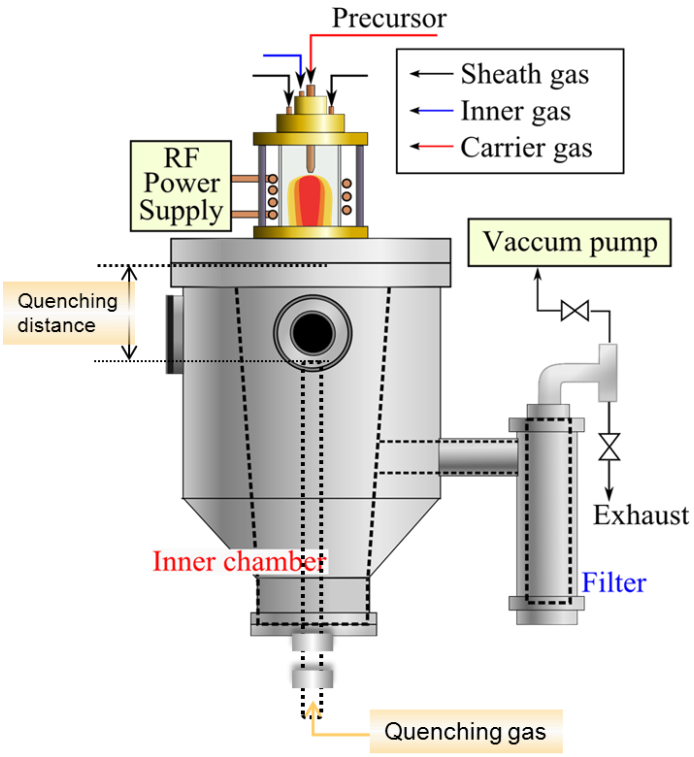

Fig. 7 Experimental set-up of RF thermal plasma for the synthesis of metal boride nanoparticles with quenching system.

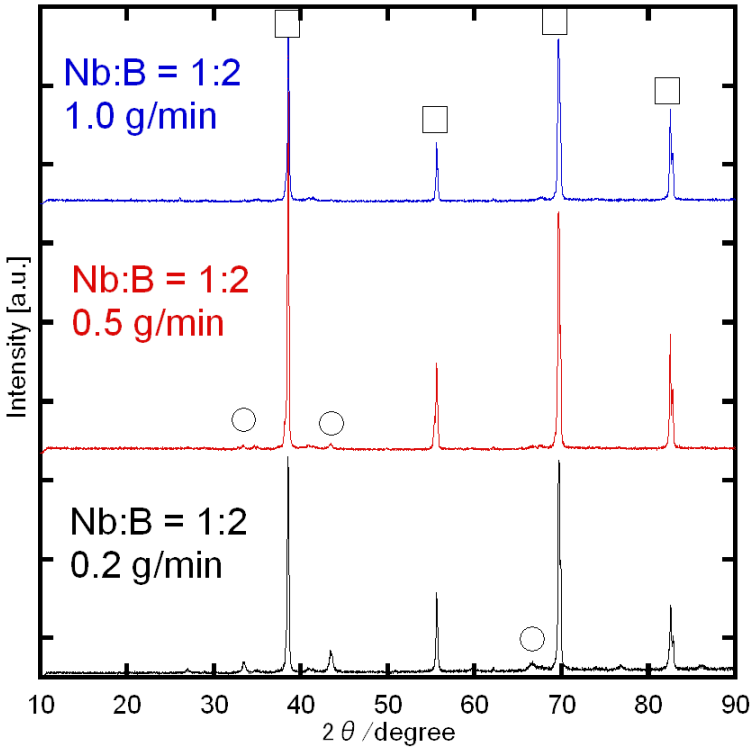

Fig. 8 XRD spectra of product collected on the reactor wall at fixed initial composition with different powder feed rate.
(○: NbB_2 □: Nb)

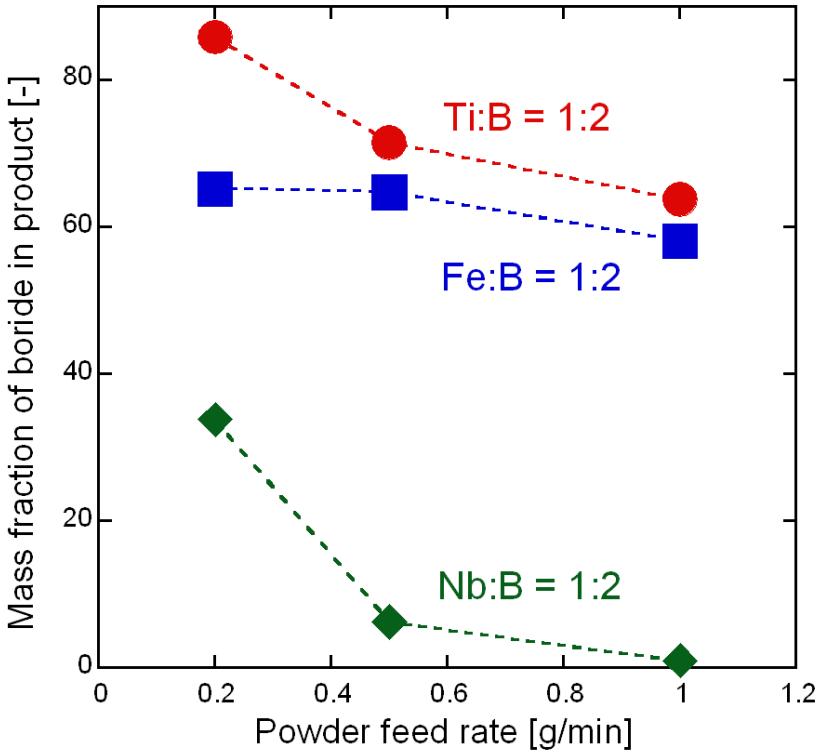

Fig. 9 Effect of powder feed rate on phase composition of product in Nb-B, Ti-B and Fe-B systems

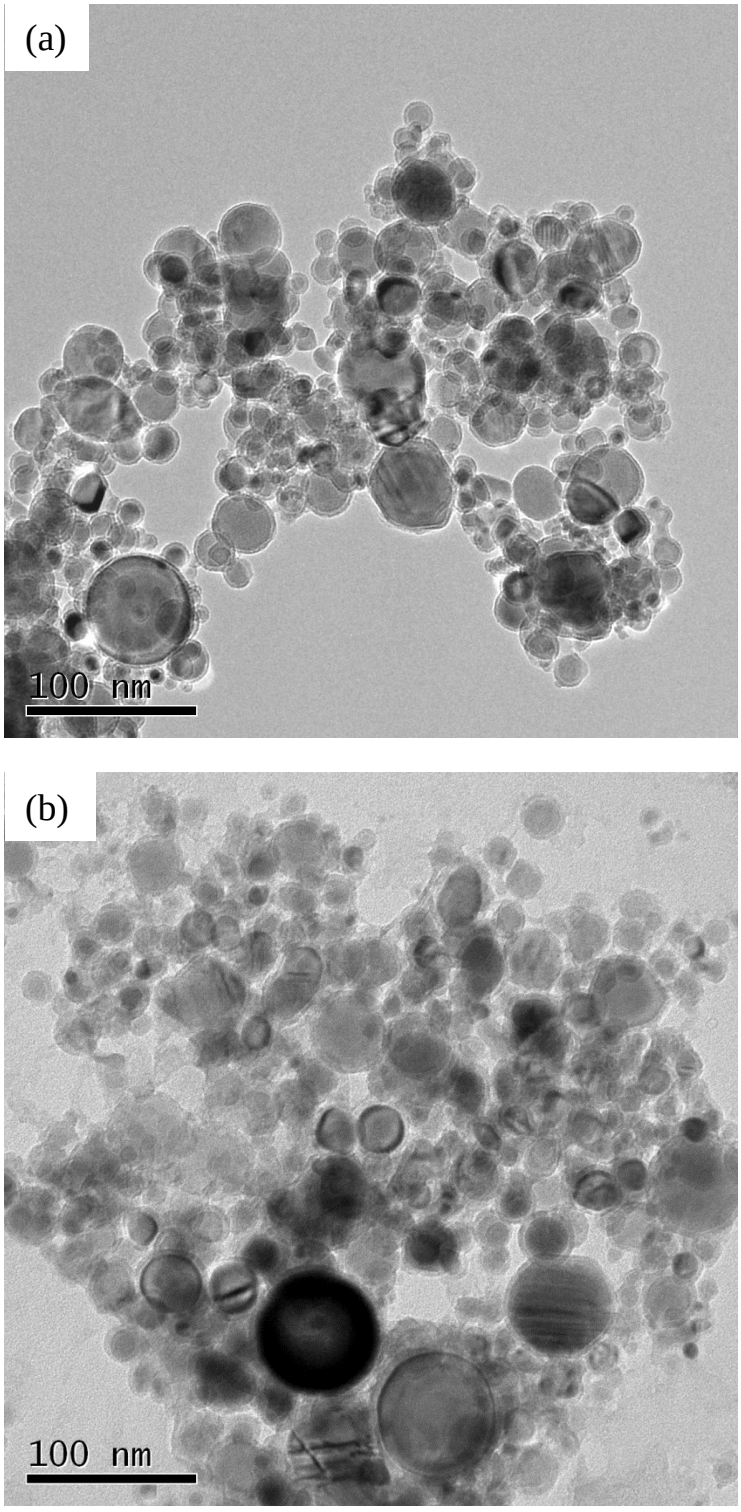

Fig. 10 TEM graphs of as-prepared product at the fixed initial composition of Nb:B = 1:2 with different powder feed rate: (a) 0.2 g/min; (b) 0.5 g/min.

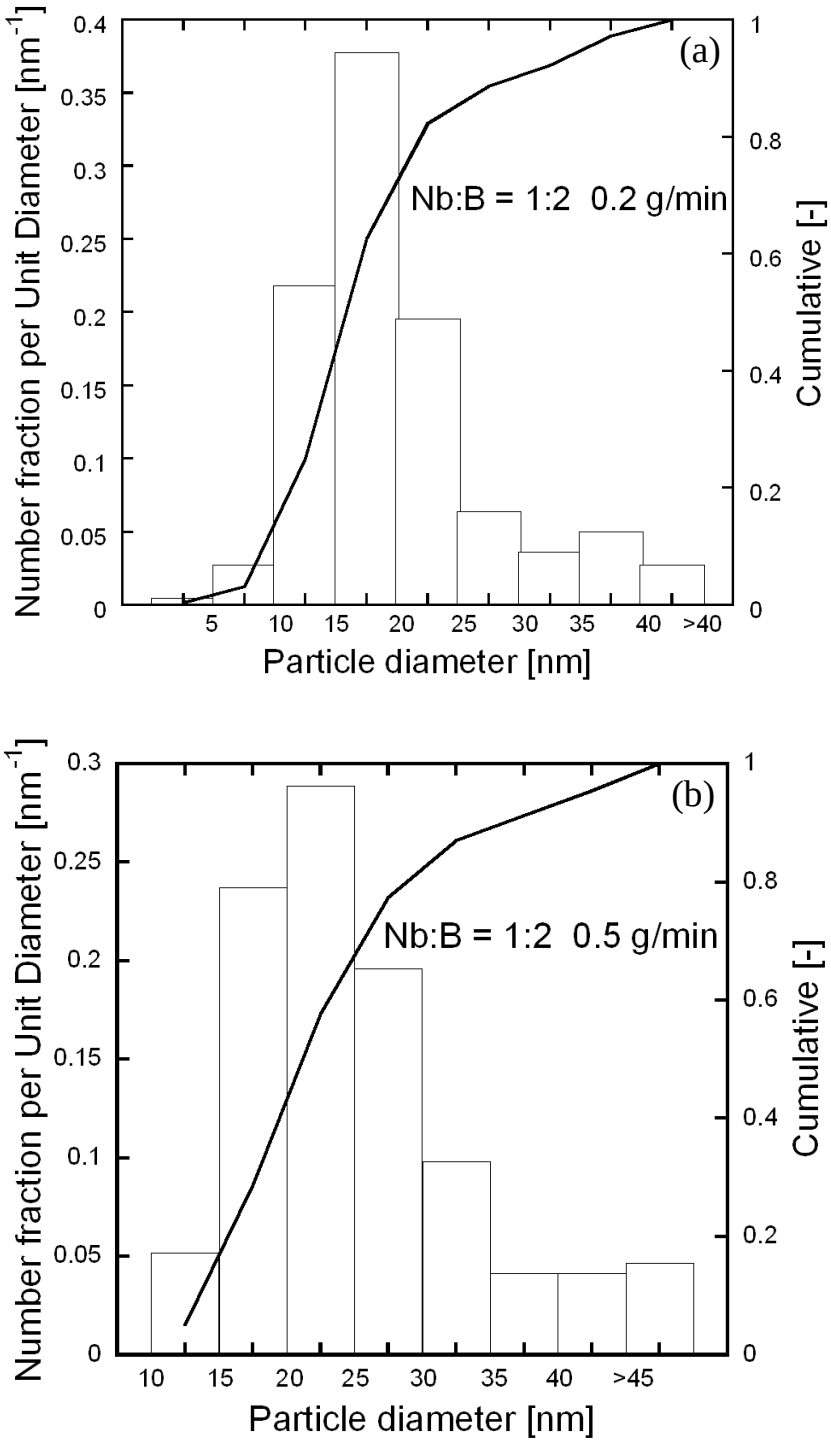

Fig. 11 Particle diameter distribution of as-prepared product at the fixed initial composition of Nb:B = 1:2 with different powder feed rate: (a) 0.2 g/min; (b) 0.5 g/min.

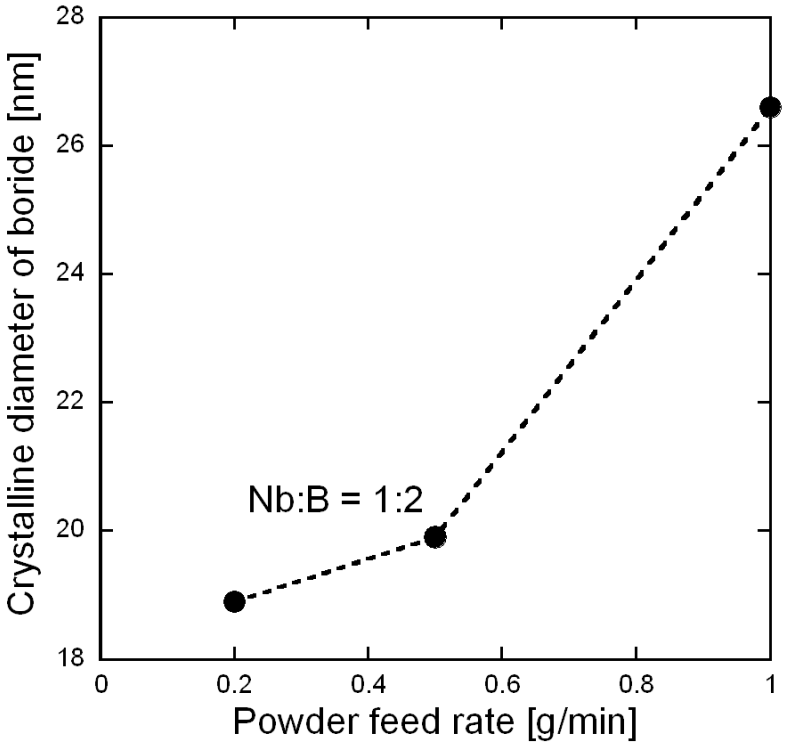

Fig. 12 Effect of powder feed rate on the crystalline diameter of NbB_2 at the fixed initial composition of Nb:B = 1:2.

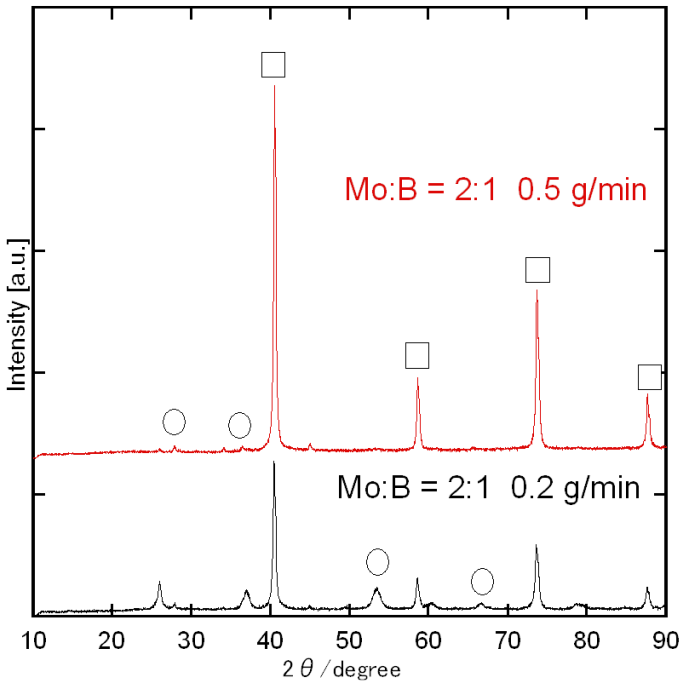

Fig. 13 XRD spectra a product collected on the reactor wall at initial composition of Mo:B = 2:1 with different powder feed rates. (○: MoB □: Mo)

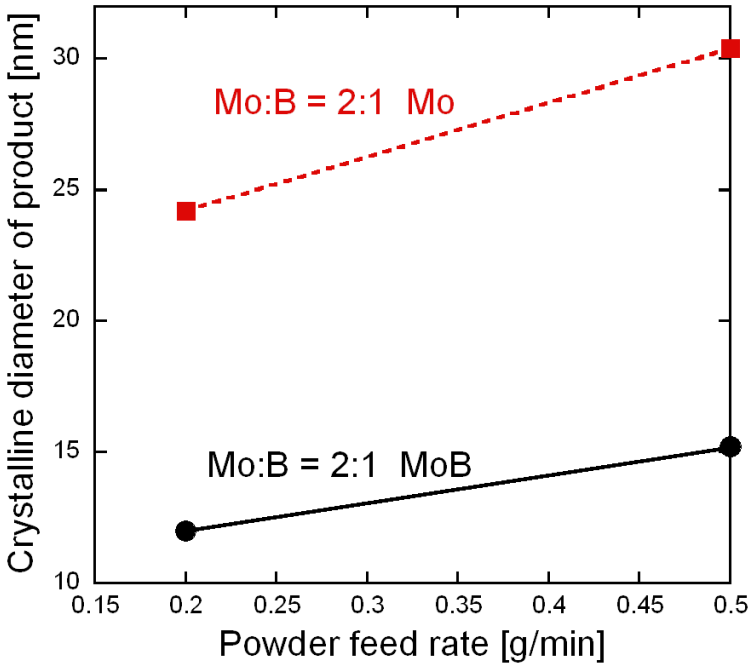

Fig. 14 Crystalline diameter of product collected on the reactor wall at initial composition of Mo:B = 2:1 with different powder feed rates.

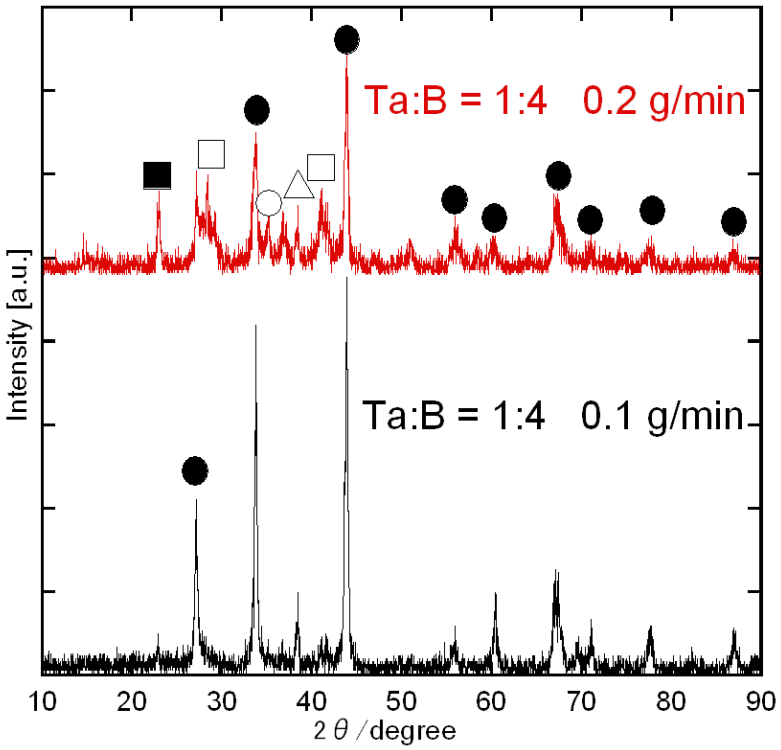

Fig. 15 XRD spectra of product at fixed initial composition of Ta:B = 1:4 with different powder feed rate.

(●: TaB_2 □: Ta_5B_6 △: Ta_3B_4 ○: TaB ■: Ta)

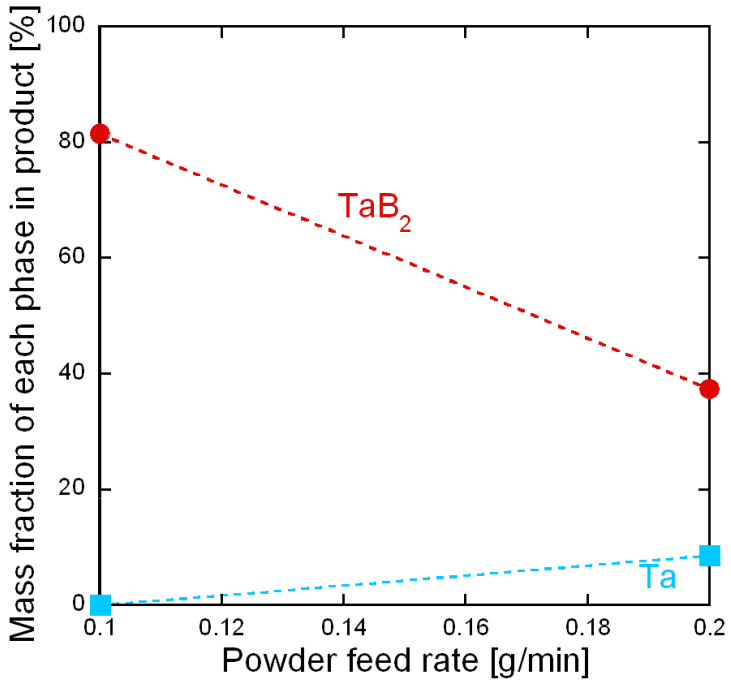

Fig. 16 Effect of powder feed rate on mass fraction of TaB_2 and Ta in product in Ta-B system.

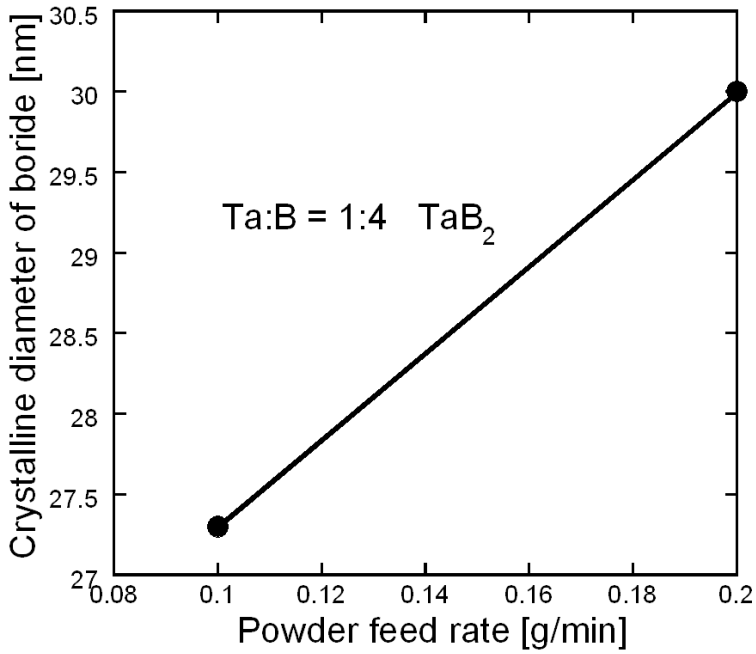

Fig. 17 Effect of powder feed rate on crystalline diameter of TaB_2 in product in Ta-B system.

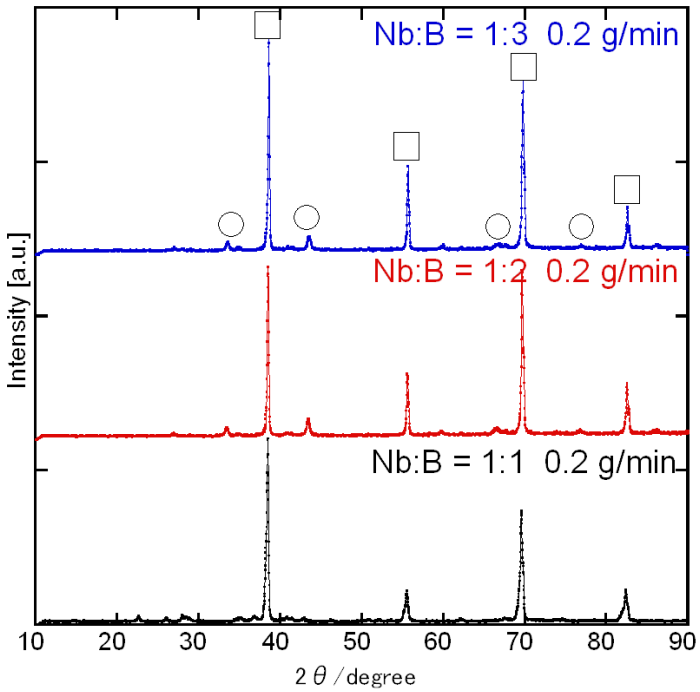

Fig. 18 XRD spectra of product collected from the reaction chamber wall with different boron content in feeding powders at powder feed rate 0.2 g/min.
(○: NbB_2 □: Nb)

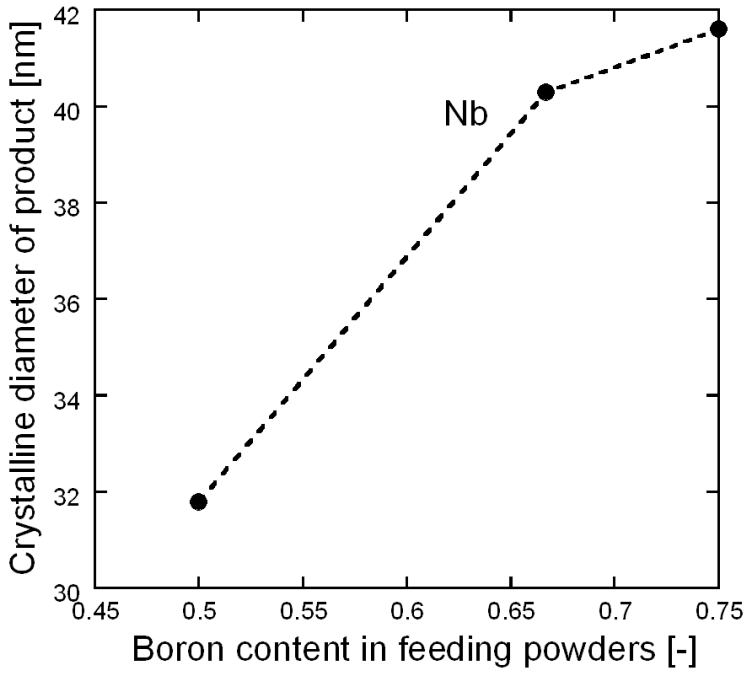

Fig. 19 Crystalline diameter of product collected from the reaction chamber wall with different boron content in feeding powders at powder feed rate 0.2 g/min.

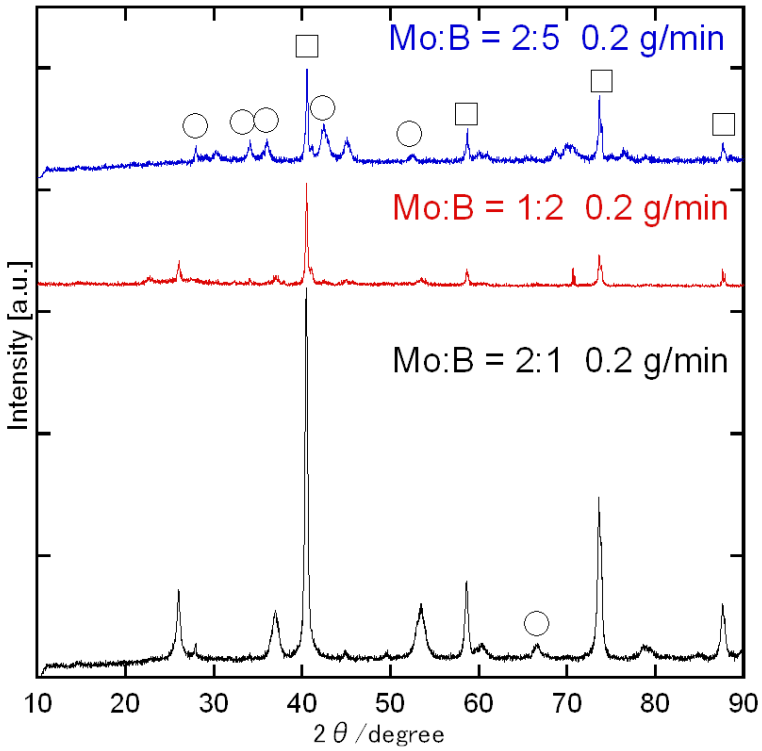

Fig. 20 XRD spectra of product collected from the reaction chamber wall with different boron content in feeding powders at powder feed rate 0.2 g/min.
(○: MoB □: Mo △: MoB_2 ◇: Mo_2B_5)

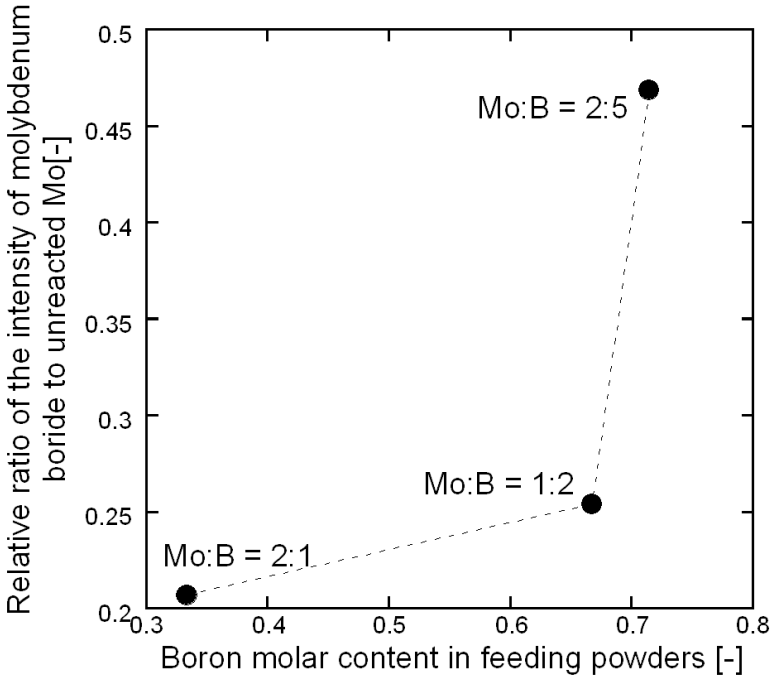

Fig. 21 Effect of boron content in feeding powders on the relative ratio of intensity of boride to unreacted Mo in product.

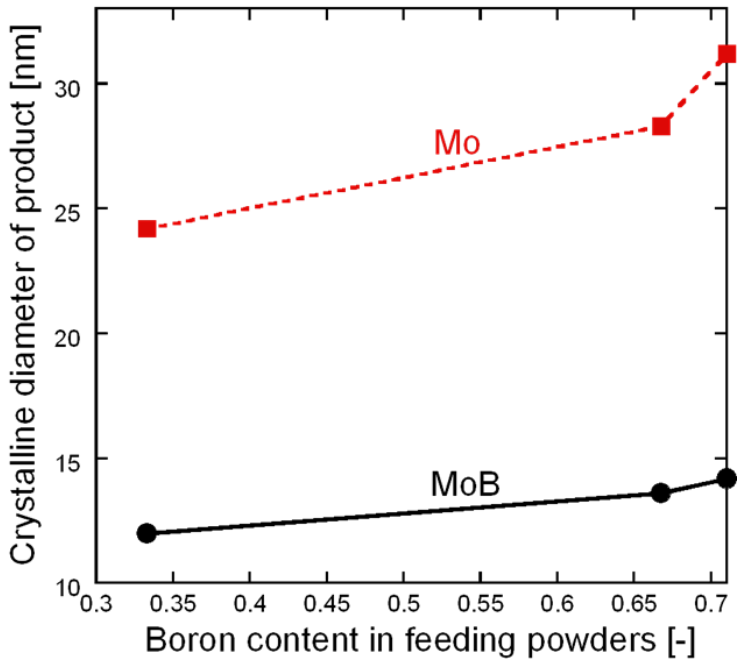

Fig. 22 Effect of boron content in feeding powders on crystalline diameter of MoB and unreacted Mo in product.

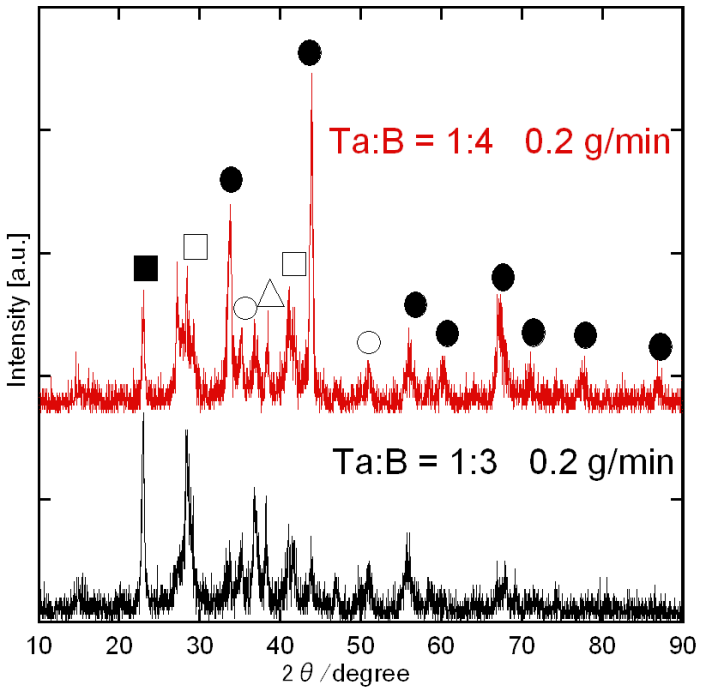

Fig. 23 XRD spectra of product collected from the reaction chamber wall with different boron content in feeding powders at powder feed rate 0.2 g/min.

(●: TaB_2 □: Ta_5B_6 △: Ta_3B_4 ○: TaB ■: Ta)

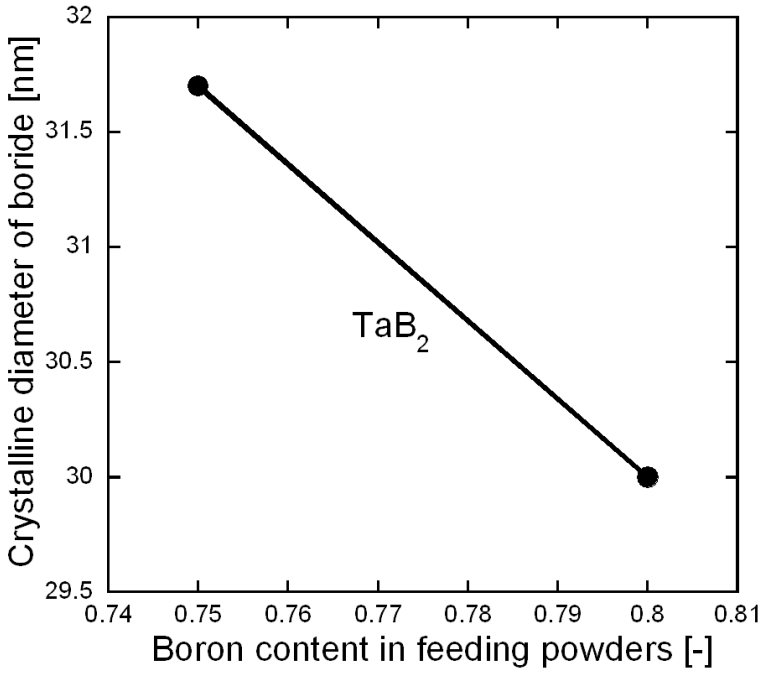

Fig. 24 Crystalline diameter of TaB_2 collected from the reaction chamber wall with different boron content in feeding powders at powder feed rate 0.2 g/min.

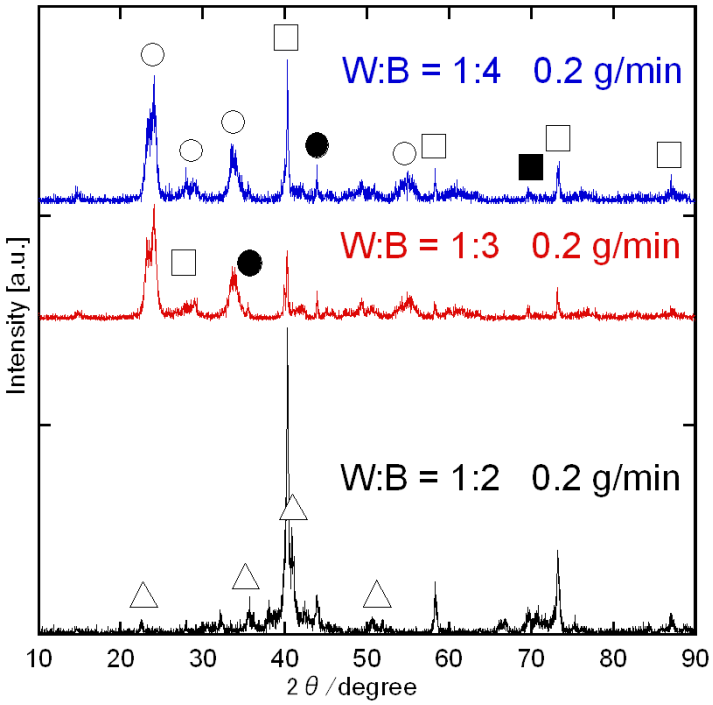

Fig. 25 XRD spectra of product collected from the reaction chamber wall with different boron content in feeding powders at powder feed rate 0.2 g/min.

(○: WB_4 □: W △: W_2B ■: WB ●: W_2B_5)

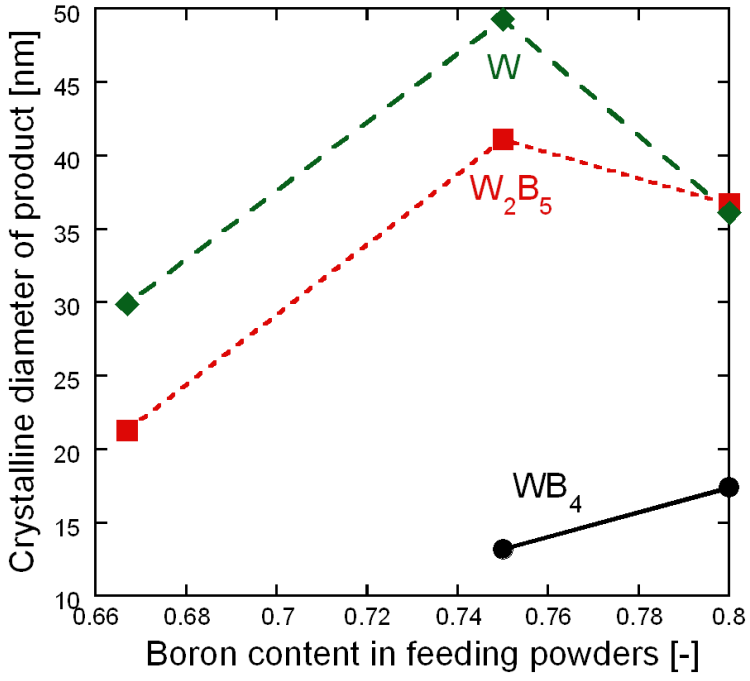

Fig. 26 Crystalline diameter of product collected from the reaction chamber wall with different boron content in feeding powders at powder feed rate 0.2 g/min.

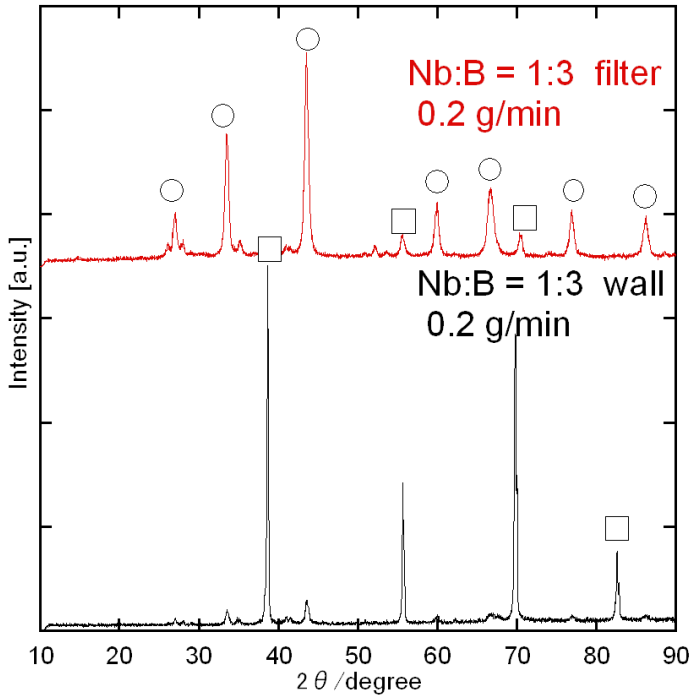

Fig. 27 XRD spectra of product from the filter and inner wall of chamber at the Nb:B = 1:3 with powder feed rate of 0.2 g/min.

(○: NbB2 □: Nb)

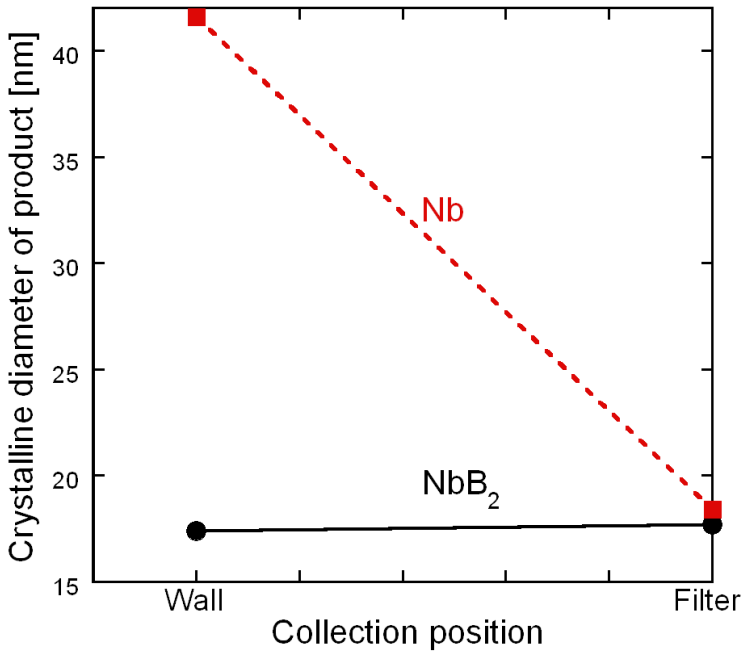

Fig. 28 Crystalline diameter of product from the filter and inner wall of chamber at the Nb:B = 1:3 with powder feed rate of 0.2 g/min.

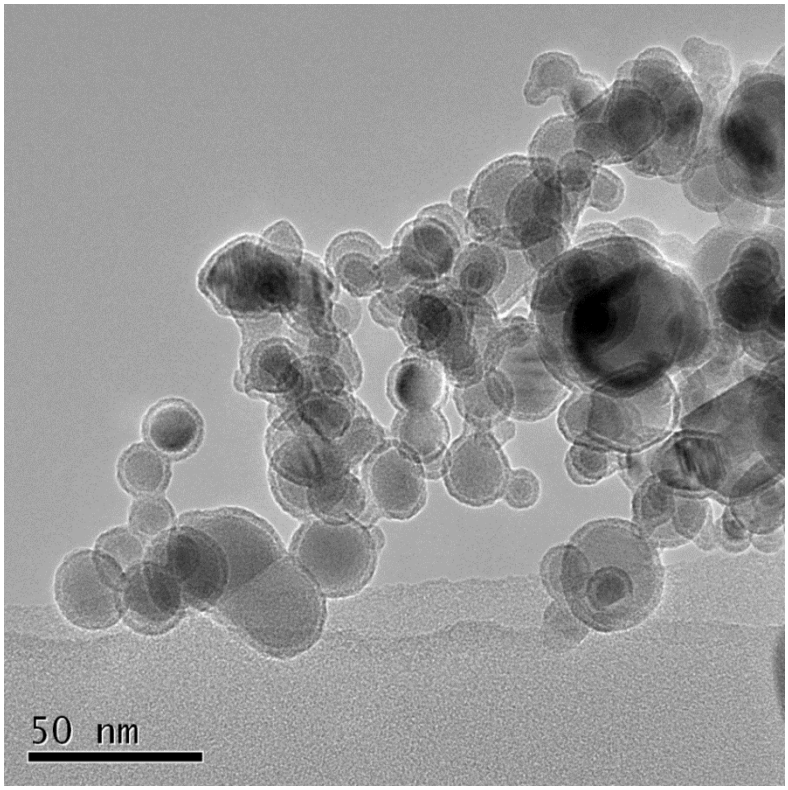

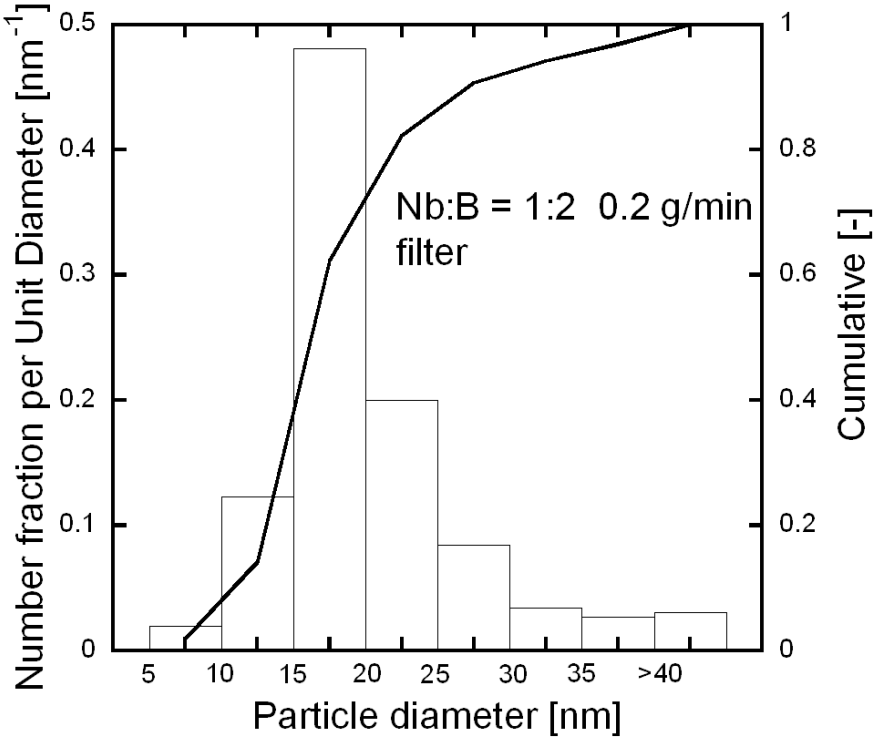

Fig. 29 TEM graph and size distribution of as-prepared product collected from the filter at the fixed initial composition of Nb:B = 1:2 with powder feed rate 0.2 g/min.

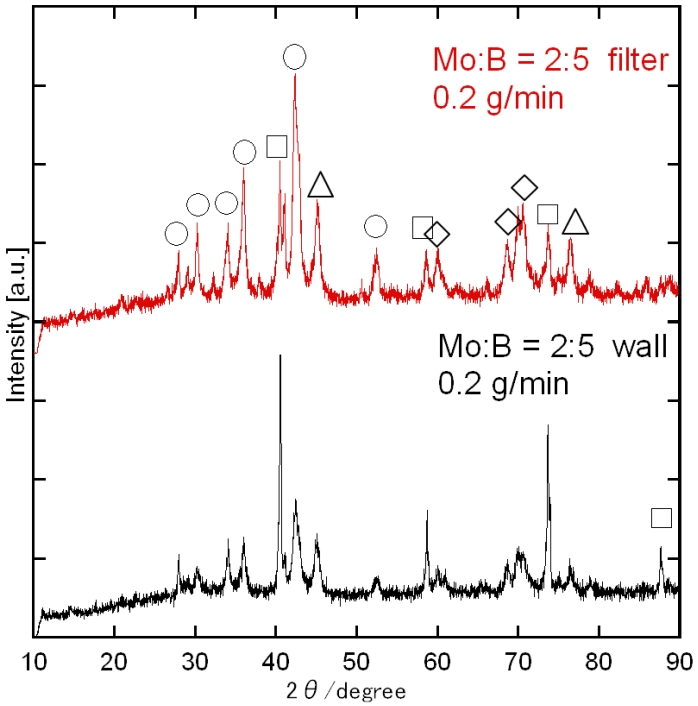

Fig. 30 XRD spectra of product from the filter and inner wall of chamber at the Mo:B = 2:5 with powder feed rate of 0.2 g/min.
(○: MoB □: Mo △: MoB_2 ◇: Mo_2B_5)

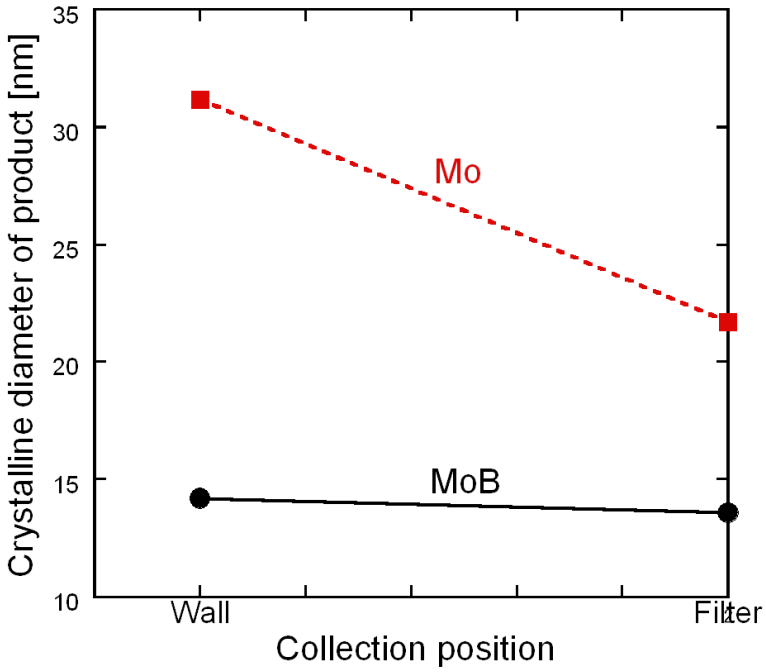

Fig. 31 Crystalline diameter of MoB and Mo from the filter and inner wall of chamber at the Mo:B = 2:5 with powder feed rate of 0.2 g/min.

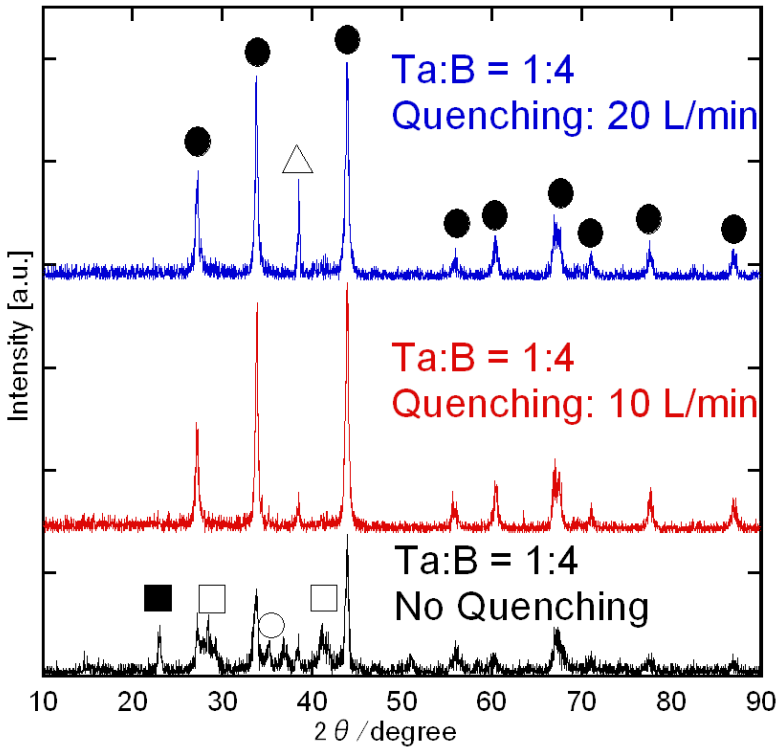

Fig. 32 XRD spectra of product at the fixed initial composition of Ta:B = 1:4 with different quenching gas flow rate.

(●: TaB_2 □: Ta_5B_6 △: Ta_3B_4 ○: TaB ■: Ta)

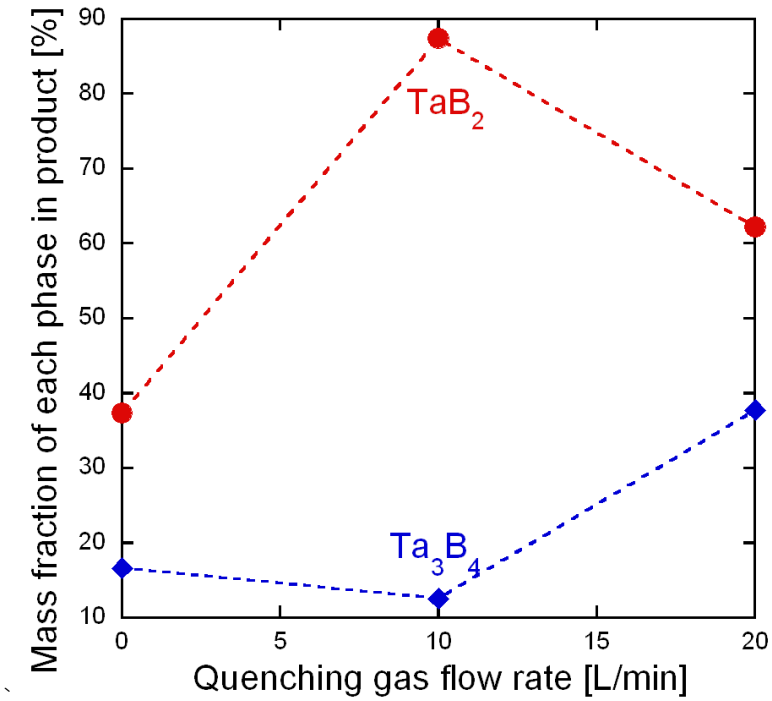

Fig. 33 Effect of quenching gas flow rate on the mass fraction of TaB_2 and Ta_3B_4 in product at the initial composition of Ta:B = 1:4.

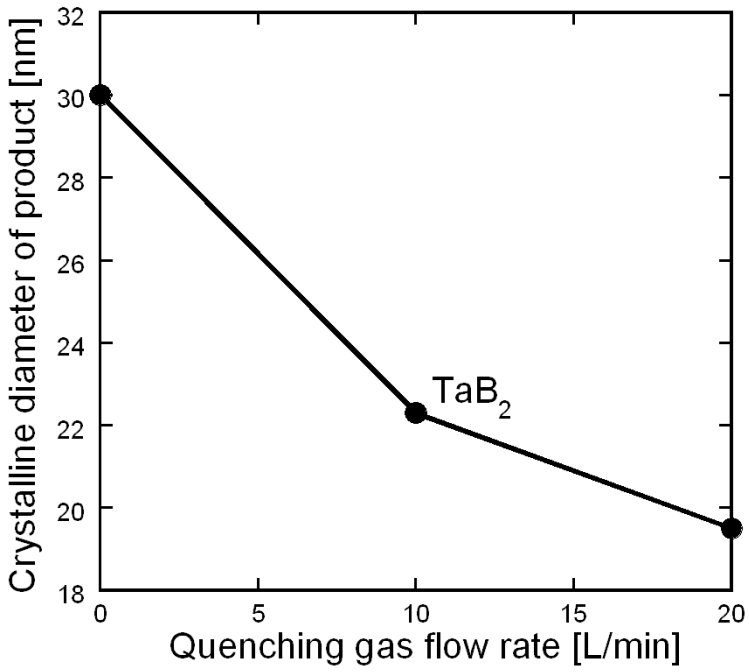

Fig. 34 Effect of quenching gas flow rate on t crystalline diameter of TaB_2 in product at the initial composition of Ta:B = 1:4.

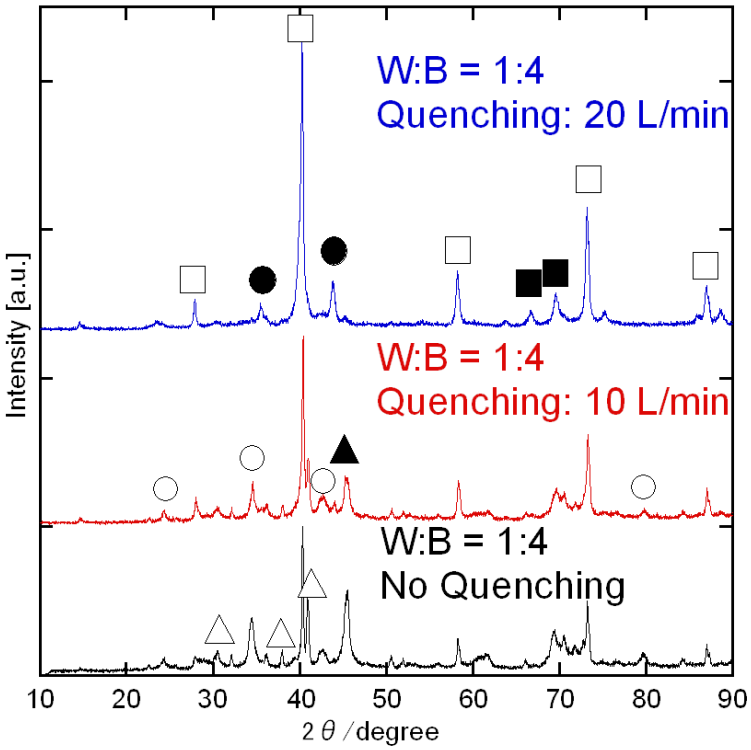

Fig. 35 XRD spectra of product at the fixed initial composition of W:B = 1:4 with different quenching gas flow rate.

(○: WB_4 □: W △: W_2B ■: WB ▲: WB_2 ●: W_2B_5)

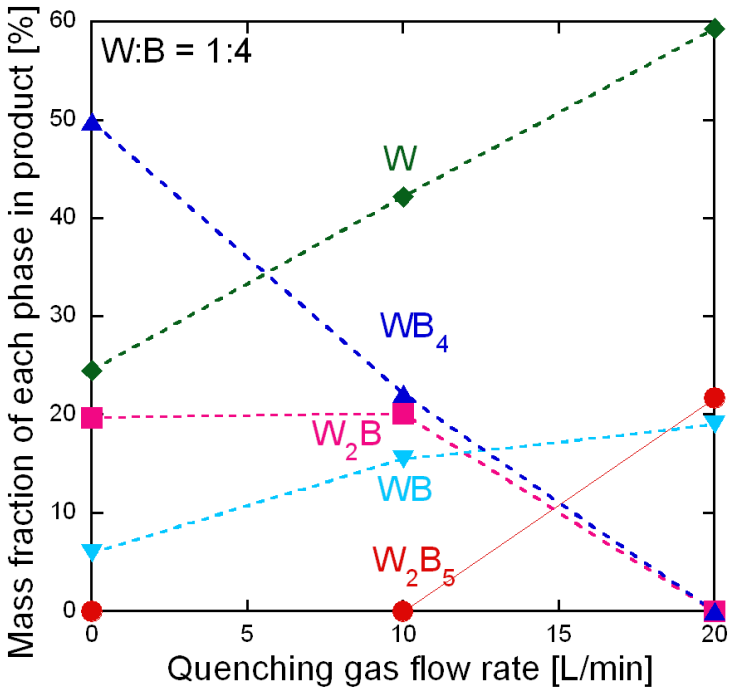

Fig. 36 Effect of quenching gas flow rate on the mass fraction of each phase in product at the initial composition of W:B = 1:4.

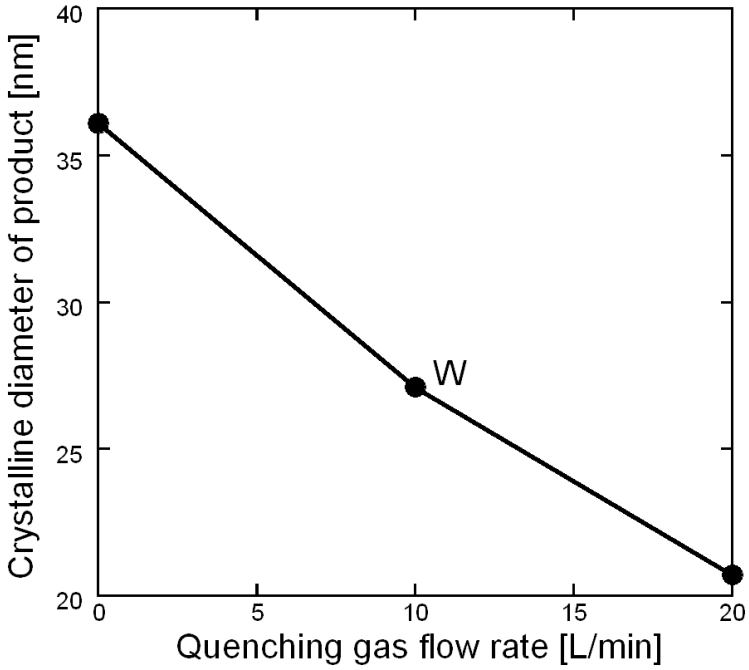

Fig. 37 Effect of quenching gas flow rate on crystalline diameter of W at the initial composition of W:B = 1:4.

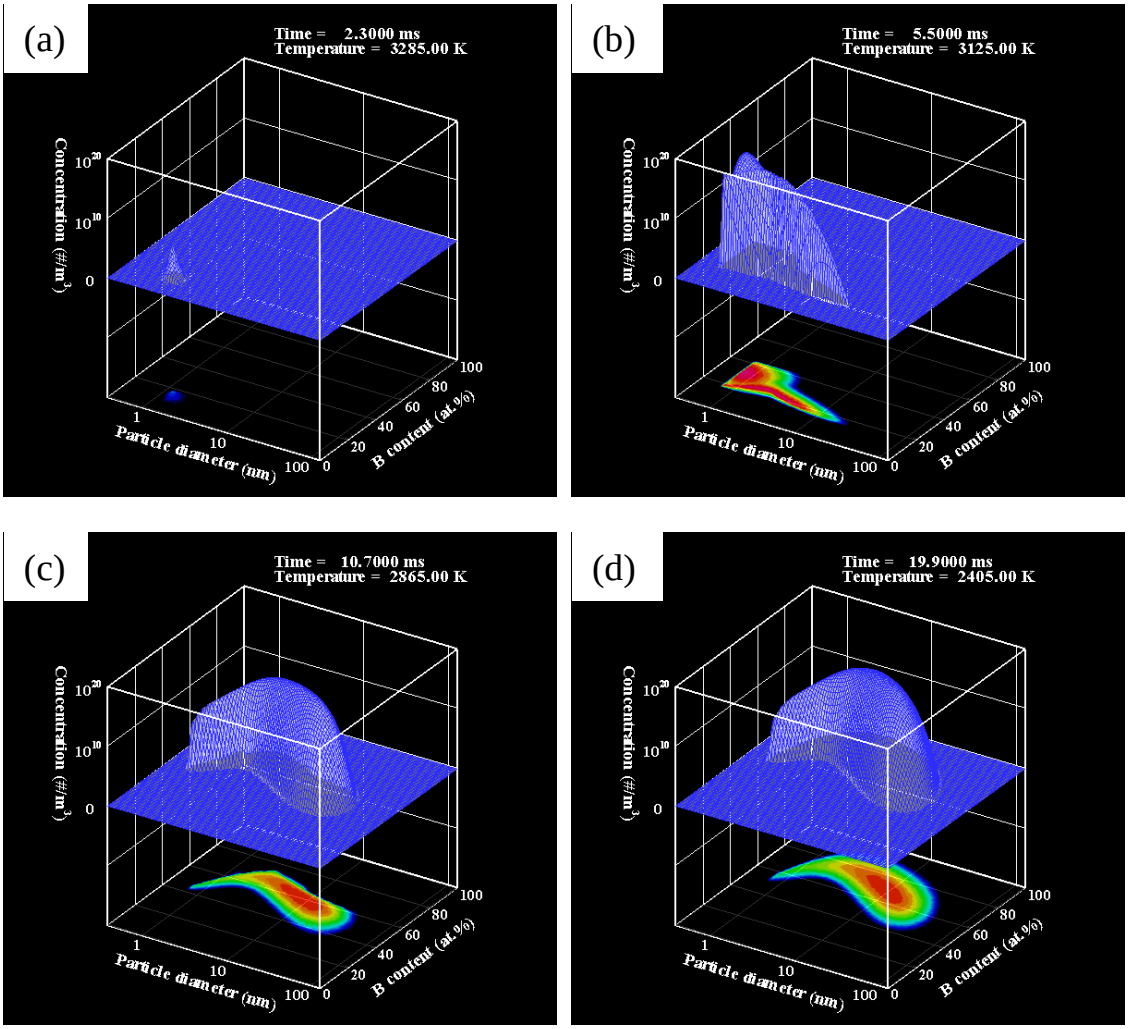

Fig. 38 The evolution of particle size-composition distribution (PSCD) at initial composition of Nb:B = 1:2: (a) 3285 K (b) 3125 K (c) 2865 K (d) 2405 K.

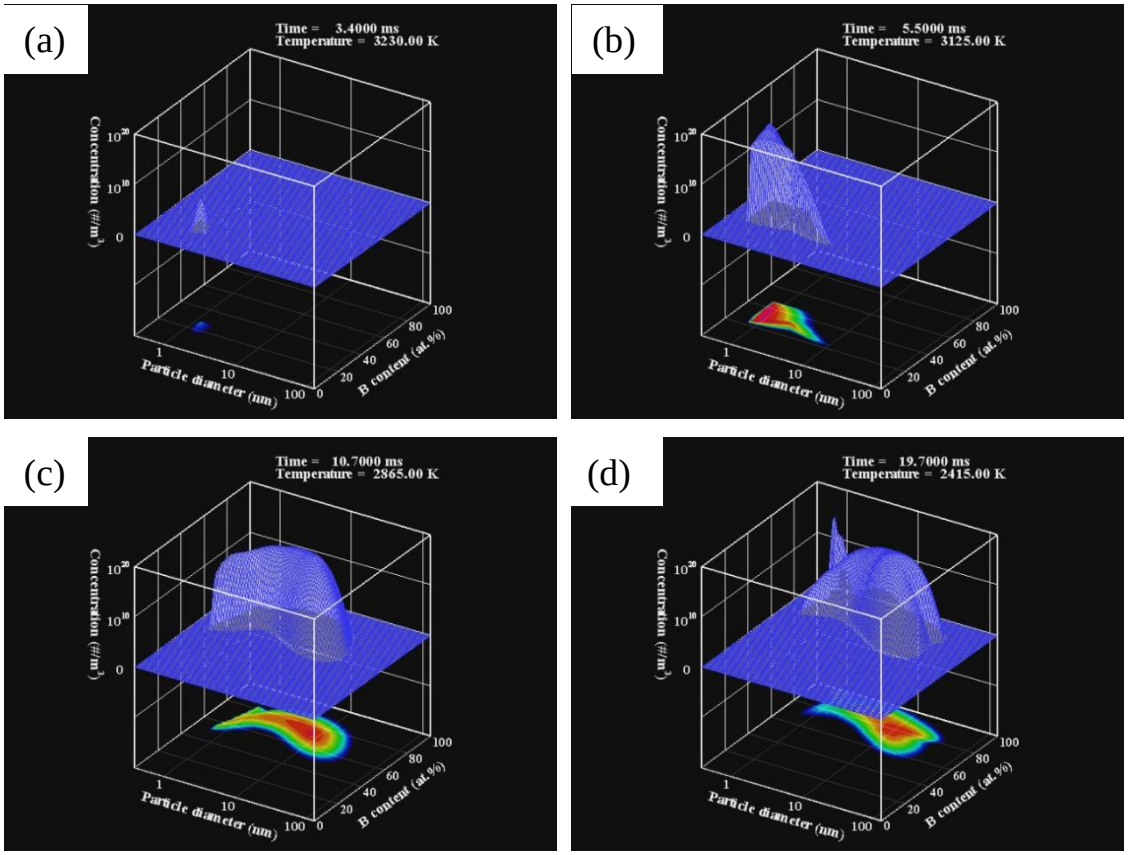

Fig. 39 The evolution of particle size-composition distribution (PSCD) at initial composition of Nb:B = 1:4: (a) 3230 K (b) 3125 K (c) 2865 K (d) 2415 K.

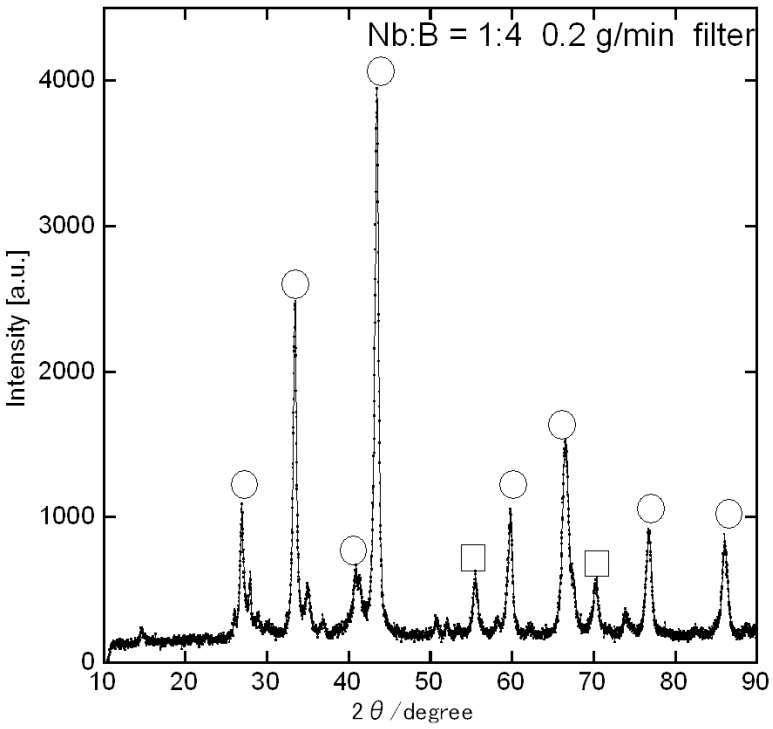

Fig. 40 XRD spectrum of product with powder feed rate of 0.2 g/min at the initial composition of Nb:B = 1:4.
(○: NbB_2 □: Nb)

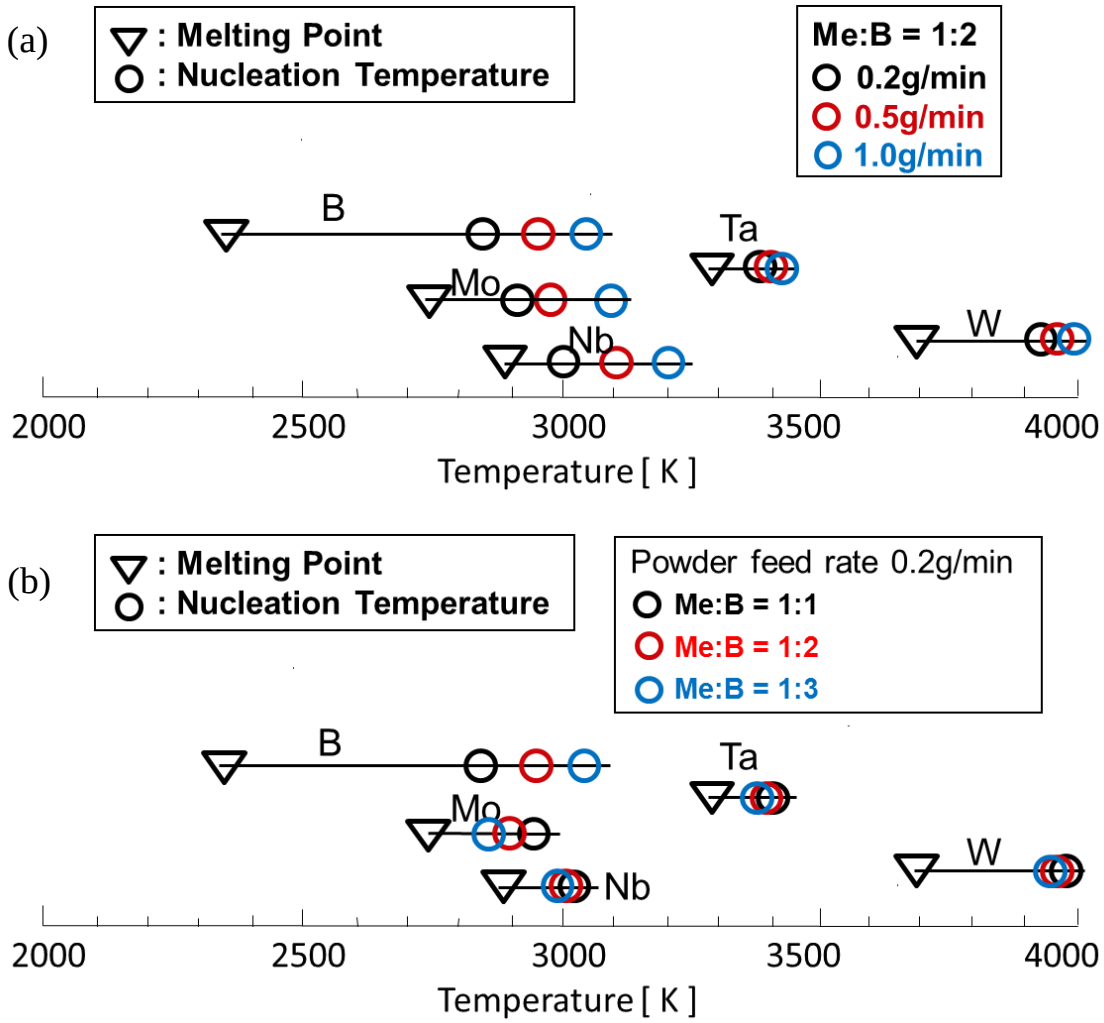

Fig. 41 Nucleation temperature at the critical saturation ratio for constituent components of boride: (a) Effect of different powder feed rate at the fixed initial composition of Me:B = 1:2; and (b) Effect of different initial composition of Me:B at the fixed powder feed rate of 0.2 g/min.

5. Synthesis of Boron Rich Boride Nanoparticle by RF Thermal Plasma

5.1 Introduction

Boron is an interesting element, tending to form 2D atomic nets and clusters in compounds. Boron-rich metal borides are characterized by boron clusters including metal atoms in the voids of them [1,2]. In general boron rich borides have interesting material properties like high hardness, high melting points, corrosion resistance, high Seebeck coefficient, low thermal conductivity, moderate electrical conductivity and great chemical stability due to the complex chemical bonding of boron atoms and unique crystal structure. Accordingly, boron-rich metal borides have diverse applications including abrasive material [3] turbine and rotor blades [4], electrode material [5-7], electronic devices, nuclear materials, semiconductor material [8], and thermoelectric material [9,10]. Especially, aluminum dodecaboride, AlB_{12}, is used as a grinding compound to replace an expensive diamond or corundum. YB_{66} has recently received much attention in some contexts. Because of its large interplanar distance and the absence of intrinsic absorption, it has been recently selected as a unique candidate for a soft X-ray monochromator in the 1-2 KeV regions for synchrotron radiation [11].

Although boron rich boride nanoparticles are strongly required in many applications due to advantages of nanoparticles in optical, chemical, mechanical, electromagnetic characteristics, they are difficult to be obtained from solution which is typically used for the preparation of nanoparticles. Several methods including melting [12,13], a long-time solid reaction in high temperature [14,15], hot-pressing [16] and chemical vapor deposition (CVD) [6,17] have been applied to synthesize these borides. Those methods, however, require high temperature and long reaction time causing contamination by reactants, crucible components, and ambient gases of nitrogen, oxygen, and hydrogen. Furthermore, the synthesis of boron-rich metal boride nanoparticle, which is an attractive form of functional material, is difficult in those methods. Although preparation of BaB_6 and LaB_6 nanoparticles by chemical reactions has been reported [18,19], it is limited in a few materials that are composed of relatively simple boron framework of B_6 octahedrons.

The RF thermal plasma is receiving much attention to synthesize nanoparticles, because it has sufficiently high temperature for the evaporation of any kinds of precursor and rapid quenching rate for nucleation and condensation [20]. RF thermal plasma which is generated in the torch without electrode has many advantages such as high enthalpy to enhance reaction kinetic and high chemical reactivity, long residence time due to the low plasma flow rate and a large volume of high temperature plasma. Additionally, the atmosphere can be chosen according to the requirement of the reaction [21-26]. In this work, boron rich aluminum and yttrium boride were synthesized by RF thermal plasma. The effect of boron content in feeding powders, powder feed rate, working gas species, raw materials and input power on the productivity of aluminum and yttrium boride were investigated. The formation mechanism of boron rich boride was studied form the consideration of Gibbs free energy and nucleation temperature.

5.2 Thermodynamic properties

1) Phase diagram of Al-B and Y-B systems

Figure 1 shows the phase diagram of Al-B system. Three incongruently melting compounds AlB_2, AlB_{10} and AlB_{12} have been identified and AlB_{12} have been reported to exist in three polymorphic forms tetragonal α and orthorhombic β. The phase transformation of AlB_{12} is based on the temperature. At 1823K, α-AlB_{12} exists, and β-AlB_{12} will appear from 1823K to 1933K. When the temperature is higher than 1933K, AlB_{12} and AlB_{10} can co-exist in the Al-B system. AlB_{12} contains 93 at% B. When the range of B is 0~66.7 at%, AlB_2 can be generated.

Figure 2 displays the phase diagram of Y-B system. The equilibrium phase diagram of Y-B binary system includes five intermetallic compounds: YB_2, YB_4, YB_6, YB_{12} and YB_{66}. The mixture of YB_2 and YB_4 occupy a composition range from 66 to 80 at% B. The mixture of YB_4 and YB_6 exist between 80 and 87 at% B. YB_{12} and YB_6 co-exist from 87 to 92 at % B. YB_{66} can be generated with 98 at% B.

2) Gibbs free energy

Figure 3 shows the relationship between the temperature and Gibbs free energy of Al-B system. Based on this graph, the Gibbs free energy of AlB_{12} and AlB_2 are negative at the melting point of boron, which indicates these borides are easy to generate. The Gibbs free

energy of AlB_2 is relatively high compared with that of AlB_{12}, we can know the synthesis of AlB_{12} may be much easier than that of AlB_2.

3) Saturation vapor pressure

The saturation pressures of vapors decrease drastically along with the temperature decrease and fall below their actual vapor pressures. This supersaturated state consequently leads to production of nuclei by nucleation. The vapor pressure ratios of Al/B and Y/B are on the order of 10^6 and 10^4 at the melting points of Al and Y, respectively. The saturation vapor pressure of constituent components of borides is displayed in **Figure 4**. Preparation of borides with large difference in vapor pressure of the constituent components is quite difficult. Therefore, the control of condensation process is important for preparation of boride nanoparticles by RF thermal plasma.

5.3 Experimental

5.3.1 Experimental apparatus

Experimental setup is shown in **Figure 5**. The raw powder mixture was injected into thermal plasma flame generated by a RF thermal plasma system. An RF power supply (JHS-35M, JEOL, Japan) connected to a plasma torch provided the input power from 24 to 33 kW at the RF frequency of 4 MHz. The RF plasma torch was attached to a reactor where nanoparticles were synthesized due to the rapid quenching of evaporated raw material. The operating pressure was constant at 101.3 kPa during the synthesis process of metal boride nanoparticles.

5.3.2 Experimental conditions

In Al–B and Y-B systems for the synthesis of boron-rich boride nanoparticles, diameters of raw powders were 10 μm for aluminum, AlB_2 (99.9%, Kojundo Chemical Laboratory, Japan) or 10 μm for yttrium tetraboride (99.0%, Japan New Metals Co. Ltd.) and 45 μm for boron (99.0%, Kojundo Chemical Laboratory, Japan). The composition of raw material was controlled at 1:5, 1:12, and 1:15 for the molar ratio of Al:B at the fixed powder feed rate of 0.1 g/min as listed in **Table** 1, while it was controlled at 1:12, 1:40, 1:66, and 1:100 for Y-B system. Raw materials were mixed uniformly at a given composition, and then the powder mixture was injected into

the RF thermal plasma by a powder feeder. Argon 2 L/min was used as carrier gas for the feeding of raw powder mixture

After the precursors were introduced into the plasma region with Ar carrier gas, they were instantaneously evaporated due to the very high enthalpy of RF thermal plasma. Therefore, the boron rich boride nanoparticles are synthesized from the gas phase.

The gas mixture of Ar 60 L/min and He 5 L/min was used as the sheath gas, which was injected into the RF plasma torch along with the inner wall of plasma confinement tube. Ar or He was injected into the plasma torch as the inner gas, in order to examine the effect of inner gas species on the production efficiency of boron rich boride nanoparticles. Since the inner gas was injected into the RF plasma torch in axial direction around a powder feeding probe, its thermal conductivity has a strong effect on the evaporation of the raw powders.

5.3.3 Analytical method

The analytical methods are the same as those which are introduced in detail in Ch. 2.

5.4 Experimental results and discussion

5.4.1 Effect of powder feed rate

1) Al-B system

Figure 6 (1) shows XRD spectra of product at initial composition of Al:B = 1:15 with different powder feed rate. Ar was used as inner gas. With low powder feed rate of 0.1 g/min, the peak of AlB_{12} can be identified. Increasing powder feed rate, AlB_{12} is not observed. Because there are much more boron with high boiling point in the feeding powders at high powder feed rate, the evaporation of boron is interfered. The difference between the amount of the Al vapor and B vapor increases, which is not beneficial for the generation of AlB_{12}.

Figure 6 (2) presents the effect of powder feed rate on the intensity of each phase in product. The intensity of AlB_{12} decreases with the increase of powder feed rate.

5.4.2 Effect of boron content in feeding powders

1) Al-B system

Figure 7 (1) shows XRD spectra of product at different boron content in feeding powders. First, the intensity of AlB_{12} is increased with increasing boron composition in raw powders. The nucleation temperature of boron is higher than that of aluminum. As a result, boride nanoparticles are produced from the condensation of boron and aluminum monomers on boron nuclei according to the synthesis mechanism of metal borides. Therefore, enough quantity of boron nuclei and monomers should be secured by increasing the composition ratio of boron in the raw powder for the synthesis of boron-rich metal boride nanoparticles. In addition, the peak for AlB_{10} is also produced together with AlB_{12} as shown in fig. 7, because both AlB_{12} and AlB_{10} nanoparticles are composed of icosahedral B_{12} units. Therefore, boron clustering from boron nuclei and monomers takes place at first, followed by chemical reactions between boron clusters and Al monomers in the high temperature environment of RF thermal plasma forming AlB_{12} and AlB_{10} nanoparticles.

A large amount of unreacted raw materials seems to be caused by the high boiling point of boron. Since the boron boiling temperature of 4,200 K is higher than the aluminum boiling temperature of 2,792 K, the evaporation of boron takes relatively long time compared with aluminum. As a result, boron vapors are located along with the thermal plasma flame, while most of aluminum is evaporated immediately after the injection of raw powders in the upstream region. Such different evaporation positions for each element lead to the insufficient boron nucleation and chemical reaction between boron and aluminum precursors. The vapor pressure of boron in the thermal plasma flame is enhanced with increasing boron content in feeding raw powders. Therefore, the area of boron nuclei expands in a high boron content allowing the boridation reaction with evaporated aluminum.

Figure 7 (2) shows the effect of boron content in feeding powders on the phase composition of product. According this graph, the relative XRD integrated intensity of AlB_{12} increases with the increase of boron content in feeding powders. While the intensity of unreacted Al decreases with increasing boron content in feeding powders.

Figure 8 (a), (b) and (c) show TEM graphs of as-prepared product at powder feed rate of 0.1 g/min with initial composition of Al:B = 1:5, 1:12, 1:15, respectively. Irregular shaped polyhedral nanoparticles are observed. It seems to be caused by the crystal structure of boron cluster composed of B_{12} icosahedrons and metal atoms [27]. **Figure 9** (a), (b) and (c) display the particle size distribution of as-prepared product at powder feed rate of 0.1 g/min with initial composition of Al:B = 1:5, 1:12, 1:15, respectively. The average diameter of product at Al:B =

1:5 is 19.5 nm. The mean value was evaluated by analyzing 200 particles in TEM images. The average diameter of product at Al:B = 1:12 is 21.9 nm. The average diameter of product at Al:B = 1:15 is 20.8 nm. Because there are large amount of unreacted boron and aluminum in product, the relationship between the boron content in feed powders and the particle average diameter is difficult to conclude.

2) Y-B system

Experimental results on the synthesis of YB_{66} from evaporated YB_4 and B powders are presented in **Figure 10 (1)**. The composition ratio of boron in the raw powders was controlled at the fixed input plasma power of 30 kW with powder feed rate of 0.1 g/min. As shown in fig. 10, peak intensity for YB_{66} is increased with increasing the composition ratio of boron in raw materials. Although YB_{66}-related peaks at 22° and 25° for 2-theta values are appeared in the lowest boron contents in raw materials as shown in fig. 10 (a), these two peaks also correspond to YB_4. In addition, XRD pattern only for YB_{66} was very weak to be detected in fig. 10 (a). Therefore, high boron content in the raw material is essentially required for the synthesis of YB_{66} nanoparticles in RF thermal plasma. However, the peak intensity of YB_{66} is still weak compared with that of YB_4 even in the highest boron composition ratio in the raw material as depicted in fig. 10 (d). In order to synthesize YB_{66} nanoparticles in the RF thermal plasma, large amount of boron nuclei and monomers are required because YB_{66} is composed of 13-icosahedron unit of $(B_{12})_{12}B_{12}$ which is called supericosahedron [28].

Figure 10 (2) displays the effect of boron content in feeding powders on the produced particle composition for Y-B. The relative XRD integrated intensity of YB_{66} increases with increasing boron content in feeding powders.

Figure 11 (a), (b) and (c) show TEM graphs of as-prepared product at powder feed rate of 0.1 g/min with initial composition of Y:B = 1:12, 1:66, 1:100, respectively. It is seen that the particles with different morphology and various size exist. Most particles seem cubic or rectangular. **Figure 12** (a), (b) and (c) display the particle size distribution of as-prepared product at powder feed rate of 0.1 g/min with initial composition of Y:B = 1:12, 1:66, 1:100, respectively. The average size of product at Y:B = 1:12 is 14.4 nm. The mean value was evaluated by analyzing 200 particles in TEM images. The average size of particle at Y:B = 1:66 is 16.6 nm. The average size of product at Y:B = 1:100 is 20.8 nm. The particle size increases with the increase of boron content in feeding powders.

Since YB_{66} has unique cubic morphology, TEM images for nanoparticles produced in Y-B system were analyzed to evaluate the ratio of YB_{66} nanoparticles in the final product. From the analysis of 200 particles for each condition, the ratio of rectangular nanoparticle in TEM images is presented in **Figure 13**. The number of YB_{66} nanoparticle is increased with increasing the composition ratio of boron in the raw material, and this result is in a good agreement with XRD results in fig. 10 (2).

Fig. 8 (b) and 9 (b) show the TEM graph and size distribution of particles at the phase composition of Al:B = 1:12. Fig. 11 (a) and 12 (a) show the TEM graph and size distribution of particles at the phase composition of Y:B = 1:12. The average size of particle in Al-B system is 21.9 nm, while the average size in Y-B system is 14.4 nm. Compared with fig. 9 (b) and fig. 12 (a), the size in Al-B system is larger than that in Y-B system. In the synthesis of boride nanoparticles by RF thermal plasma, the growth time is the temperature area from the nucleation temperature of boron to the melting point of metal. The growth time in Al-B system is much wider than the growth time of yttrium boride nanoparticles. Additionally, the surface tension of Al is 0.90 N/m, which is a little higher than the surface tension of Y (0.799 N/m). The high surface tension leads to large particle size. Therefore, the average size of particles in Y-B system is smaller than the particle size in Al-B system.

5.4.3 Effect of raw materials

1) Al-B system

The effect of raw material on the phase composition of product is displayed in **Figure 14**, which shows XRD spectra of product at initial composition of Al:B = 1:12 with powder feed rate of 0.1 g/min. Raw material Al or AlB_2 was used. Only when AlB_2 and B were used as precursors, the peaks of AlB_{12} and AlB_{10} can be identified. The main product is unreacted boron. After the injection of raw materials Al and B, Al will evaporate soon due to the lower boiling point, while it takes long time to evaporate boron with high boiling point. So the Al vapor exists in the upstream of plasma flow and the B vapor generates in the downstream of plasma flow. Due to the diffusion of Al in the downstream, it is difficult for the synthesis of AlB_{12}. Compared with Al, the boiling point of AlB_2 is higher. The vapor phase of Al and B can co-exist in the same region during the evaporation process. It is possible to generate AlB_{12} nanoparticles.

5.4.4 Effect of work gas species

1) Carrier gas

Figure 15 (1) shows XRD spectra of product at different boron content in feeding powders with He carrier gas flow rate of 4 L/min. For Al:B = 1:5, only the peak of AlB_{12} is observed. Increasing boron content in feeding powders Al:B = 1:12 and 1:15, the peaks of AlB_{10} and AlB_{12} can both be detected. Compared with fig. 8, the AlB_{12} was identified only at the initial composition Al:B = 1:15 with Ar carrier gas and AlB_{10} cannot be generated. Because He carrier gas with high thermal conductivity can make the evaporation of raw materials easy. In addition, the intensity of AlB_{12} and AlB_{10} increases with increasing the boron content in feeding powders according to the XRD measurement.

The relationship between the phase composition of product and boron content in feed powders with He carrier gas is displayed in **Figure 15 (2)**. The relative XRD integrated intensity of AlB_{10} and AlB_{12} increase with increasing boron content in feed powders.

However, helium is not suitable to be used as carrier gas due to the lightness and small momentum of helium. It is difficult to introduce raw powders with high powder feed rate into the plasma with low He carrier gas flow rate. But if a large amount of He is injected into the plasma, the plasma will be unstable. So the powder feed rate is limited with He carrier gas. In order to improve the evaporation of raw materials, the use of He as inner gas is considered.

2) Inner gas

Although boron-rich compounds were identified in the case of Al:B = 1:15 for raw material composition, measured intensities of their XRD peaks were considerably weak under the condition of Ar inner gas. Since a slow evaporation of boron is regarded as the main reason for the low productivity of aluminum borides, He was used as the inner gas of thermal plasma. The thermal conductivity of He is about four times higher than that of Ar around 10,000 K, which is a typical temperature for the upstream region of RF thermal plasma flame for the heating of feeding raw powder [29,30]. The use of He as inner gas is an effective way to heat up raw materials, because the inner gas is introduced into plasma generation region surrounding the powder feeding probe.

Figure 16 (1) displays XRD results of products from RF thermal plasma synthesis at different boron content in feeding powders with He inner gas. Effects of raw material composition on product were examined at the fixed input power of 33 kW like as the synthesis experiment with Ar inner gas. The peak of AlB_{12} is clearly seen in the highest boron content

case of Al:B = 1:15. Furthermore, boron-rich compounds of AlB_{10} and AlB_{12} are synthesized even in the case of Al:B = 1:12 due to the enhanced evaporation of raw materials. Therefore, He inner gas is essentially required to synthesize aluminum borides with a high production rate.

The relationship between the phase composition of product and boron content in feeding powders with He inner gas is displayed in **Figure 16 (2)**. The relative XRD integrated intensity of AlB_{10} and AlB_{12} increase with increasing boron content in feed powders.

Figure 17 (1) shows XRD spectra of as-prepared particles with different gas species of carrier gas and inner gas at initial composition of Al:B = 1:15. When Ar was used as carrier gas and inner gas at the same time, the peak of AlB_{12} can be identified. The peak of AlB_{10} is not observed and the dominant product is unreacted B. When He was used as inner gas or carrier gas, AlB_{12} and AlB_{10} are both generated and the relative intensity of AlB_{12} in product in the highest. The peaks of unreacted Al are not observed. The use of He improves the generation of AlB_{12} and AlB_{10} nanoparticles.

The effect of work gas species on phase composition with different initial composition in Al-B system is displayed in **Figure 17 (2)**. Although, the relative intensity of AlB_{12} increases with increasing boron content in feeding powders in all of the cases. The relative intensity of AlB_{12} is higher when He was used as carrier gas or inner gas.

5.4.5 Effect of plasma power

1) Al-B system

The increase of input power is the most convenient method to enhance the evaporation of raw material in RF thermal plasma process for nanoparticle synthesis. Since the maximum power used in this work was limited at 33 kW, effects of input power on the synthesis of boron-rich aluminum borides were examined changing the plate power from 24 to 33 kW as shown in **Figure 18 (1)**. In these experiments, the raw material composition and inner gas condition were fixed at Al:B = 1:15 and He 5 L/min, respectively. In the XRD result of fig. 18, intensities of aluminum boride peaks are enhanced with increasing the input power, while unreacted boron is reduced at the same time. It is because the high temperature area of thermal plasma is enlarged with increasing the plate power. As a result, the evaporation of boron in the plasma upstream region is increased in the case of high input power.

Figure 18 (2) displays the effect of input power on the relative XRD integrated intensity of AlB_{10} and AlB_{12}. The relative XRD integrated intensity of AlB_{10} and AlB_{12} both increase with

the increase of input power. In addition, the synthesis of AlB_{12} is easier than that of AlB_{10}.

5.5 Nucleation temperature

The nucleation temperature at the critical saturation ratio is presented in **Figure 19** for constituent components of borides; fig. 19 (a) was drawn at the boron molar content of 66.7% with different powder feed rate, and fig. 19 (b) was calculated at the fixed powder feed rate of 0.2 g/min with different initial composition of Me:B. The detailed explanation of nucleation temperature is in Ch. 6. The difference of nucleation temperature between metal and boron is an important factor for the controlled preparation of boride nanoparticles in RF thermal plasmas. The nucleation temperatures of Al and Y are lower than that of B. The nucleation of boron first, and then the cluster is formed. The condensation of Al or Y takes place dominantly. The forming of cluster makes the generation of metal boride difficult. In other words, the evaporation of boron is important in the generation of boron rich metal boride nanoparticles.

5.6 Conclusions

In this chapter, boron-rich boride nanoparticles of AlB_{12} and YB_{66} were synthesized by the RF thermal plasma. The effect of boron content in feeding powders, powder feed rate, working gas species, raw materials and input power on the phase composition and crystalline size of product were investigated. The evaporation of boron is a key process for the growth of boron rich boride nanoparticles. For this reason, the productivity of aluminum boride is increased in conditions of high input power, high boron content in raw material and the use of thermally conductive helium as inner gas. Synthesized aluminum boride nanoparticles were polyhedral shape due to the unique crystal structure of boron-rich compounds. Whereas cubic YB_{66} nanoparticles is found when YB_4 and B powders is used as the raw material. Because boron clusters are required to form boron-rich compound, the content of boride nanoparticles in final products is increased with increasing the composition ratio of boron in the raw material. In the RF thermal plasma, boron vapor is nucleated because nucleation temperature of boron is higher than that of aluminum or yttrium. With the clustering of boron nuclei, aluminum or yttrium monomers condensed onto them leading to the growth of boron-rich boride nanoparticles.

References

[1] B. Albert and H. Hillebrecht, Angewandte Chemie International Edition, 48, 8640 (2009)

[2] I. Higashi, M. Kobayshi, Y. Takahashi, S. Okada, K. Hamano, Journal of Crystal Growth, 99, 998 (1990)

[3] A.Y. Artamonov, A.I. Bezykornov, A.N. Ivanov, Powder Metallurgy and Metal Ceramics, 5, 722 (1966)

[4] B.S. Mann, Wear, 224, 8 (1999)

[5] T.T. Xu, J.G. Zheng, A.W. Nicholls, S. Stankovich, R.D. Piner, R.S. Ruoff, Nano Letters, 4, 2051 (2004)

[6] H. Zhang, Q. Zhang, J. Tang, L.C. Qin, Journal of American Chemical Society, 127, 2862 (2005)

[7] S. Zhou, J. Zhang, D. Liu, Z. Lin, Q. Huang, L. Bao, R. Ma, Y. Wei, Acta Materialia, 58, 4978 (2010)

[8] H.J. Tromp, P.V. Gelderen, P.J. Kelly, G. Brocks, P.A. Bobbert, Physical Review Letters, 87, 016401 (2001)

[9] H. Werheit, Materials Science and Engineering B, 29, 228 (1995)

[10] Y. Imai, M. Mukaida, M. Ueda, A. Watanabe, Intermetallics, 9, 721 (2001)

[11] T. Tanaka, Y. Ishizawa, J. Wong, Z.U. Rek and M. Rowen, Japanese Journal of Applied Physics Series, 10, 110 (1994)

[12] M.G. Kanatzidis, R. Pottgen, W.T. Jeitschko, Angewandte Chemie International Edition, 44, 6996 (2005)

[13] M. Bouchacourt and F. Thevenot, Journal of Material Science, 20, 1237 (1985)

[14] G. Wang, J.R Brewer, J.Y. Chan, D.R. Diercks and C.L. Cheung, Journal of Physical Chemistry C, 113, 10446 (2009)

[15] Y. Liu, W.J. Lu, J.N. Qin and D. Zhang, Journal of Alloys and Compounds, 431, 337 (2007)

[16] K. Koumoto, T. Seki, C.H. Pai and H. Yanagida, Journal of the Ceramic Society of Japan,

100, 853 (1992)

[17] T. Goto, J. Li and T. Hirai, Proc. 11th Int. Cod. Composite Mater., (Edited lby M. L. Scott), 603

[18] X. Zhao, G. Min, International Journal of Modern Physics B, 23, 1553 (2009)

[19] Y. Yuan, L. Zhang, L. Liang, K. He, R. Liu, G. Min, Ceramics International, 37, 2891 (2011)

[20] F.E. Kruis, H. Fissan and A. Peled, Journal of Aerosol Science, 29, 511 (1998)

[21] M.I. Boulos, IEEE Transactions on Plasma Science, 19, 1078 (1991)

[22] J.Y. Huang, T. Ishigaki, T. Tanaka, S. Horiuchi, Journal of Materials Science, 33, 4141 (1998)

[23] T. Watanabe, K. Fujiwara, Chemical Engineering Communications, 191, 1343 (2004)

[24] T. Watanabe, Y. Abe, Y. Ishii, K. Adachi, Transactions of the Materials research Society of Japan, 29, 3407 (2004)

[25] Y. Cheng, T. Watanabe, Journal of Chemistry Engineering Japan, 44, 583 (2011)

[26] M.T. Swihart, Current Opinion in Colloid and Interface Science, 8, 127 (2003)

[27] I. Higashi, Journal of Solid State Chemistry, 154, 168 (2000)

[28] S.M. Richards and J.S. Kasper, Acta Crystallographica, B25 237 (1969)

[29 A.B. Murphy, IEEE Transactions on Plasma Science, 25, 809 (1997)

[30] A.B. Murphy, Journal of Physics D, 34, R151 (2001)

Table 1 Operating condition for the synthesis of boron rich boride nanoparticles

Process parameters	Value
Raw materials size	Al and YB_4 = 10 μm, B = 45 μm
Metal to boron ratio	Al:B = 1:2, 1:12, 1:15
	Y:B = 1:12, 1:40, 1:66, 1:100
Sheath gas and flow rate	Ar-He(60:5) 65 L/min
Inner gas and flow rate	He 5 L/min
Carrier gas and flow rate	Ar 3 L/min
Plasma power	24, 27, 30, 33 kW
Reactor pressure	101.3 kPa
Frequency	4 MHz
Powder Feed rate	0.1-1.0 g/min

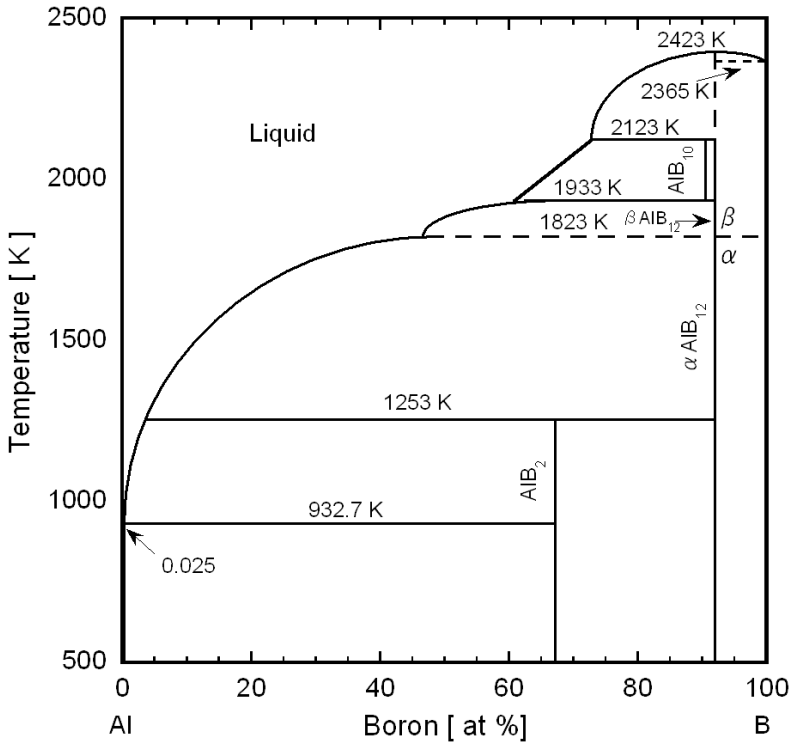

Fig. 1 Binary Al–B phase diagram.

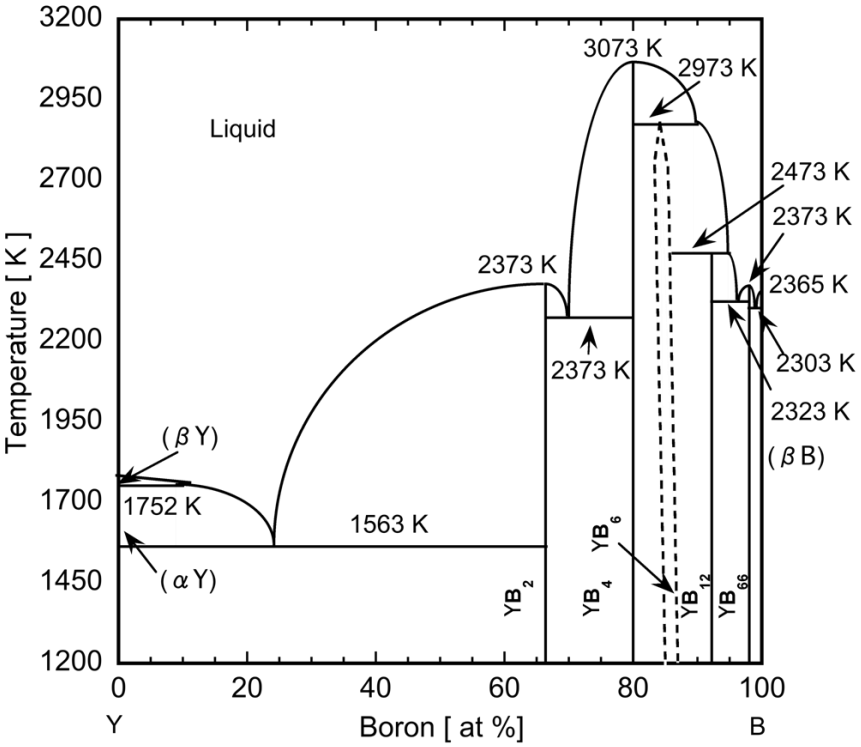

Fig. 2 Binary Y–B phase diagram.

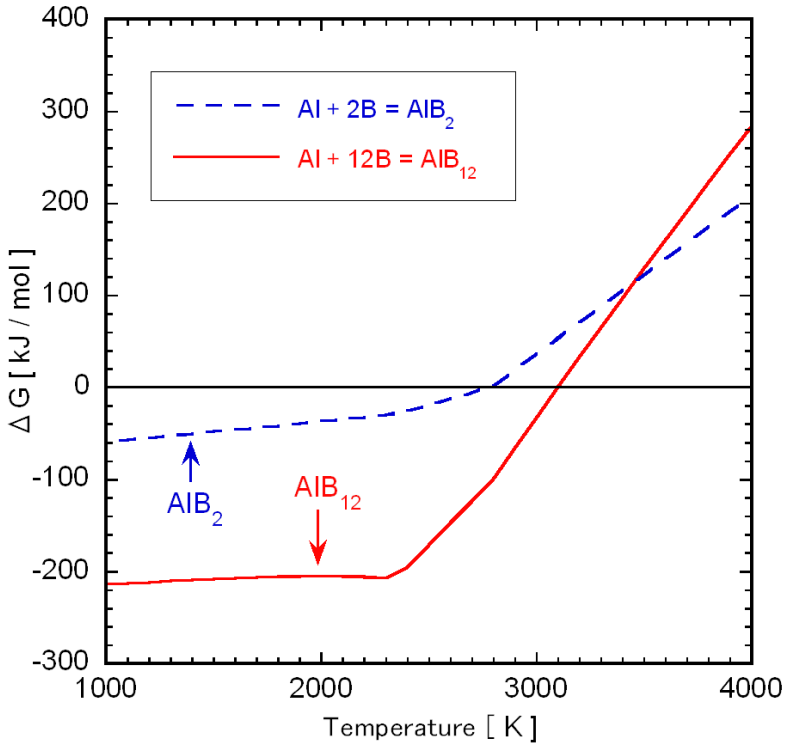

Fig.3 Gibbs free energy of Al-B system.

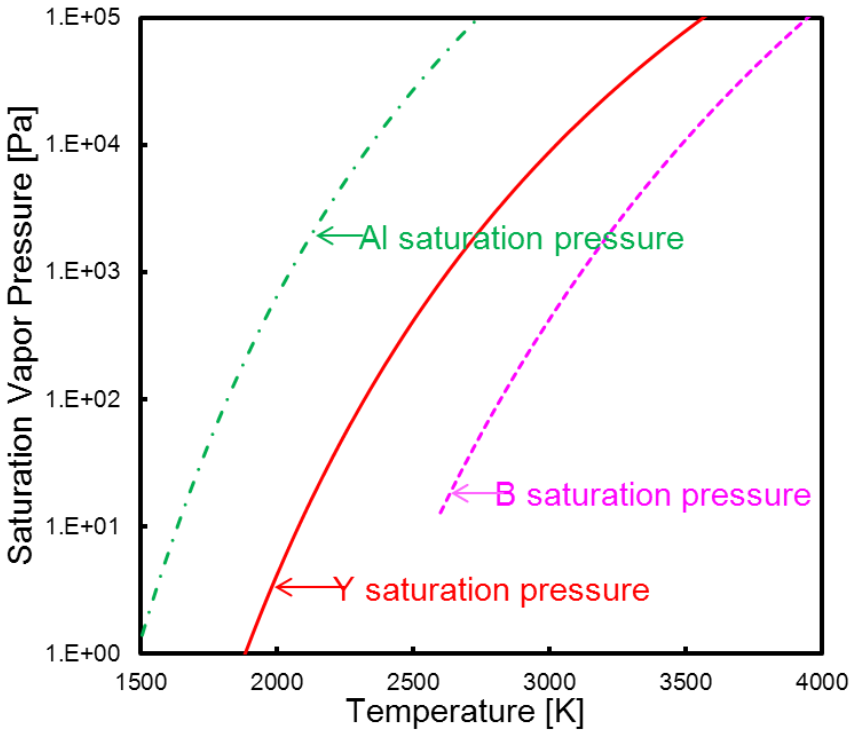

Fig.4 Saturation vapor pressure of Al, Y and B.

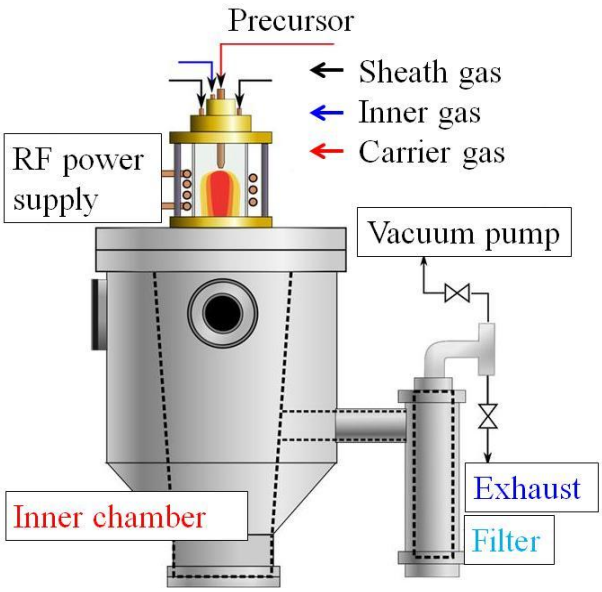

Fig. 5 Experimental set-up of RF thermal plasma for the synthesis of boride nanoparticles.

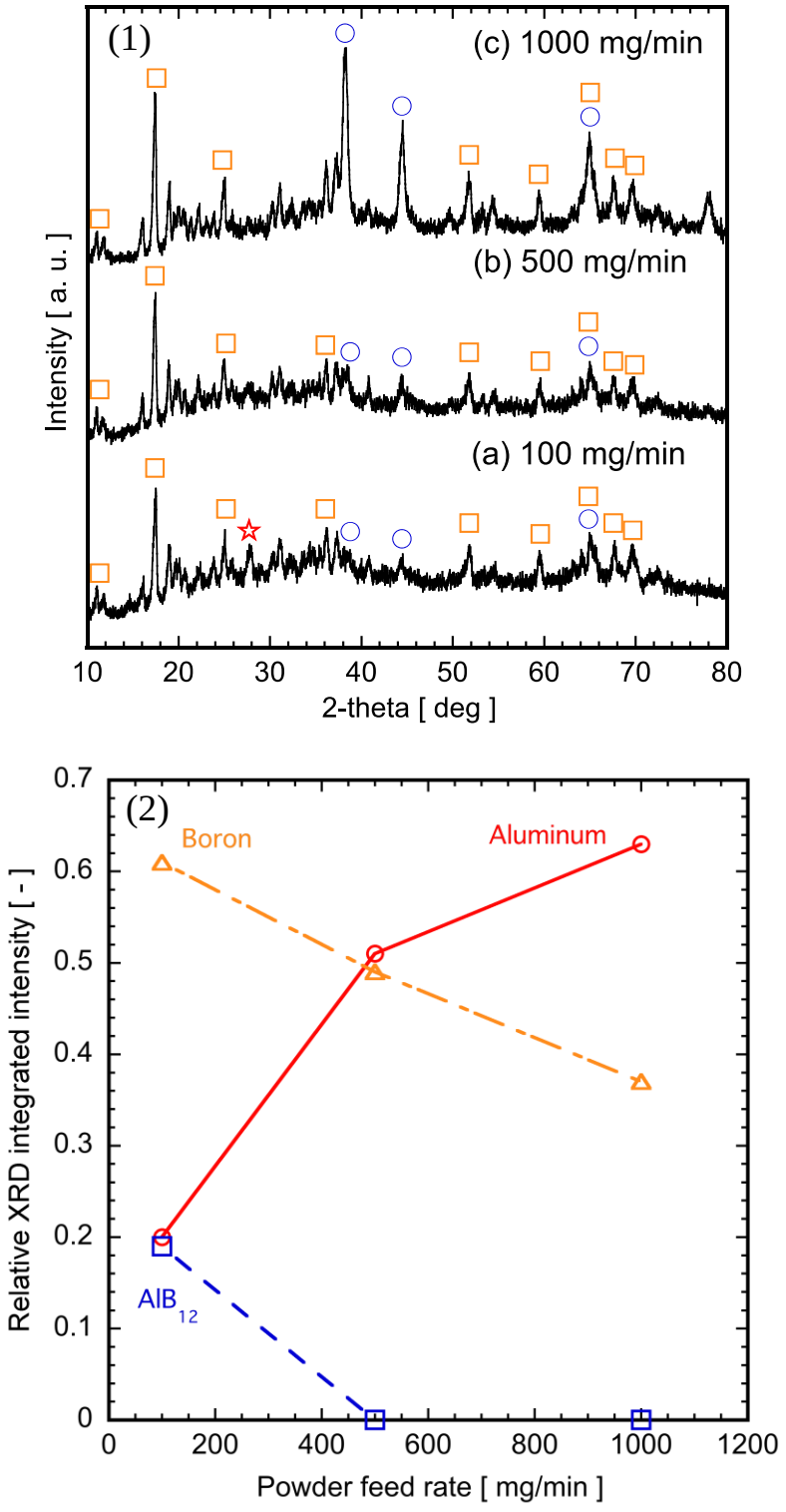

Fig. 6 XRD spectra and integrated intensity of prepared particles for Al-B system;
Powder feed rate: (a) 100, (b) 500, (c) 1000 mg/min
Composition ratio of Al and B: 1:15; Inner gas: Ar.
(☆: AlB_{12}, △: AlB_{10}, □: B, ○: Al)

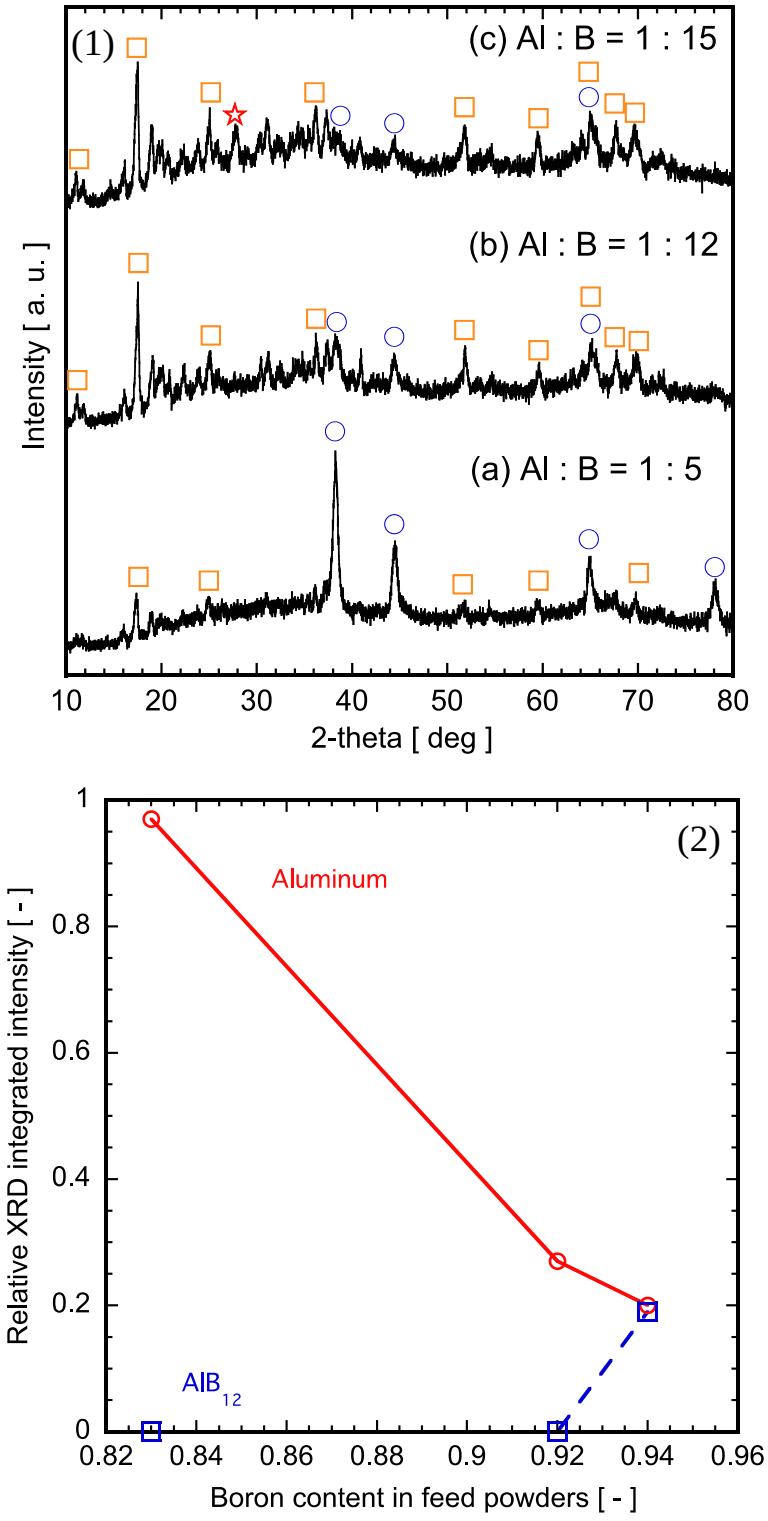

Fig. 7 XRD spectra and integrated intensity of prepared particles for Al-B system;
Composition ratio of Al and B: (a) 1:5, (b) 1:12, (c) 1:15;
Inner gas: Ar.
(☆: AlB_{12}, △: AlB_{10}, □: B, ○: Al)

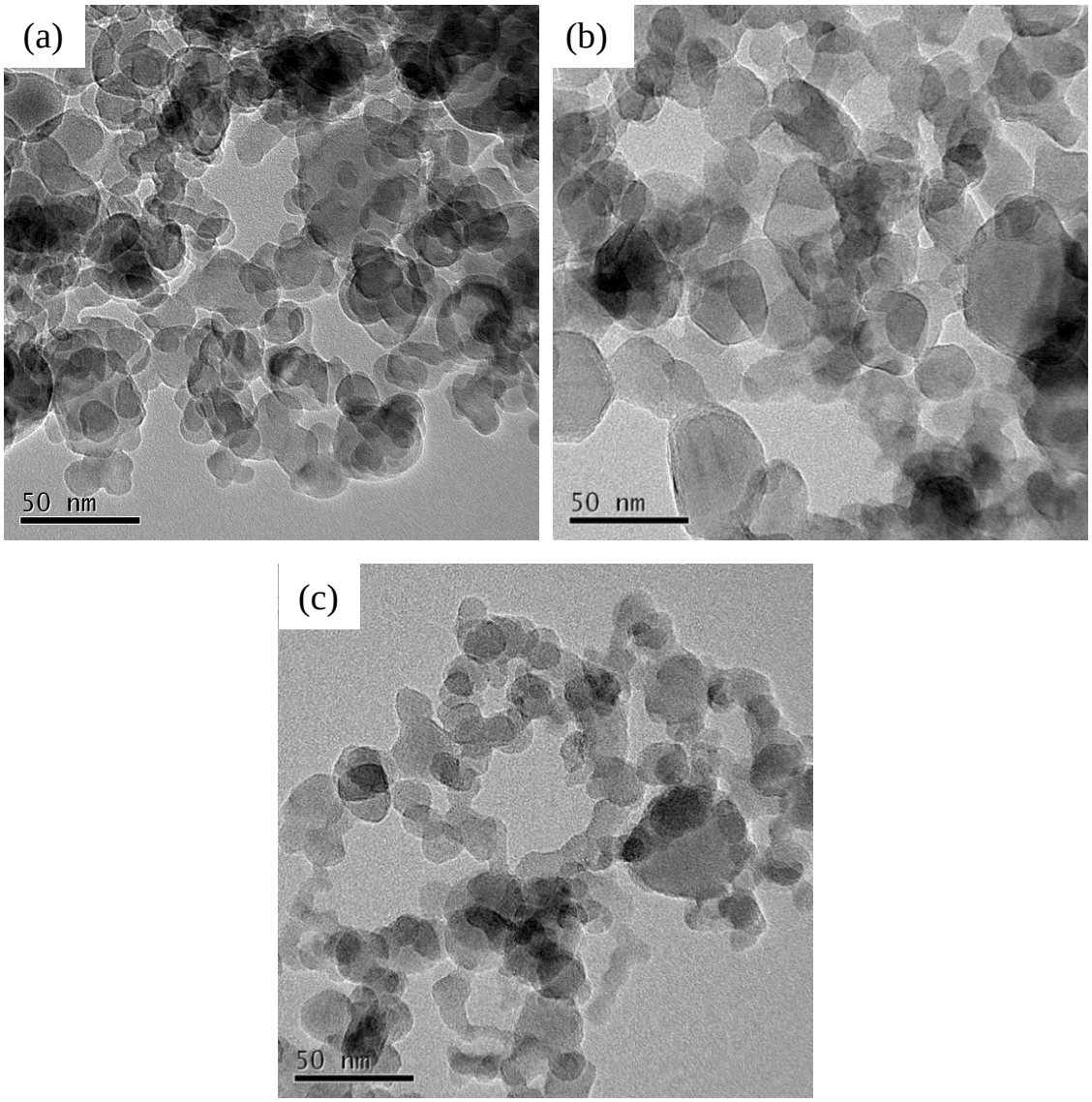

Fig. 8 TEM photographs of nanoparticles for Al-B system;
Inner gas: He. (a) 1:5 (b) 1:12 (c) 1:15.

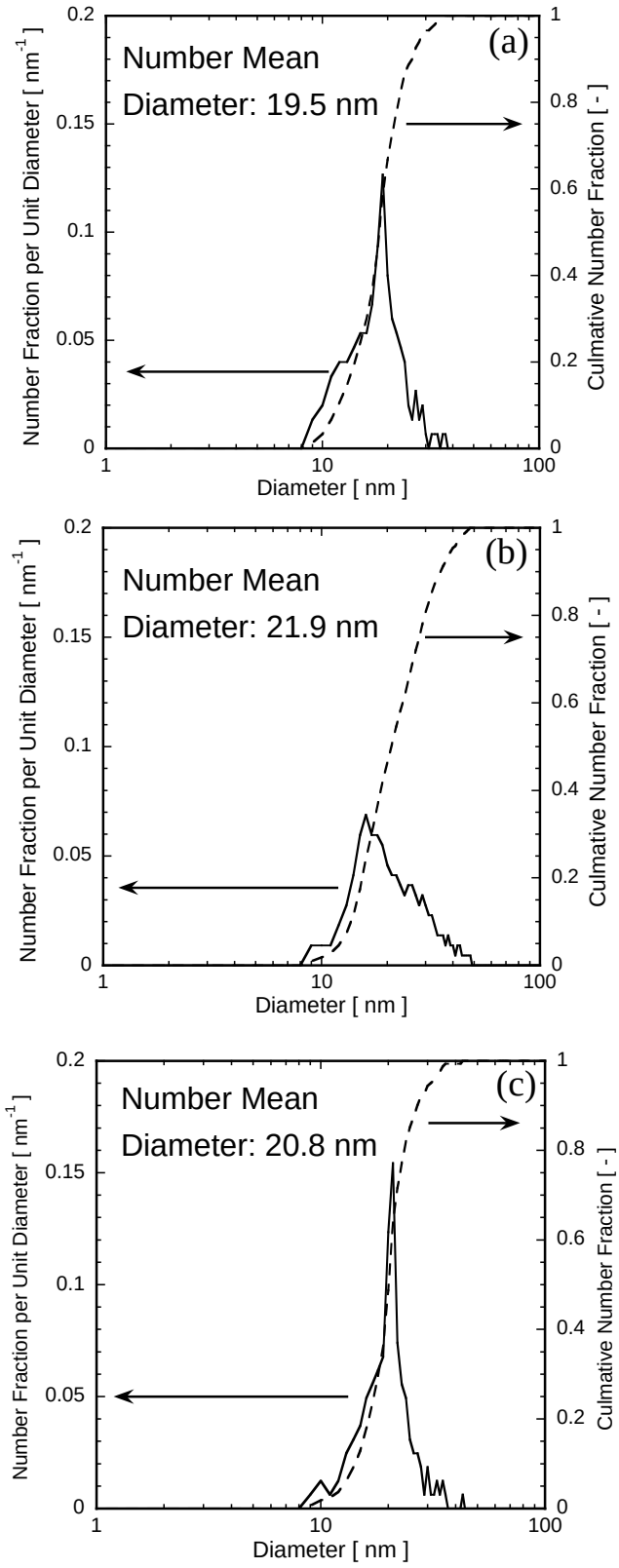

Fig. 9 Particle size distribution of nanoparticles; Inner gas: He. (a) 1:5 (b) 1:12 (c) 1:15.

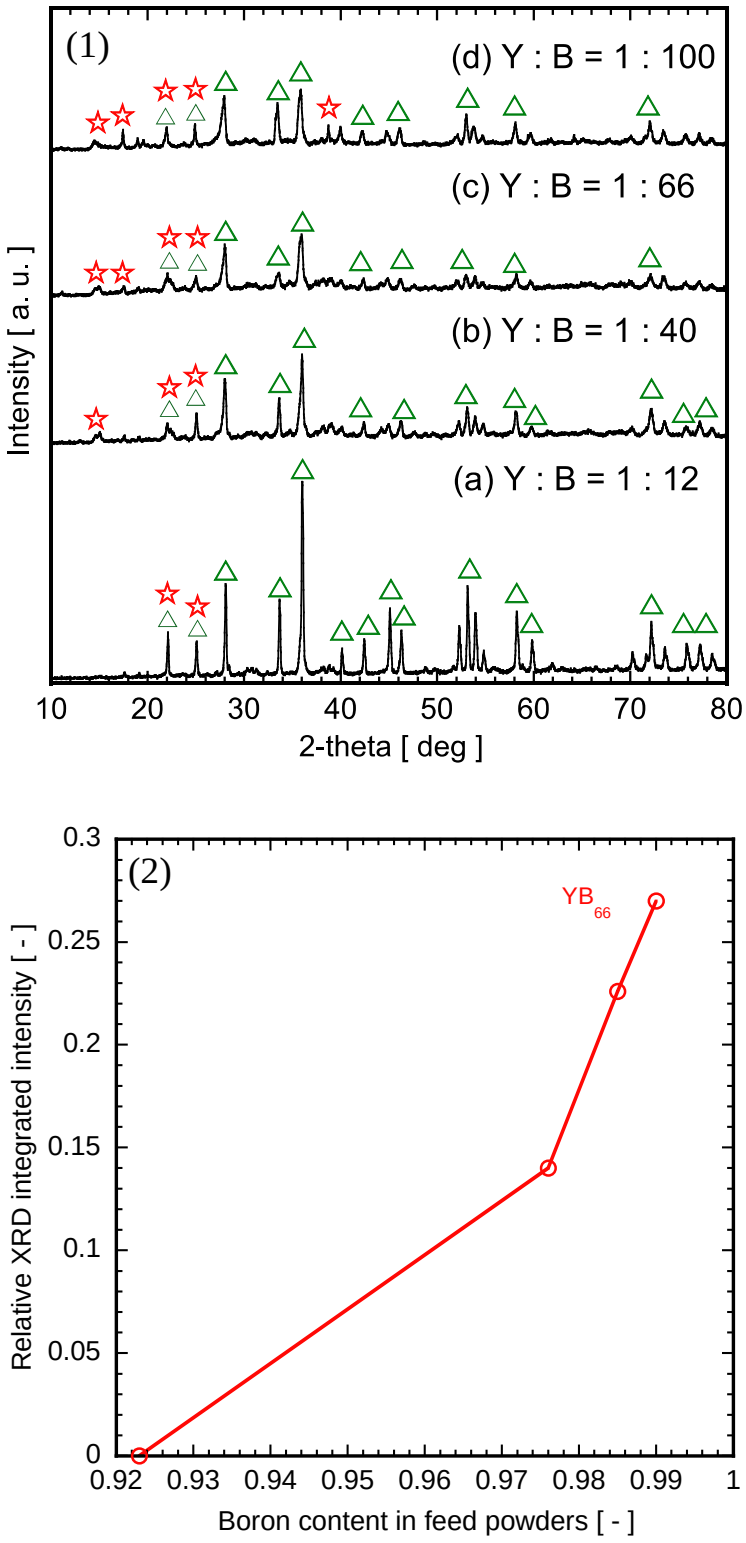

Fig. 10 XRD spectra and integrated intensity of prepared particles for Y-B system; Composition ratio of Al and B: (a) 1:12, (b) 1:40, (c) 1:66, (d) 1:100; Inner gas: He.
(☆: YB_{66}, ▲: YB_4)

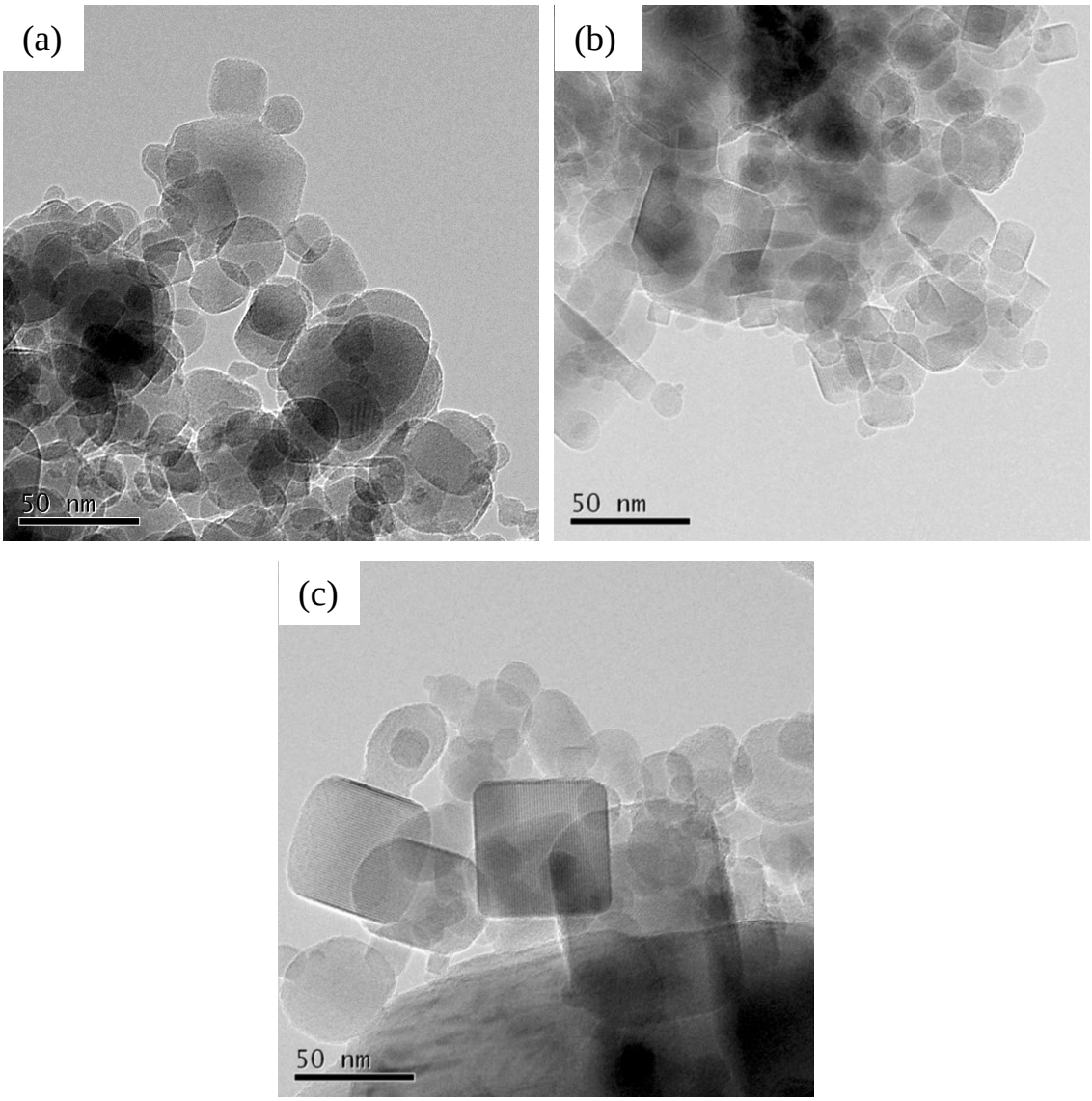

Fig. 11 TEM photographs of nanoparticles for Y-B system;
Inner gas: He. (a) 1:12, (b) 1:66, (c) 1:100

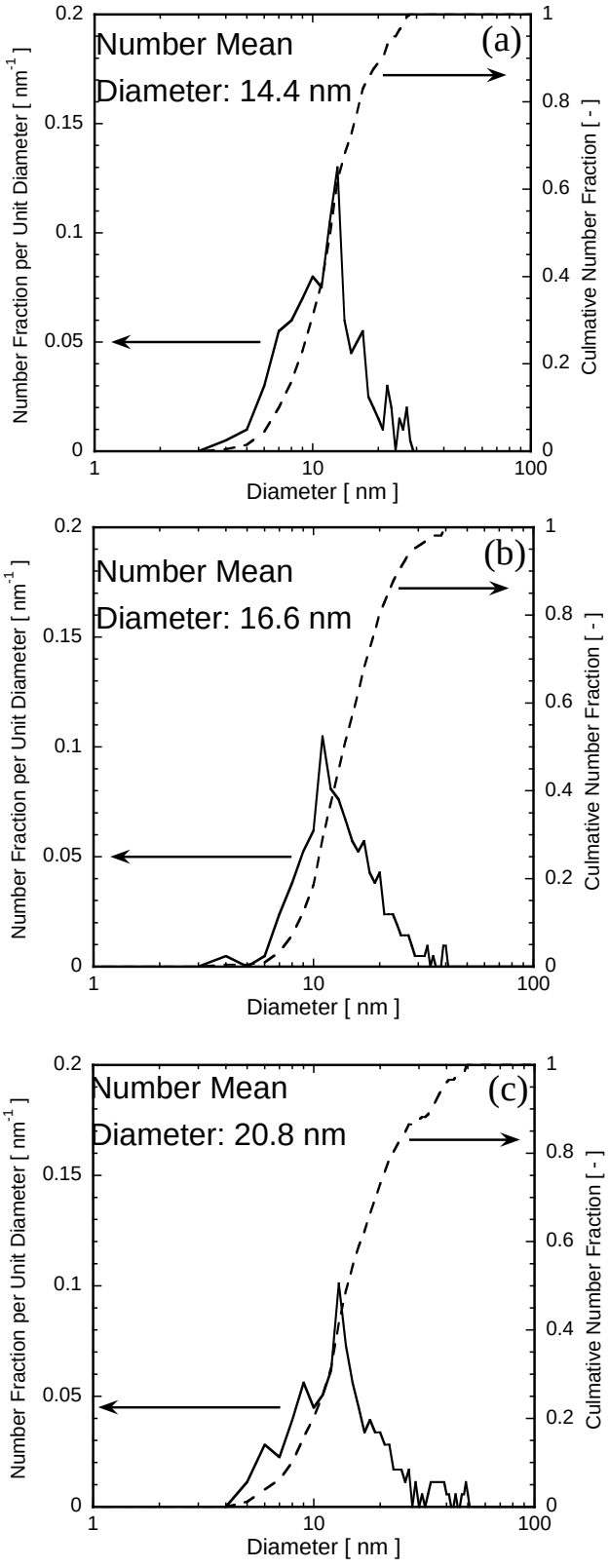

Fig. 12 Particle size distribution of nanoparticles; Inner gas: He. (a) 1:12, (b) 1:66, (c) 1:100.

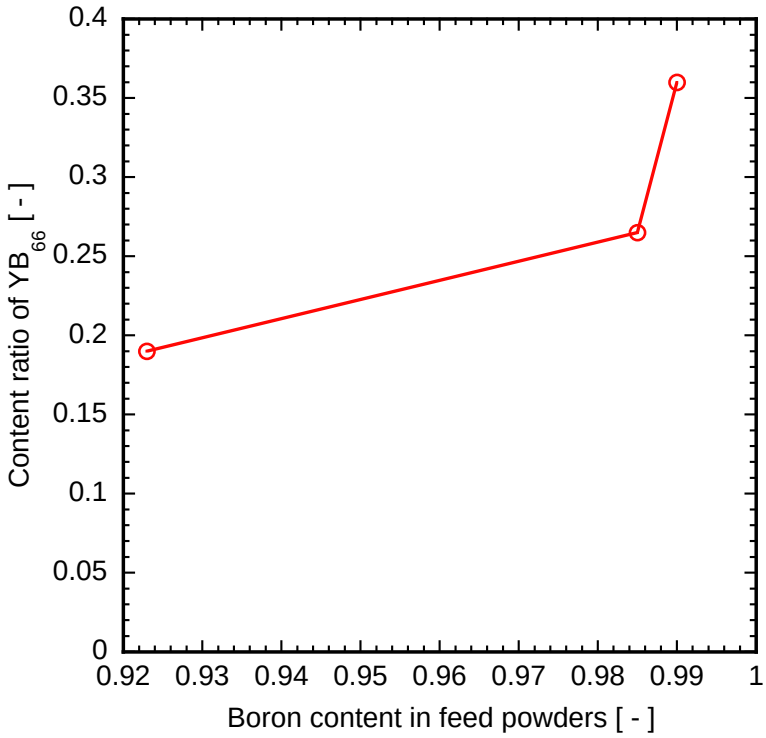

Fig.13 Effect of boron content in feed powder on the produced particle composition estimated from TEM photographs.

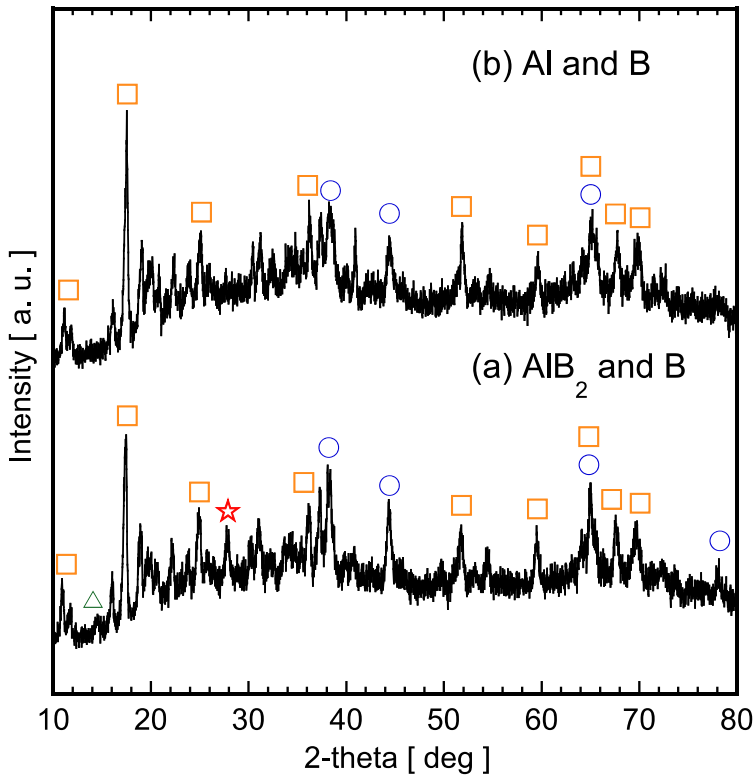

Fig.14 XRD spectra chart of prepared particles for Al-B system;
Raw material powders: (a) AlB_2 and B, (b) Al and B;
Composition ratio of Al and B: 1:15; Inner gas: Ar.
(☆: AlB_{12}, △: AlB_{10}, □: B, ○: Al)

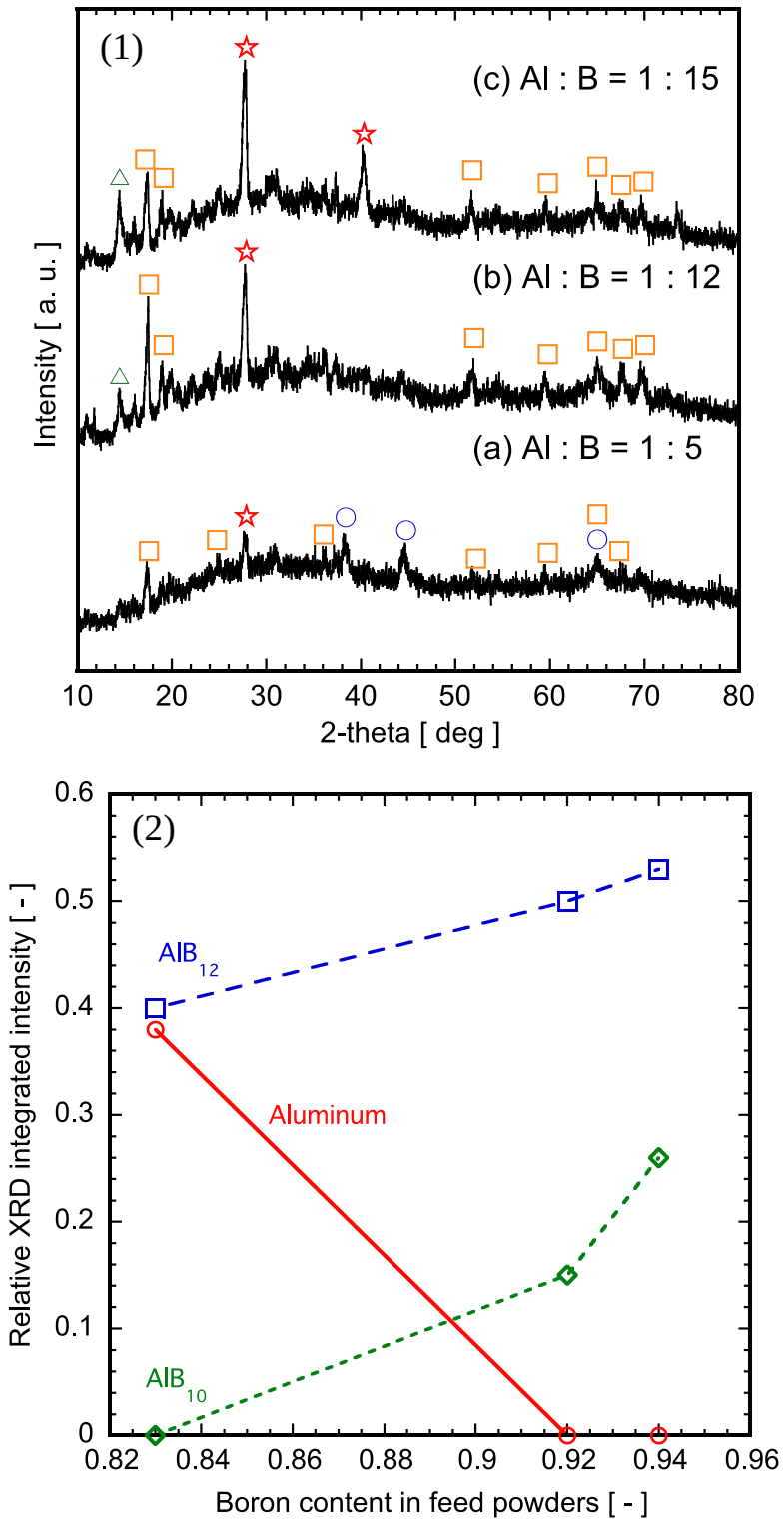

Fig. 15 XRD spectra and integrated intensity of prepared particles for Al-B system;
Composition ratio of Al and B: (a) 1:5, (b) 1:12, (c) 1:15;
Carrier gas: He.
(☆: AlB_{12}, △: AlB_{10}, □: B, ○: Al)

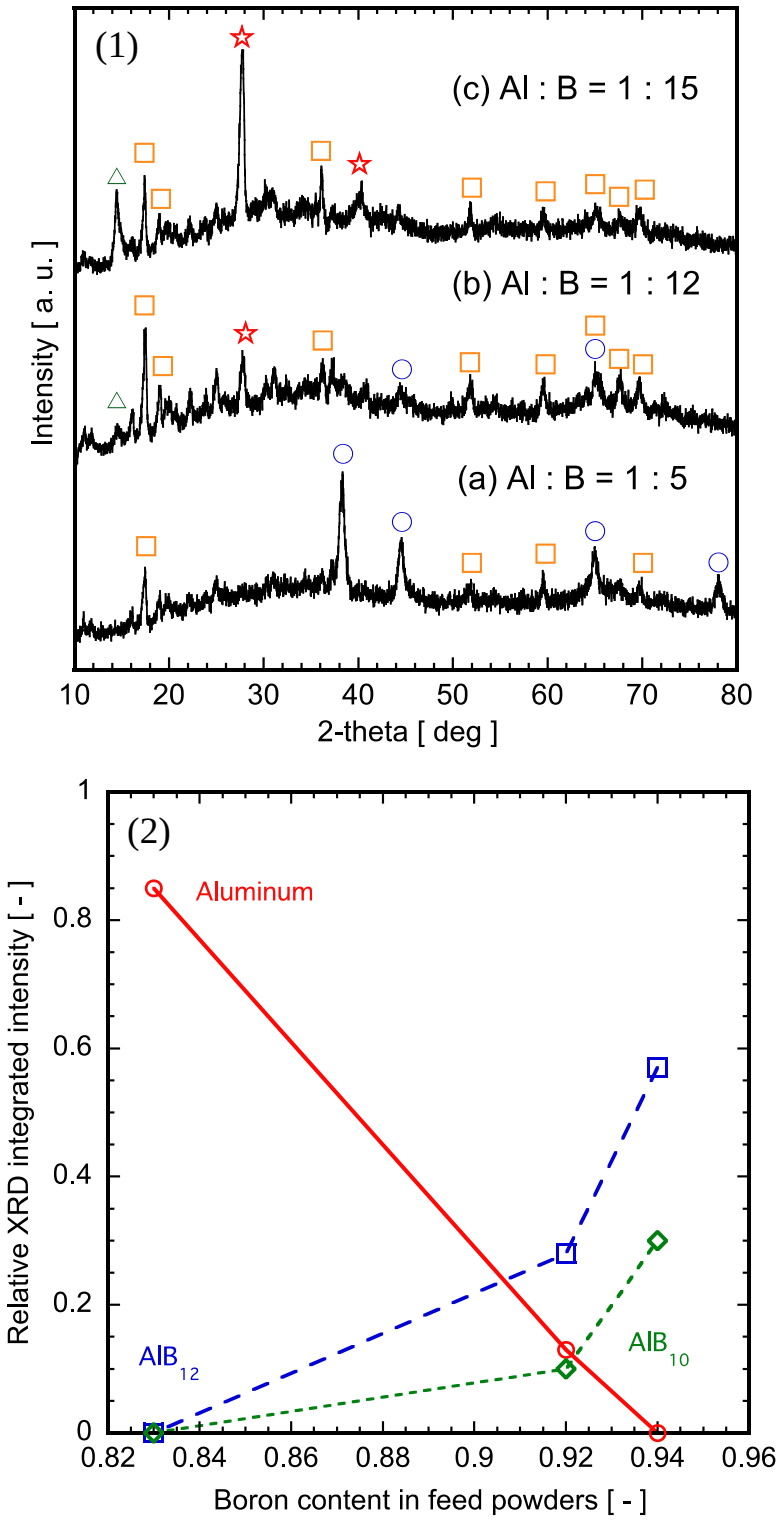

Fig. 16 XRD spectrum and integrated intensity of prepared particles for Al-B system;
Composition ratio of Al and B: (a) 1:5, (b) 1:12, (c) 1:15;
Inner gas: He.
(☆: AlB_{12}, △: AlB_{10}, □: B, ○: Al)

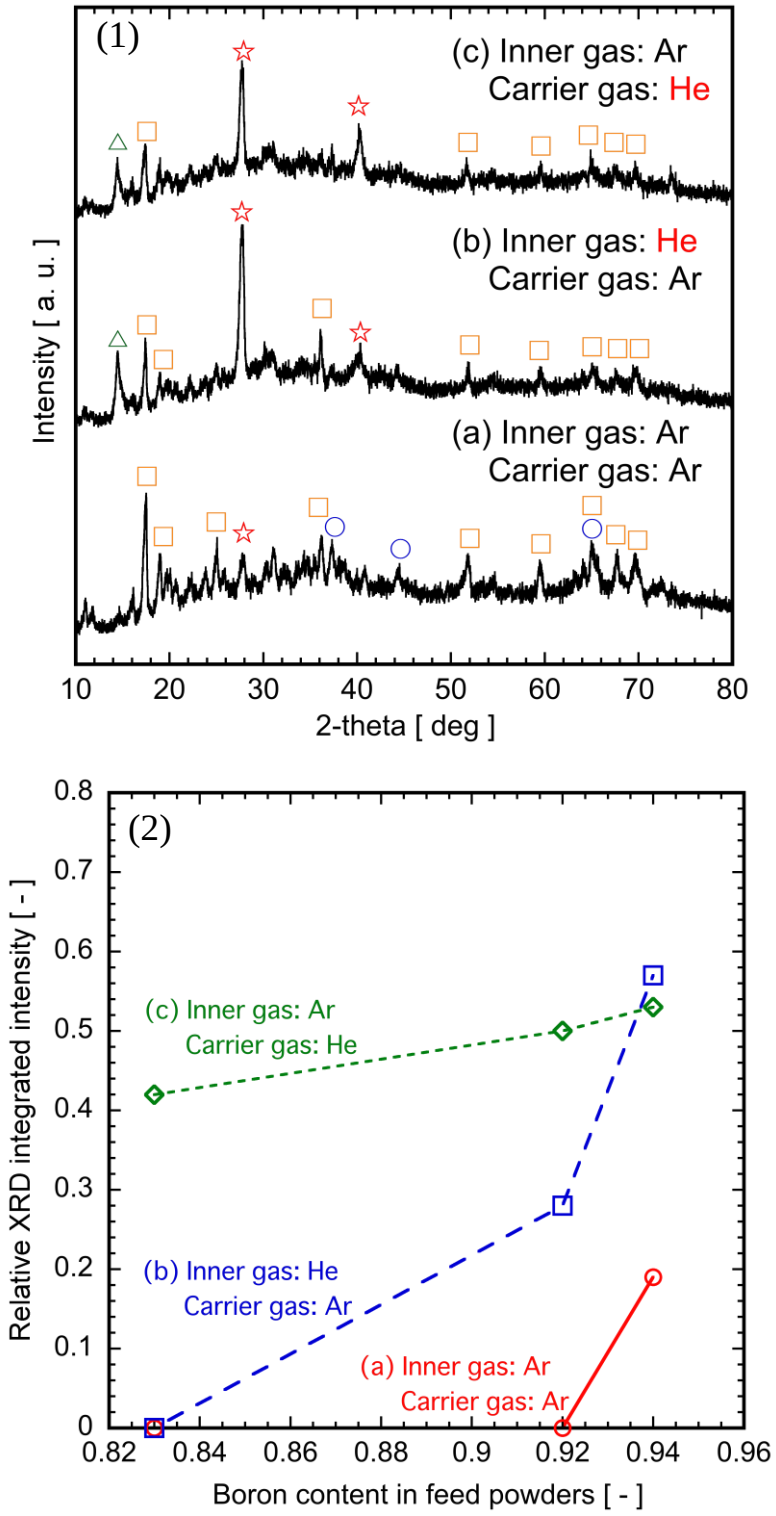

Fig. 17 XRD spectra and integrated intensity of prepared particles for Al-B system; Gas composition; (a) Inner gas: Ar, Carrier gas: Ar, (b) Inner gas: He, Carrier gas: Ar, (c) Inner gas: Ar, Carrier gas: He; Composition ratio of Al and B: 1:15.
(☆: AlB_{12}, △: AlB_{10}, □: B, ○: Al)

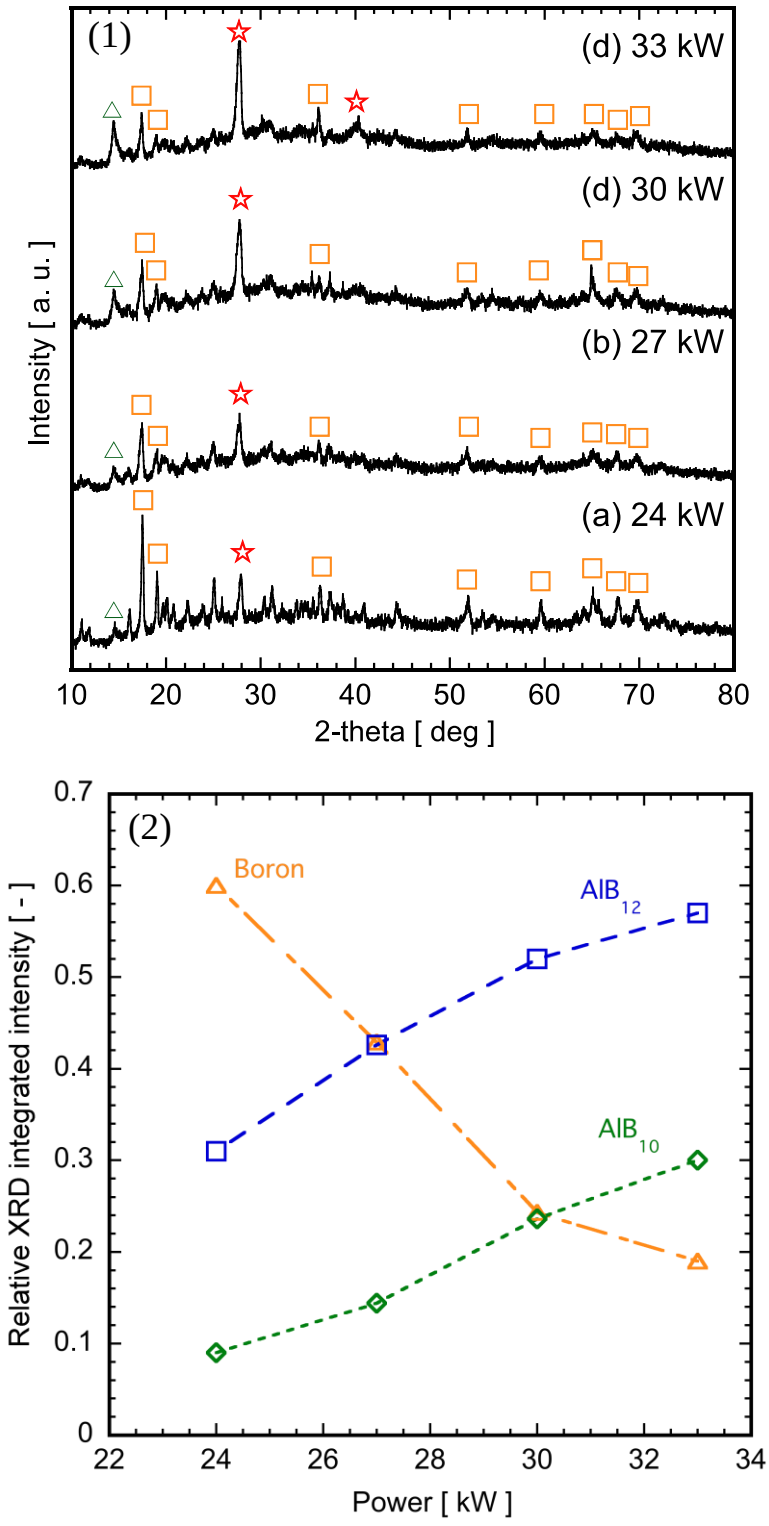

Fig. 18 XRD spectrum and integrated intensity of prepared particles for Al-B system;
Change of power: (a) 24, (b) 27, (c) 30, (d) 33 kW;
Composition ratio of Al and B: 1:15; Inner gas: He.
(☆: AlB_{12}, △: AlB_{10}, □: B, ○: Al)

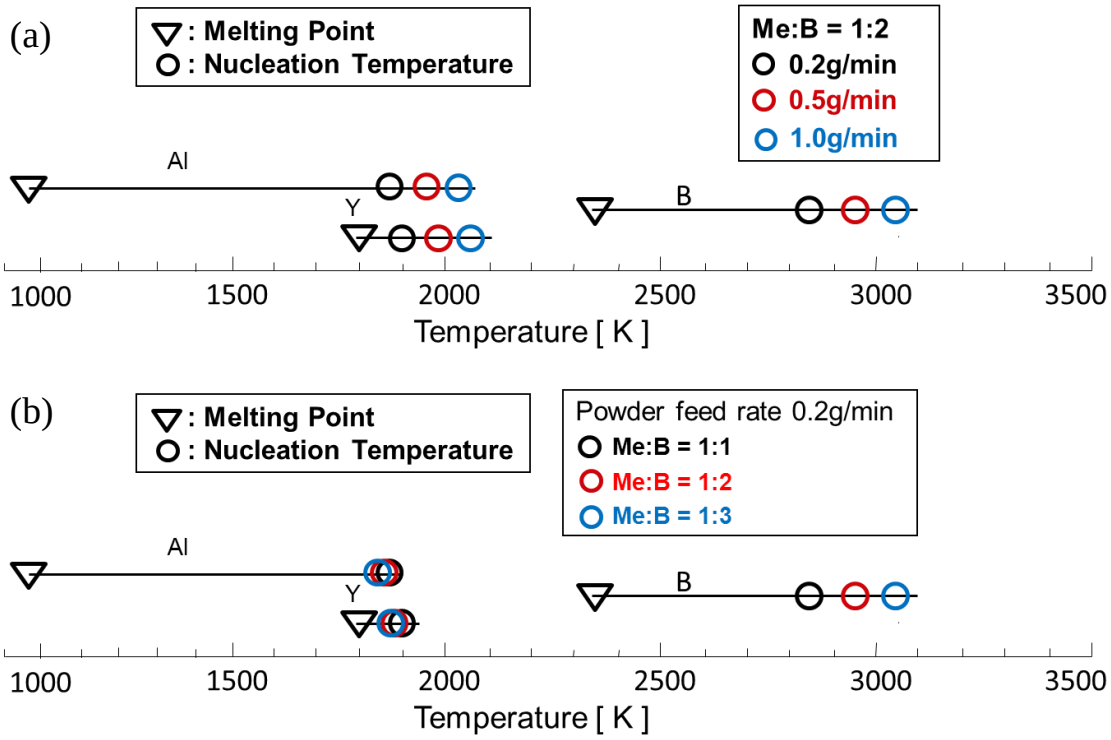

Fig. 19 Nucleation temperature at the critical saturation ratio for constituent components of boride: (a) Effect of different powder feed rate at the fixed initial composition of Me:B = 1:2; and (b) Effect of different initial composition of Me:B at the fixed powder feed rate of 0.2 g/min.

6. Formation Mechanism of Metal Boride Nanoparticles by RF Thermal Plasma

RF thermal plasma provides effective preparation of boride nanoparticles, because it provides large high temperature area to evaporate raw materials and the plasma is clean without electrode. In addition, the residence time of materials is comparatively long. For the synthesis of nanoparticles with required characteristics for the application, the composition and particle size of prepared nanoparticles are correlated with thermodynamic parameters. If the formation mechanism is well-understood and controlled precisely, mass-production of boride nanoparticles will be easily achieved using RF thermal plasma with low costs.

RF thermal plasma synthesis of binary alloy nanoparticles starts from vaporization of the raw materials in the high enthalpy field of the plasma. The binary metal vapors are transported with the flow to the plasma tail where the temperature drastically decreases. Consequently, the metal vapors become supersaturated, which engenders homogeneous nuclei composed of two materials (binary nucleation). Immediately, the binary metal vapors co-condense heterogeneously on the nuclei (binary condensation). Additionally, during their growth, the nanoparticles mutually collide and merge into larger nanoparticles (coagulation). These three processes progress collectively and simultaneously in a few tens of milliseconds.

6.1 Thermodynamic considerations

6.1.1 Gibbs free energy

Some reactions are spontaneous because they give off energy in the form of heat ($\Delta H < 0$). Others are spontaneous because they lead to an increase in the disorder of the system ($\Delta S > 0$). Therefore, the change of Gibbs free energy (ΔG) which is defined below reflects the balance between potential driving forces behind a chemical reaction.

$$\Delta G = \Delta H - T\Delta S \quad (1)$$

The Gibbs free energy of the system is a state function because it is defined in terms of thermodynamic properties that are state functions. The beauty of the equation defining the free energy of a system is its ability to determine the relative importance of the enthalpy and entropy

terms as driving forces behind a particular reaction. The change in the free energy of the system that occurs during a reaction measures the balance between the two driving forces that determine whether a reaction is spontaneous. We can therefore conclude that any reaction for which ΔG is negative should be favorable, or spontaneous.

The Gibbs free energy plays an important role in the synthesis process of metal boride nanoparticles by RF thermal plasma. The relationship between the Gibbs free energy of boride and temperature in Al-B, Ti-B, Fe-B, Co-B, Ni-B, Nb-B and Mo-B systems is shown in **Figure 1**. The Gibbs free energy of boridation is negative. Therefore, the chemical stability of boride is the driving force and the generation of metal boride can take place spontaneously. The Gibbs free energy of niobium boride is lower than that of iron boride, indicating that the synthesis of niobium boride is easier than that of iron boride.

6.1.2 Surface tension

Surface tension is a contractive tendency of the surface of a liquid that allows it to resist an external force. Surface tension is caused by the attraction between the molecules of the liquid by various intermolecular forces. In the bulk of the liquid each molecule is pulled equally in all directions by neighboring liquid molecules, resulting in a net force of zero. At the surface of the liquid, the molecules are pulled inwards by other molecules deeper inside the liquid and are not attracted as intensely by the molecules in the neighboring medium (e.g., vacuum, air or another liquid). Therefore all of the molecules at the surface are subject to an inward force of molecular attraction which can be balanced only by the resistance of the liquid to compression. This inward pull tends to diminish the surface area, and in this respect a liquid surface resembles a stretched elastic membrane. Thus the liquid squeezes itself together until it has the locally lowest surface area possible.

This size dependence, which is due to the surface tension of the solution-air interface, is known as the Kelvin effect [1,2]. The Kelvin equation relates the vapor pressure of a liquid to the effect of surface curvature i.e. a meniscus with radius. The equation illustrates that due to the surface tension and the surface being larger than the volume, there is much higher evaporation rate for smaller droplet liquids when compared to that of larger droplets.

$$ln\ P/P_0 = 2\sigma V_m / rRT \quad (2)$$

where P and P_0 display actual vapor pressure and saturation vapor pressure, respectively. σ

means surface tension of liquid, V_m is molar volume, r is radius, R represents universal gas constant (8.314 J K^{-1} mol^{-1}). Therefore, the larger surface tension provides larger particle size. Taking boron as the example, the smallest diameter of boron nanoparticle is 0.8 nm with powder feed rate is 0.2 g/min according to Eq. (2). Plasma gas and carrier gas Ar flow rates are 65 and 3 L/min, respectively. The smaller droplets are not stable due to the higher pressure, thus tend to fuse into larger ones.

There is empirical equation Eotvos rule to relate surface tension and temperature:

$$\sigma V^{2/3} = k(T_C - T) \tag{3}$$

where V is the molar volume of a substance, T_C is the critical temperature and k is a constant valid for almost all substances. A typical value is k = 2.1 x 10^{-7} (J K^{-1} $mol^{-2/3}$).

6.2 Homogeneous nucleation and co-condensation processes

6.2.1 Saturation vapor pressure

The difference of saturation vapor pressure between metal and boron is the important factor for the controlled composition and diameter of metal boride nanoparticles in RF thermal plasma. The saturation vapor pressures of metal and boron decrease along with the plasma temperature decrease. When the saturation vapor pressure of material falls below its actual pressure, this material reaches the supersaturated state at the upstream in plasma, and starts to nucleate simultaneously. The relationship between temperature and saturation vapor pressure is demonstrated in **Figure 2**. The saturation vapor pressures of Al, Y, Ti, Fe, Co and Ni are higher than that of boron, while the saturation vapor pressures of Mo, Nb, Ta and W are much lower than that of boron. Fe, Co and Ni have the similar saturation vapor pressure and are all higher than that of Ti. W has the lowest saturation vapor pressure and Al has the highest saturation vapor pressure. Therefore, W first reaches its supersaturation state and has highest nucleation temperature. Al has the lowest nucleation temperature.

6.2.2 Nucleation temperature and nucleation rate

The difference of nucleation temperature between metal and boron plays an important role in the controlled phase composition and diameter of metal boride nanoparticles in RF thermal plasma. Nucleation temperature is based on saturation vapor pressure and surface tension. When the nucleation rate is over 1.0 $cm^{-3}{\cdot}s^{-1}$, particle formation can be observed experimentally as

mentioned in the reference [3]. The corresponding value of saturation ratio and temperature at the nucleation rate of 1.0 $cm^{-3} \cdot s^{-1}$ are defined as the critical saturation ratio and nucleation temperature, respectively. The nucleation temperature at the critical saturation ratio is presented in **Figure 3** for constituent components of borides; fig. 3 (a) and (b) were calculated at the boron molar content of 66.7 % with different powder feed rate without and with boiling point of metal and boron, respectively, and fig. 3 (c) and (d) were drawn at the fixed powder feed rate of 0.2 g/min with different initial composition of Me:B without and with boiling point of metal and boron, respectively. Fig. 3 (a) has mainly two aims. One is to compare the difference of nucleation temperature of metal and boron. Since the melting point of boron is fixed at 2349 K, different nucleation temperatures of metal lead to different temperature gap between the nucleation temperature of metal and melting point of boron. Another purpose is to examine the change of boron nucleation temperature according to powder feed rate. The nucleation temperature of boron increases with increasing powder feed rate; in fig. 3 (b) displays the difference between the boiling point, melting point and nucleation temperature of metal and boron with different powder feed rate; in fig. 3 (c), the nucleation temperature of boron increases with increasing boron content in feeding powders; in fig. 3 (d) displays the difference between the boiling point, melting point and nucleation temperature of metal and boron with different boron molar content in feeding powders. In fig. 3, *Me* denotes metal used in the present work. The nucleation temperature was calculated by Eq. (4) from the beginning of particle formation observed experimentally at J = 1.0 $cm^{-3}\,s^{-1}$ [4].

$$J = \frac{\beta_{ll} N_S^2 S}{12} \sqrt{\frac{\Theta}{2\pi}} \exp\left[\Theta - \frac{4\Theta^3}{27(\ln S)^2}\right] \tag{4}$$

Here, N_S is the equilibrium saturation monomer concentration at temperature T, and it is estimated by the saturation vapor pressure. β_{11}, S, and Θ are collision frequency function between monomers, saturation ratio, and dimensionless surface tension, respectively.

Equilibrium saturation monomer concentration at temperature T is calculated by:

$$N_s = \frac{P_s}{1.38 \times 10^{-23} \cdot T} \tag{5}$$

Supersaturation ratio is defined as

$$S = \frac{n_l}{n_s} = \frac{p_l}{p_s} \tag{6}$$

Dimensionless surface tension, Θ is given as follows:

$$\Theta = \frac{\sigma s_l}{kT} \tag{7}$$

where σ is surface tension [5], and s_l is monomer surface area ($S_1 = \pi d^2$). In this calculation, the surface tension was obtained from the bulk properties, because the reliable data for binary clusters are not available at present. The collision frequency function β can be estimated by Eq. (8) when the Knudsen number is more than 10 (Girshick *et al*., 1990).

$$\beta_{ij} = \left(\frac{3v_l}{4\pi}\right)^{\frac{1}{6}} \sqrt{\frac{6kT}{\rho}\left(\frac{1}{i}+\frac{1}{j}\right)}\left(i^{\frac{1}{3}} + j^{\frac{1}{3}}\right)^2 \tag{8}$$

where ρ is the particle mass density and v_l the monomer volume ($v = \pi d^3/6$) In this model, the particle nucleation is due to the monomer collision, therefore $i = j = 1$. The means of i and j is the number of molecule contained in a cluster when colliding.

Nuclei are considered to be produced by homogeneous nucleation in higher supersaturation, since nuclei in the low supersaturation are unstable due to the large evaporation rate. The nuclei have the critical diameter expressing the well balanced condition of growth and evaporation. The critical size of the nucleus is determined by Eq. (9)

$$d = \frac{4\sigma v}{kT \ln S} \tag{9}$$

where σ and v are surface tension and volume of nucleated material, respectively.

The particles mass density ρ is given by the following equation:

$$\rho = \frac{M}{6.02 \times 10^{23} \cdot v_1 \cdot 10^3} \tag{10}$$

where M is the atomic mass.

The molar ratio of plasma gas is estimated:

$$x_g = \frac{R_g}{22.4} \cdot \frac{273}{298} \tag{11}$$

where R is gas flow rate.

The actual pressure of material in chamber is estimated as follows:

$$P_M = \frac{x_M}{x_g + x_M + x_B} \cdot 101325 \tag{12}$$

where x_M is the molar ratio of raw materials metal. x_B is the molar ratio of boron, x_M and x_B can be estimated by the initial composition of Me:B and powder feed rate.

Boron vapor becomes supersaturated earlier than Al, Y, Ti, Co, Ni and Fe due to the relatively lower saturation vapor pressure. While Mo, Nb, Ta and W with lower saturation vapor

pressure reach their supersaturation state a little earlier than boron. Therefore, the nucleation temperature of boron is higher than those of Al, Y, Ti, Co, Ni and Fe, and a little lower than the nucleation temperature of Mo, Nb, Ta and W. The order of the nucleation temperature is: W > Ta > Nb > Mo > B > Ti > Ni > Y > Al > Co > Fe. The wide liquid range combination of boron with metals leads to better preparation of boride nanoparticles. According to the fig. 3, among the metals and boron, boron has the widest liquid range between the nucleation and melting temperature. While refractory metals (Mo, Nb, Ta and W) have narrow liquid region from the nucleation temperature to its melting temperature.

Once nuclei are generated by homogeneous nucleation, binary metal vapors condense on the nuclei heterogeneously, resulting in significant growth of the particles. The binary condensation is a key process to determine a nanoparticle's profile. In the state of high concentrations of nucleated particles and at low supersaturation, heterogeneous condensation becomes dominant and occurs on the surface of the nuclei, resulting in nanoparticle growth.

Nanoparticle growth is linked inextricably to vapor consumption because the concentration of material vapor determinately affects the features of homogeneous nucleation and heterogeneous condensation. During nanoparticle growth with temperature decrease, the nanoparticles will be solidified. Once they are solidified, they can no longer increase their size as spherical particles by coagulation. Coagulation of nanoparticles plays a considerably important role in nanoparticle growth.

6.2.3 Spatial vapor distribution

The evaporated vapor is transported by convection and diffusion, and forms a vapor concentration profile in plasma. A significant fraction of the vapor, about 50%, diffuses to the wall of the plasma tube and is deposited there. The vapor concentration at the entrance to the particle growth tube is highest in the hot core and declines toward the cold walls [6].

In the core of upstream vapor is too hot to nucleate. As vapor diffuses radially outward, it crosses this isotherm and particles nucleate. These particles are prevented from depositing on the wall by the transpiration flow, so that there is an axial flow of particles close to the wall, with the concentration increasing in the downstream direction. As the vapor is convected downstream, the central core eventually cools enough for nucleation to occur. The region downstream thus contains two classes of particles: particles which were formed from vapor diffusing radially toward the cold wall, and particles which were formed from vapor convected

axially in the flow direction.

It is difficult of the vapors toward the cold wall to react with the other material vapor due to lower plasma temperature and low vapor concentration, which will mainly generate unreacted raw materials. The vapor in the flow direction can react with the other material vapor easily due to the high plasma temperature and excessive vapor, which will generate metal boride nanoparticles. As a result, spatial vapor distribution can affect the composition of product.

One-dimensional models [7-9] indicate that the crucial factor is the local cooling rate experienced by the vapor in the region where nucleation occurs. The vapor in the position where much vapor exists becomes supersaturated at more upstream position. The nucleation temperature increases. It is noted that the supersaturation ratio decreases with the increase of temperature. And then the nucleation rate is low due to low supersaturation ratio based on Eq. (4). According to Eq. (9), critical size is strongly dependent on the supersaturation ratio and surface tension. The supersaturation ratio is varied along with the spatial vapor distribution. So the critical size of the nucleus can be varied according to the spatial vapor distribution. Thus the critical size is large because of the low supersaturation ratio. The consumption of vapor is contributed to the nucleation and condensation. So the condensation rate is high based on the low nucleation rate. In addition, the residence time which is represented by the temperature region between the nucleation temperature and melting point of material becomes long. Fewer stable large nuclei can share a large amount of vapor to grow large. In the position where fewer vapors exist smaller particles can be generated. Therefore, size distribution is influenced by spatial vapor distribution.

6.3 Synthesis mechanism of boride nanoparticles

Figure 4 shows the temperature field in RF thermal plasma system. A remarkably high temperature region (higher than 9000 K) is produced in the plasma torch by the Joule heating due to the induced electromagnetic fields. The high enthalpy in plasma torch is transported into the reaction chamber by the convection, and then the temperature decreases drastically with the cooling rate of 10^4-10^5 Ks^{-1}. Immediately after the plasma flow enters the reaction chamber, the high temperature of 8500 K decreases drastically to below 500 K. This rapid temperature drop leads to a highly supersaturated state of raw materials, which promotes nanoparticle formation.

The compositions of metal borides vary from metal rich to boron rich phases depending on the atomic size and charge of the metal atom. Generally, when boron combines with metals

having small atomic radii, the corresponding borides tend to be metal rich, and boron rich phase form with metals that have large atomic radii [10]. In all these compounds, the driving force for chemical bonding is the covalent interaction between *s* and *p* orbitals on neighboring boron atoms. Boron chemistry is dominant by the tendency of B atoms to form covalently bonded clusters and in the solid state these are most often comprised of 12 atoms [11]. Metal rich borides tend to be formed by the transition elements whereas boron rich borides are characteristic of the more electropositive elements. Metal rich borides are stabilized by filling the voids of the metal host lattice with boron atoms. For boron rich borides, boron atoms form B_{12} icosahedra which are linked into a three-dimensional boron framework, and the metal atoms reside in the voids of this framework to donate electrons to form boron-rich metal borides.

6.3.1 Metal rich boride

The formation mechanism of metal rich boride nanoparticle is attributed to the nucleation temperature of the constituent components of boride. Hence, the formation mechanism can be divided to the following two kinds based on their nucleation temperature: (1) in the case of $T_{Me} < T_B$, boron nucleates firstly, and then metal and boron co-condensate on the boron nuclei; and (2) in the case of $T_{Me} > T_B$, metal nucleates firstly, and then metal and boron co-condensate on the metal nuclei.

a Ti-B, Co-B, Ni-B and Fe-B systems

For Ti-B, Co-B, Ni-B and Fe-B systems, the formation mechanisms of metal borides nanoparticles are considered to be the same as displayed in **Figure 5 (a)**, because the nucleation temperatures of metal are lower than that of boron.

The model including evaporation, nucleation, condensation and coagulation in plasma is shown in **Figure 5 (b)**. After the precursors are injected into the plasma, they instantaneously start to evaporate. According to the simulation analysis on precursor particle behaviors, all of raw materials can be evaporated completely in plasma [12]. The evaporated vapors are transported with the plasma flow to the reaction chamber where the temperature decreases rapidly. As discussed above, the saturation vapor pressure of vapor decreases drastically along with the temperature decrease and will fall below their actual pressures to reach supersaturated state. This supersaturated state consequently leads to the production of nuclei by homogeneous nucleation. At the upstream in plasma boron vapor with lower saturation vapor pressure first

become supersaturated, and then the nucleation process of boron takes place homogeneously. If plasma temperature is higher than boron melting point, boron nuclei are on molten condition. The heterogeneous co-condensation of metal and boron dominantly occurs on the surface of the nucleated boron nuclei. Boridation is believed to take place after the co-condensation process with boron diffusion in the transition metal. The pressure of boron vapor decreases rapidly, which is attributed to the vapor consumption by homogeneous nucleation and heterogeneous condensation of boron vapor. The pressure of metal vapor decreases by heterogeneous condensation on boron nanoparticles. This combined mechanism makes nanoparticles grow. And nanoparticles also grow by coagulation among themselves. Nuclei are considered to be produced by homogeneous nucleation in higher supersaturation ratio of nucleated particles at high temperature. Nuclei in the low supersaturation are unstable due to the large evaporation rate. Following homogeneous nucleation, heterogeneous condensation dominantly occurs on the surface of the nucleated particles when the supersaturation ratio is relatively low.

Metal with low melting point is easy to evaporate, while the evaporation of boron with high melting point, specific heat and latent heat is difficult. Gibbs free energies of metal borides are negative, indicating metal borides can be generated spontaneously. Boron with high nucleation temperature first nucleates. The generation of boron nuclei is the most important to produce metal boride. Nucleation is promoted in the circumstances where larger amount of boron vapors can simultaneously nucleate, the promoted nucleation generates more nuclei. Therefore, high boron content in feeding powders is important in the synthesis of metal boride.

The production rate is directly proportional to the temperature gap between the nucleation temperature and melting point of boron. From the formation mechanism of metal boride nanoparticle, the growth process including nucleation and condensation processes is not finished until the melting point of metal. In Ti-B, Co-B, Ni-B and Fe-B systems, injected raw powders become vapor in thermal plasma quickly. When boron vapor reaches supersaturated state first at the nucleation temperature, it can transform into condensed phase by homogeneous nucleation process. The nucleation process of boron occurs only around the nucleation temperature of boron in an instant. Simultaneously, boron and metal vapors co-condensate on the surface of boron nuclei during the temperature gap between the nucleation temperature and melting point of boron, where the vapor of boron and metal can mix well. It is easy for vapor to condensate on the boron nuclei in liquid state heterogeneously. The co-condensation process of boron and metal also takes place in the temperature gap between the melting point of boron and

melting point of metal, where the vapor of boron and metal cannot mix well due to the lower plasma temperature compared with the melting point of boron. Therefore, relatively large temperature gap between boron nucleation temperature and boron melting point in the boridization process which takes place in the temperature range between boron nucleation temperature and metal melting point results in the better synthesis of boride product. Therefore, the high temperature region where evaporated boron and metal are mixed well contributes to the synthesis of boride nanoparticles dominantly.

According to the formation mechanism, the growth of metal boride nanoparticle including homogeneous nucleation and heterogeneous condensation processes in the temperature range from boron nucleation to metal solidification. This temperature range is divided into two regions by the melting point of boron. In the high temperature region above the melting point of boron, well mixed boron and metal in liquid state co-condensate on the surface of boron nuclei heterogeneously producing boride nanoparticles. In the relatively low temperature region below the melting point of boron, only supercooled boron can be mixed with metal.

In the synthesis of metal boride nanoparticles, core-shell structured nanoparticles were generated. The synthesis mechanism of core-shell structured metal boride nanoparticle was examined based on the calculation of nucleation temperature. Take Ti-B system as example, boron nucleates first with relatively higher nucleation temperature compared with that of titanium. Simultaneously, boron and titanium vapors condense on the surface of boron nuclei in the temperature gap between the nucleation temperature and melting point of boron forming metal boride nanoparticles. The large temperature gap between melting points of titanium and boron leads to excessive titanium on the molten condition promoting the formation of metal shell. During this period, titanium boride nanoparticles act as nucleation sites for titanium monomers creating metal covered boride nanoparticles. In boron rich condition, more boron nuclei are generated. Most of boron nuclei can first react with titanium to form titanium boride due to the negative Gibbs free energy. The excessive boron nuclei can form B nanoparticles. However, B nanoparticles are not stable [13]. In addition, the melting point of B nanoparticle is lower than those measured at the bulk. The melting point of B nanoparticle is estimated to be 1800 K by Eq. (13) [14]. They grow along the surface of titanium boride until the whole boride nanoparticle is encapsulated inside. The shell of boron is formed.

To characterize size effect on the melting point, Eq. (13) is used:

$$T_m = T_{m,\infty}\left(1 - \frac{\alpha_{shape}}{2L}\right) \tag{13}$$

where $\alpha_{shape} = 2AL(\gamma_s - \gamma_l)/(V\Delta H_{m,\infty})$. $T_{m,\infty}$ is melting temperature of the considered bulk material, whereas γ_l and γ_s are the surface tensions in liquid and solid-phase, respectively, and $\Delta H_{m,\infty}$ represents the bulk melting enthalpy. A and V mean surface area and volume. L represents the length size of nanostructure, i.e., the radius for the case of a spherical structure.

Because the condensation of excessive material takes place on the generated metal boride nanoparticles on the solid state, there is no chemical reaction between the care and the shell. So the peaks of Ti, TiB_2 or TiB can all be identified in XRD patterns, though their intensities are different according to each species and core-structure. The peak of composite cannot be observed. For the peaks of boron, the content of boron is too low to detect in XRD measurement. If we use very high boron content, the peak of boron will be identified.

b) Nb-B, Mo-B, Ta-B and W-B systems

Figure 6 demonstrates the formation mechanism of boride nanoparticles in Nb-B, Mo-B, Ta-B and W-B systems. The nucleation temperatures of metal are higher than that of boron.

After the precursors are injected into the plasma, they instantaneously start to evaporate. The evaporated vapors are transported with the plasma flow to the reaction chamber where the temperature decreases rapidly. At the upstream in plasma metal vapor with lower saturation vapor pressure first become supersaturated, and then the nucleation process of metal takes place homogeneously. Co-condensation of boron occurs on the surface of metal-rich nuclei spontaneously and simultaneously. If plasma temperature is higher than metal melting point, metal-rich nuclei are on molten condition. And then the heterogeneous co-condensation of metal and boron dominantly occurs on the surface of the nucleated metal boride nanoparticles. The metal vapor has a higher rate of condensation than the boron vapor at the upstream in plasma due to the lower saturation vapor pressure. Following the consumption of metal vapor, boron vapor is consumed with a high rate of condensation. In addition to such nucleation and condensation processes, coagulation among the nanoparticles takes place. In the present synthesis condition of refractory metal, vapors of refractory metal and boron are expected to co-condense on the existing metal-rich nuclei, which results in the formation and growth of refractory metal boride nanoparticles. The numerical simulation of synthesis of niobium boride nanoparticles in Ch. 4 demonstrates that the nucleation process of niobium and boron takes place simultaneously. The nucleation rate of niobium is higher than that of boron. And then the co-condensation of niobium and boron occurs on the surface of Nb rich nuclei.

Immediately after the precursors are injected into the plasma, their temperature increases quickly and reach their boiling points. Their diameters decrease by evaporation keeping their temperature at their boiling points. The evaporation time in the growth process is very short and can be negligible due to the large high temperature region [15]. But in Mo-B system, raw materials with high melting/boiling points as well as relatively high specific heat and large latent heat of evaporation are difficult to evaporate completely. It takes a long time to evaporate Mo. The evaporation time is calculated considering spherical particles with radius R, temperature T, and infinite thermal conductivity exposed to a thermal plasma with a temperature $T_p > T$ by Eq. (14) [16]:

$$T(t) = T_P + \left(T_0 - T\right) exp\ \frac{3\lambda_P t}{\rho c_P R^2} \tag{14}$$

where ρ is the mass density and T_0 is the initial temperature of the particle. c_p is the specific heat of the particle and λ_p is the thermal conductivity of the plasma. The thermal conductivity for an atmospheric argon plasma at a temperature of 10,000 K, λ_p = 1 W/Km. Evaporation time of Mo, B and Ti with the same diameter of 2.5 μm is estimated to be 140, 115 and 72 μs, respectively.

Supersaturation reaches a higher value due to the high temperature gradient if the quenching rate is increased. The higher supersaturation causes a decrease in the critical nucleus size. The nucleus size distribution for early times is monotonically decreasing, and a larger number of mostly smaller stable nuclei are made available for condensation. Therefore, we would expect a higher cooling rate to produce much smaller particles [17]. Also the synthesis of metal boride needs special boron content and temperature according to phase diagram. Quenching gas can stop the reaction at certain temperature. As a result, quenching gas is important in the generation of refractory metal boride nanoparticles.

6.3.2 Boron rich boride

In Al-B system, AlB_2 the structure of which is the same as TiB_2 can be generated in general case. While Gibbs free energy of AlB_2 is relatively high and it is difficult to produce. In addition, the reaction between Al and B is slow, the unstable B nucleus need to form stable cluster B_{12}. The closo-cluster $(B_{12})^{2-}$ has intrinsic stability. The sp^2 hybridization of valence electrons, electron deficiency, large coordination numbers, and short covalent radius allow boron to form strong directed chemical bonds. The sp^2 hybridization mainly contributes to the stability of clusters forming hybrid bonds, and their three valence electrons can form strong multiple

three-centered bonds with σ and πp orbitals. The energy of B_{12} clusters is higher than 5 eV which is higher than those of elemental, the convex or the quasiplanar clusters [18,19].

Figure 7 shows XRD pattern of plasma treated B nanoparticle with raw material pure boron. *β*-rhombohedral form of crystalline B is generated. *β*-boron is the simplest allotropic modification and consist of nearly regular B_{12} icosahedra in slightly deformed cubic close packing as displayed in **Figure 8** [20]. **Figure 9** displays XRD patterns of product in Al-B and Ti-B systems. In the initial composition of Al:B = 1:5, sharp peaks of B can be detected, indicating crystal B with B_{12} icosahedra is generated in Al-B system. While in the initial composition of Ti:B = 1:5, the peaks of B are not observed. It is concluded that B_{12} cluster is formed in Al-B system.The formation mechanism of AlB_{12} is proposed in **Figure 10**.

Since AlB_{12} is composed of icosahedral B_{12} and B_{20} units, boron clusters are required to form boron-rich compound. At this moment, boron-rich aluminum boride requires the clustering of boron nuclei before the boridation.

After the precursors are injected into the plasma, they instantaneously start to evaporate. The evaporated vapors transported with the plasma flow to the reaction chamber where the temperature decreases quickly. When the saturation vapor pressure falls to the partial vapor pressure, it will reach its supersaturated state which leads to the nucleation process. At the upstream boron with high nucleation temperature starts to nucleate homogeneously. Immediately, boron nuclei and monomers start to form boron clusters. Then, metal and boron monomers are condensed onto boron clusters forming boron-rich metal boride nanoparticles heterogeneously. Boridation is believed to take place after the co-condensation process of boron clusters diffusion in the metal. The pressure of boron vapor decreases due to the consumption of boron vapor by nucleation, clustering and condensation processes. The aluminum vapor is consumed by the heterogeneous condensation process. In the downstream of the plasma flame, the coagulation process takes place between nanoparticles without materials vapor. This combined mechanism makes the nanoparticles grow. Because the nucleation temperature of aluminum is lower than that of boron, the nucleation, condensation and solidification processes are similar with these in Ti-B system except the boron clustering. The growth time includes binary nucleation, boron clustering, condensation and coagulation process does not stop until the melting point of aluminum.

Gibbs free energy of AlB_{12} is negative in fig. 1, indicating AlB_{12} is stable thermodynamically and can be generated spontaneously. However, B is difficult to evaporate. Al

with low melting point is easy to evaporate at upstream. The existence area of B vapor is extended compared with that of Al. The co-existence area of B and Al vapor is small and less Al and B cluster can react with each other due to the diffusion of Al vapor. The synthesis of AlB_{12} needs B cluster. Gas with high thermal conductivity can improve the evaporation of boron. So it can enlarge the co-existence area of Al and B vapor and promote the formation of B cluster to produce AlB_{12}.

Because of the formation of B cluster, the synthesis of boron rich boride is more difficult than the production of metal rich boride nanoparticle in Ti-B, Fe-B, Co-B and Ni-B systems.

6.3.3 Comparison of different materials

a) Metal rich boride

Figure 11 shows the effect of powder feed rate on the phase composition of product at the fixed initial composition of Me:B = 1:2 in all systems. These systems have the same tendency that the mass fraction of metal boride in product decreases with increasing powder feed rate except Co-B system. Co-B system is very different from the other Me-B system. With the low powder feed rate, both of boron and metal are quickly evaporated just after the injection of raw powders, and then the evaporated boron or metal is nucleated in the high temperature area at the upstream region of plasma flow where metal and boron co-exist and can react with each other. On the other hand, the amount of raw materials increases at high powder feed rate, though the heat from the plasma keeps constant at the fixed input power of 30.0 kW. The less heat transferring from the plasma to each particle takes longer time to evaporate raw materials at high powder feed rate rather than the low powder feed rate. In addition, boron, molybdenum and niobium are difficult to be evaporated due to the relatively higher melting point, evaporation temperature and latent heat. For this reason, the existence area of evaporated boron, molybdenum and niobium is extended along with the thermal plasma flame. The boridization occurs easily in the upstream region of plasma flow due to high temperature and abundant titanium, iron, nickel or boron vapor, in different system while it is difficult in the downstream region because of relatively low temperature and diffuse of titanium, iron, nickel or boron vapor which is produced in the upstream region. Moreover, the nucleation position shifts more upstream at higher powder feed rate, and then the nucleation rate of boron or molybdenum or niobium becomes lower. According to the Eq. (4) for the homogeneous nucleation rate, the nucleation rate is lower at larger surface tension or higher temperature. The nuclei become less,

and the mass fraction of metal boride decreases at higher powder feed rate.

The relationship between powder feed rate and the molar ratio of unreacted boron in product is presented in **Figure 12**. The molar ratio of unreacted boron in product increases with the increase of powder feed rate. Because the reduced heat transferring from the plasma to each particle at higher powder feed rate extends evaporation time and area of boron as mentioned above. From fig. 13, the molar ratios of unreacted B in product in Nb-B and Mo-B systems are less than the case of Ti-B, Co-B, Ni-B and Fe-B systems. That is because the mass fraction of titanium, cobalt, nickel and iron boride in product is higher than that of niobium and molybdenum boride nanoparticles as mentioned in fig. 11, indicating there is more boron reacting with titanium, cobalt, nickel and iron and less unreacted boron remains.

In Mo-B/Nb-B system, the mass fraction of molybdenum boride in Mo-B system is higher than that of niobium boride in Nb-B system. The main reason is the wider temperature range from nucleation temperature of Mo to the melting point of Mo, in which Mo nuclei are on molten state. Moreover, the supersaturation ratio of Mo and B is similar and their nucleation temperatures are similar. Molybdenum and boron are considered to be well-mixed in a liquid state in this co-condensation process, which results in the better synthesis of molybdenum boride. In Nb-B system, the temperature range between the nucleation temperature and melting point of Nb is relatively narrow. The less amount of niobium nuclei are on the molten state, which leads to the little preparation of niobium boride. In addition, Gibbs free energy of molybdenum boride is more negative compared with that of niobium boride. Though, the surface tension of molybdenum is larger than that of niobium, indicating the nucleation rate of niobium is higher compared with that of molybdenum according to Eq. (4). The melting point of niobium is higher. Therefore, it is concluded that the influence of surface tension is less important than these of nucleation temperature and Gibbs free energy on the phase composition.

The synthesis of titanium, iron, and cobalt and nickel boride is easier than that of molybdenum and niobium boride. In Ti-B, Co-B, Ni-B and Fe-B systems, boron has wide temperature range from the nucleation temperature of boron to melting point of boron, which leads to a large amount of boron nuclei are on the molten state. For Mo-B and Nb-B systems, metal nucleates first. They have relatively narrow temperature range between the nucleation temperature and melting point of metal compared with that of boron. So less metal nuclei are on the molten state. In addition, larger surface tension results in lower nucleation rate according to the nucleation rate Eq. (4). The surface tension of B is 1.09 N/m, while the surface tensions of

Mo and Ni are 2.25 and 1.90 N/m, respectively. Molybdenum and niobium provide lower nucleation rate, and less metal nuclei can be generated. Moreover, molybdenum and niobium with high melting/boiling point, high specific heat and latent heat are difficult to evaporate. As a result, fewer nuclei on molten state can be mixed well with the vapor of another material. In a word, little preparation of molybdenum and niobium boride nanoparticles occurs. Therefore, it is demonstrated that the nucleation temperature and surface tension are important factors in the control of phase composition of product.

In Ti-B system, the product is mainly composed of TiB_2 in boron rich condition. Gibbs free energy of TiB_2 is relatively high compared with that of molybdenum boride, but the mass fraction of TiB_2 in product is higher than that of Mo boride. The main reason is that the nucleation temperature of Ti is lower than that of B and the wide temperature region between nucleation and melting temperature of B for generating B nuclei on liquid state. Boron nucleus is very small with high pressure and the boron nuclei are not stable. Because the reaction between Ti and B is fast, B cluster will not be formed. Ti and B condense on the surface of B nucleus to produce TiB_2. The similar results are obtained in Fe-B, Co-B and Ni-B systems.

In Mo-B system, produced nanoparticles mainly are composed of unreacted raw material with small fraction of boride, though Gibbs free energy of Mo boride is relatively negative. The main reason of little preparation of boride results from the higher nucleation temperature of Mo than that of B. The temperature region between the nucleation and melting temperature of Mo is narrower compared with that of B. In the downstream, nucleation and solidification of Mo occurs simultaneously. After the nucleation and solidification, B condenses around the solidified Mo particles. It is difficult to condense on the solid nuclei. Therefore, the nucleation mechanism leads to little preparation of Mo boride nanoparticles.

Effect of powder feed rate on particle diameter of product in Ti-B, Co-B, Fe-B, Ni-B, Nb-B and Mo-B systems is presented in **Figure 13.** The particle in Co-B system has the smallest size, while molybdenum boride has the largest size among these systems. The order of boride particle diameter in Me-B system is: Mo > Ni > Fe > Nb > Ti > Co. The growth process including nucleation and co-condensation does not stop until the melting point of metal in Ti-B, Co-B, Fe-B, Ni-B systems, while in Nb-B and Mo-B systems the growth time is from the nucleation temperature of metal to the melting point of boron. **Figure 14 (a)** shows the relationship between the crystalline diameter of boride and the corresponding temperature range of growth time. The order of growth time of particle in Me-B system is: Ni-B > Co-B > Fe-B > Ti-B >

Nb-B > Mo-B. The temperature range from the nucleation temperature of boron to melting point of cobalt in Co-B system is wider, while cobalt boride has the smallest diameter. The molybdenum has the narrowest growth time, while the particle size is the largest. Moreover, the order of the surface tension of each element is: Mo (2.25 N/m) > Ni (2.1 N/m) > Fe (1.92 N/m) > Nb (1.90 N/m) > Ti (1.39 N/m) > Co (1.29 N/m) > B (1.09 N/m), which is displayed in **Figure 14 (b)**. The surface tensions of metal boride are not available. According to fig. 13 and fig. 14, the order of particles diameter in Me-B system is consistent with the order of the surface tension of each metal, while the order of diameter is different from the order of growth time. So the surface tension is also an important factor for the control of particle size and the large surface tension leads to the large particle diameter. It is concluded that the influence of surface tension in the control of particle diameter is more important than the influence of growth time.

Figure 15 reveals the effect of boron molar content in feeding powders on the phase composition of product at the constant powder feed rate 0.2 g/min in Me-B system. The effect of boron content in feeding powders on the phase composition of product has the same tendency that the mass fraction of metal boride in product increases with the increase of boron content in feeding powders. The generation of metal boride needs the well mixture of nuclei and another material vapor. In Ti-B, Fe-B, Ni-B and Co-B systems, more boron content in feeding powders leads to the co-existence of more boron nuclei and metal vapor in the upstream and promoted nucleation, which are beneficial for the synthesis of metal boride. In Mo-B/Nb-B cases, metal nuclei are generated. The metal is more difficult to evaporate compared with boron, so the existence area of metal is extended along with the plasma flame to the relatively downstream region with low temperature. Boron can evaporate in the upstream region in plasma and co-exist with metal vapor in high temperature region. So the partial of metal vapor can react with boron in high temperature region. In the downstream region of plasma, there is little boron vapor due to the diffusion of boron vapor can react with evaporated metal vapor. Diffusion of boron will make the synthesis of metal boride difficult in the relatively downstream region of plasma. High boron content in feeding powders will overcome this problem. In summary, high boron content in feeding powder results in the better synthesis of metal boride nanoparticles.

The relationship between the boron molar content in feeding powders and the molar ratio of unreacted boron in product is presented in **Figure 16**. Due to the dominant product with different phase composition in boron poor and boron rich conditions, the tendencies in different systems are not consistent. In Ti-B and Mo-B systems, the molar ratio of unreacted boron

increases with increasing boron content in feeding powders. For Nb-B = 1:3, the molar ratio of boron in material is 75 at% and the molar ratio of unreacted boron in product is 80 at%. So the molar ratio of niobium boride is 20 at%. NbB_2 is observed in Nb-B system. The molar ratio of reacted boron in all boron is 25 at%. For Nb:B = 1:2, the molar ratio of boron in material is 66.7 at% and the molar ratio of unreacted boron in product is about 74 at%. So the molar ratio of the niobium boride is 26 at%. NbB_2 is generated. The molar ratio of reacted boron in all boron is 27.5 at%. In a word, the molar ratio of reacted boron in plasma is reduced by the increase of boron content in feeding powders. In Fe-B, Co-B and Ni-B systems, the molar fraction of unreacted boron decreases with the increasing of boron content in feeding powders. For Fe:B = 1:3, the molar ratio of boron in material is 75 at% and the molar ratio of unreacted boron in product is 65 at%. So the molar ratio of iron boride is 35 at%. FeB is observed in Fe-B system. The molar ratio of reacted boron in all boron is 26 at%. For Fe:B = 1:2, the molar ratio of boron in material is 66.7 at% and the molar ratio of unreacted boron in product is about 70 at%. So the molar ratio of the iron boride is 30 at%. FeB is generated. The molar ratio of reacted boron in all boron is 20 at%. The molar ratio of reacted boron in plasma is increased by the increase of boron content in feeding powders.

b) Boron rich and metal rich borides

The structure of AlB_{12} includes the B_{12} icosahedrons. In the structure of TiB_2, boron atoms lie in hexagonal aromatic graphite-like layers with a charge of −1 on each boron atom and Ti (II) ions lie between layers.

According to TEM graphs in **Figure 17**, irregular shaped polyhedral nanoparticles are observed in Al-B system, which seems to be caused by the crystal structure of B_{12} clusters, composed of B_{12} icosahedrons and metal atoms. While in Ti-B system, the particles are almost spherical due to the solidification.

The XRD measurements on products were carried out in different initial composition of Al:Ti:B = 1:1:5, 1:1:7, 1:1:15, and 1:1:20, while the input power and inner gas were fixed at 33 kW and helium 5 L/min in **Figure 18**, respectively. TiB_2 was well synthesized in all composition conditions. The main peak of AlB_{12} overlaps with one of characteristic peaks for TiB_2 at 27.8°. For this peak, intensities are almost constant until Al:Ti:B = 1:1:15 even though boron content in raw material is increased. The peak intensity at 27.8°, however, is suddenly increased at the highest boron content condition of Al:Ti:B = 1:1:20. Since AlB_{12} is difficult to

be synthesized with low boron content in feeding powders due to the formation of clusters, it is expected that AlB_{12} is prepared only in the case of Al:Ti:B = 1:1:20. AlB_{10} is also identified only in the same condition. In addition, Gibbs free energy of TiB_2 is lower than that of AlB_{12} in the whole temperature range in fig. 1.

Figure 19 displays the relationship between boron content in feeding powders and the relative XRD intensity of each phase in product. The relative intensity of TiB_2 and AlB_{12} increases with increasing boron content in feeding powders. The increase of boron content improves the forming of B_{12} cluster. The relative intensity of TiB_2 is much higher than that of AlB_{12}, indicating the synthesis of TiB_2 is easier than the generation of AlB_{12} due to the forming of B_{12} cluster.

6.3.4 Size distribution

In Ti-B, Fe-B, Co-B and Ni-B systems, boron nucleates first. Even though plasma power is kept constant, the fraction of evaporated B and Me is different in each system. So the nucleation position and supersaturation ratio are different. In addition, increasing boron content promotes nucleation in the circumstances where larger amount of vapors can simultaneously nucleation, the promoted nucleation generates more nuclei so that each nuclei shares a less amount of vapors with high concentration. Therefore, the size distribution in each system is different.

In Mo-B and Nb-B systems, metal Mo/Nb nucleates first. The nucleation position and the supersaturation ratio in each system are different. In addition, the surface tension of metal is different. So the critical size of metal nuclei is different. Moreover, increasing boron content suppresses nucleation in the circumstances where larger amount of vapors can simultaneously co-condense, the suppressed nucleation generates fewer nuclei so that each nucleus shares a larger amount of vapors. The size distributions in Mo-B and Nb-B systems are different.

According to formation mechanism of nanoparticles, the vapors starts to nucleate at suitable supersaturation ratio, and then it will grow into nanoparticle by condensation and coagulation. The condensation and nucleation are contributed to the vapor consumption. So particle size is determined by vapor pressure distribution and residence time. The residence time can be evaluated by the velocity of plasma flow based on the assumption that the velocities of particle and plasma flow are same. Also the residence time is related with the nucleation position which is determined by the spatial vapor distribution. Therefore, the size distribution mainly results from the spatial vapor distribution and velocity distribution.

a Spatial vapor distribution

The spatial vapor distribution is mainly related to the temperature profile and vapor concentration. So parameters affecting temperature profile and vapor concentration are investigated.

✓ **Powder feed rate**

High powder feed rate results in low plasma temperature and velocity [21]. So the evaporation efficiency is reduced and the residence time becomes long.

In addition, when powder feed rate increases, the amount of evaporated vapor is increased. The nucleation position shifts to more upstream and the nucleation temperature increases. The nucleation rate is reduced according to Eq. (4). So high powder feed rate leads to particles with larger diameter and wide size distribution. Low powder feed rate can obtain uniform temperature and short residence time, thus get narrow size distribution.

✓ **Quenching gas**

Quenching rate could control particle size distribution in plasma [8,22]. In general, the greater the temperature gradients, the smaller are the created nanoparticles. Cooling gas injection quenches the flow and the temperature decreases drastically and radial temperature profile in the downstream region is more uniform. High quenching rate favor the nucleation of smaller particles due to the high nucleation rate, short residence time and smaller vapor consumption of each nucleus. Additionally, injecting quenching gas can reduce the fluid recirculation which results in the aggregation of particles. System with quenching gas can obtain narrow size distribution.

✓ **Particle size of precursors**

Small particles will evaporate at more upstream positions than the larger ones, which have a smoothing effect on the axial vapor distribution due to high heat-transfer coefficient [23,24]. The surface temperature of small particle and the mass fraction of evaporated vapor are increased. At the downstream of the torch the velocity of small particles is higher than that of large particles, and the residence time is short. So small powders provide small particles size and obtain narrow size distribution.

✓ **Plasma power**

The particles provide smaller diameter with high plasma power. High power results in high plasma temperature and particle velocities [25,26]. Since the plasma to particles heat transfer rate increases. The evaporation is increased. On the other hand, because the nucleation process cannot takes place in high temperature region, nucleation start in a relatively downstream position and the residence time is reduced.

✓ **Carrier gas flow rate**

Lower carrier gas flow rate leads to larger particle size. When carrier gas flow rate is increased, the temperature decreases due to the large heat transfer to the cold carrier gas and the velocity is increased. The total power transferred to particles and the evaporation efficiency decrease [27]. So particles have longer residence time to grow large with low gas flow rate.

✓ **Position of injection powder tube**

When the tip of powder injection tube is put into the plasma, it is possible for particles to penetrate the hot zone easily because they are injected after the recirculation zone. However, the unused portion of high temperature plasma flame increases with larger insertion length. In addition, the total flight time of particles in plasma contact decreases with longer insertion length [28]. Thus for the maximum energy transfer efficiency, the nozzle insertion length should be as short as possible.

b Velocity distribution

The lower velocity leads to longer residence time, thus large nanoparticle size. In addition, the evaporation zone is shifted downstream in the plasma for conditions exhibiting increased gas velocities, so the residence time is reduced. Because the velocity distribution mainly depends on the temperature distribution, above methods could be employed to control the residence time indirectly. Also pressure and radius of injection powder tube can affect the velocity directly.

✓ **Pressure**

High pressure can reduce the gas velocity. When the pressure increases, the temperature is

changed a little and the velocity decreases and almost all of the powders evaporated shifted to more upstream along the axis [29]. The increase in discharge pressure (higher density ρ) at constant gas flow rates cause a decrease in gas velocity, since the flow j is constant and the relation $j = \rho v$ applies [30]. Correspondingly, the residence time becomes long. Moreover, condensation prevails over nucleation. As a result, the particles have long residence time to grow large with high pressure.

The decrease of pressure gave the narrowing of size distribution, as the plasma flow at the lower pressure is more strongly suppressed than that at the higher pressure.

✓ **Radius of injection powder tube**

The wider tube leads to large particles due to lower velocity. The velocity decreases with increasing the radius of injection powder tube. And almost all of the powders evaporated shifted to more upstream along the axis. Thus the residence time becomes long [28]. The particles can grow large.

Electric charging, London-van der Waals forces and thermophoresis might all be considered to play a significant role in the growth of nanoparticles.

Therefore, according to spatial effects and the related influence factors, the controllability of particle size can be improved.

6.4 Conclusions

Gibbs free energy, surface tension and nucleation temperature have considerable effect on the composition and diameter of the prepared metal boride nanoparticle in RF thermal plasma. It is demonstrated that the nucleation temperature is the most important factor in control of phase composition of product among Gibbs free energy, surface tension and nucleation temperature. And surface tension has more important influence in the control of particle diameter than the growth in the temperature range between the melting point of metal and boron.

The formation mechanism of metal boride is depended on the nucleation temperature of constituent composition of boride.

For Me-B (Me = Ti, Co, Fe and Ni) system, the saturation vapor pressure of boron is lower than these of metals, starts nucleate first and the vapors of metal and boron co-condense on the surface of existing boron nuclei. The better preparation of metal boride nanoparticle results from the wide temperature range between the nucleation temperature and melting point of boron.

For Me-B (Me = Mo, Nb, Ta and W) system, the saturation vapor pressure of metal is lower than that of boron, starts nucleate first and the vapors of metal and boron co-condense on the surface of existing metal-rich nuclei. The little preparation of metal boride nanoparticle in plasma owe to the narrow temperature range between the nucleation temperature and melting point of metal.

For Me-B (Me = Al and Y), boron vapor is nucleated because nucleation temperature of boron is higher than that of aluminum or yttrium. With the clustering of boron nuclei, metal monomers condensed onto them leading to the growth of boron rich boride nanoparticles.

Therefore, RF thermal plasmas provide a powerful tool for the synthesis of functional metal boride nanoparticles because phase composition and particle diameter can be well controlled.

References

[1] S.W. Thomson, Philosophical Magazine, 4, 448 (1871)

[2] E.R. Lewis, Journal of Aerosol Science, 37, 1605 (2006)

[3] S.K. Friedlander, John Wiley & Sons: New York, 1977

[4] S.L. Girshick, C.P. Chiu and P.H. McMurry, Aerosol Science and Technology, 13, 465 (1990)

[5] R.J.M. Blocherj and I.E. Campbell, Battelle Memorial Institute, 71, 4040 (1949)

[6] J.F. Bilodeaua and P. Proulx, Aerosol Science Technology, 24, 175 (1993)

[7] S.L. Girshick, C.P. Chiu and P.H. McMurry, Plasma Chemistry and Plasma Processing, 8, 145 (1988)

[8] S.L. Girshick and C.P. Chiu, Plasma Chemistry and Plasma Processing, 9, 355 (1989)

[9] S.L. Girshick and C.P. Chiu, Journal of Chemistry Physics, 93, 1273 (1990a)

[10] J.V. Romero, Syracuse University, Graduate School, 2008

[11] D.W. Bullett , Physics & Chemistry of Carbides, Nitrides & Borides, 185, 513 (1990)

[12] M. Shigeta and T. Watanabe, Journal of Materials Research, 20, 2801 (2005)

[13] W.G. Shin, S. Calder, O. Ugurlu and S.L. Girshick, Journal of Nanoparticle Research, 13, 7187 (2011)

[14] G. Guisbiers, M. Kazan, O.V. Overschelde, M. Wautelet and S. Pereira, Journal of Physics Chemistry C, 112, 4097 (2008)

[15] M. Shigeta and T. Watanabe, Thin Solid Films, 515, 4217 (2007)

[16] G. Lins and D.W. Branston, Mie Scattering from Zirconia Evaporating in an Inductively Coupled Plasma

[17] M. Shigeta and T. Watanabe, Journal of Applied Physics, 103, 074903 (2008)

[18] I. Boustani, Physics Review B, 55, 16426 (1997)

[19] W. Hayami and S. Otani, Journal of Physics Chemistry A, 115, 8204 (2011)

[20] M.J. van Setten, M.A. Uijttewaal, G.A. de Wijs and R.A. de Groot, Journal of American Chemistry Society, 129, 2458 (2007)

[21] P. Proulx, J. Mostaghimi and M.I. Boulos, Plasma Chemistry and Plasma Processing, 7, 29 (1987)

[22] M. Shigeta and T. Watanabe, Journal of Applied Physics, 103, 074903 (2008)

[23] F. Marion, R. J. Munz, R. Dolbec, S. Xue, and M.I. Boulos, Effect of plasma power and precursor size distribution on alumina nanoparticles produced in an inductively coupled plasma (ICP) reactor

[24] T. Yoshida and K. Akashi, Journal of Applied Physics, 48, 2252 (1977)

[25] L. Jia and F. Gitzhofer, Plasma Chemistry and Plasma Processing, 29, 497 (2009)

[26] J.W. Shin, H. Miyazoe, M. Leparoux, S. Siegmann, J.L. Dorier and C. Hollenstein, Plasma Sources Science Technology, 15, 441 (2006)

[27] M.M. Hossain, Y. Yao, Y. Oyamatsu, T. Watanabe, F. Funabiki and T. Yano, Proceedings of the 4th WSEAS International Conference on Heat and Mass Transfer, Gold Coast, Queensland, Australia, January 17-19, 2007

[28] M.M. Hossain, Y. Yao and T. Watanabe, Material Science Technology, 393 (2007)

[29] P. Buchner, H. Ferfers, H. Schubert and J. Uhlenbusch, Plasma Sources Science Technology, 6, 450 (1997)

[30] P. Buchner, H. Schubert, J. Uhlenbusch and K. Willee, Plasma Chemistry and Plasma Processing, 19, 341 (1999)

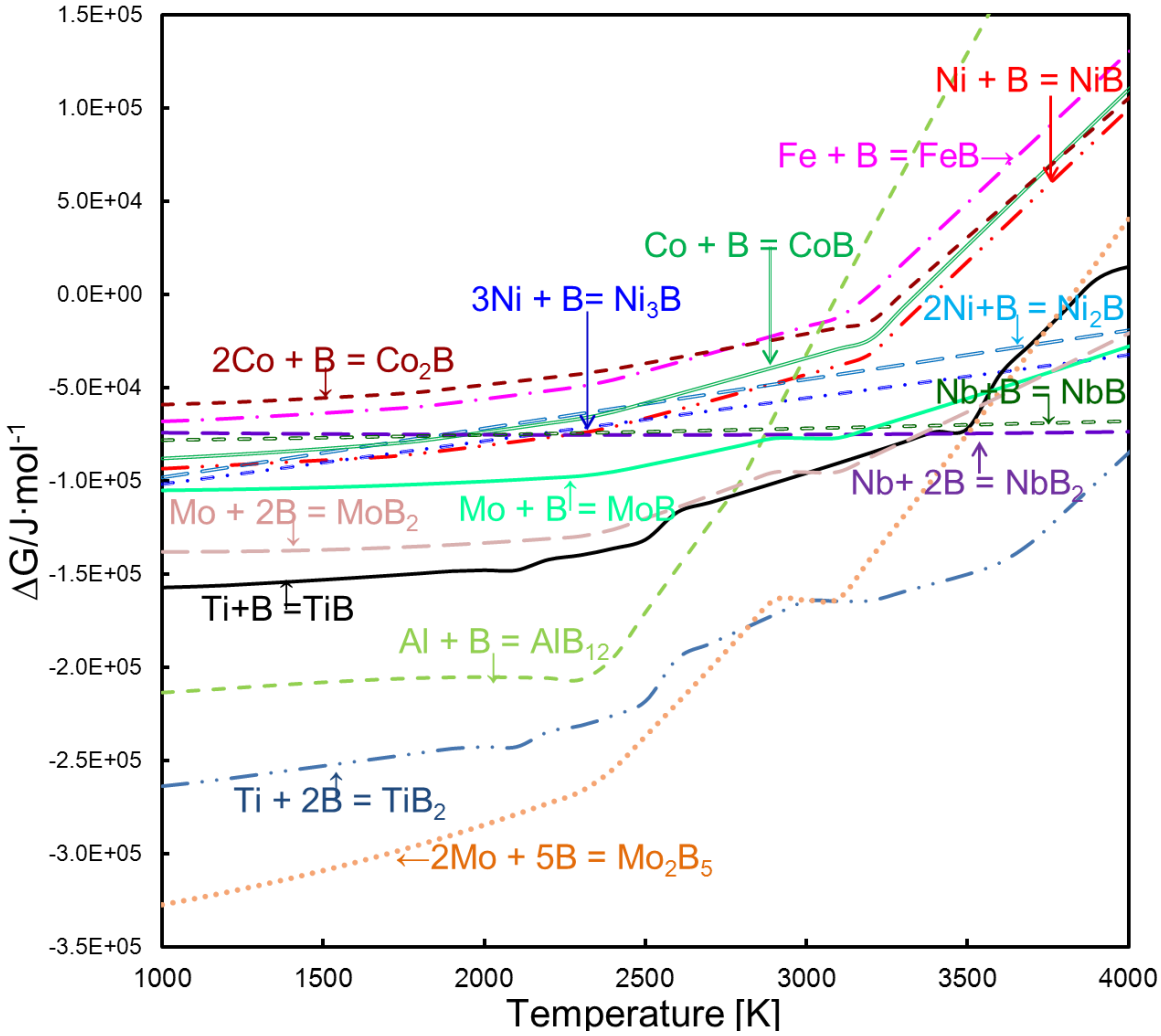

Fig. 1 Gibbs free energy of metal borides.

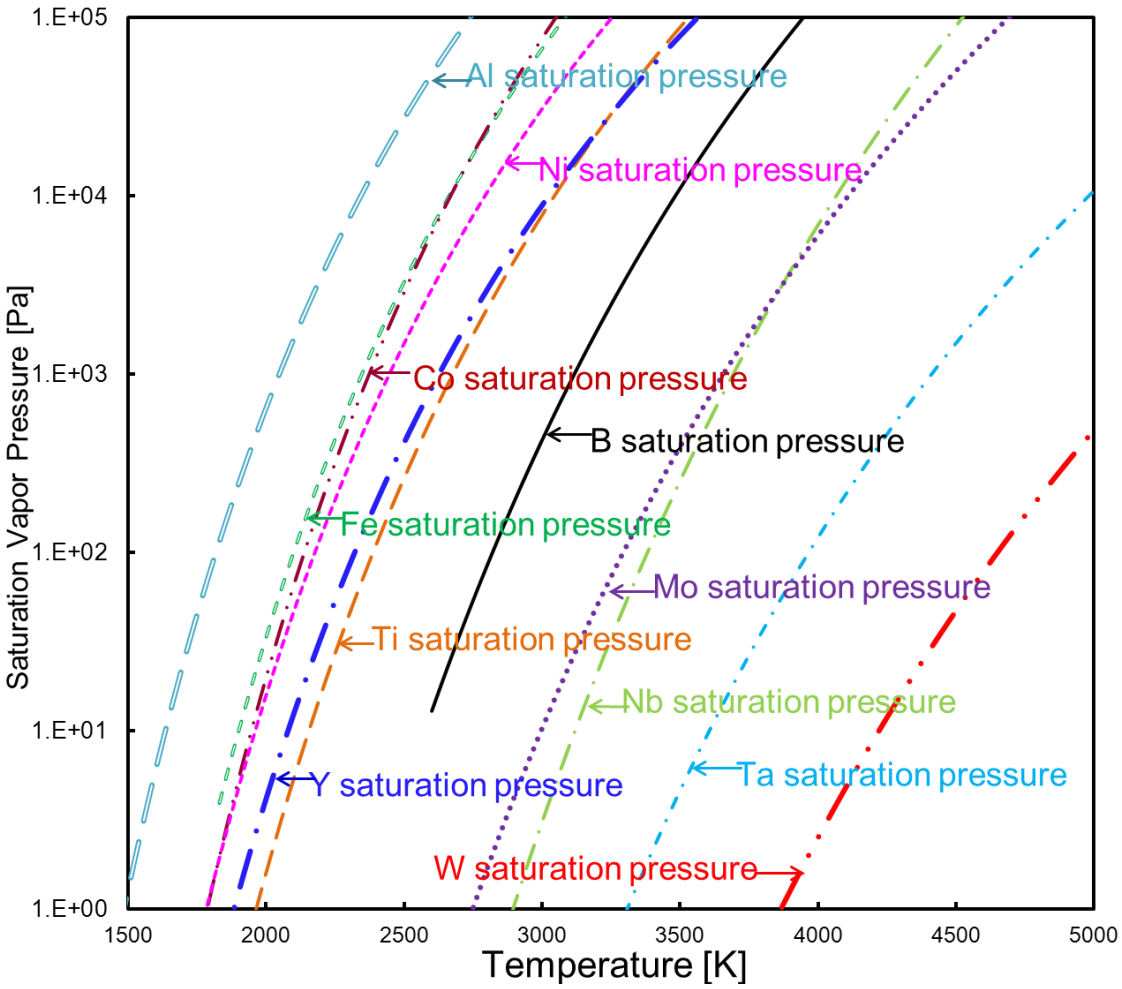

Fig.2 The relationship between temperature and saturation vapor pressure of constituent composition of metal boride.

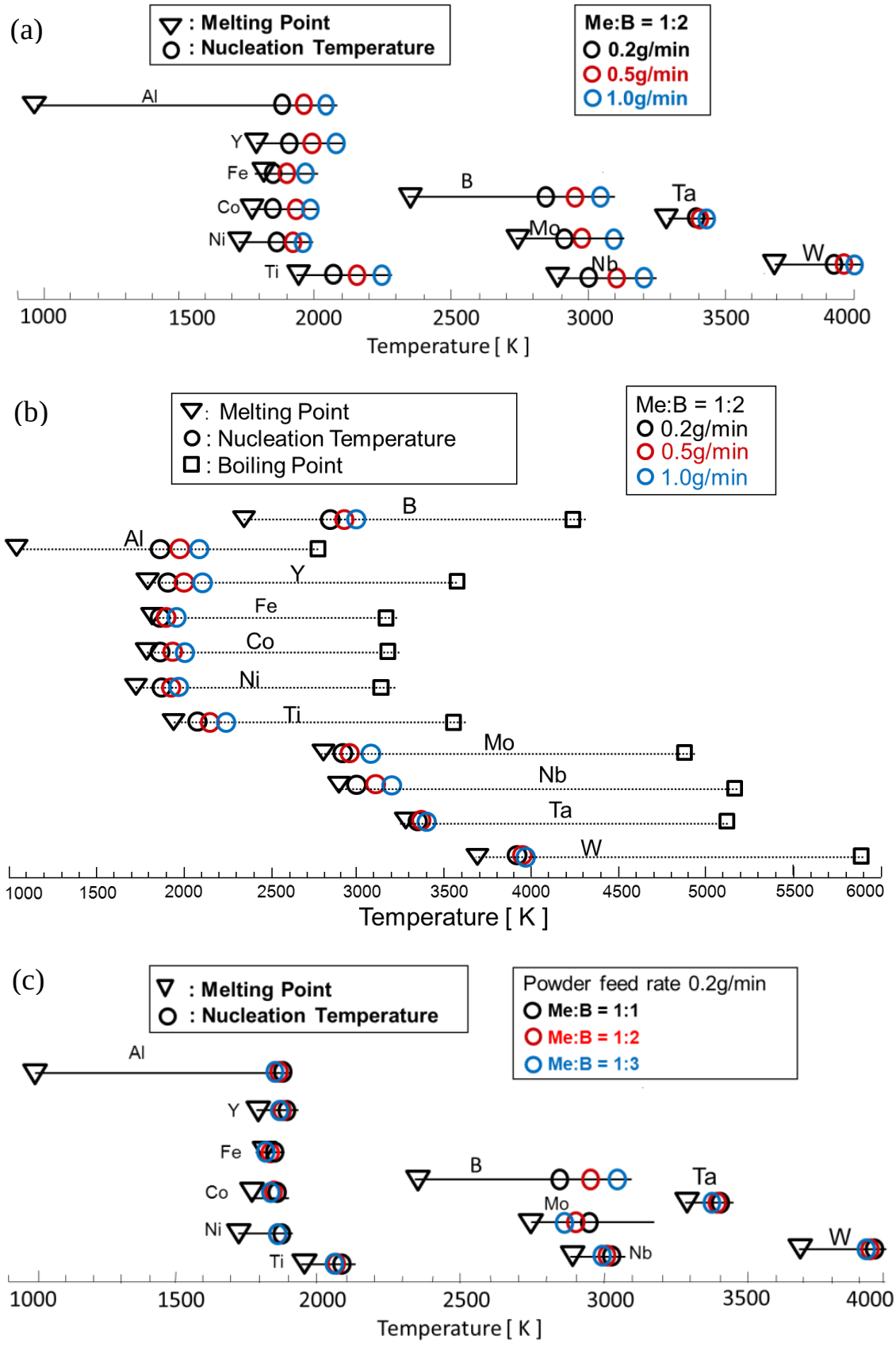
(a)
: Melting Point
: Nucleation Temperature
Me:B = 1:2
0.2g/min
0.5g/min
1.0g/min
Al
Y
Fe
Co
Ni
Ti
B
Ta
Mo
Nb
W
1000
1500
2000
2500
3000
3500
4000
Temperature [K]
(b)
: Melting Point
: Nucleation Temperature
: Boiling Point
Me:B = 1:2
0.2g/min
0.5g/min
1.0g/min
B
Al
Y
Fe
Co
Ni
Ti
Mo
Nb
Ta
W
1000
1500
2000
2500
3000
3500
4000
4500
5000
5500
6000
Temperature [K]
(c)
: Melting Point
: Nucleation Temperature
Powder feed rate 0.2g/min
Me:B = 1:1
Me:B = 1:2
Me:B = 1:3
Al
Y
Fe
Co
Ni
Ti
B
Mo
Nb
Ta
W
1000
1500
2000
2500
3000
3500
4000
Temperature [K]

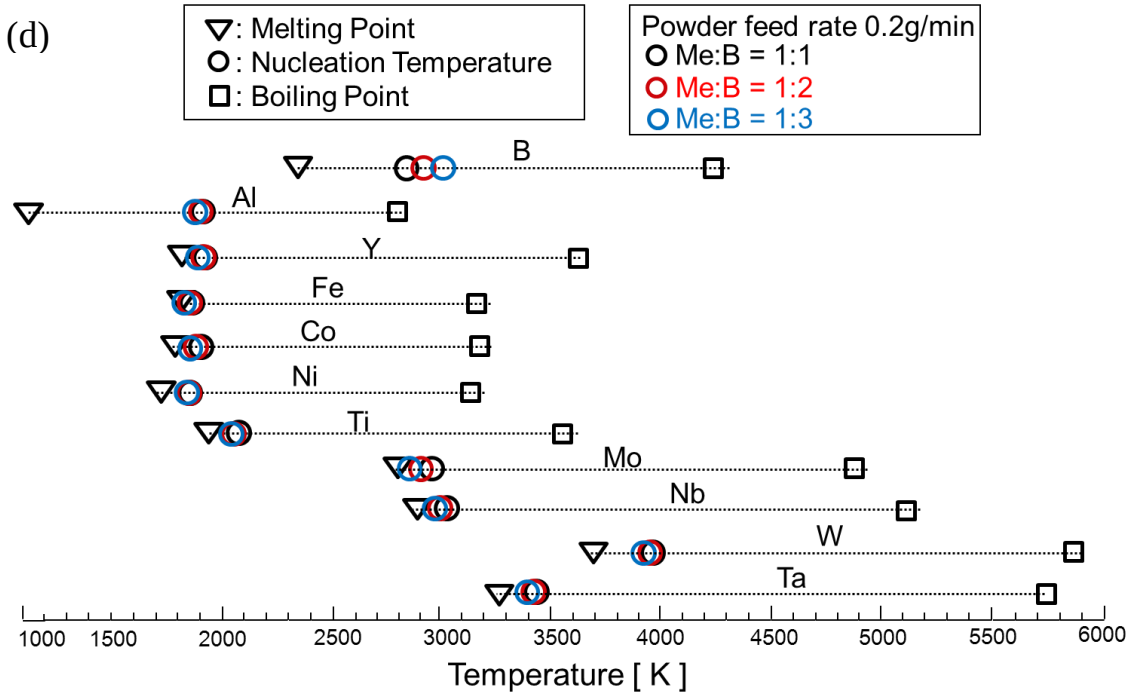

Fig. 3 Nucleation temperature of metal and boron: (a) and (b) Effect of different powder feed rate at the initial composition of Me:B = 1:2 without and with boiling point of metal and boron, respectively; (c) and (d) Effect of different initial composition of Me:B at powder feed rate of 0.2 g/min without and with boiling point of metal and boron, respectively.

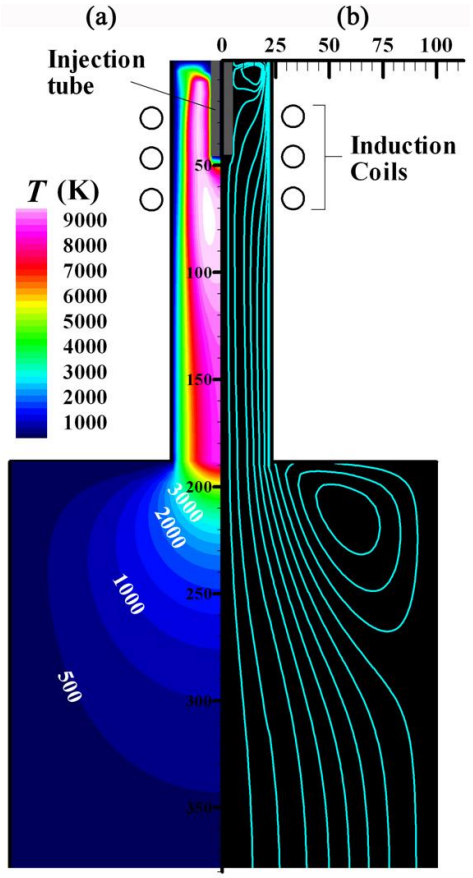

Fig. 4 Thermofluid field in the nanoparticle fabrication system:
(a) temperature and (b) streamlines.

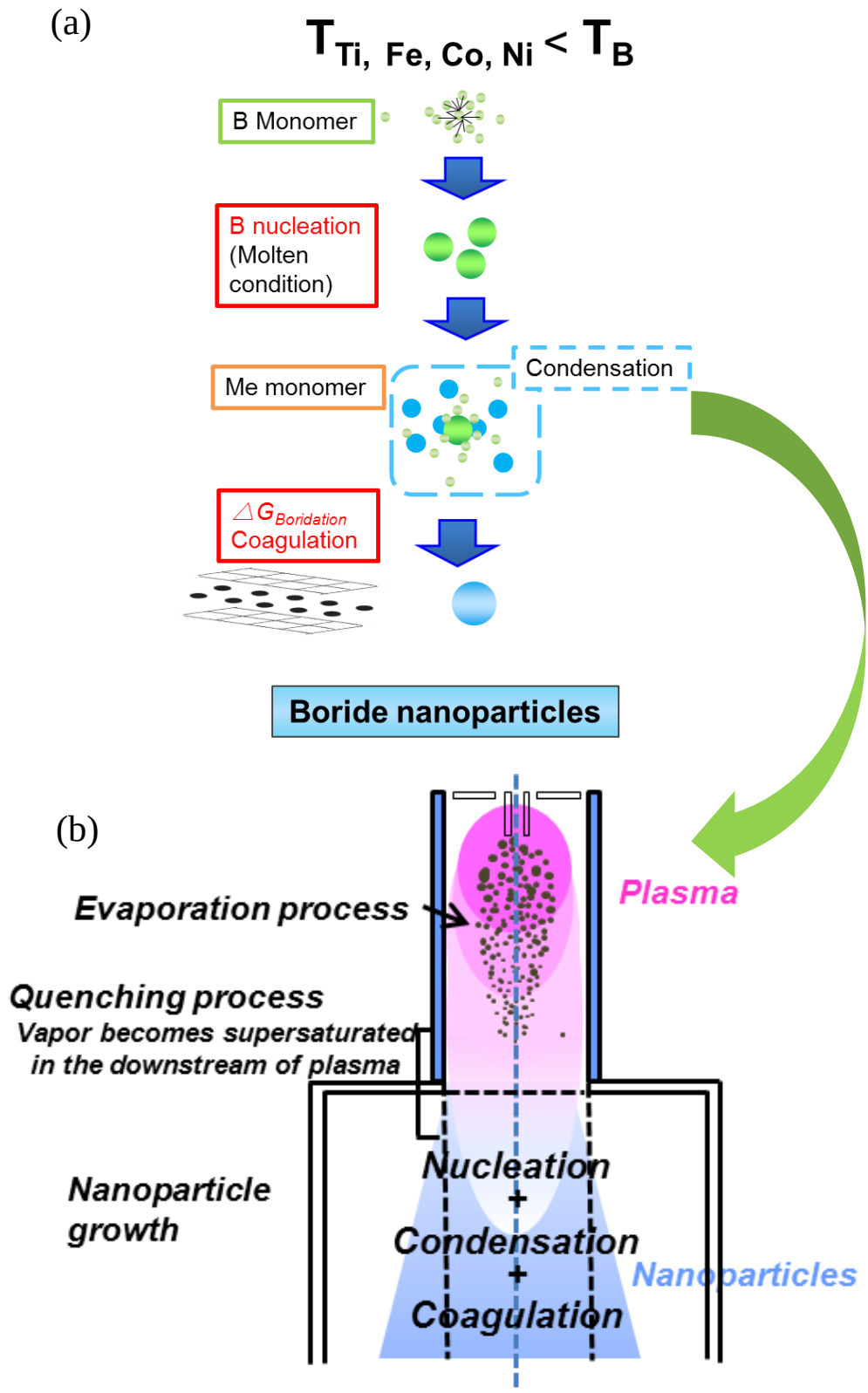

Fig. 5 (a) Formation mechanism of Ti, Fe. Co or Ni boride nanoparticles in RF thermal plasma. (b) Homogeneous nucleation model.

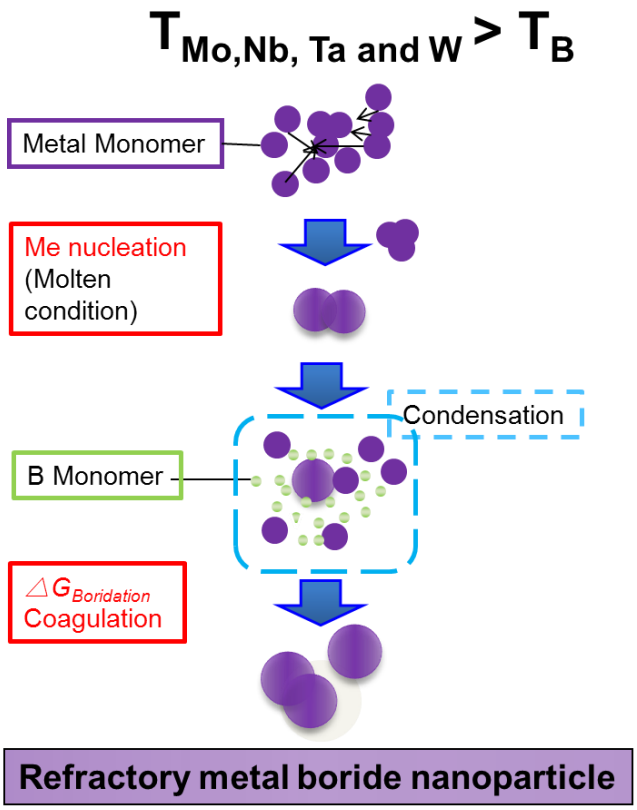

Fig. 6 Formation mechanism of refractory metal boride nanoparticles in RF thermal plasma.

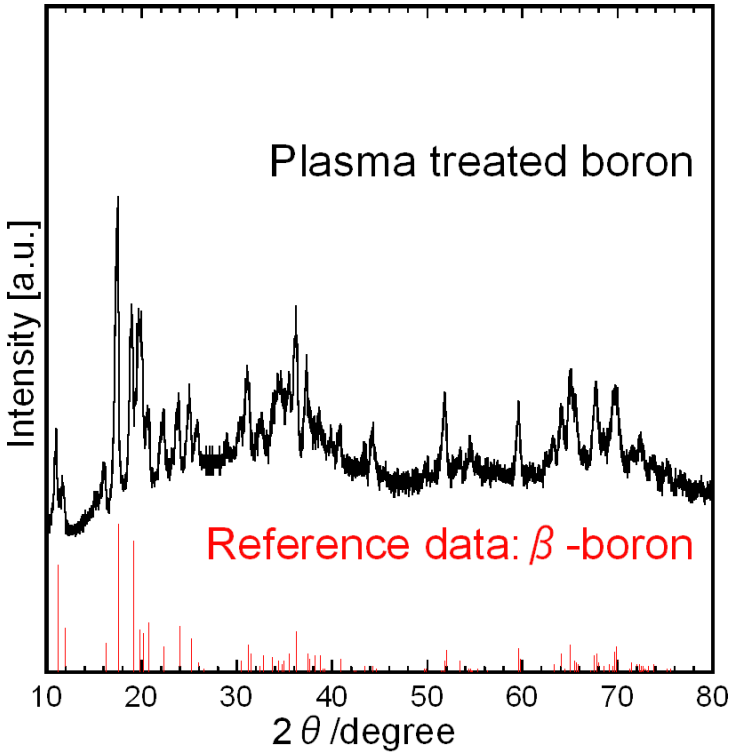

Fig. 7 XRD pattern of plasma treated B nanoparticle with raw material pure boron.

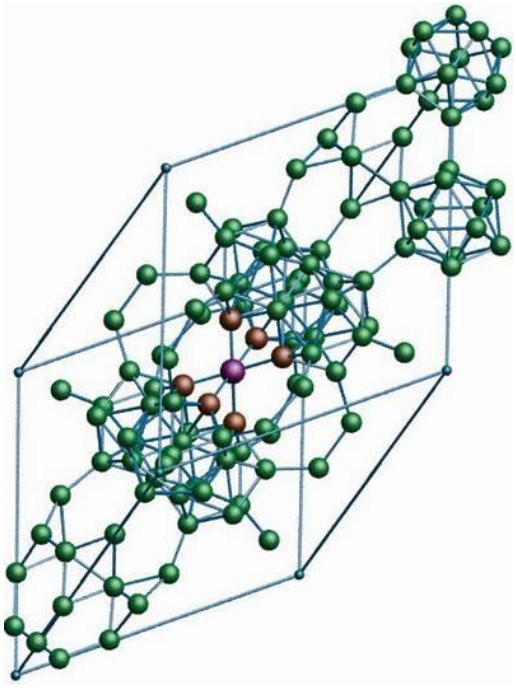

Fig. 8 Structure of β-boron.
(Michiel J. van Setten *et al.* 2007)

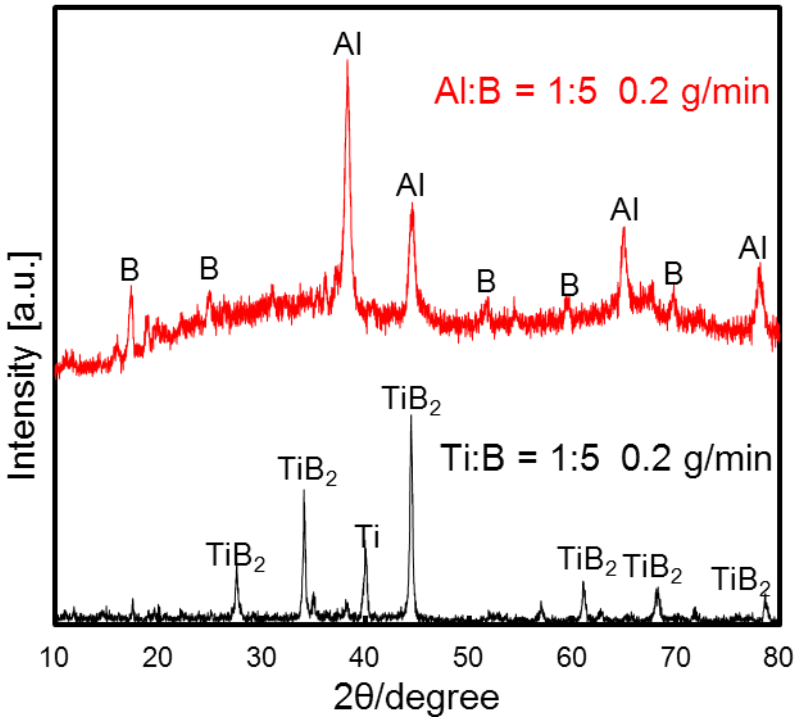

Fig. 9 XRD patterns of product with Me:B = 1:5 in Al-B and Ti-B systems.

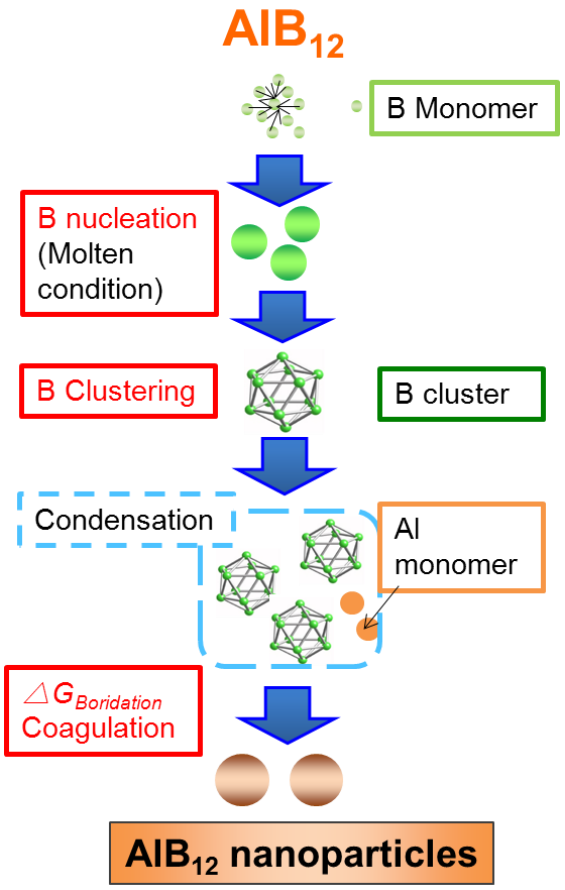

Fig. 10 Formation mechanism of AlB_{12} boride nanoparticles in RF thermal plasma.

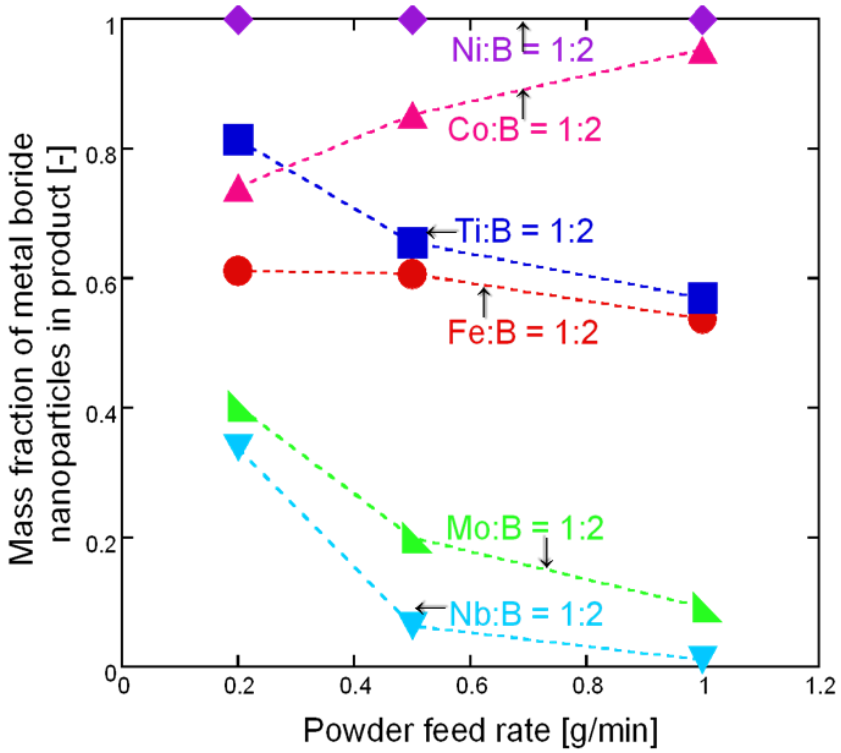

Fig. 11 Effect of powder feed rate on phase composition of product in Mo-B, Nb-B, Ti-B, Co-B, Ni-B and Fe-B systems.

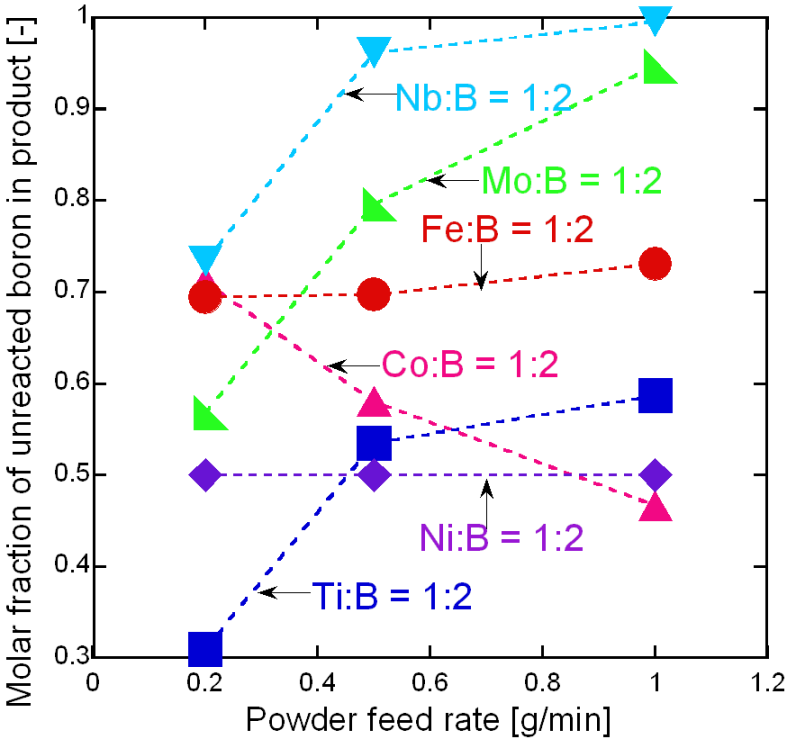

Fig. 12 Effect of powder feed rate on unreacted boron in product in Mo-B, Nb-B, Ti-B, Co-B, Ni-B and Fe-B systems.

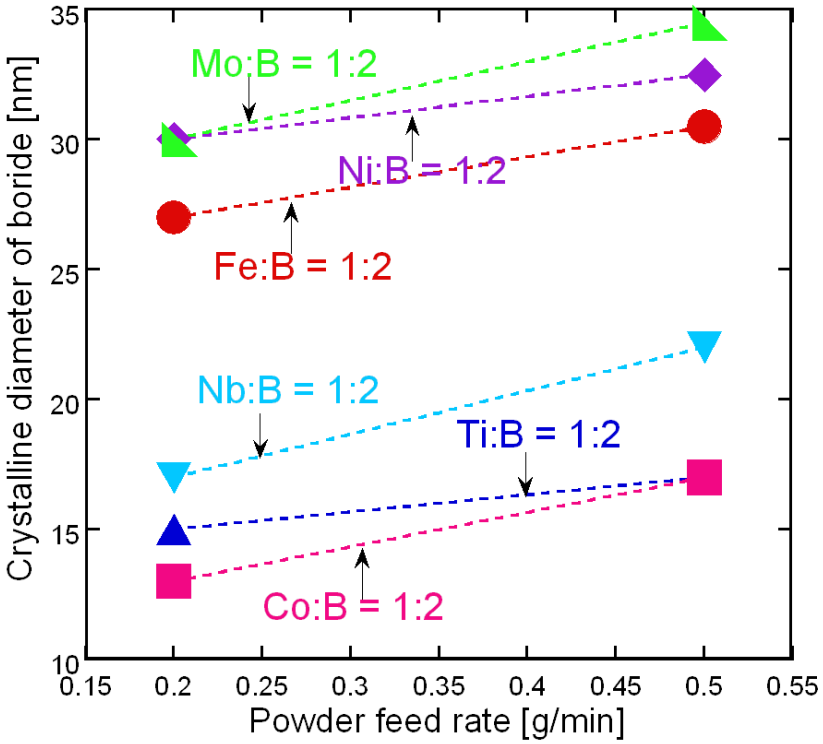

Fig. 13 Effect of powder feed rate on particel diameter of product in Ti-B, Co-B, Fe-B, Ni-B, Nb-B and Mo-B systems.

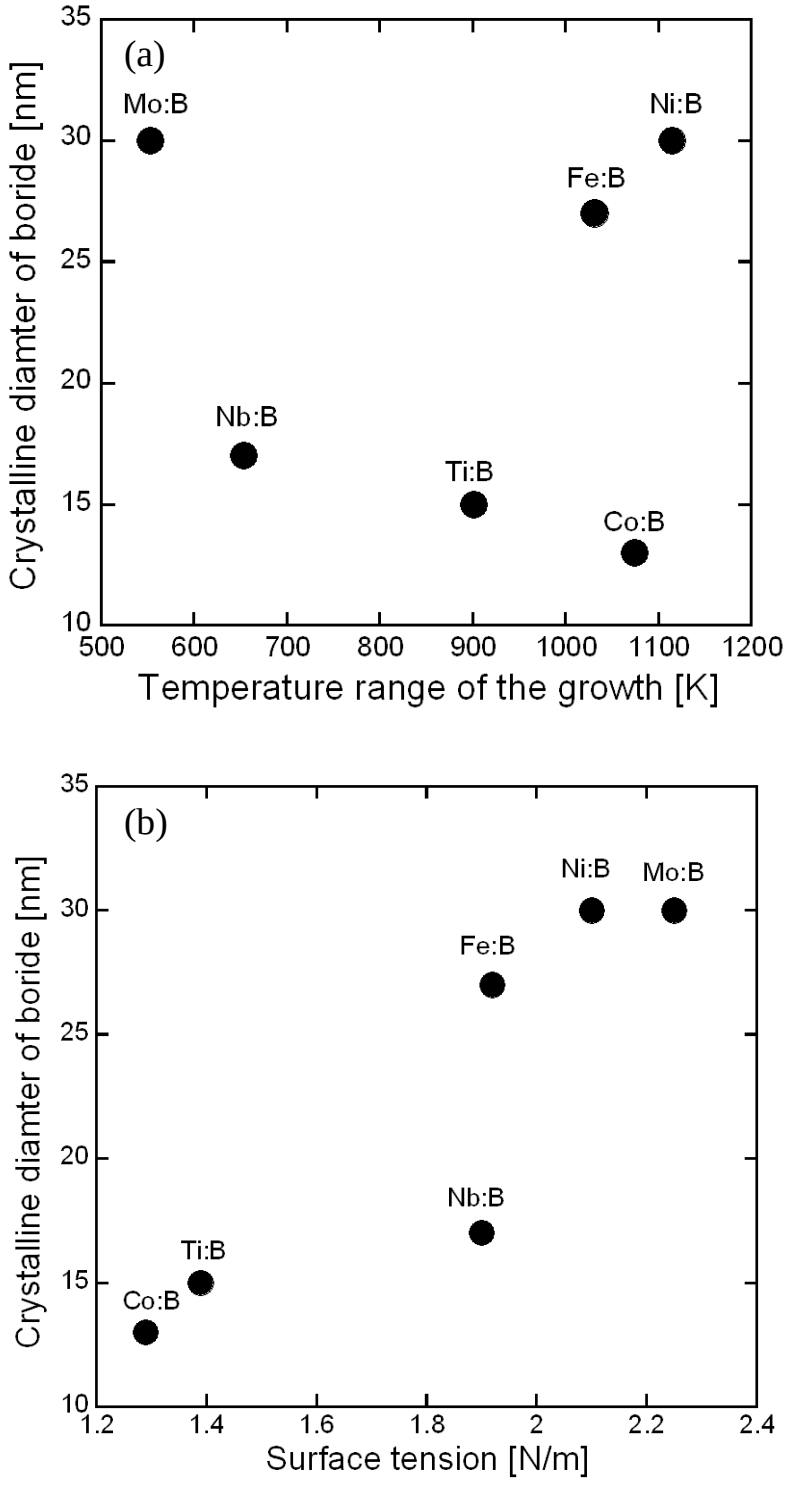

Fig. 14 Effect of the temperature range of the growth and surface tension on the crystalline diameter of boride: (a) Temperature range of the growth (b) Surface tension.

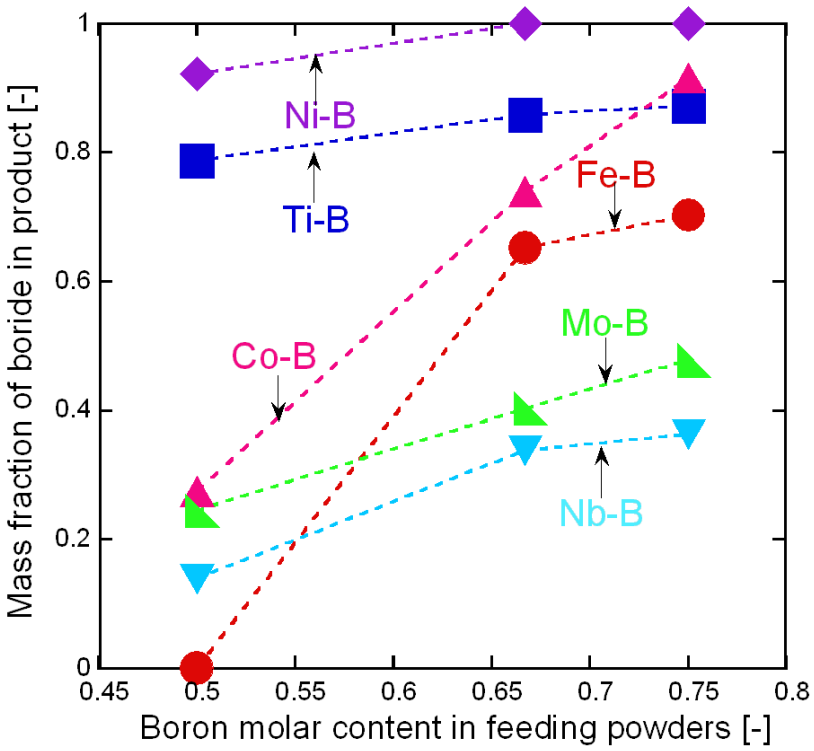

Fig. 15 Effect of boron content in feeding powders on phase composition of product at constant powder feed rate of 0.2 g/min in Mo-B, Nb-B, Ti-B, Co-B, Ni-B and Fe-B systems.

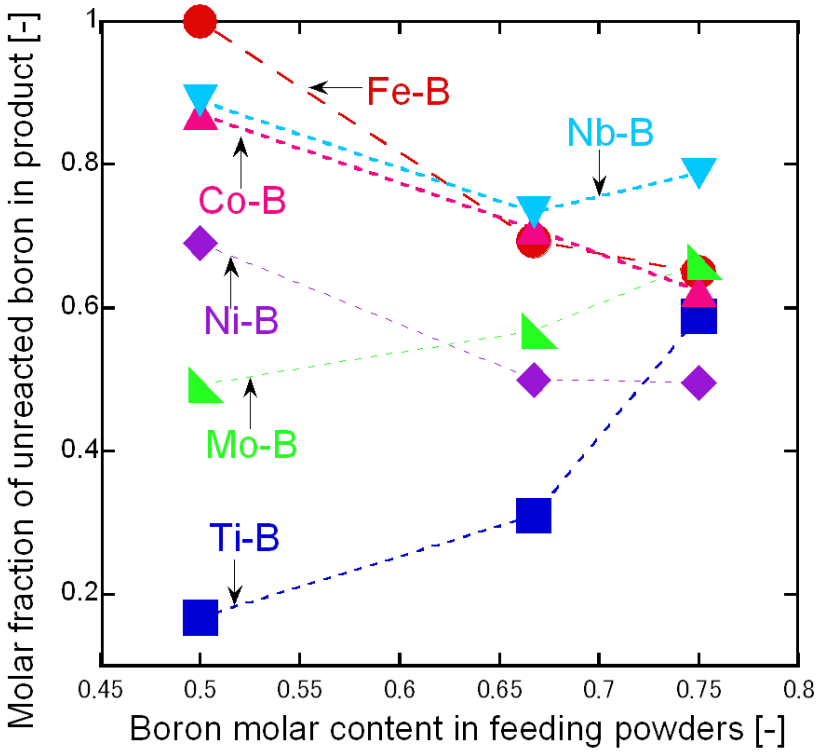

Fig. 16 Effect of boron content in feeding powders on unreacted boron in product at constant powder feed rate of 0.2 g/min in Mo-B, Nb-B, Ti-B, Co-B, Ni-B and Fe-B systems.

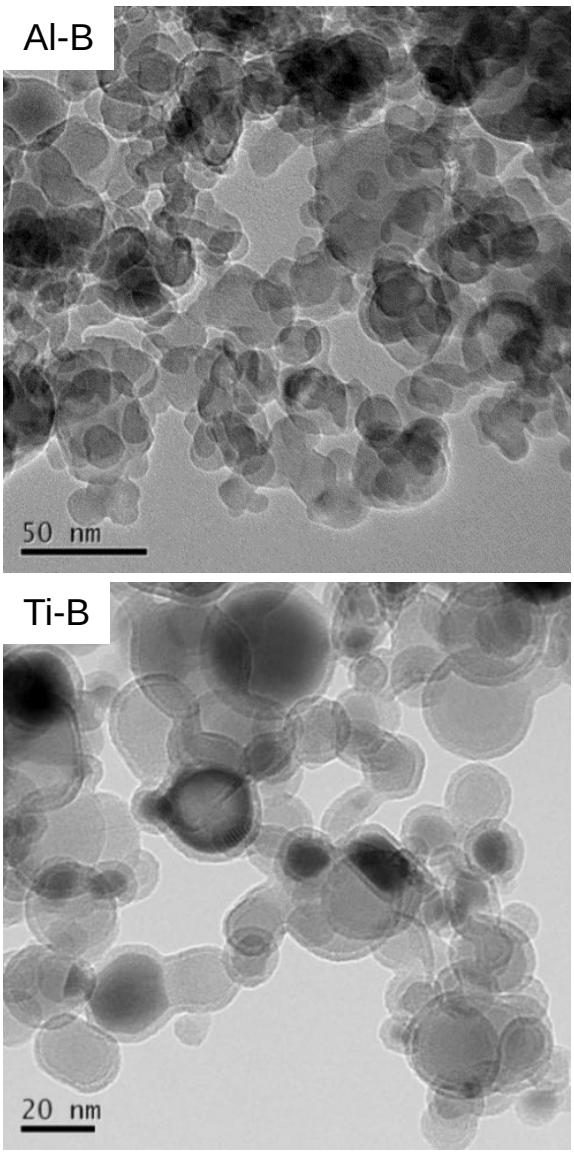

Fig. 17 TEM graphs of particles in Al-B and Ti-B systems.

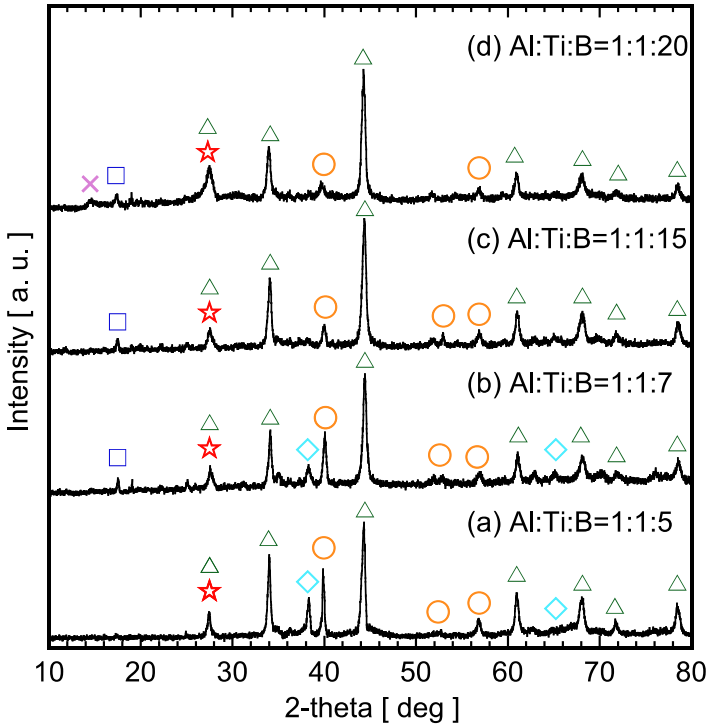

Fig. 18 XRD spectra of prepared particles at different initial composition of Al:Ti:B: (a) 1:1:5, (b) 1:1:7, (c) 1:1:15, (d) 1:1:20; Inner gas: He.
(☆: AlB_{12}, △: TiB_2, ○: Ti, □: B, ◇: Al, ×: AlB_{10})

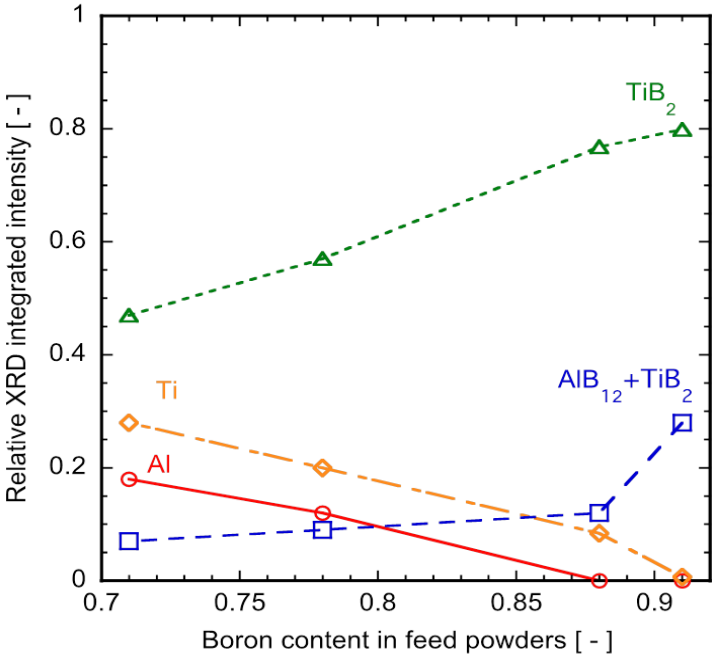

Fig. 19 Integrated intensity of prepared particles at different initial composition.

7. Conclusions

7.1 Summary in this work

RF thermal plasma is considered to be a powerful tool to produce functional metals boride nanoparticles with high purity. The advantages of RF thermal plasma are high purity due to electrodeless, large high temperature area and long residence time owing to low velocity.

In this dissertation, parametric research was carried out to investigate the formation mechanism of metal boride nanoparticle in RF thermal plasma experimentally and numerically. The phase composition and size of particles can be well controlled by the operation conditions of powder feed rate, boron content in feeding powders, work gas species and so on.

Chapter 1 introduces the principles of thermal plasma, and presents the generating methods and applications of thermal plasma in the industry. In addition, the synthesis of different kinds of nanoparticles by RF thermal plasma is displayed in detail.

Chapter 2 explores the successful synthesis of titanium boride nanoparticle in RF thermal plasma from mixture of titanium and boron powders, the comparison of experimental and numerical results were performed. The nucleation temperature plays an important role in the generating titanium boride nanoparticles. The crystalline diameter of as-prepared particles increases with powder feed rate; the mass fraction of titanium boride decreases with increasing powder feed rate. When a larger amount of boron is included in feeding powders, nanoparticles provide a smaller diameter and the mass fraction of TiB decreases in product of TiB and TiB_2. In addition, when He was used as work gas, the synthesis of titanium boride nanoparticle in product was improved due to the high thermal conductivity and electron temperature of He. The decrease of particle diameter and the mass fraction of titanium boride nanoparticle in product results from the increase of carrier gas flow rate. The experimental and numerical results show good agreement that the crystalline diameter of particles increases with powder feed rate and titanium content in feeding powders. In boron-rich condition, the mass fraction of TiB_2 decreases with the increase of powder feed rate. In boron-poor condition, the mass fraction of TiB_2 increases with powder feed rate. Although the numerical analysis predicted some different tendency from the experimental results, the boron-rich condition will be the ideal condition to synthesize titanium boride nanoparticle by RF induction thermal plasma. Based on TEM graphs,

the particles in Ti-B system are all almost spherical and have core-shell structure. The composition of the shell depends on the boron content in feeding powders.

Iron group metals borides were produced by RF thermal plasma in Chapter 3. The synthesis of iron group metals boride is a little difficult compared with that of titanium. The study concluded that RF thermal plasma was effective with the large vapor pressure differences. Powder feed rate and boron content in the feeding powders play an important role in generating the iron group metals boride nanoparticles. The controlled synthesis of metal boride can be achieved. The particle size of particles increases with powder feed rate. Cobalt boride nanoparticles have the smallest diameter due to lowest surface tension, and nickel boride nanoparticles have the largest size. The surface tension is an important factor in the control of particle size. The mass fraction of FeB and Ni_3B in product decreases with the increase of powder feed rate in Fe-B and Ni-B system, respectively. However, the mass fraction of cobalt based boride nanoparticles increases with increasing powder feed rate. Nanoparticles provide a smaller diameter and the mass fraction of metal boride increases in product with higher boron content in feeding powders. Quenching gas plays an important role in the synthesis of metal boride by RF thermal plasma. Based on TEM graphs, the particles in Fe-B, Ni-B and Co-B systems are all almost spherical and have core-shell structure. The composition of the shell depends on the boron content in feeding powders.

Chapter 4 shows the synthesis of refractory metals boride nanoparticles in RF thermal plasma. The refractory metal boride nanoparticles with high purity can be successfully generated from raw materials with high melting/boiling point by RF thermal plasma. The little production of refractory metal boride nanoparticles collected from the reaction chamber wall results from the relatively narrow temperature gap between the nucleation and melting temperatures of metal. The mass fraction of refractory metal boride nanoparticles in product decreases with increasing powder feed rate due to the extended evaporation region of raw materials, and increases with the increase of boron content in feeding powders. High mass fraction of Nb and Mo based boride nanoparticle in product is collected from the collecting filter due to high boiling temperatures of metal and low density of metal boride. Quenching gas improves the synthesis of Ta and W based boride. Based on the numerical simulation, the metal-rich nuclei are generated at the early stage in plasma, and boron vapor spontaneously condenses on the surface of metal-rich nuclei.

Chapter 5 reveals the synthesis of boron rich boride nanoparticles in RF thermal plasma.

Boron-rich boride nanoparticles of AlB_{12} and YB_{66} were synthesized. This is the first time to investigate the synthesis of boron rich boride nanoparticles by RF thermal plasma. The evaporation of boron is a key process for the growth of boron rich boride nanoparticles. For this reason, the productivity of aluminum boride is increased in conditions of high input power, high boron content in raw material and the use of thermally conductive helium as inner gas. Synthesized aluminum boride nanoparticles were polyhedral shape due to the unique crystal structure of boron-rich compounds. Whereas cubic YB_{66} nanoparticles is found when YB_4 and B powders is used as the raw material. Because boron clusters are required to form boron-rich compound, the content of boride nanoparticles in final products is increased with increasing the boron content in feeding powders and the synthesis of boron rich boride is difficult. With the clustering of boron nuclei, aluminum or yttrium monomers condensed onto them leading to the growth of boron-rich boride nanoparticles.

Chapter 6 concluded the formation mechanism of metal boride nanoparticle by RF thermal plasma, which can be divided as metal rich and boron rich boride. Gibbs free energy, surface tension and nucleation temperature have considerable effect on the composition and diameter of metal boride nanoparticle in RF thermal plasma. It is demonstrated that the nucleation temperature is the most important factor in control of phase composition of product. And surface tension has important influence in the control of particle diameter than the growth in the temperature range between the melting point of metal and boron. For Me-B (Me = Ti, Co, Fe and Ni) system, the saturation vapor pressure of boron is lower than these of metals, starts nucleate first and the vapors of metal and boron co-condense on the surface of existing boron nuclei. The better preparation of metal boride nanoparticle results from the wide temperature range between the nucleation temperature and melting point of boron. For Me-B (Me = Mo, Nb, Ta and W) system, the saturation vapor pressure of metal is lower than that of boron, starts nucleate first and the vapors of metal and boron co-condense on the surface of existing metal-rich nuclei. The little preparation of metal boride nanoparticle in plasma owe to the narrow temperature range between the nucleation temperature and melting point of metal. For Me-B (Me = Al and Y), boron vapor is nucleated because nucleation temperature of boron is higher than that of aluminum yttrium. With the clustering of boron nuclei, metal monomers condensed onto them leading to the growth of boron rich boride nanoparticles.

Therefore, RF thermal plasmas provide a powerful tool for the synthesis of functional metal boride nanoparticles because the phase composition and particle diameter can be well

controlled.

7.2 Prospect in future work

This work investigated the synthesis of metal boride nanoparticles by RF thermal plasma. The phase composition and diameter of product can be controlled by operation parameters. According to the phase diagram of Me-B system and XRD results, there are several phases product in each system. The product contains mixture of different phases. It is difficult to produce single phase with high purity in each system. In order to produce single phase metal boride nanoparticle, it is necessary to control the operation parameters. The loading effect (powder feed rate) is chosen.

On the other hand, the coagulation between nanoparticles makes the particles agglomerate, and the size distribution is very large. We first need try to investigate the proper quenching gas configuration to get the well-dispersed nanoparticles and reduce the size distribution, such as radial-top quench or radial-bottom quench. Second, the reactor configuration and the material of the reactor chamber should be investigated. There is a gradual expansion instead of a sudden expansion in the reactor inlet such as alumina-wall reactor design.

The metal boride nanoparticles have many species properties, but we do not know the properties in detail. The controlled synthesis of metal boride nanoparticles is fundamental research and the metal boride nanoparticles with excellent properties should be widely applied for industrial application. It is necessary to investigate the properties particles we prepared by RF thermal plasma.

Especially, Pt catalysts suffer from several drawbacks including low kinetics, high polarization, low resistance to acids and high cost. So a very important challenge is to develop candidate for electrode catalysts that inhibit the poisoning, and increase the rate of the reaction. Titanium and nickel boride nanoparticles have some excellent properties such as excellent electrical conductivity and catalytic activities, high resistance to acids, etc. Titanium and nickel boride are particularly suitable as an electrode catalyst for a fuel cell. However, few studies have been carried out for the investigation of catalytic activity of titanium and nickel boride nanoparticles in fuel cell. In the future research, the investigation of application in fuel cell can be performed.

Acknowledgments

I would like to express my gratitude to all those who helped me during the writing of this thesis. My deepest gratitude goes first and foremost to Professor Takayuki Watanabe, my supervisor, Professor of the Department of Chemical Engineering, Kyushu University, for his assistance, constant encouragements and support throughout my Ph.D. study. With his kind guidance, I was able to participate in various international conferences during my doctor's course in Tokyo Institute of Technology. It is an excellent experience where I got to make new friends from different countries and enrich my life. His guidance, support and encouragement during my studies at Tokyo Institute of Technology are indeed a blessing for me.

I wish to express my sincere appreciation to Dr. Sooseok Choi, research professor of Inha University and Dr. Manabu Tanaka, special associate professor of Department of Environmental Chemistry and Engineering in Tokyo Institute of Technology, for their instructive advice and useful suggestions on my research and life. Appreciation is also extended to Dr. Masaya Shigeta, assistant professor of Department of mechanical Systems and Design in Tohoku University, for his assistance in numerical simulation in finalizing this thesis. I am deeply grateful of their help in the completion of this thesis.

I sincerely thank to all those who contributed to the accomplishment of my work, in particular: I wish to thank to Teisuke Hiyama and JiroMatsuo, Masahito Yagishita, Jun Noda for their help, friendship, and support. Also, I am deeply indebted to all the colleague and friends for their direct and indirect help to me.

Lastly, special thanks are expressed to my beloved family, my parents for their unwavering support, financially and spiritually, during my 28-year journey to achieve the degree of Doctor of Engineering. I believe this dissertation is a blessing not only for me but also for my family.